SISSA
Scuola
Internazionale
Superiore di
Studi Avanzati

Physics Area - PhD course in Statistical Physics

# Chaos and thermalization in semi-classical and Floquet systems

Candidate:
Lorenzo Correale

Advisor:
Alessandro Silva

Academic Year 2022-23

*This thesis is dedicated to Anna Lilian.*
*For the laughs, the tears, the adventures.*

# Preface

Exploring the intricate dynamics of quantum many-body systems, especially in non-equilibrium settings, remains a cornerstone research goal in the realms of condensed matter and statistical physics. The focus has recently turned to isolated systems, attracting theoretical research due to the possibility to manipulate them within advanced experimental platforms. These platforms empower researchers with an unprecedented level of control over quantum matter, ushering in an era where novel phases of matter can be engineered and examined. This progress not only advances our understanding of the fundamental principles governing quantum mechanics but also raises vital questions about how quantum many-body systems approach thermal equilibrium. Understanding the nuances of thermalization is indeed critical for two compelling reasons. Firstly, it poses a fundamental research question, seeking to establish the intricate links between microscopic dynamics and macroscopic thermodynamic behavior. Moreover, thermalization represents a significant impediment in realizing non-equilibrium phases of matter, as it results in the loss of coherence among microscopic degrees of freedom. This issue becomes particularly relevant in periodically driven systems. In many instances, the heating caused by the external drive enables the observation of non-trivial dynamical phases only during a preliminary prethermal stage of the dynamics. Since the foundations of statistical mechanics, thermalization has been also intertwined with the emergence of chaotic properties in dynamics. Given these connections and the challenges posed by non-equilibrium scenarios, also the quantum generalization of chaos has recently emerged as an active research field. Yet, despite the efforts put into both theoretical understanding and experimental exploration over the past two decades, a complete understanding of how chaos, thermalization and their breakdown emerge from the intricate microscopic structure of a many-body system has not been fully achieved.

This thesis represents an attempt to progress in this direction. We adopt a *semi-classical* perspective, which allow us to investigate the out of equilibrium dynamics by employing tools from classical dynamical systems. In pursuit of this goal, we explore two distinct classes of systems. The first class encompasses long-range interacting spins, whose coherent dynamics is effectively classical in the thermodynamic limit. These models often emerge as effective descriptions of experimental setups, as in atomic, molecular and optical systems. The second class of models involves systems with continuous degrees of freedom, where the Planck constant can be tuned as a continuous parameter, thereby controlling the system's "quantumness". According to the quantum-to-classical correspondence principle, much of the quantum dynamics in these systems can be understood through their corresponding classical counterparts. For systems within each of these classes, the scope of this thesis is twofold. First, it

aims to investigate the connections between the emergence of chaos in semi-classical dynamics and their underlying energy landscape. Second, it delves into the dynamics of thermalization and its breakdown in periodically driven systems. Consequently, this thesis is divided into two parts, each addressing one of these objectives and encompassing two chapters.

This thesis work is organized as follows. In Chapter 1, we give a concise historical overview of classical and quantum chaos. We review two key models, which will turn useful for a comparative analysis in later chapters. Additionally, this chapter establishes fundamental concepts of thermalization in quantum systems, offering essential background for the subsequent presentation of our findings. Chapters 2 to 5 house the original contributions of this thesis. In Chapter 2 we study the out of equilibrium dynamics of a long-range $p$-spin model. In the thermodynamic limit, its dynamics is effectively classical and the corresponding energy landscape exhibits few stationary points. We show how tuning a transverse field leads to a transition between two distinct dynamical phases, whose order is connected with the topology of the landscape. We also show that the effect of fluctuations, acting as a self-generated dissipation on top of the classical dynamics, is to either generate an asymptotically stable dynamics or to induce chaos, depending on the stability of the fixed points in the energy landscape. In Chapter 3 we study a $p$-spin glass system. Its complex energy landscape features an exponentially increasing number of stationary points as the system size grows. We show that the chaos emerging in its classical dynamics mirrors the corresponding quantum behavior. Moreover, we show that the degree of classical chaos is correlated with the number of unstable stationary configurations in the landscape. We also discuss the ergodicity of the model. Despite the entirely classical nature of the dynamics, we show that the onset of slow dynamics is detected by an observable traditionally employed to detect ergodicity breaking in quantum spin systems, namely the fidelity susceptibility. In Chapter 4 we shift our focus to periodically driven systems. Here, we observe that the introduction of a smooth periodic driving atop an ergodic system with an unbounded energy spectrum leads to signatures of an emergent conservation law in late-time dynamics. Through an analytical perturbation scheme, we compute the corresponding conserved quantity in specific asymptotic limits. We show that our results apply across different systems, both classical and quantum, without dependency on specific forms of the driving force. Chapter 5 delves into the periodically driven dynamics of long-range interacting systems. We focus on their time-translation symmetry-breaking phases, also known as Floquet time crystals. Here, we introduce a novel order parameter, able to detect the transition from a time crystalline phase to chaos. In this thesis, each chapter is accompanied by a dedicated section providing a concise summary and outlook. In the last Chapter 6 we summarize the key questions that remain unanswered within this work, paving the way for potential future investigations.

# List of publications

[1] **L. Correale** and A. Silva. *Changing the order of a dynamical phase transition through fluctuations in a quantum p-spin model*, arxiv:2110.13524.
Chapter 2.

[2] **L. Correale**, A. Polkovnikov, M. Schirò and A. Silva, *Probing chaos in the spherical p-spin glass model*, SciPost Phys. 15, 190 (2023).
Chapter 3.

[3] G. Giachetti, A. Solfanelli, **L. Correale** and N. Defenu, *Fractal nature of high-order time crystal phases*, Phys. Rev. B 108, L140102 (2023), *(editor's suggestion)*.
Chapter 5.

[4] **L. Correale**, L.F.C. Cugliandolo, M. Schirò and A. Silva, *Heating to finite temperature in periodically driven ergodic systems* (in preparation).
Chapter 4.

# Contents


**1 Introduction** **1**
- 1.1 An historical note on classical chaos . . . 1
- 1.2 From classical to quantum thermalization in closed systems . . . 5
- 1.3 Thermalization in periodically driven isolated many-body systems . . . 7

**I Semi-classical dynamics and chaos in presence of multiple equilibria** **9**

**2 Dynamical phase transitions in long-range spin systems** **11**
- 2.1 The classical limit of fully connected models . . . 12
  - 2.1.1 Dynamics of permutationally invariant models . . . 12
  - 2.1.2 Fully connected spin models . . . 14
- 2.2 Mean -field dynamical transitions in $p$-spin model . . . 15
  - 2.2.1 Classical dynamics following a quench . . . 15
  - 2.2.2 The dynamical phase transition . . . 18
- 2.3 First order transitions driven by non-equilibrium fluctuations . . . 20
  - 2.3.1 Non-equilibrium spin-wave theory . . . 21
  - 2.3.2 Modified non-equilibrium phase diagram . . . 23
  - 2.3.3 The mechanism behind the localization of the magnetization . . . 28
- 2.4 Summary and perspectives . . . 29

**3 Probing chaos in a $p$-spin glass** **31**
- 3.1 Tools for probing chaos in classical and quantum systems . . . 33
  - 3.1.1 Lyapunov exponents . . . 33
  - 3.1.2 Fidelity susceptibility . . . 35
- 3.2 Classical dynamics of the $p$-spin spherical model . . . 37
- 3.3 Results: Chaos indicators . . . 40
- 3.4 Chaos, Ergodicity and Energy Landscape . . . 43
- 3.5 The fidelity susceptibility against the dynamical slowing down . . . 47
- 3.6 Summary and perspectives . . . 49

**II Periodically-driven dynamics of ergodic and long-range systems** **53**

**4 Heating to finite temperature in periodically driven ergodic systems** **55**

4.1 A multiple scale approach to the classical driven Duffing oscillator . . . 56
4.2 The lattice $\phi^4$ model . . . 60
4.3 Periodically driven dynamics in a large-$N$ system: the $p$-spin spherical model . . . 63
4.4 Summary and perspectives . . . 70

**5 From chaos to discrete Floquet time crystals in long-range systems 71**
5.1 Review of discrete Floquet time crystals . . . 72
5.2 The order parameter . . . 73
5.3 The dynamical phase diagram of the Lipkin-Meshkov-Glick model . . . 75
5.3.1 A stroboscopic map for the mean-field dynamics . . . 75
5.3.2 Dynamical phase diagram . . . 77
5.4 Floquet eigenstates at finite size . . . 78
5.5 Beyond mean-field: spin-wave fluctuations . . . 79
5.6 Summary and perspectives . . . 82

**6 Outlook 83**

**Acknowledgements 85**

**A Details on the $p$-spin model without disorder 89**
A.1 The period of classical orbits and its relation with dynamical singularities 89
A.2 Details on the first-order transition line . . . 91

**B Review of the non-equilibrium spin-wave theory 95**
B.1 Rotating frame of reference coordinates . . . 95
B.2 Holstein-Primakoff transformation . . . 96
B.3 Equations of motion for weak spin-wave excitation . . . 97

**C Supplemental details about chaos in the $p$-spin spherical model 101**
C.1 The Truncated Wigner approximation for the p-spin spherical model . 101
C.2 Correlation function on a longer time-scale . . . 102
C.3 Details on the fidelity susceptibility . . . 102
C.4 Calculation of the complexity . . . 105

**D Derivation and details about the Mode-Coupling equations 113**
D.1 Derivation of the mode-coupling equations . . . 113
D.1.1 System-Bath Coupling . . . 114
D.1.2 Disorder Averaging . . . 114
D.1.3 Transformed Order Parameters . . . 115
D.1.4 Saddle-Point Equations . . . 115
D.1.5 Dynamical Equations . . . 117
D.2 The evolution equation for the Lagrange multiplier . . . 117
D.3 Predictor-corrector scheme for the Mode-Coupling equations . . . 118

# Chapter 1

# Introduction

In this chapter, we provide a brief historical overview on chaos and thermalization, focusing on the specific aspects we will delve into in the rest of this thesis. Specifically, in Section 1.1 we review the foundations of classical chaos and ergodicity, established between the 18th and 19th century. In Section 1.2 we review the modern approach to the description of thermalization in isolated, time-independent quantum systems. Finally, in Section 1.3, we explore the extension of the notion of quantum thermalization to periodically driven isolated systems.

## 1.1 An historical note on classical chaos

The exploration of many-body physics has posed a complex challenge since the early days of classical mechanics. As far back as the 17th century, astronomers recognized the intricate nature of celestial motion; for instance, predicting the trajectories of three celestial bodies like the Moon, Earth, and Sun in terms of an explicit solution proved a formidable task. The complexity deepened in the late 19th century, when the mathematician H. Poincaré made a groundbreaking discovery [4]. He found that in the classical dynamics of a three-body problem, there were no analytic conserved quantities, apart from energy. From his discovery, he conjectured that the evolution of three interacting bodies could exhibit a *chaotic* behavior. Chaos, in this context, means that small perturbations in initial conditions could lead to qualitatively different outcomes in the system's future states. Poincaré's revelation carried a profound implication: even within a deterministic framework, a system's dynamics could be *unpredictable*.

Despite their relevance, Poincaré's discoveries remained relatively overlooked by physicists for several decades. The spotlight returned to chaotic behavior only in the 1960s, thanks to meteorologist Edward Lorenz's rediscovery of deterministic chaos in a simplified model for convection [5], a topic we will briefly review in the following. In

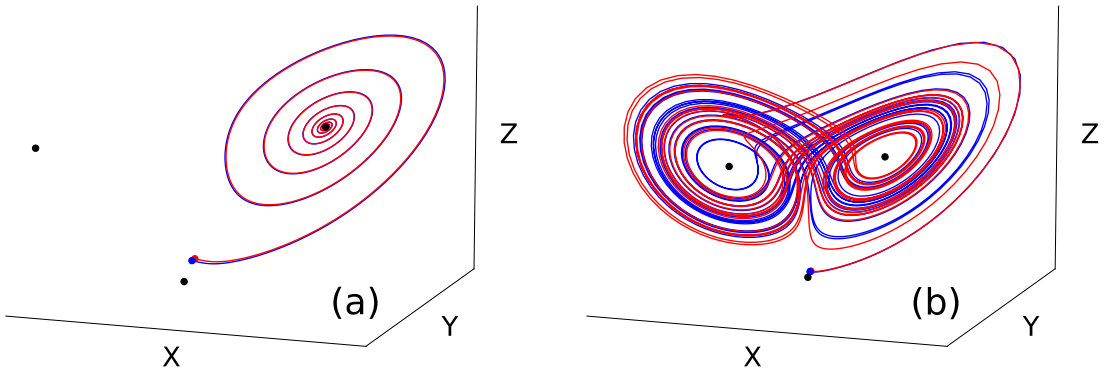


Figure 1.1: Two representative orbits, in blue and red, of the Lorenz model from Eqs. (1.1). The black dots represent the fixed points of the dynamics. We fix $\sigma = 15$ and $\beta = 8/3$. **(a)** $\rho = 10$. The dynamics converges towards a stable fixed point. **(b)** $\rho = 28$. The dynamics is erratic and encompasses the three unstable fixed points.

a nutshell, the Lorenz model consists of a set of three coupled differential equations:

$$\begin{cases} \dfrac{dX}{dt} = \sigma(Y - X) \\ \dfrac{dY}{dt} = X(\rho - Z) - Y \\ \dfrac{dZ}{dt} = XY - \beta Z \ . \end{cases} \tag{1.1}$$

Here, $\sigma$, $\rho$, and $\beta$ represent three dimensionless, positive, and constant parameters. The dynamics of the Lorenz model crucially depends on the interplay among its stationary points. Notably, two different choices of these parameters can lead to distinct outcomes: a configuration with a single stable fixed point or another with three unstable ones[1]. In Fig. 1.1-(a), it is evident that under the first scenario, the dynamics consistently converge toward the only stable and stationary configuration. Conversely, Fig. 1.1-(b) demonstrates that when all fixed points are unstable, the system's behavior becomes chaotic, exhibiting erratic motion encompassing all stationary configurations. This intriguing phenomenon, characterized by the unpredictable and sensitive dependence on initial conditions, was named later on as the *butterfly effect* [6] due to the

[1]It is worth mentioning that these two choices do not encompass all possible stationary point configurations. For a comprehensive analysis, we refer to Ref. [5].

peculiar shape of the subset of phase space where trajectories asymptotically converge. To summarize, the transition to chaos in the Lorenz model is due to a drastic change in the stability properties of its fixed points. This phenomenon, rather general in dynamical systems, is said *Hopf bifurcation* [7]. In Chapters 2 and 3, we will explore how the presence of unstable fixed points is similarly connected to the emergence of chaos in many-body systems.

The establishment of chaos theory alone cannot resolve the paradox that logically arises from Poincaré's studies: the dynamics of a system like the Moon-Earth-Sun system should theoretically be chaotic, yet it is experimentally observed to be regular. In particular, the motion of the Moon-Earth-Sun system appears qualitatively similar to that of *integrable* Hamiltonian systems, where trajectories form regular tori due to the presence of a conservation law for each body. The paradox was resolved between the 1950s and 1960s by Kolmogorov, Arnold, and Moser [8–10]. They rigorously proved that most of the tori that foliate phase space in an integrable system persist under the inclusion of a small, non-integrable perturbation. Their theory was named KAM, an acronym combining their names.

Due to its complexity, we will not delve into the mathematical details of KAM theory here and refer the interested reader to more comprehensive reviews on the topic, such as the ones found in Refs. [11, 12]. Instead, to provide a practical intuition of the KAM theory, we will discuss its application to a prototype model: the kicked rotor. The kicked rotor is a periodically-driven, one dimensional Hamiltonian system, whose time-dependent Hamiltonian is given by

$$\mathcal{H}(\phi, I, t) = \frac{I^2}{2} + h(t)\cos(\phi) \ . \tag{1.2}$$

Here, $\phi$ and $I$ constitute a pair of canonically conjugated angle-action variables, while the field $h(t)$ is expressed as a series of "kicks":

$$h(t) = K \sum_{n=1}^{N} \delta(t - n\mathcal{T}) \ . \tag{1.3}$$

The parameter $K$ controls the strength of the kicks, while their period is $\mathcal{T}$. At stroboscopic times $t_n = n\mathcal{T}$, the dynamics becomes equivalent to the Chirikov standard map [13]:

$$\begin{cases} I_{n+1} &= I_n + K\sin(\phi_n) \\ \phi_{n+1} &= \phi_n + I_{n+1} \ . \end{cases} \tag{1.4}$$

We show the phase portrait of the map in Fig. 1.2, for several values of the kick strength $K$. In the absence of kicks ($K = 0$), the model is integrable, and the phase space is filled with unperturbed tori, represented by straight lines. When a small nonzero kick strength $K$ is introduced, we observe the survival of two types of tori. The first type, known as "separating tori" [14], are smooth KAM deformations of the unperturbed ones. These tori are characterized by the variable $\phi(t)$ covering the entire interval $[0, 2\pi]$. The second type, termed "non-separating", manifests as isolated regions of the phase space. Non-separating tori exhibit finite oscillations of $\phi(t)$ around a fixed

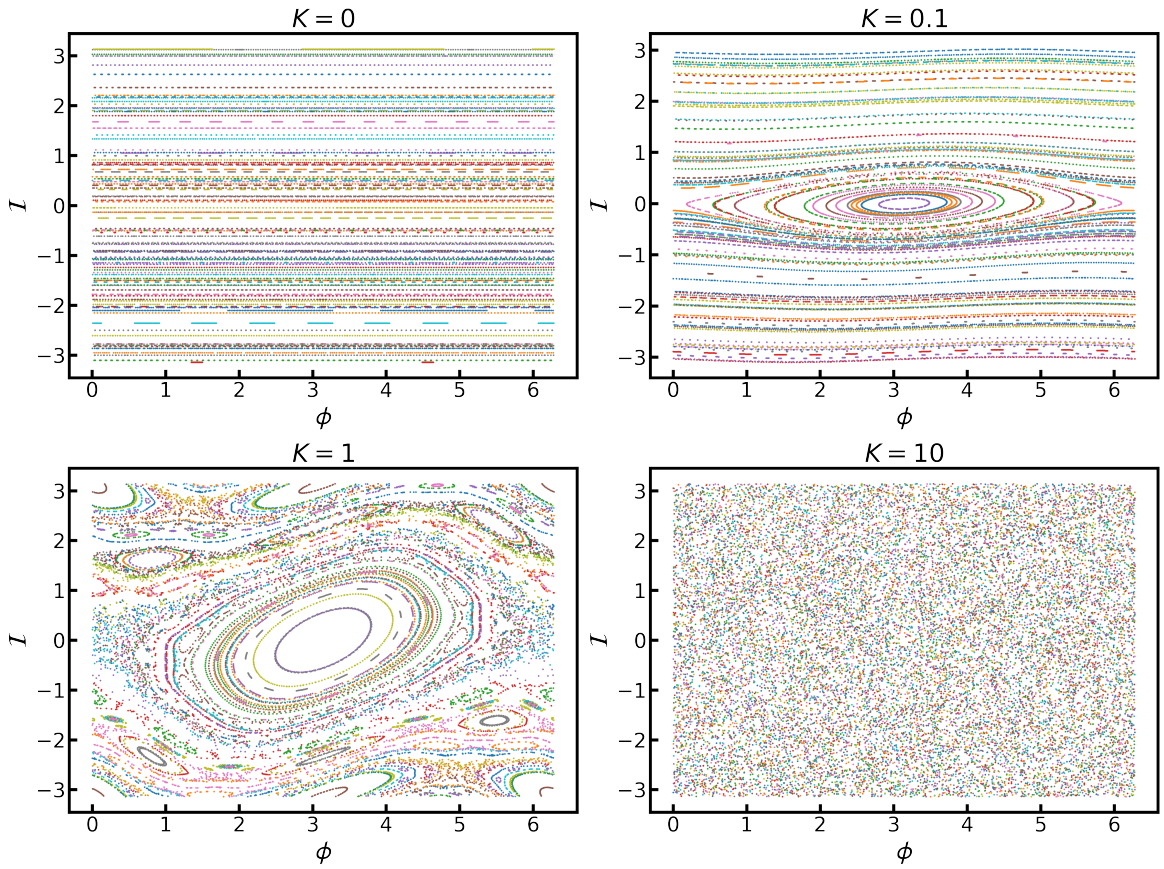


Figure 1.2: Phase portraits of the Chirikov map, defined in Eq. (1.4),for several values of the kick strength $K$. Each portrait is composed by 100 different trajectories, evolving from distinct, randomly sampled initial configurations $(\phi_0, I_0)$. The evolution of each trajectory spans 200 iterations of the Chirikov map.

value. The boundary distinguishing separating and non-separating tori is referred to as a *separatrix*. The presence of island of non-separating tori can not be explained from KAM theory, as they are topologically distinct from the unperturbed ones. Instead, these islands find their origins in the Poincaré-Birkhoff theorem [15, 16]. According to this theorem, every torus with a rotation frequency commensurate with the driving period disintegrates, under the influence of the non-integrable perturbation, into smaller *resonant islands*. For the Chirikov map, these islands correspond precisely to the non-separating tori. By further increasing the kick strength $K$ the tori are progressively swallowed by a chaotic sea. As $K$ exceeds a critical value, the last separating torus dissolves, and the system, initiated from any arbitrary state, displays a diffusive dynamics throughout the entire phase space. When this happens, the corresponding kinetic energy $I_n^2/2$ is expected to grow diffusively, without upper bound.

## 1.2 From classical to quantum thermalization in closed systems

In addition to its inherent complexity, chaos plays a central role in the field of statistical mechanics, serving as the bridge connecting the microscopic behavior of individual particles to the macroscopic thermodynamic properties of closed systems. In classical systems, a chaotic orbit resulting from a time-independent Hamiltonian dynamics is expected densely explore the entire energy manifold over long times[2]. This behavior leads to the convergence of time-averages of local observables toward their microcanonical averages, forming the foundation of the renowned "ergodic hypothesis" [17]. In the transition from classical to quantum dynamics, these classical concepts can not be applied anymore, due to the unitary nature of quantum dynamics. More recently, it has been suggested [18] that the correspondence between ergodicity and chaos in classical systems can be understood through the evolution of observables, specifically *local* ones, rather than focusing on the evolution of states.

To illustrate this framework practically, consider a non-integrable Hamiltonian operator $\hat{H}$ with $N$ degrees of freedom. Assuming there are no degeneracies in the spectrum, each eigenvalue $E_n$ is associated with a unique eigenstate $|E_n\rangle$. Then, the time evolution of the system in isolation, starting from an initial state $|\psi_0\rangle$, can be expressed as follows:

$$|\psi(t)\rangle = \sum_n c_n e^{-iE_n t/\hbar} |E_n\rangle \ . \tag{1.5}$$

Here, $c_n = \langle E_n|\psi_0\rangle$ represents the overlap between the $n$-th eigenstate and the initial state. Throughout our discussion, we assume that the initial state $|\psi_0\rangle$ is associated with an extensive energy and sub-extensive energy fluctuations, satisfying the conditions:

$$\begin{gathered} \langle\psi_0|\hat{H}|\psi_0\rangle = E \propto N \\ \sqrt{\langle\psi_0|\hat{H}^2|\psi_0\rangle - \langle\psi_0|\hat{H}|\psi_0\rangle^2} \propto \sqrt{N} \end{gathered} \tag{1.6}$$

for large $N$. The corresponding evolution of an observable $\hat{O}$ from $|\psi_0\rangle$ can be expressed as

$$\langle\hat{O}(t)\rangle = \sum_{nm} c_n c_m^* e^{i(E_m - E_n)t/\hbar} \langle E_m|\hat{O}|E_n\rangle \ . \tag{1.7}$$

As in classical mechanics, the ergodic hypothesis in quantum systems can formulated by requiring that the infinite-time average of $\langle\hat{O}(t)\rangle$,

$$\overline{O} \equiv \lim_{T\to\infty} \frac{1}{T} \int_0^T dt \, \langle\hat{O}(t)\rangle \ , \tag{1.8}$$

coincides with the *microcanonical* average:

$$\overline{O} = \mathrm{Tr}[\hat{\rho}_{MC}\hat{O}] \equiv \frac{1}{\mathcal{N}(E)\Delta} \sum_{|E_n - E|<\Delta} \langle E_n|\hat{O}|E_n\rangle \ , \tag{1.9}$$

[2]One exception to this behaviour is observed in *glasses*, a class of system we will delve into in Chapter 3.

representing a uniform average over all states within an energy shell around $E$, where the shell width is $\Delta \ll E$. Here, $\mathcal{N}(E)$ denotes the density of states at energy $E$.

We observe that Eq. (1.9) is not satisfied by *all* quantum systems. In fact, the time average $\overline{O}$ can in general be rewritten as

$$\overline{O} = \langle \hat{O} \rangle_{DE} \equiv \sum_n |c_n|^2 \langle E_n | \hat{O} | E_n \rangle \tag{1.10}$$

and is expected to depend on the specific form of the initial state, through the square amplitudes $|c_n|^2$. Instead, Eq. (1.10) coincides with a microcanonical average for a generic initial state satisfying Eqs. (1.6) only if all the diagonal matrix elements $\langle E_n | \hat{O} | E_n \rangle$ match the corresponding microcanonical averages at energy $E_n$. This requirement is nowadays accepted as a quantum extension of ergodic hypothesis and lies at the core of eigenstate thermalization hypothesis (ETH) [19, 20]. In its more refined version, ETH provides an ansatz for the matrix elements of any local observable $\hat{O}$ in the energy basis of an Hamiltonian $\hat{H}$, given by

$$\langle E_n | \hat{O} | E_m \rangle = \mathcal{O}(\overline{E}) \delta_{nm} + e^{-S(\overline{E})/2} f_O(\overline{E}, \omega) R_{nm} \ , \tag{1.11}$$

where $\overline{E} = (E_n + E_m)/2$, $\omega = (E_n - E_m)/2$ and $S(\overline{E}) = \log \mathcal{N}(\overline{E})$ is the thermodynamic entropy. The coefficients $R_{nm}$ are random numbers, with a vanishing average and unit variance. More precisely, the ETH ansatz conjectures that the off-diagonal matrix elements $\langle E_n | \hat{O} | E_m \rangle$ are *pseudo-random* numbers. In the thermodynamic limit $N \to \infty$, their occurrence frequency is set by the statistics of $R_{nm}$. It is important to note that the joint distribution of the variables $R_{nm}$ is non-trivial and and is currently under active investigation in the literature [21–23].

ETH has been verified for a wide range of non-ergodic systems and has many implications on the thermodynamics of the ergodic systems which will not discuss here. We refer the interested reader to the review in Ref. [24]. Here we limit ourselves to mention that the central connection between Eq. (1.11) and the ergodic hypothesis lies in the assumption that the function $\mathcal{O}(E)$ *smoothly* depends on $E$. In this case, it is straightforward to show that $\mathcal{O}(E)$ also coincides with the microcanonical average of $\hat{O}$ and that Eq. (1.9) is satisfied. Interestingly, ETH also implies that the typical deviations in time of $\langle \hat{O}(t) \rangle$ from the microcanonical average are exponentially small from the system size. Quantitatively, this property is obtained from by bounding the time average fluctuations as

$$\overline{O^2} - \overline{O}^2 = \sum_n \sum_{m \neq n} |c_n|^2 |c_m|^2 |O_{mn}|^2 \lesssim \exp[-S(E)] \ , \tag{1.12}$$

where $E$ is again the energy density of the initial state. Thus, the ETH ansatz implies ergodicity in a strong sense.

## 1.3 Thermalization in periodically driven isolated many-body systems

The main assumption underlying both the ergodic hypothesis and ETH is that the asymptotic state is determined by the total energy. However, there are case where even the energy is not a conserved quantity. This occurs, for instance, in periodically driven systems, characterized by a time-dependent Hamiltonian with a period denoted as $\mathcal{T}$. In the quantum domain, the dynamics of an isolated periodically driven system is governed by the Schrodinger equation. Over one cycle, the corresponding unitary evolution operator is given by:

$$\hat{U}_F = \mathrm{T}\left\{\exp\left[-\frac{i}{\hbar}\int_0^{\mathcal{T}} ds\hat{H}(s)\right]\right\} = e^{-i\hat{H}_F\mathcal{T}} \ . \tag{1.13}$$

Here, T represents the time ordering. We will refer to the operator $\hat{U}_F$ as *Floquet operator*. The last equality in Eq. (1.13) arises from the unitarity of $\hat{U}_F$ and the Hermitian operator $\hat{H}_F$ at the exponent is commonly known as *Floquet Hamiltonian* [25]. Notably, the Floquet operator can be decomposed as

$$\hat{U}_F = \sum_m |\eta_m\rangle\, e^{-im\phi_m}\, \langle\eta_m| \ , \tag{1.14}$$

where the phases $\phi_m$ are defined modulo $2\pi$. We will use the term *Floquet eigenstates* to refer to the states $|\eta_m\rangle$.

For an interacting and ergodic many-body system, one might expect that its thermalization properties can be obtained by using an ansatz akin to ETH, applied to the Floquet Hamiltonian $\hat{H}_F$. However, as observed in previous studies [25–27], this is generally not the case. To understand why, let us consider a system evolving from an initial state $|\psi_0\rangle$. The long time average of any local observable $\hat{O}$, as given from Eq. (1.8), is still associated with an average over a diagonal ensemble, expressed as:

$$\overline{O} = \sum_m |\,\langle\eta_m|\psi_0\rangle\,|^2\, \langle\eta_m|\hat{O}|\eta_m|\rangle \ . \tag{1.15}$$

The crucial observation from Refs. [25–27] is that the elements $\langle\eta_m|\hat{O}|\eta_m\rangle$ are completely independent from the phases $\phi_m$, except for finite size fluctuations, instead of being a smooth function of $\phi_m$. Specifically, these studies revealed that each diagonal matrix elements approximately coincide with a featureless, infinite-temperature average:

$$\langle\eta_m|\hat{O}|\eta_m\rangle \simeq \frac{1}{\mathcal{D}}\sum_m \langle\eta_m|\hat{O}|\eta_m|\rangle \ , \tag{1.16}$$

where $\mathcal{D}$ is the size of the many-body Hilbert space. Remarkably, it was observed that the time evolution of a local observable, $\hat{O}(t)$, consistently relaxes at long time to this infinite temperature state. Additionally, these studies consistently ruled out the possibility that $\hat{H}_F$ could be a well-defined conserved quantity of the dynamics, as its

spectral properties did not align with the typical ones of a local Hamiltonian.

The observations outlined above have been justified through numerical simulations on specific spin-1/2 chains. Subsequently, similar results where retrieved for a larger class of quantum [28–32] and classical [31, 33, 34] systems. These investigations encompassed systems characterized by either a *bounded* energy spectrum [28, 32–34] or cases where the driving force consisted of a series of kicks acting upon an otherwise integrable dynamics. In the latter scenario, akin to the many-body version of the kicked rotor defined in Eq. (1.2), the relaxation to infinite temperature manifested as an unbounded growth in the system's energy density over time. In Chapter 4, we will consider a third scenario, by exploring the behavior of an ergodic many-body system possessing an unbounded energy spectrum when subjected to a smooth periodic force.

# Part I

# Semi-classical dynamics and chaos in presence of multiple equilibria

# Chapter 2

# Dynamical phase transitions in long-range spin systems

As we discussed in Chapter 1, an ingredient that often recurs in the generation of dynamical chaos is the presence of multiple equilibrium configurations. In statistical mechanics, this aspect holds significant interest, especially from a thermodynamic perspective, as the presence of more energy minima is often linked to the symmetry-breaking phenomena fundamental to equilibrium phase transitions [35]. Moreover, equilibrium criticality is known to leave a signatures in the non-equilibrium dynamics of a quantum many-body system [36–42]: one example is given by dynamical phase transitions (DPTs). In this chapter, we will investigate the occurrence of these transitions in long-range models, as well as their possible disruption due to the emergence of chaos once fluctuations are included.

A dynamical quantum criticality can be observed for example as singular temporal patterns in the Loschmidt echo (LE), particularly following a quench across a quantum phase transition [43–45]. This phenomenon occurs even when long-range order cannot be maintained in stationary states. However, in systems with long-range interactions, a distinctive Landau-type critical behavior emerges, intertwined with the singular characteristics of the LE [46]. This behavior is characterized by the dependence of a time-averaged order parameter on the quench parameters [47, 48]. Peculiar to the dynamical transitions occurring in long-range models is their association with critical trajectories characterized by a divergent time scale in the dynamics, marking the separation between revivals with a finite order parameter [46]. When fluctuations are introduced, these critical trajectories become unstable, and second-order dynamical critical points widen up into chaotic dynamical phases [49–52].

The previously discussed DPTs are primarily second-order transitions, like their equilibrium counterparts occuring within the same models. The concept of dynamical criticality has been overall less explored in systems exhibiting first-order equilibrium transitions, with few exceptions [53, 54]. In this chapter, we delve into this underexplored area by investigating possible dynamical phase transitions and their stability against fluctuations in a system displaying a first-order equilibrium transition: a spin system featuring infinite-range $p$-spin interactions and coupled to a global transverse

field. At the mean-field level, its dynamics is effectively classical [47]. We show that the system undergoes a DPT following a quench of the transverse field $g$. The order of this DPT is determined by the parity of $p$, despite its equilibrium counterpart always being of the first order. In particular, we show that the order of the dynamical transition can be deduced entirely from the interplay between the various equilibria present in the underlying energy landscape. We then perturb the model by a short-range two-body interaction, enabling spin fluctuations [49, 50, 55]. While for $p = 2$ a chaotic dynamical region opens up near mean-field criticality [49, 50], we show that for $p > 2$ dynamical chaos is almost entirely replaced by a new prethermal regime, which we define as "dynamical paramagnetic phase", appearing for sufficiently large short-range coupling. This is due to the emission of energy in the form of spin-waves, which predominantly drive the system into a paramagnetic minimum even in the presence of other minima in the energy landscape.

The chapter is structured as follows. In Section 2.1, we provide an overview of the general theory governing the dynamics of fully connected models, introduced in Ref. [47]. Then, in Section 2.2, we apply this theory to explore dynamical transitions in the fully connected $p$-spin model. Finally, in Section 2.3, we discuss the impact of fluctuations on the mean-field dynamics.

## 2.1 The classical limit of fully connected models

Whenever a system displays infinite-range interactions, mean-field theory is intuitively expected to become exact in the thermodynamic limit. In the context of equilibrium statistical mechanics, this assertion is well-established and can be found in standard textbooks [35]. The extension of this notion to the non-equilibrium quantum dynamics has been formulated much later, in the general theory developed from B. Sciolla and G. Biroli in Ref. [47]. The key result of the theory is that when the Hamiltonian of a quantum system remains invariant under arbitrary permutations of its elementary degrees of freedom, the corresponding quantum dynamics, when initialized in the totally symmetric subspace, becomes effectively low-dimensional. Quantum fluctuations are controlled by an effective Planck constant $\hbar_{eff} \sim \hbar/N$, where $N$ is the number of the original degrees of freedom. In the following, we will first describe general theory of Ref. [47], then we will specialize our discussion to spin systems, which will be our subject of interest in the rest of this chapter.

### 2.1.1 Dynamics of permutationally invariant models

To set the stage, we consider a quantum system made of $N$ identical $q$-level systems, each of them defining a microscopic degree of freedom. A basis of the many-body Hilbert space can then be constructed as the tensor product of identical single-unit bases $\{|\alpha\rangle\}$, with $\alpha = 1, \dots, q$. We also define a binary permutation as any unitary transformation $\hat{P}_{ij}$ exchanging to a pair of degrees of freedom in the tensor product

basis, that is

$$\hat{P}_{ij} \left|\alpha_1, \ldots, \alpha_i, \ldots, \alpha_j, \ldots, \alpha_N\right\rangle = \left|\alpha_1, \ldots, \alpha_j, \ldots, \alpha_i, \ldots, \alpha_N\right\rangle \ , \tag{2.1}$$

for every pair $i, j$, with $i < j$. Any more general permutation can then be obtained by arbitrary combination of binary permutations operators. Within this framework, an Hamiltonian is said to display full permutational symmetry if it commutes with $\hat{P}_{ij}$ for any choice of $i$ and $j$. Although binary permutations do not all commute with each other, it is in general possible to find a nontrivial subspace of the full many-body Hilbert space which is simultaneously invariant under all permutations. We call this subspace as the totally-symmetric subspace (TSS). A basis for the TSS can be straightforwardly obtained by symmetrization of the tensor product basis $|\boldsymbol{\alpha}\rangle = |\alpha_1, \ldots, \alpha_N\rangle$. The corresponding symmetrized states can then be univoquely labelled by the occupation numbers $N_1, \ldots, N_q$ of each orbital, with $\sum_i N_i = N$. Such states can be expressed as

$$|N_1, \ldots, N_q\rangle \propto \sum_{\boldsymbol{\alpha} \in [N_1, \ldots, N_q]} |\boldsymbol{\alpha}\rangle \tag{2.2}$$

where the sum is restricted to the configurations of $\alpha_1, \ldots, \alpha_N$ compatible with the chosen occupation numbers. The dimension of the TSS is equal to the number of partitions of $N$ into $q$ non-negative integers, given by [56]

$$\dim \mathrm{TSS} = \binom{N+q-1}{q-1} \underset{N\to\infty}{\sim} \frac{N^{q-1}}{(q-1)!} \ , \tag{2.3}$$

and scales only polynomially in $N$, allowing for a numerical analysis even for large values of $N$.

The main result of Ref. [47] is that the dynamics of intensive observable into the TSS is effectively classical in the thermodynamic limit. To prove it, we straightforwardly project the Schrodinger dynamics into the TSS. We first consider two generic states belonging to the TSS, $|N_1, \ldots, N_q\rangle$ and

$$|N_1 + m_1, \ldots, N_q + m_q\rangle \tag{2.4}$$

where $\mathbf{m} = (m_1, \ldots, m_q) \in \mathbb{Z}^q$, and compute the matrix elements of the Hamiltonian between two such states. For convenience, we also replace the occupation numbers $N_\alpha$ with the fractions $x_\alpha = N_\alpha / N$, with $0 \leq x_\alpha \leq 1$ and $\sum_{\alpha=1}^{q} x_\alpha = 1$, and denote the basis states as $|\mathbf{x}\rangle = |x_1, \ldots, x_q\rangle$. With this notation, a matrix element of the Hamiltonian can in general be expressed as

$$\langle \mathbf{x}| \hat{H} |\mathbf{x}'\rangle = V(\mathbf{x}) \delta_{\mathbf{x},\mathbf{x}'} - \sum_{\mathbf{m} \neq \mathbf{0}} T_{\mathbf{m}}(\mathbf{x}) \delta_{\mathbf{x},\mathbf{x}'+\mathbf{m}/N} \ , \tag{2.5}$$

where we separated the diagonal part from the off-diagonal one. We also assume time-reversal symmetry of the problem, implying that $T_{\mathbf{m}}(\mathbf{x})$ is real. In the rest of this chapter, we will focus on physical Hamiltonians which are extensive and local. The first property implies that both $V(\mathbf{x})$ and $T_{\mathbf{m}}(\mathbf{x})$ are extensive quantities, so we may rewrite them as

$$V(\mathbf{x}) \sim N v(\mathbf{x}) \ , \qquad T_{\mathbf{m}}(\mathbf{x}) \sim N t_{\mathbf{m}}(\mathbf{x}) \ . \tag{2.6}$$

In the thermodynamic limit $N \to \infty$, the extensivity of $\hat{H}$ also guarantees that $v(\mathbf{x})$ and $t_{\mathbf{m}}(\mathbf{x})$ are smooth functions of $\mathbf{x}$ [47]. Moreover, the locality of the Hamiltonian implies that it can be decomposed as a sum of operators involving up to $k$ elementary units, where $k$ is some finite number, so that the sum on the right-hand side of Eq. (2.5) can limited to indices $\mathbf{m}$ such that $|\mathbf{m}| = |\sum_\alpha m_\alpha| \leq 2k$. Finally, decomposing the wave-function into the TSS as $|\psi(t)\rangle = \sum_{\mathbf{x}} \psi(\mathbf{x}, t) |\mathbf{x}\rangle$, we can rewrite the Schrodinger equation as

$$\frac{i\hbar}{N}\frac{\partial}{\partial t}\psi(\mathbf{x},t) = \left[v(\mathbf{x}) - 2\sum_{0\leq|\mathbf{m}|\leq 2k} t_{\mathbf{m}}(\mathbf{x})\cosh\left(\frac{\mathbf{m}}{N}\cdot\frac{\partial}{\partial\mathbf{x}}\right)\right]\psi(\mathbf{x},t)\ , \tag{2.7}$$

where we used the identity $\psi(\mathbf{x}+\mathbf{m}) = \exp(\mathbf{m}\cdot\partial/\partial\mathbf{x})\psi(\mathbf{x})$.

In the thermodynamic limit, $\mathbf{x}$ becomes an effectively continuous variable, so that the dynamics generated from Eq. (2.7) is effectively governed by the effective Hamiltonian

$$\mathcal{H}_{eff}(\hat{\mathbf{x}},\hat{\mathbf{p}}) = v(\hat{\mathbf{x}}) - 2\sum_{0\leq|\mathbf{m}|\leq 2k} t_{\mathbf{m}}(\hat{\mathbf{x}})\cosh\left(i\frac{\mathbf{m}\cdot\hat{\mathbf{p}}}{\hbar_{eff}}\right) \tag{2.8}$$

and quantum fluctuations are governed by an effective Planck constant

$$\hbar_{eff} = \frac{\hbar}{N}\ . \tag{2.9}$$

In Eq. (2.8) we also identified the momentum operator $\hat{\mathbf{p}} = -i\hbar_{eff}\partial/\partial\mathbf{x}$, canonically conjugate to $\hat{\mathbf{x}}$. As $\hbar_{eff}$ vanishes in the thermodynamic limit, the original dynamics becomes effectively classical and described by the Hamilton equations generated by the Hamiltonian $\mathcal{H}_{eff}(\mathbf{x},\mathbf{p})$ from Eq. (2.8). We also observe that, due to the constraint $\sum_{\alpha=1}^{q} x_\alpha = 1$, $\mathbf{x}$ is an effectively $q-1$ dimensional variable.

### 2.1.2 Fully connected spin models

For systems whose elementary degrees of freedom are spin-$s$, the semi-classical description described in Section 2.1.1 can be rephrased in a more intuitive way [57]. We begin by considering a general, extensive Hamiltonian:

$$\hat{H} = -N\sum_{p\geq 1}\sum_{\mu_1\ldots\mu_p=x,y,z}\frac{J_{\mu_1,\ldots,\mu_p}}{N^{p-1}}\sum_{i_1,\ldots,i_p}\hat{s}_{i_1}^{\mu_1}\ldots\hat{s}_{i_p}^{\mu_p} = -N\sum_{p\geq 1}J_{\mu_1,\ldots,\mu_p}\hat{S}^{\mu_1}\ldots\hat{S}^{\mu_p}\ . \tag{2.10}$$

where in the last equality we defined the *collective spin* components $\hat{S}^\alpha = \sum_j \hat{s}_i^\alpha$. The operators $\hat{s}_i^\alpha$ represent the microscopic, spin-$s$ degrees of freedom.

For the Hamiltonian in Eq. (2.10), the TSS is the maximal spin sector, where

$$\hat{\mathbf{S}}^2 = \sum_{\alpha=x,y,z}(\hat{S}^\alpha)^2 = Ns(Ns+1)\ . \tag{2.11}$$

A fundamental observation is then that the collective spin variables satisfy the algebra

$$\left[\frac{\hat{S}^{\alpha}}{N}, \frac{\hat{S}^{\beta}}{N}\right] = i\frac{\hbar}{N}\sum_{\gamma}\epsilon^{\alpha\beta\gamma}\frac{\hat{S}^{\gamma}}{N} \tag{2.12}$$

controlled once again by an effective Planck constant $\hbar_{eff} = \hbar/N$. In the thermodynamic limit, the commutators from Eqs. (2.12) vanish and the modulus of the effectively continuous, average spin $\vec{\mathcal{S}} = \langle\hat{\mathbf{S}}\rangle/N$ is given by

$$|\vec{\mathcal{S}}| \sim \sqrt{\langle\hat{\mathbf{S}}^2\rangle} \sim Ns \ . \tag{2.13}$$

Furthermore, as $\hbar_{eff}$ vanishes, the Ehrenfest dynamics of $\vec{\mathcal{S}}$ is asymptotically given by the Hamilton equations

$$\frac{d}{dt}\vec{\mathcal{S}} = \{\mathcal{H}_{cl}(\vec{\mathcal{S}}), \vec{\mathcal{S}}\} \ , \tag{2.14}$$

obtained through the Poisson bracket $\{\mathcal{S}^{\alpha}, \mathcal{S}^{\beta}\} = \sum_{\gamma}\epsilon^{\alpha\beta\gamma}\mathcal{S}^{\gamma}$. Here, $\mathcal{H}_{cl}(\vec{\mathcal{S}})$ is computed by replacing the components of the operator $\hat{\mathbf{S}}$ with the ones of $\vec{\mathcal{S}}$, in Eq. (2.10).

## 2.2 Mean -field dynamical transitions in $p$-spin model

In this section, we apply the theory described in Section 2.1 to a system of $N$ spins 1/2 subject to all-to-all $p$-body and a global transverse field $g$. Its Hamiltonian is defined as

$$\hat{H}_0 = -\frac{\lambda}{2N^{p-1}}\sum_{i_1\dots i_p=1}^{N}\hat{\sigma}^x_{i_1}\dots\hat{\sigma}^x_{i_p} - \frac{g}{2}\sum_i\hat{\sigma}^z_i \ , \tag{2.15}$$

where $\hat{\sigma}^{\alpha}_i$ are the Pauli matrices at site $i$ and coincide with the rescaled spin operators on each site, $2\hat{s}_i$. The fully connected $p$-spin model in Eq. (2.15), which was originally introduced in the context of spin glasses [58, 59], plays a central role for studies on quantum annealing [60, 61]. Its zero-temperature phase diagram can be derived analytically [60–63] and displays a quantum phase transition driven by $g$, continuous for $p = 2$ and of the first-order for $p > 2$ [60, 63]. In this section we will address its dynamics and dynamical phase transitions.

### 2.2.1 Classical dynamics following a quench

We aim to study the dynamics of the average magnetization $\vec{\mathcal{S}}(t) = \langle\sum_j\vec{\sigma}_j(t)\rangle/N$, following a quench in the transverse field $g$. More precisely, we fix the initial state as a ferromagnetic ground state of the Hamiltonian in Eq. (2.15) at $g_0 = 0$, represented as $|\psi_0\rangle = |\rightarrow\cdots\rightarrow\rangle$. As discussed in Section 2.1.2, the Ehrenfest dynamics of $\vec{\mathcal{S}}(t)$, evolving from $|\psi_0\rangle$, is effectively classical in the thermodynamic limit $N \to \infty$ and can be described by the Hamilton equations [54, 64]:

$$\frac{d\vec{\mathcal{S}}}{dt} = \{\mathcal{H}_{cl}(\vec{\mathcal{S}}), \vec{\mathcal{S}}\} = \frac{\partial\mathcal{H}_{cl}}{\partial\vec{\mathcal{S}}} \wedge \vec{\mathcal{S}} \ , \tag{2.16}$$

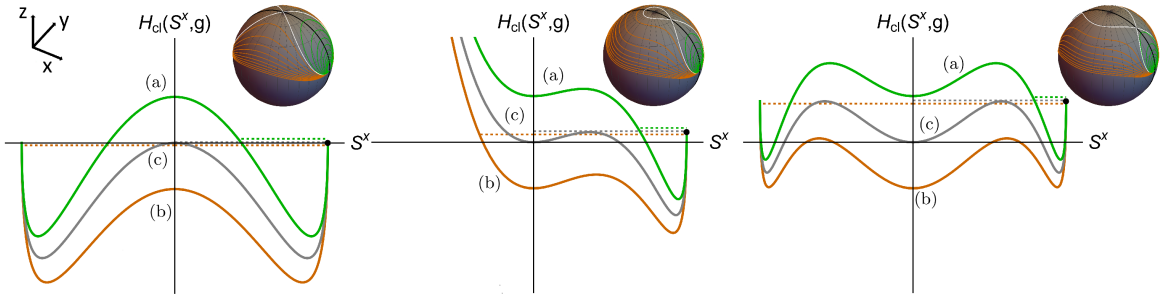


Figure 2.1: Energy profiles described by the equation (2.17), for several values of $g > 0$ and for $p = 2$ (left), $p = 2n+1$ (center) and $p = 2n+2$ (right), respectively, with $n \geq 1$ integer. All the three profiles lie in the plane $\mathcal{S}^y = 0$ (black cut on the Bloch spheres, where $\mathcal{S}^z = \sqrt{1-(\mathcal{S}^x)^2}$). Depending on the post quench values of the transverse field $g$, orbits starting from $\vec{\mathcal{S}} = \hat{\mathbf{x}}$ display qualitatively different behaviours: they are either confined in a single well (a) or explore the whole landscape (b), for values of $g$ respectively below and above a dynamical critical point $g_{dyn}$. Exactly at $g = g_{dyn}$, the system lies on a separatrix (c) with diverging period. See also the orbits in Fig. 2.2 (a) and (d) for a comparison.

with initial condition $\vec{\mathcal{S}}(0) = \hat{\mathbf{x}}$. The effective classical Hamiltonian $\mathcal{H}_{cl}(\vec{\mathcal{S}}, g)$ appearing on the right-hand side of Eq. (2.16) is given by

$$\mathcal{H}_{cl}(\vec{\mathcal{S}}, g) = -\lambda(\mathcal{S}^x)^p - g\mathcal{S}^z \ . \tag{2.17}$$

We remind that the Poisson bracket are given by $\{\mathcal{S}^\alpha, \mathcal{S}^\beta\} = \epsilon^{\alpha\beta\gamma}\mathcal{S}^\gamma$. From Eq. (2.17) is straightforward to see that the modulus of the spin $|\vec{\mathcal{S}}|^2$ is a constant of motion, so that the effectively classical dynamics is constrained on the Bloch sphere $|\vec{\mathcal{S}}|^2 = 1$. The dynamics in Eq. (2.16) is out of equilibrium, as all microscopic spins perform a coherent, undamped precession under the dynamics described by Eq. (2.16).

The dynamics described by Eq. (2.16) is also strongly influenced by the shape of the effective Hamiltonian $\mathcal{H}_{cl}(\vec{\mathcal{S}}, g)$. Depending on the value of $p$ and for sufficiently small values of $g$, the profile $\mathcal{H}_{cl}(\vec{\mathcal{S}}, g)$ on the sphere exhibits various topologies, characterized by the number and positions of its maxima and minima. Such stationary point can be quantitatively characterized by parameterizing the magnetization with the spherical angles $(\theta, \phi) \in [0, \pi/2] \times [0, 2\pi]$, as $\vec{\mathcal{S}} = \big(\sin\theta\cos\phi, \sin\theta\sin\phi, \cos\theta\big)$. Then, the equations for the stationary points of $\mathcal{H}_{cl}(\vec{\mathcal{S}}, g)$ are given by:

$$\begin{cases} \dfrac{\partial \mathcal{H}_{cl}}{\partial \phi} = -\lambda p(\sin\theta)^p(\cos\phi)^{p-1}\sin\phi = 0 \\ \dfrac{\partial \mathcal{H}_{cl}}{\partial \theta} = -\lambda p(\sin\theta)^{p-1}(\cos\phi)^p\cos\theta + g\sin\theta = 0 \ . \end{cases} \tag{2.18}$$

In the following we will focus on the case where $g > 0$. Moreover, we will focus only on stationary points falling in the in the Northern hemisphere($\mathcal{S}^z > 0$) of the Bloch sphere, where we will show a posteriori that the dynamics takes place, for the initial condition $\vec{\mathcal{S}}(0) = \hat{\mathbf{x}}$. One possible solution of the system of Eqs. (2.18) is given by $\theta = 0$

(the North Pole of the Bloch sphere), being a maximum for $p = 2$ and a minimum for $p > 2$. All the other solutions are obtained by solving the system:

$$\begin{cases} \sin\phi = 0 \\ (\sin\theta)^{p-2}\cos\theta(\cos\phi)^p = \dfrac{g}{\lambda p} \end{cases} \tag{2.19}$$

From the first equation, we get that stationary points lie in the plane $\mathcal{S}^y = 0$ for every $p$, while the number and the precise location of the solutions depend on the value of $p$. Specifically, for $p = 2$, we observe two symmetric minima separated by a maximum at the North pole ($\vec{\mathcal{S}} = \hat{\mathbf{z}}$). For $p \geq 3$ odd, the same topology persists, but the profile becomes asymmetric with respect to the North pole. Conversely, for $p \geq 4$ even, the potential features three minima: one at the North pole and two symmetric minima with respect to it. Consequently, the projection of $\mathcal{H}_{cl}(\vec{\mathcal{S}}, g)$ in the plane $\mathcal{S}^y = 0$ displays three possible shapes, each corresponding to a different value of $p$:

- a symmetric double-well for $p = 2$;
- an asymmetric double-well for $p \geq 3$ (odd), with one paramagnetic and one ferromagnetic minimum:
- a symmetric triple-well for $p \geq 4$ (even), with one paramagnetic minimum and two opposite ferromagnetic minima.

These profiles undergo qualitative changes when $g$ exceeds the critical value $g_{sp} = p(p-2)^{(p-2)/2}/(p-1)^{(p-1)/2}$. Beyond this point, the second of Eqs. (2.18) no longer has a solution, and the North pole $\vec{\mathcal{S}} = \hat{\mathbf{z}}$ becomes the sole stationary point, coinciding with a minimum. $g_{sp}$ is commonly referred to as the *spinodal point* [61].

The presence of multiple local minima in the profile has a strong impact on the dynamics of $\vec{\mathcal{S}}(t)$, which exhibits qualitatively different orbits, depending on the value of the post-quench transverse field $g$[1], as depicted in Fig. 2.1:

1. Below a certain threshold, $g_{dyn}$ (trajectory (a)), such that $g_{dyn} < g_{sp}$, the dynamics starts from a ferromagnetic well, and the initial energy is insufficient to surmount the nearest maximum at $\vec{\mathcal{S}} = \vec{\mathcal{S}}_m(g)$. Consequently, the magnetization oscillates around the ferromagnetic minimum, with $\mathcal{S}^x(t) > \mathcal{S}^x_m(g)$ at every time $t$.

2. For $g > g_{dyn}$ (trajectory (b)), the system possesses enough energy to explore the entire landscape.

3. At precisely $g = g_{dyn}$ (trajectory (c)), the system has sufficient energy to reach the top of the barrier but is unable to surpass it. Here the period of the oscillations, $T_{cl}(g)$, diverges and the magnetization approaches the local maximum infinitely slowly. The resulting orbit forms a *separatrix*.

[1] Our discussion can also be generalized to non-vanishing pre-quench values of the transverse field, $g_0 > 0$, following the approach of Ref. [47].

The three cases listed above correspond to three different possible topologies for the underlying orbits at large times. We classify each distinct topology as a *dynamical phase* [65]. Consequently, the singular dynamics at $g = g_{dyn}$ leads to a *dynamical phase transition* (DPT). The dynamical critical point $g_{dyn}$ is obtained by equating the energy of the initial configuration $\vec{\mathcal{S}}(0) = \hat{\mathbf{x}}$ to that of the local maximum $\vec{\mathcal{S}}_c = \vec{\mathcal{S}}_m(g_{dyn})$, which in terms of the variables $\theta$ and $\phi$ reads:

$$-\lambda(\sin\theta)^p - g\cos\theta = -g. \tag{2.20}$$

More precisely, simultaneous solutions of Eqs. (2.19) and (2.20) determine both $g_{dyn}$ and the spherical coordinates of the corresponding maximum in $\vec{\mathcal{S}}_c$.

From a practical point of view, the DPT can be studied also in terms of a "dynamical order", such as the time-averaged longitudinal magnetization,

$$\overline{\mathcal{S}^x} = \frac{1}{T}\lim_{T\to\infty}\int_0^T dt\mathcal{S}^x(t)\ . \tag{2.21}$$

As discussed also in Appendix A.1, the two indicators are equivalent to each other: as $g$ approaches $g_{dyn}$, the change of topology in the orbits is signalled by a divergence of their period $T_{cl}(g)$, in turn creating a non-analiticity in the function $\overline{\mathcal{S}^x}(g)$. In particular, both $T_{cl}(g)$ and $\overline{\mathcal{S}^x}(g)$ display a log-singularity while approaching the dynamical transition, a feature already known for other mean-field models driven away from equilibrium [47, 66].

In the following, we show that for the nature of the the mean-field DPT is qualitatively influenced by the interplay between various stationary points, which depends solely on the parity of $p$ (for $p > 2$). Therefore, we will study Eq. (2.16) for $p = 3$ and $p = 4$. These cases, together with $p = 2$, are paradigmatic and represent the three possible shapes of the landscape listed above, respectively.

### 2.2.2 The dynamical phase transition

The first observation we make is that the order of the DPT is not necessarily the same of the thermal equilibrium phase transition displayed by the $p$-spin model for the same value of $p$.

The case $p = 2$ is special, as it displays a thermal phase transition [67] and a dynamical phase transition which are both of the second order [46, 47, 62]. The dynamical one is detected by $\overline{\mathcal{S}^x}$ which, for a symmetry breaking initial condition $\vec{\mathcal{S}}(0)$, is finite for $g < \lambda$ and vanishes for $g > \lambda$ (due to the symmetry of the two wells), corresponding respectively to *dynamical ferromagnetic* and *dynamical paramagnetic* phases. The continuity of this DPT is not a consequence of the symmetry of $\mathcal{H}_{cl}(\vec{\mathcal{S}}, g)$ under the reflection $\mathcal{S}^x \to -\mathcal{S}^x$, but it is rather a general property related to the topology of the effective potential. Indeed, when $g$ approaches $g_{dyn}$ both from above and below, the energy of the orbit gets close to the one of the separatrix, which has a crossing at

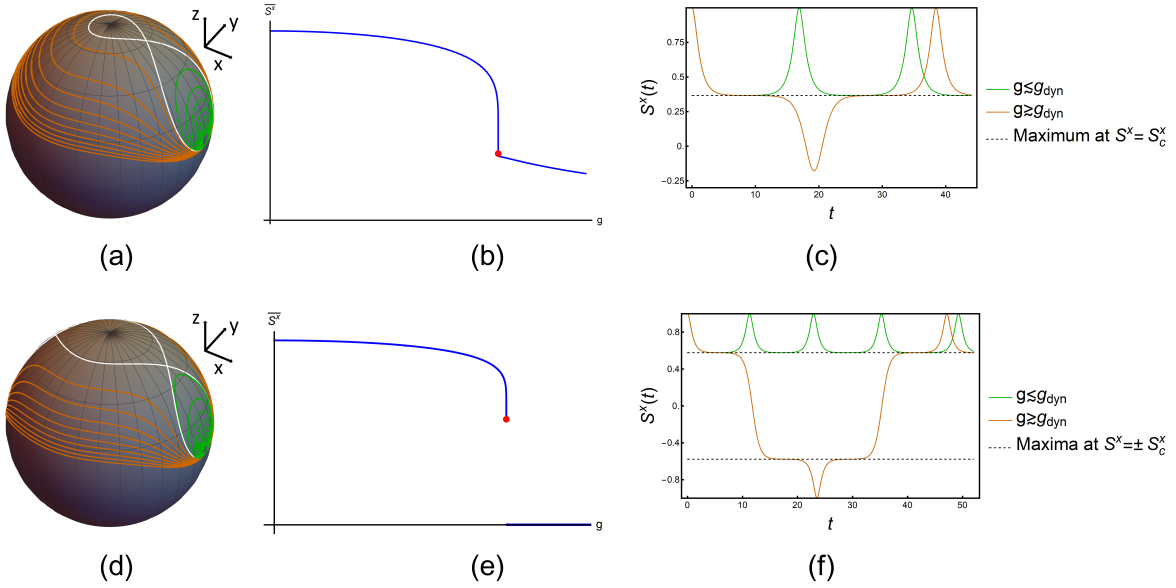


Figure 2.2: From left to right, we plot the orbits of the magnetization on the Bloch sphere, described after a quench starting in $\mathcal{S}^x(0) = 1$ ((a) and (d)), the corresponding time-averaged magnetization $\overline{\mathcal{S}^x}$ ((b) and (e)) and the behaviour of $\mathcal{S}^x(t)$ near the critical point (((c) and (f)). The plots on the upper row corresponds to the case of $p = 3$, the ones below to $p = 4$. **(Left)** For both values of $p$, the system evolves on trajectories which either are confined in a ferromagnetic well (green), for $g < g_{dyn}$, or enclose all the local minima (orange), for $g > g_{dyn}$. The two regions are divided by a critical trajectory (white), corresponding to $g = g_{dyn}$. **(Center)** Plot of the dynamical order parameter $\overline{\mathcal{S}^x}$ as a function of $g$. At the critical point (red dot), this is continuous for $p = 3$ only. **(Right)** Behaviour of the longitudinal magnetization for $g \simeq g_{dyn}$: for $p = 3$, $\mathcal{S}^x(t)$ exhibits a pleateau at the only maximum in $\mathcal{S}^x_m(g_{dyn}) = \mathcal{S}^x_c$(of the landscape $\mathcal{H}_{cl}(\vec{\mathcal{S}}, g_{dyn})$), both above and above the transition; for $p = 4$, the dynamics is characterized by a single plateau above $g_{dyn}$ and two, symmetric plateaus below $g_{dyn}$.

the only local maximum of $\mathcal{H}_{cl}(\vec{\mathcal{S}}, g_{dyn})$, located in $\vec{\mathcal{S}}_c = \hat{\mathbf{z}}$. At $g = g_{dyn}$, the dynamics starts on the separatrix and approaches asymptotically $\vec{\mathcal{S}}_c$ i.e.

$$\lim_{t\to\infty} \vec{\mathcal{S}}(t) = \vec{\mathcal{S}}_c \ . \tag{2.22}$$

The orbits asymptotically close to the separatrix, retrieved for $g \to g^{\pm}_{dyn}$, develop a plateau at $\vec{\mathcal{S}}_c$ whose length diverges with the period $T_{cl}(g)$, so that

$$\lim_{g\to g^{\pm}_{dyn}} \overline{\mathcal{S}^x}(g) = \mathcal{S}^x_c = 0 \tag{2.23}$$

and the dynamical transition is continuous.

For $p > 2$, the results summarized Fig. 2.2 always show the emergence of a DPT at some $g = g_{dyn}$ (such that $g_{dyn} < g_{sp}$ for every $p$), whose qualitative features depend on the parity of $p$, unlike its static counterpart. For $p = 3$ the topology of the phase space is the one of a double well, like in the case of $p = 2$ (though without $\mathbb{Z}_2$ symmetry),

hence the transition is continuous. In particular, a dynamical ferromagnetic phase is again retrieved for some $g < g_{dyn}$, where all the orbits are confined in a ferromagnetic well (green trajectories, Fig. 2.2-(a)), while for $g > g_{dyn}$ the to oscillations of the orbits between the two wells (orange trajectories, Fig. 2.2-(a)) lead to the emergence of a *dynamical bistable phase*, where $\overline{\mathcal{S}^x}$ is a weighted average of the values of $\mathcal{S}^x$ at the two minima. Thus, $\overline{\mathcal{S}^x}$ varies continuously with $g$ and exhibits a cusp at $g = g_{dyn}$. The validity of the argument relating the continuity of $\overline{\mathcal{S}^x}$ to the presence of a single unstable stationary point is proven in Fig. 2.2-(c), which shows that $\mathcal{S}^x(t)$ displays plateaus, whose length diverges as $g$ approaches $g_{dyn}$ either from above or below, in proximity of the local maximum at $\mathcal{S}^x_c > 0$.

The situation changes, due to a drastic change in the phase space topology, for $p = 4$. While approaching the critical point from below, the dynamics is confined in the rightmost ferromagnetic sector and $\overline{\mathcal{S}^x}$ still tends to a local maximum (green trajectories, Fig. 2.2-(d)), whose longitudinal coordinate $\mathcal{S}^x_c$ is non-vanishing. Conversely, moving even slightly above the transition point the trajectories become symmetric with respect to the $y - z$ plane (orange trajectories, Fig. 2.2-(d)), like the stationary points of $\mathcal{H}_{cl}(\vec{\mathcal{S}}, g)$, hence $\overline{\mathcal{S}^x} = 0$. In a more general perspective, we see that the important topological feature here is the presence of *two maxima* of $\mathcal{H}_{cl}(\vec{\mathcal{S}}, g_{dyn})$ with the same energy, at $\mathcal{S}^x = \pm\mathcal{S}^x_c$, where the separatrix (white trajectory in Fig. 2.2-(d)) has crossings. As a consequence, slightly below or above the transition, $\mathcal{S}^x(t)$ respectively exhibits plateaus of diverging length in proximity of the positive maximum or symmetrically near the two maxima (see respectively green and orange plot in Fig. 2.2 (f)), creating a discontinuity in $\overline{\mathcal{S}^x}$.

## 2.3 First order transitions driven by non-equilibrium fluctuations

The dynamical transitions studied in Section 2.2 arise from the out of equilibrium coherent dynamics performed by the local spins in the $N \to \infty$ limit, where they are effectively decoupled from each other due to the all-to-all interaction among them. This phenomenon is expected to be unstable with respect to the inclusion of fluctuations in the dynamics, which lead the system to eventually thermalize. However, if the coupling between the magnetization and fluctuations is not too large, the amplitude of fluctuations is expected to be small for a parametrically long time, leaving possible instances of dynamical phases in the *prethermal* stage of the dynamics [68–70].

This possibility was investigated in Ref. [49] using the non-equilibrium spin-wave theory (NEQSWT). Therein it was shown that, for $p = 2$, the dynamical critical point retrieved at the mean-field level is melted into an entire chaotic region of the phase diagram when fluctuations are included. In this section, we use the NEQSWT to perform the same analysis in the more general case of $p > 2$, considering the post-quench dynamics of the $p$-spin model under the influence of an extra, short-range term in the Hamiltonian. We assume that our system is on a one-dimensional lattice with periodic boundary conditions, and the short-range interaction term is expressed in real

space as [49]

$$\hat{U} = -J \sum_i \hat{\sigma}_i^x \hat{\sigma}_{i+1}^x + \frac{J}{N} (\sum_i \hat{\sigma}_i^x)^2 \ . \tag{2.24}$$

In momentum space, Eq. (2.24) can be rewritten as:

$$\hat{U} = -\frac{J}{N} \sum_{k \neq 0} \cos k \ \tilde{\sigma}_k^x \tilde{\sigma}_{-k}^x \tag{2.25}$$

where $k$ is an integer multiple of $2\pi/N$, $N$ being the system size. We leave out the term with $k = 0$, given by $J(\sum_i \hat{\sigma}_i^x)^2/N$, which does not create fluctuations and just modifies the mean-field component of the Hamiltonian from Eq. (2.15). Equation (2.25) give us the easiest perturbation that breaks the permutation symmetry in Eq. (2.15). Nevertheless, as we shall discuss later, all our results are expected to be independent of the range of interaction and of the dimensionality of the lattice.

In Section 2.3.1, we first provide a concise summary of the essential steps required for the implementation of NEQSWT, reserving a more comprehensive derivation and technical details for Appendix B. Subsequently, in Section 2.3.2, we discuss the effect of fluctuations, induced by the short-range perturbation, on the mean-field dynamical transitions of the $p$-spin model.

### 2.3.1 Non-equilibrium spin-wave theory

The fundamental hypothesis underlying NEQSWT is that, at least as long as $J$ is sufficiently small, the net effect of the term from Eq. (2.25) is to give rise to small spin-wave excitations on top of the collective classical spin $\vec{\mathcal{S}}(t)$. In particular, when the magnetization length is close to its maximal value, $|\vec{\mathcal{S}}(t)| \simeq 1$, the dynamics of $\vec{\mathcal{S}}(t)$ can still be effectively described in terms of trajectories close to the Bloch sphere, perturbed by fluctuations induced by the finite $k$ degrees of freedom. Thus, we implement NEQSWT by first rewriting the spin operators in Eq. (2.15) in a time-dependent, rotating reference frame $\mathcal{R} = \big(\mathbf{X}(t), \mathbf{Y}(t), \mathbf{Z}(t)\big)$, by applying the rotation $V\big(\theta(t), \phi(t)\big) = \exp\left(-i\phi(t) \sum_i \hat{\sigma}_i^z/2\right) \exp\left(-i\theta(t) \sum_i \hat{\sigma}_i^y/2\right)$, where the spherical angles $\theta(t)$ and $\phi(t)$ are fixed such that the magnetization $\vec{\mathcal{S}}(t)$ is aligned with the $Z$-axis in the new frame, for any $t > 0$. Then, assuming that the fluctuations transverse to $\mathbf{Z}(t)$ are small, we expand the spin variables in the new frame $\mathcal{R}$ using the HolsteinPrimakoff (HP) transformation [71]:

$$\begin{aligned} &\hat{\sigma}_i^X \simeq \hat{q}_i/\sqrt{s}, \quad \hat{\sigma}_i^Y \simeq \hat{p}_i/\sqrt{s}, \\ &\hat{\sigma}_i^Z = 1 - \frac{\hat{q}_i^2 + \hat{p}_i^2 - 1}{2s}, \end{aligned} \tag{2.26}$$

where $s = 1/2$ for the current case. We retain perturbative terms in the spin-wave modes $(\tilde{q}_k, \tilde{p}_k)$, i.e., the Fourier transform of $(\hat{q}_i, \hat{p}_i)$, at the leading order only. In our case, this amounts to retain only terms in Eq. (2.15) that are quadratic in $\tilde{q}_k$ and $\tilde{p}_k$.

The evolution of the spherical angles is consequently determined by the self-consistent equations $\mathcal{S}^X(t) = \mathcal{S}^Y(t) = 0$, which in our analysis read as:

$$\begin{cases} s\dot{\phi} = & p\lambda(\sin\theta)^{p-2}(\cos\phi)^p \cos\theta\big\{1-(p-1)\epsilon(t)\big\} - g \\ & - 2J\delta^{qq}(t)\cos\theta\cos^2\phi + 2J\delta^{qp}(t)\sin\phi\cos\phi \\ s\dot{\theta} = & p\lambda(\sin\theta\cos\phi)^{p-1}\sin\phi\{1-(p-1)\epsilon(t)\} + \\ & - 2J\delta^{pp}(t)\sin\theta\sin\phi\cos\phi \\ & + 2J\delta^{qp}(t)\sin\theta\cos\theta\cos^2\phi \ . \end{cases} \tag{2.27}$$

The term

$$\delta^{\alpha\beta}(t) \equiv \sum_{k\neq 0} \Delta_{\mathbf{k}}^{\alpha\beta}(t)\cos k/(Ns) \ , \tag{2.28}$$

for $\alpha, \beta \in \{p, q\}$, is a "quantum feedback" by which the classical spin gets coupled to the corresponding spin-wave correlation functions, defined by

$$\begin{aligned} &\Delta_k^{qq}(t) \equiv \langle \tilde{q}_k(t)\tilde{q}_{-k}(t)\rangle \ , \quad \Delta_k^{pp}(t) \equiv \langle \tilde{p}_k(t)\tilde{p}_{-k}(t)\rangle \ , \\ &\Delta_k^{qp}(t) \equiv \langle \tilde{q}_k(t)\tilde{p}_{-k}(t) + \tilde{p}_k(t)\tilde{q}_{-k}(t)\rangle /2 \ . \end{aligned}$$

These evolve according to the linear differential equations of motion

$$\begin{cases} s\dfrac{d}{dt}\Delta_k^{qq} = & (4J\cos k\cos\theta\sin\phi\cos\phi)\Delta_k^{qq} \\ & + \{2p\lambda(\sin\theta)^{p-2}(\cos\phi)^p - 4J\cos k\sin^2\phi\}\Delta_k^{qp} \\ s\dfrac{d}{dt}\Delta_k^{qp} = & -\{p\lambda(\sin\theta)^{p-2}(\cos\phi)^p \\ & - 2J\cos k\cos^2\phi\cos^2\theta\}\Delta_k^{qq} \\ & + \{p\lambda(\sin\theta)^{p-2}(\cos\phi)^p - 2J\cos k\sin^2\phi\}\Delta_k^{pp} \\ s\dfrac{d}{dt}\Delta_k^{pp} = & -\{2p\lambda(\sin\theta)^{p-2}(\cos\phi)^p \\ & - 4J\cos k\cos^2\phi\cos^2\theta\}\Delta_k^{qp} \\ & - (4J\cos k\cos\theta\sin\phi\cos\phi)\Delta_k^{pp} \ , \end{cases} \tag{2.29}$$

defined for each value of $k = 2\pi n/N$, where $n = 1, \ldots, N-1$. We notice that, in the limit of $J \to 0$, the Eqs. (2.27) decouple from the quantum feedback and reduce to a representation of the mean-field dynamics in Eq. (2.16) in the spherical coordinates $\theta(t)$ and $\phi(t)$.

Our expansion is expected to be valid as long as the density of spin-wave excitations is small, that is

$$\epsilon(t) = \frac{1}{Ns}\sum_{k\neq 0}\frac{\Delta_k^{qq}(t) + \Delta_k^{pp}(t) - 1}{2} \ll 1 \ . \tag{2.30}$$

In this case, the modulus of the magnetization $|\vec{\mathcal{S}}(t)| = 1 - \epsilon(t)$ is close to one, so that the dynamics can still be described in terms of classical trajectories. In this regime, spin waves behave as free bosonic excitations, which interact with the macroscopic collective spin only, corresponding to the $k = 0$ mode. Higher-order terms appearing

in Eq. (2.15), which account for nonlinear scattering among the spin waves, can be neglected: they are expected to contribute significantly to the dynamics only at longer times and to drive the system away from the prethermal regime relevant for the DPT discussed here.

### 2.3.2 Modified non-equilibrium phase diagram

The presence of spin-waves opens a channel for internal dissipation: the magnetization $\vec{\mathcal{S}}(t)$ is damped by the emission of spin waves. For $p = 2$, the energy damping leads the orbits close to the mean-field separatrix to localize asymptotically down one of the two wells, with equal probability. The corresponding prethermal dynamics becomes thus unpredictable and the mean-field dynamical critical point melts into an entire chaotic region of the phase diagram [49, 50]. It is natural to ask if spin-wave emission is going to have the same effect in the first-order case $p > 2$.

To understand the effects of fluctuation on the mean-field dynamical transition, we study the post-quench dynamics of the system at $J \neq 0$, by simultaneously integrating equations (2.27) and (2.29), for a range of values of the couplings $g$ and $J$. We verify that, for each choice of $g$ and $J$ and at the time-scales explored, the spin wave density $\epsilon(t)$ is small (some examples are shown in Fig. 2.3), so that the dynamics we study is consistently in a prethermal regime. Before the quench, we again prepare the system in the fully polarized state along the $x$-direction, so that $\theta(0) = \pi/2$ and $\phi(0) = 0$, and assume that no spin-wave mode is excited, by imposing that $\Delta_k^{qq}(0) = \Delta_k^{pp}(0) = 1/2$ and $\Delta_k^{qp}(0) = 0$. Below we will reconstruct the various dynamical phases by looking at $\overline{\mathcal{S}^x}$ as a function of $g$ and $J$ and at individual trajectories. As we study the dynamics for values of $g$ below the spinodal point $g_{sp}(p)$, defined in Section 2.2.2, the new dynamics is still equivalent to the one of a particle moving in a multi-well shaped energy profile, like the mean-field one. The effect of the short-range perturbation is thus to generate additional damping due to the exchange of energy with the spin-wave degrees of freedom, the latter acting as a self-generated bath, as we will discuss in greater detail in Section 2.3.3.

The exchange of energy between the magnetization and the spin-waves opens the route for the appearance of new dynamical phases. In particular, for the dynamical protocol we described and generic values of $g$ and $J$, $\epsilon(t)$ grows from zero saturating to a typical small value (see Fig. 2.3), while the magnetization is correspondingly damped from its initial mean-field orbit to another one where the unperturbed energy $\mathcal{H}_{cl}(\vec{\mathcal{S}}(t), g)$ is slightly different, possibly even localizing in a single well. We define the new dynamical phases in terms of the topology of the trajectories asymptotically reached after the damping. Once again, we stress that such new dynamical phases are *prethermal* and are expected to be disappear at long-times as soon as the non-linear interaction among the spin-waves degree of freedom is taken into account, leading to the eventual thermal relaxation of the system.

If spin waves were emitted at a constant rate in time, the orbits encompassing all the minima (that is, orange trajectories in Fig. 2.2-(a) and (d) ) would localize down

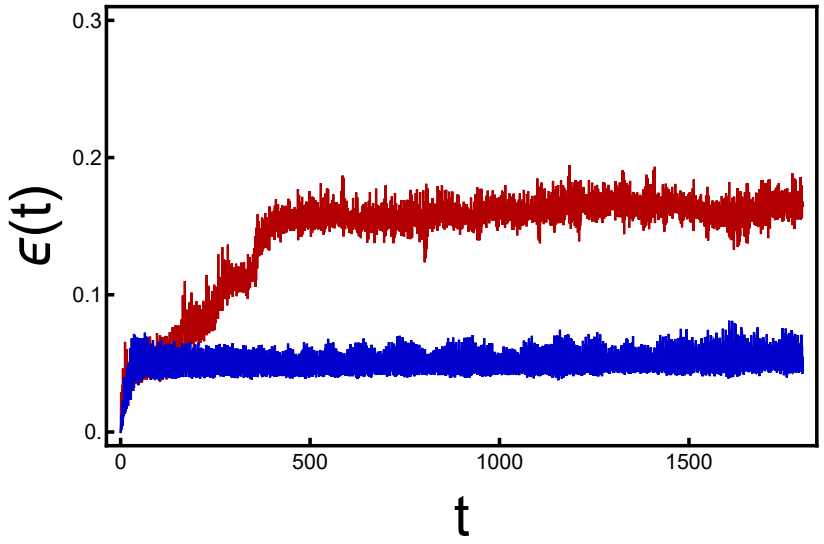


Figure 2.3: Plots of two examples of the profile of the function $\epsilon(t)$, defined in Eq. (2.30) and computed by within the NEQSW described in the main text, by fixing either $p = 3$, $J = 0.25$, $g = 1.15$ (red plot) or $p = 4$, $J = 0.2$, $g = 1.12$ (blue plot). In both plots we fix $N = 100$ and $\lambda = 1$.

one the wells of the effective potential on the Bloch sphere, either the paramagnetic minimum or one of the ferromagnetic minima ( a single one for $p \geq 3$ odd or a pair for $p \geq 4$ even), with approximately equal probability. The plot obtained for $p = 3$ in Fig. 2.4 shows that this is not the case: the dynamical ferromagnetic phase is of course always robust against fluctuations, while the dynamical bistable one is not and for sufficiently large values of $J$ the trajectories asymptotically localize inside the paramagnetic minimum, associated with asymptotically stable oscillations, thus identifying a new *dynamical paramagnetic phase*. Quantitatively, in Fig. 2.4 we observe three typical asymptotic behaviour for the trajectories (either encompassing all the wells or orbiting around one of the two minima): to each of them corresponds to a narrow interval of values for $\overline{\mathcal{S}^x}$, being greatest in the dynamical ferromagnetic phase and smallest in the paramagnetic one (although non vanishing due to the asymmetry of the energy profile). The dynamical order parameter $\overline{\mathcal{S}^x}$ also exhibits a discontinuity when crossing the border line $J_{dyn}(g)$ (discussed in greater detail A.2), between the dynamical bistable and paramagnetic regions, giving rise also to a new first-order transition driven by $J$. The predominance of localization around $\mathcal{S}^x = 0$ is softened close to the mean-field critical point $g = g_{dyn}$, where the asymptotic localization within the ferromagnetic basin becomes more frequent and the line limiting the dynamical ferromagnetic phase is melted in a narrow chaotic crossover region, equivalent to the one observed for $p = 2$ [49].

As shown in Fig. 2.5, a similar phenomenon is observed for $p = 4$, where the collective spin $\vec{\mathcal{S}}(t)$, initially oscillating in the mean-field paramagnetic region, suddenly falls into the well around the North pole of the Bloch sphere, as soon as $J$ is moved above a critical threshold $J_{dyn}(g)$. Unfortunately, this discontinuity in the time-evolution can not be appreciated by looking at the average $\overline{\mathcal{S}^x}$, displayed in Fig. 2.5 (left), which vanishes for orbits either surrounding all the minima or localizing in the paramagnetic

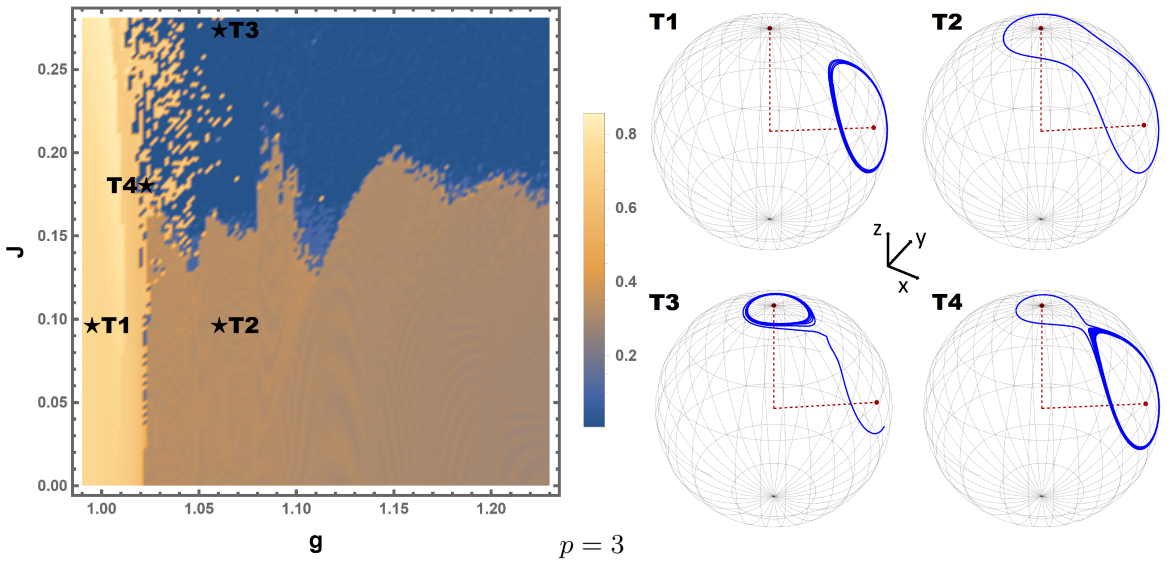


Figure 2.4: Non-equilibrium phase diagram of the $p$-spin model, for $p = 3$, obtained integrating simultaneously equations Eqs. (2.27) and (2.29) and for a quench, starting from the fully polarized state $\vec{\mathcal{S}}(0) = \hat{\mathbf{x}}$ and several values of $g$ and $J$. The maximum integration time is $t_{max} = 2000$. Here we posed $N = 100$ and $\lambda = 1$. The color of each point on the phase diagram corresponds to a value of the time-averaged magnetization $\overline{\mathcal{S}^x}$, as specified in the interval shown on the right of the diagram. In particular, the yellow and the orange regions correspond to dynamical ferromagnetic and paramagnetic phases, respectively, where the orbits are either confined in the ferromagnetic well (plot T1) or encircle both the two minima (plot T2). The blue region corresponds to the dynamical paramagnetic region where the magnetization revolves around the minimum on the North pole (plot T3); here $\overline{\mathcal{S}^x}$ is closer to 0 than in any other phase, though non-vanishing, and increases discontinuously when moving across the border with the orange zone. The crossover region is a narrow chaotic phase, reminiscent of the one found in Ref. [49], where collective spin can localize at large times in either the paramagnetic or the ferromagnetic minima (plot T4).

well, while showing once again the stability of the dynamical ferromagnetic phase (where $\overline{\mathcal{S}^x} > 0$) against fluctuations. Thus, we also examine the behaviour of the time-averaged fluctuation [54], defined as

$$\overline{(\delta\mathcal{S}^x)^2} = \lim_{T\to\infty} \frac{1}{T} \int_0^T dt \, \left(\mathcal{S}^x(t) - \overline{\mathcal{S}^x}\right)^2 . \tag{2.31}$$

The value of $\overline{(\delta\mathcal{S}^x)^2}$ depends on the integration parameters $g$ and $J$ and decreases discontinuously as $J$ is again raised above a threshold $J_{dyn}(g)$ (distinct from the threshold found for $p = 3$), as it can clearly observed Fig. 2.5 (right). From the corresponding phase diagram, we see that the dynamical paramagnetic phase, corresponding to $\overline{\mathcal{S}^x} = 0$, can be divided in two sub-phases:

- a *dynamical paramagnetic phase* 1, where the orbits surround all the minima, like in the corresponding mean-field phase ;

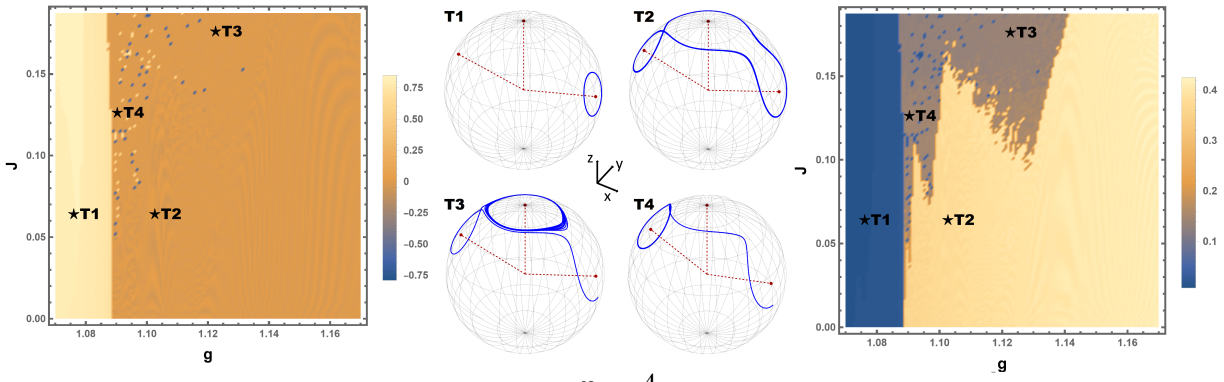


$p = 4$

Figure 2.5: Simultaneous plot of the time-averaged magnetization $\overline{\mathcal{S}^x}$ (left) and time-averaged fluctuations $\overline{(\delta\mathcal{S}^x)^2}$ (right), for $p = 4$. These are obtained integrating equations Eqs. (2.27) and (2.29) for the same parameters of $N$,$\lambda$ and the same maximum integration time $t_{max}$ listed in the caption of Fig. 2.4. For both the plots, each color corresponds to a value of the observable we plot, as specified in the respective legends. **(Left)** Plot of $\overline{\mathcal{S}^x}$. We identify two main regions: one corresponds to a dynamical ferromagnetic phase(yellow), where $\overline{\mathcal{S}^x} > 0$ (plot T1), while the other is a paramagnetic phase (orange) where $\overline{\mathcal{S}^x} = 0$. Between the two, we occasionally find chaotic (blue and yellow) spots, signalling that the magnetization eventually falls in one of the other two symmetric, ferromagnetic minima (plot T4). **(Right)** Plot of the time-averaged fluctuations $\overline{(\delta\mathcal{S}^x)^2}$. The in dynamical paramagnetic phase, corresponding to the non-blue region of the phase diagram, can be split in a sub-phase 1 (yellow), where the dynamical trajectories either surround symmetrically all the three minima of the landscape (plot T2) and a sub-phase 2 (blue), where the magnetization localizes (predominantly) in a paramagnetic well (plot T3). The border between the two identifies the transition line $J = J_{dyn}(g)$.

- a *dynamical paramagnetic phase* 2, where the trajectories localize around the minimum at $\mathcal{S}^x = 0$, confined in the paramagnetic well.

Specifically, smaller values of $\overline{(\delta\mathcal{S}^x)^2}$ correspond to localization inside the paramagnetic well.

At the transition line $J_{dyn}(g)$ between the two dynamical paramagnetic phases, $\overline{(\delta\mathcal{S}^x)^2}$ is discontinuous (see also Appendix A.2) and thus we can identify a dynamical transition for $p \geq 4$ even, driven by $J$, being of the first-order like the one retrieved in the mean-field case. In passing we also observe that, close to the mean-field critical point $g = g_{dyn}$, the dynamical paramagnetic phase 2 is filled with few "chaotic" spots, where the orbits eventually localize instead in one of the two ferromagnetic wells (each of them associated to a different sign of $\overline{\mathcal{S}^x}$). These spots become more frequent as we cross over to the dynamical paramagnetic phase retrieved at smaller values of $g$.

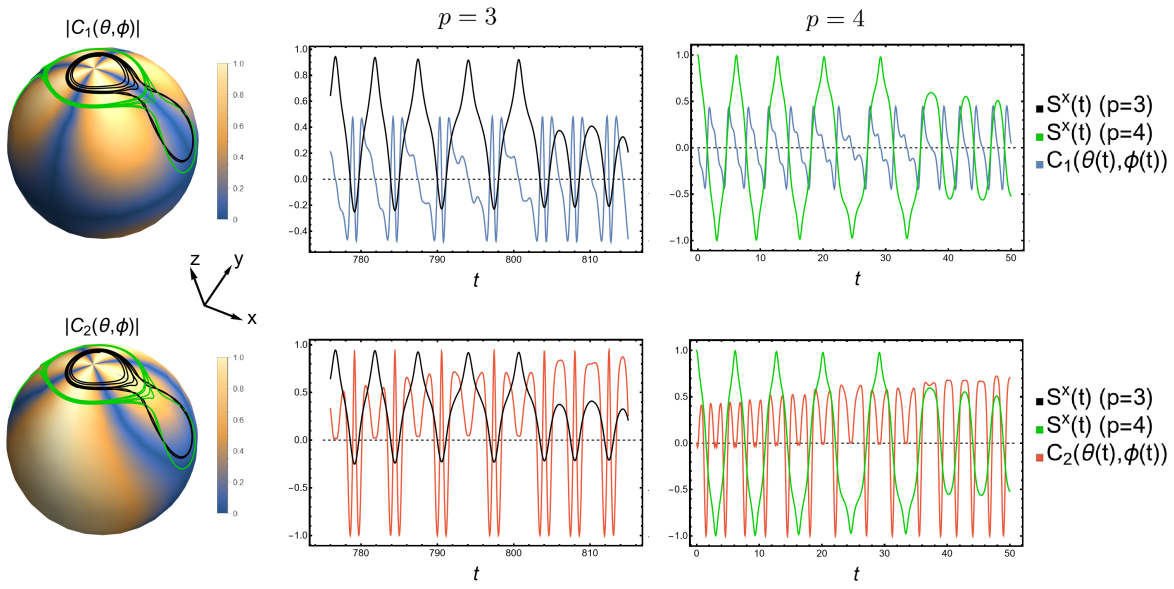


Figure 2.6: Dynamics of two trajectories, parametrized by $\theta(t)$ and $\phi(t)$ and computed respectively for $p = 3$, $g = 1.09$, $J = 0.26$ (black plots) and $p = 4$, $g = 1.13$, $J = 0.15$ (green plots). **(Left)** Spherical plots of the magnitude of the couplings $C_1(\theta, \phi)$ and $C_2(\theta, \phi)$, against the dynamical evolution of the two trajectories on the Bloch Sphere. **(Center)** Time evolution of the couplings $C_1(\theta(t), \phi(t))$ (blue) and $C_2(\theta(t), \phi(t))$ (red) along the trajectory obtained at $p = 3$, each compared against the longitudinal magnetization $\mathcal{S}^x(t) = (1 - \epsilon(t)) \sin\phi(t) \cos\phi(t)$ (black). **(Right)** Same plots represented at the center, this time for the trajectory computed at $p = 4$.

### 2.3.3 The mechanism behind the localization of the magnetization

Our results are very different from the ones found in Ref. [49] for the case of $p = 2$, where the same fluctuations lead to dynamical chaos. In this section we show that, despite the apparent difference, the dynamical phases retrieved both for $p = 2$ and $p > 2$ share a common origin, which can be related to the predominant emission of spin waves when the classical trajectory traverses the paramagnetic well.

Intuitively, the inhomogeneous emission is due to the specific form of the short-range perturbation in Eq. (2.25), which induces fluctuations in the collective dynamics when the local spins are not aligned with the $x$-axis: as the maximal misalignment in the dynamics is reached when the magnetization is close to the North pole $\vec{\mathcal{S}} = \hat{\mathbf{z}}$, and in particular close to the plane $\mathcal{S}^x = 0$, spin-waves are expected to be mostly emitted there. From a quantitative point of view, it is useful to investigate the spin-wave density rate, which using Eq. (2.30) reads as

$$\frac{d\epsilon(t)}{dt} = \frac{1}{2Ns}\sum_{k\neq 0}\Big(\frac{d\Delta_k^{qq}(t)}{dt} + \frac{d\Delta_k^{pp}(t)}{dt}\Big) \ . \tag{2.32}$$

Plugging Eqs. (2.29) into Eq. (2.32), we obtain

$$\begin{aligned}\frac{d\epsilon(t)}{dt} &= -4\frac{J}{s}(\mathbf{X}\cdot\hat{\mathbf{x}})(\mathbf{Y}\cdot\hat{\mathbf{x}})\ (\delta^{qq}(t) - \delta^{pp}(t)) + 4\frac{J}{s}\big((\mathbf{X}\cdot\hat{\mathbf{x}})^2 - (\mathbf{Y}\cdot\hat{\mathbf{x}})^2\big)\delta^{qp}(t) \\ &= 4\frac{J}{s}\cos\theta\sin\phi\cos\phi\ (\delta^{qq}(t) - \delta^{pp}(t)) + 4\frac{J}{s}(\cos^2\theta\cos^2\phi - \sin^2\phi)\ \delta^{qp}(t)\ ,\end{aligned} \tag{2.33}$$

where the quantum feedback terms $\delta^{\alpha\beta}(t)$ are defined in Eq. (2.28). From Eq. (2.33), we observe that the emission rate $d\epsilon/dt$ is determined by the coefficients

$$\begin{aligned}C_1(\theta,\phi) &= (\mathbf{X}(t)\cdot\hat{\mathbf{x}})(\mathbf{Y}(t)\cdot\hat{\mathbf{x}}) = \cos\theta\sin\phi\cos\phi \\ C_2(\theta,\phi) &= (\mathbf{X}(t)\cdot\hat{\mathbf{x}})^2 - (\mathbf{Y}(t)\cdot\hat{\mathbf{x}})^2 = \cos^2\theta\cos^2\phi - \sin^2\phi\end{aligned} \tag{2.34}$$

which couple $d\epsilon/dt$ to the quantum feedback. $C_1(\theta,\phi)$ and $C_2(\theta,\phi)$ are independent of $p$ and depend only on the projection of the time-dependent frame $\mathcal{R}$ on the $x$-axis, along which the local spins interact through the perturbation introduced in Eq. (2.25). More precisely, in Appendix B.3, we show explicitly that the expression for the coefficients $C_1(\theta,\phi)$ and $C_2(\theta,\phi)$ in Eq. (2.34) depends only on the form of the perturbation in Eq. (2.25). Moreover, from Eq. (2.34) we can see explicitly that $d\epsilon/dt = 0$ when the magnetization is along the $x$-axis ($\theta = \pi/2$), while the magnitude of both $C_1(\theta,\phi)$ and $C_2(\theta,\phi)$ is maximised around the North Pole (see Fig. 2.6, left panels). This observation confirms our intuition that the maximum spin-wave emission occurs concomitantly with the maximal misalignment between $\vec{\mathcal{S}}(t)$ and $\hat{\mathbf{x}}$. Our intuition is further confirmed by the plots in Fig. 2.6 (central and right panels), where we show the time-evolution of $C_1(\theta,\phi)$ and $C_2(\theta,\phi)$, along two generic classical trajectories, respectively for $p = 3, 4$: when the magnetization visits the ferromagnetic well, both the couplings vanish and no spin-wave is excited, while their magnitude is maximised when the magnetization

is close to the plane $\mathcal{S}^x = 0$.

As the predominant emission around the North pole is determined only by the short-range perturbation, the different phenomena observed for $p = 2$ and $p > 2$ respectively can be addressed to the different stability properties of the stationary point $\theta = 0$ of the energy landscape in Eq. (2.17): while, for $p = 2$, $\theta = 0$ is unstable and symmetric fluctuations in the two wells[2] induce dynamical chaos [49, 50], for $p > 2$ $\theta = 0$ becomes a stable minimum so that the magnetization moves on stationary orbits after being damped, giving birth to the dynamical paramagnetic regions shown in Fig. 2.4 (left) and Fig. 2.5 (right). This phenomenon is reminiscent of Hopf bifurcations [7] occurring in classical dynamical systems.

It is also worth noticing that the way by which the fluctuations induce the localization of the collective spin is slightly more subtle than a simple dissipation mechanism. In particular, we observe that when $\epsilon(t) > 0$, the magnetization length is $|\vec{\mathcal{S}}(t)| = 1 - \epsilon(t)$ decreases, so that the dynamics in Eq. (2.27) takes place in the time-dependent modified potential

$$\mathcal{H}_{\epsilon(t)}(\theta, \phi) = -(1 - \epsilon(t))^p \left[ \lambda (\sin\theta \cos\phi)^p - \frac{g}{(1 - \epsilon(t))^{p-1}} \sin\theta \right] . \tag{2.35}$$

As shown in the animated plots[3], the profile of the $\mathcal{H}_{\epsilon(t)}(\theta, \phi)$ is squeezed towards zero energy when $\epsilon(t)$ grows: this eventually leads the magnetization to be trapped in the paramagnetic region, where $\epsilon(t)$ exhibits large spikes, while the spin-wave dynamics is nearly stationary across the ferromagnetic wells.

Our results are expected to be independent of the range of interaction of the perturbation in Eq. (2.25) and of the dimensionality of the lattice: replacing the $k$-dependent couplings $J\cos(k)$ with generic $\tilde{J}_{\mathbf{k}}$[4] leaves Eq. (2.33) invariant[5] and spin-waves are still expected to be emitted around $\theta = 0$, as explicitly shown for the case of $p = 2$ [50]. On the other hand, introducing a short-range interaction along a direction not coinciding with the $x$-axis changes the couplings in Eq. (2.34) and spin-wave emission may occur in different regions on the Bloch sphere, possibly leading to different non-equilibrium phases.

## 2.4 Summary and perspectives

In conclusion, in this chapter we have studied the the post-quench dynamics of a fully connected $p$-spin model (for $p > 2$) perturbed by a short-ranged interaction, controlled by the coupling $J$, generalizing to arbitrary values of $p$ the system studied in previous

[2] Notice that the right-hand side of Eq. (2.33) is invariant under reflection $\phi \to \phi + \pi$ with respect to the $z$-axis, so that spin-wave emission are symmetric in the two wells for $p = 2$.

[3] See the ancillary files at https://arxiv.org/e-print/2110.13524, in the folder "anc".

[4] Here $\mathbf{k}$ is a $d$-dimensional vector if the lattice has dimensionality $d > 1$.

[5] Up to replacing all the terms in the form of $J\delta^{\alpha\beta}(t)$ with the more generic expression $J\delta^{\alpha\beta}(t) \equiv \sum_{\mathbf{k}\neq\mathbf{0}} \Delta_k^{\alpha\beta}(t)\tilde{J}_{\mathbf{k}}/(Ns)$.

works [46, 47, 49].

In the mean-field limit of $J = 0$, the dynamics is equivalent to the one of a particle in a classical energy landscape: a DPT emerges, driven by the transverse field $g$, whose order depends on the parity of $p$, which determines the qualitative shape of the effective potential. In particular, we have found a second order dynamical transition for odd $p$ (where the potential is an asymmetric double-well) and first order one for even $p$ (where the profile is made by three basins). The nature of this transition is modified by the presence of a short-range perturbation, treated within the non-equilibrium spin-wave theory. Spin waves generate an effective damping in the dynamics which is maximal in a region close to the paramagnetic North pole: this changes the nature of the dynamical phases, now being defined by the behaviour of the magnetization in a prethermal regime. In the phase diagram, the short-range coupling drives a new first-order transition for $p \geq 3$.

The analysis discussed here can be straightforwardly generalized to a wider class of fully connected spin models with generic integrability breaking terms: the profile of the energy landscape and the direction where interaction induced by the integrability breaking perturbation is oriented are the only two ingredients which fully determine the features of the non-equilibrium phase diagram.

# Chapter 3

# Probing chaos in a $p$-spin glass

In Chapter 2, we demonstrated that within an effectively low-dimensional system, the delicate balance between dissipation and the underlying energy landscape leads to two markedly distinct outcomes of the dynamics: the emergence of either an asymptotic localization or chaotic behavior. However, the situation becomes more intricate as we shift our attention to high-dimensional systems, as we will show in this chapter. In these systems, the number of stationary configurations increases rapidly with the system size, possibly revealing a new and more complex phenomenology.

Among high-dimensional systems displaying a large number of equilibria, a prominent role is played by spin glasses, a class of models originally introduced to describe magnetic alloys [72, 73]. The dynamics of spin glasses is a longstanding problem: it has been estabilished that, at low temperature, the dynamics is trapped into one of the exponentially many possible metastable states [74–77] for a long-time and explores the phase space through rare, activated jumps between different states [78–80], leading to ergodicity-breaking phenomena [81–84]. The inclusion of quantum fluctuations usually opens up a new route for thermalization in the equilibrium dynamics due to tunnelling between metastable states [85–88], even though counter-intuitive effects of quantum fluctuations inducing glassiness has been found in quantum quench protocols [89] or more recently in presence of more complex energy landscapes [90]. Within such a rich variety of phenomena, the recent theoretical [91–95] and experimental [96] observation of many-body chaos in quantum spin-glasses has drawn particular attention. Specifically, in Refs. [93, 94] chaos was detected in the dynamics of a quantum spherical $p$-spin glass model [87], from the exponential growth of an out-of-time-order correlator (OTOC) [97–103]: the corresponding *Lyapunov exponent* $\lambda_L$ exhibits a single broad peak at a temperature scale where the dynamics is still ergodic, but at the onset of slow relaxation.

The behaviour of the Lyapunov exponent $\lambda_L$ extracted from the OTOCs was connected in Ref. [93] to a dynamical crossover between two step and one step time relaxation in the spin-spin correlation functions. This behaviour suggests a deeper connection between this dynamical feature and the structure of the underlying stationary configurations of the model. In particular, if such relation exists other features associated to the peak in other chaos indicators would be observed. Among these chaos

indicators, one example is the *Kolmogorov-Sinai* (KS) *entropy* [8, 14, 104], that is the sum of all the positive Lyapunov exponents describing growth of the sub-leading terms appearing either in the OTOC for quantum systems [105, 106] or in the distance between nearby trajectories for classical chaotic systems [107]. The KS entropy would indeed provide a deeper insight on the emergence on the strength of chaos and to the entanglement production in a wide range of quantum systems [105, 106, 108–110]. A second, example of indicator focusing on the transition from integrability to chaos in genuine quantum spin systems is the *fidelity susceptibility* [111, 112]. Such quantity, despite being closely connected to the magnetic response obtained in quantum spin-glass experiments [85], has never been investigated in the context of spin-glasses.

The purpose of this chapter is to develop a qualitative understanding of the chaotic behavior in the $p$-spin spherical model, in the classical limit. Specifically, we compute $\lambda_L$ as function of the energy density, using phase-space methods and find a broad peak around $E = 0$, while $\lambda_L$ vanishes in the low and high-energy limits. We observe that the maximum in $\lambda_L$ occurs when the energy landscape has the maximum possible number of stationary points, as characterized by the complexity [113]. We find that the profile of the Kolmogorov-Sinai entropy is qualitatively identical to that of $\lambda_L$. To further investigate the dynamical features of our model, we also introduce a quantity classically equivalent to the fidelity susceptibility $\chi$ in the ergodic phase finding that, as a function of $E$, it has a single peak aligning with the onset of non-ergodic behavior in the dynamics. We give a physical interpretation of our results in terms of the behaviour of the underlying trajectories at different energy scales: while the low and high-energy limits respectively correspond to regular trajectories, either oscillating around a local minimum or performing a uniform circular motion around the $N$-sphere, for intermediate energies the nontrivial interplay between the saddles of the landscape enhance dynamical chaos. Our method can be straightforwardly generalized to other spin-glass models, for example describing spins 1/2 in a transverse field [92], where a similar behaviour for the trajectories is expected both for the low and high-energy limit.

The chapter is organized as follows. In Section 3.1 we review the indicators of chaos and ergodicity that we will use in the rest of this chapter. In Section 3.2 we describe the model and its dynamics we focus on. In Section 3.3 we will present our results for $\lambda_L$ and $\Lambda_{KS}$ and in Section 3.4 we will discuss their connection with the properties of the underlying energy landscape. We also discuss the relation between dynamical relaxation and the fidelity susceptiblity in Section 3.5. Finally, we summarize our results and perspectives in Section 3.6.

## 3.1 Tools for probing chaos in classical and quantum systems

### 3.1.1 Lyapunov exponents

#### Classical Lyapunov spectrum

In Chapter 1, we highlighted that the defining trait of chaotic systems is their inherent unpredictability, especially in the presence of uncertainty in the initial condition. Quantitatively, this instability can be characterized by the system's Lyapunov exponents, which we will briefly review in this section. For a more detailed exploration, readers are encouraged to consult the comprehensive Reference [14].

Consider dynamical system with arbitrary dimensionality $d$, described by the equations:

$$\begin{cases} \dot{\mathbf{y}} = \mathbf{f}(\mathbf{y}, t) \\ \mathbf{y}(0) = \mathbf{y}_0 \ . \end{cases} \tag{3.1}$$

To study the stability of a reference trajectory $\tilde{\mathbf{y}}(\mathbf{y}_0, t)$, evolving from $\mathbf{y}_0$, we examine the evolution of a nearby trajectory $\tilde{\mathbf{y}}(\mathbf{y}_0 + \delta\mathbf{y}, t)$, originating from a slightly perturbed initial condition $\mathbf{y}_0 + \delta\mathbf{y}$. Assuming that the initial separation $\Delta(0) = |\delta\mathbf{y}|^2$ between the two trajectories is infinitesimally small, we define the reference trajectory as *chaotic* if the square distance $\Delta(t) = |\tilde{\mathbf{y}}(\mathbf{y}_0 + \delta\mathbf{y}, t) - \tilde{\mathbf{y}}(\mathbf{y}_0, t)|^2$ grows exponentially over time. In more precise terms, this condition means that the corresponding *maximum Lyapunov exponent*

$$\lambda_L = \lim_{t\to\infty} \lim_{\Delta(0)\to 0} \frac{1}{t} \log \frac{\Delta(t)}{\Delta(0)} \ , \tag{3.2}$$

is positive. In practice, for $\Delta(0) \to 0$, we can approximate the difference between $\tilde{\mathbf{y}}(\mathbf{y}_0 + \delta\mathbf{y}, t)$ and $\tilde{\mathbf{y}}(\mathbf{y}_0, t)$ as:

$$\tilde{\mathbf{y}}(\mathbf{y}_0 + \delta\mathbf{y}, t) - \tilde{\mathbf{y}}(\mathbf{y}_0, t) \sim \frac{\partial \tilde{\mathbf{y}}(\mathbf{y}_0, t)}{\partial \mathbf{y}_0} \cdot \delta\mathbf{y} + O(\delta\mathbf{y}^2) \ . \tag{3.3}$$

Thus, the positive $\lambda_L$ is also reflected in the exponential growth over time of the matrix elements of the *derivative matrix*, denoted as $\mathbf{M}(\mathbf{y}_0, t) = \partial\tilde{\mathbf{y}}(\mathbf{y}_0, t)/\partial\mathbf{y}_0$.

The maximum Lyapunov exponent alone does not fully characterize the instability of a high-dimensional dynamical system. Actually, by perturbing the initial condition $\mathbf{y}_0$ in $d$ orthogonal directions, it is possible to obtain a set of hierarchically ordered exponents, defined as $\lambda_L = \lambda_1 \geq \lambda_2 \geq \cdots \geq \lambda_d$ [107, 114, 115]. This is set is often referred to as the *Lyapunov spectrum*. Mathematically, it can be defined by inspecting the dynamics of the derivative matrix in the tangent space, expressed as:

$$\frac{d}{dt}\mathbf{M} = \mathbf{A}(\mathbf{y}, t) \cdot \mathbf{M} \ . \tag{3.4}$$

The corresponding evolution operator is defined as the time-ordered exponential:

$$\mathbf{U}(\mathbf{y}_0, t) = \mathrm{T} \exp\left\{ \int_0^t ds \mathbf{A}\left[\tilde{\mathbf{y}}(\mathbf{y}_0, s), s\right] \right\} \ . \tag{3.5}$$

Then, according to the Odeselec theorem [116], the matrix

$$\mathbb{V}(\mathbf{y}_0) = \lim_{t\to\infty} \left[\mathbf{U}^T(\mathbf{y}_0, t)\mathbf{U}(\mathbf{y}_0, t)\right]^{\frac{1}{t}} \tag{3.6}$$

exists for almost all initial conditions in phase space. The Lyapunov exponents are then straightforwardly defined from the (positive) eigenvalues $\nu_j(\mathbf{y}_0)$ of the matrix in Eq. (3.6), as

$$\lambda_j(\mathbf{y}_0) = \log \nu_j(\mathbf{y}_0) \ . \tag{3.7}$$

In the most general case, the exponents depend on the initial condition $\mathbf{y}_0$, although this dependence can be neglected when the system is ergodic. We notice that our definition for the Lyapunov exponents might differ by a factor of 2 from the conventional one found in the literature.

An essential consequence of the Oseledec theorem pertains to the expansion rate of $k$-dimensional oriented volumes $\mathrm{Vol}_k(t) = \mathrm{Vol}[w_1(t), w_2(t), \ldots, w_k(t)]$, enclosed by the $k$ linearly independent vectors $w_1, w_2, \ldots, w_k$ in tangent space. Under the influence of the dynamics, this $k$-parallelepiped undergoes distortion, and its rate of expansion/contraction is determined by the sum of the first $k$ Lyapunov exponents:

$$\sum_{j=1}^{k} \lambda_j = \lim_{t\to\infty} \log \frac{\mathrm{Vol}_k(t)^2}{\mathrm{Vol}_k(0)^2} \ . \tag{3.8}$$

In the next sections, our focus will primarily be on Hamiltonian systems, whose symplectic structure leads to the pair rule $\lambda_{2N+1-j} = -\lambda_j$, where $N = d/2$ represents the system size. In such systems, the deformation of the volumes is often quantified by the *Kolmogorov-Sinai* (KS) *entropy* [8, 104], whose density $\Lambda_{KS}$ is the average of the first non-negative $N$ exponents

$$\Lambda_{KS} = \frac{1}{N}\sum_{j=1}^{N} \lambda_j \ . \tag{3.9}$$

### Quantum Lyapunov exponent and 4-point correlators

In this section, we briefly explore how the definition of Lyapunov exponents discussed earlier can be readily extended to quantum systems with a well-defined classical limit. However, as our primary focus shifts to classical chaos from Section 3.2 onwards, we will not delve deeply into the specifics of these definitions or the associated calculations. For a comprehensive understanding, we recommend consulting the respective references for further insights.

We begin by considering an Hamiltonian system, whose degrees of freedom $\mathbf{y} = (\mathbf{q}, \mathbf{p})$ are canonically conjugate variables, which can be straightforwardly quantized by imposing the equal-time commutation relations $[\hat{q}_j(t), \hat{p}_l(t)] = i\hbar\delta_{jl}$, in the Heisenberg picture. Then, a quantum generalization of the Lyapunov exponent can be defined from the exponential growth of the average square commutators [97]

$$\mathcal{F}(t) = -\frac{1}{N^2\hbar^2}\sum_{ij} \langle [\hat{q}_i(t), \hat{p}_j(0)]^2 \rangle \ , \tag{3.10}$$

retrieved also in the corresponding out of time order correlator (OTOC)

$$\mathcal{C}(t) = \frac{1}{N^2\hbar^2}\sum_{ij}\langle \hat{q}_i(t)\hat{p}_j(0)\hat{q}_i(t)\hat{p}_j(0)\rangle \ , \tag{3.11}$$

often studied in its regularized form [101]. Such a generalization comes from the observation that, in the limit of small $\hbar$, the commutator $[\hat{q}_i(t), \hat{p}_j(0)]/i\hbar$ can be replaced by the corresponding Poisson bracket:

$$\mathcal{F}(t) \simeq \frac{1}{N^2}\sum_{ij}\langle\{q_i(t), p_j(0)\}^2\rangle = \frac{1}{N^2}\sum_{ij}\langle\Big|\frac{\partial q_i(t)}{\partial q_j(0)}\Big|^2\rangle \ , \tag{3.12}$$

where the quantum average $\langle\cdot\rangle$ is replaced by a suitable average over the classical trajectories. Then, for $\hbar \to 0$, $\mathcal{F}(t)$ is expected to grow with the same Lyapunov exponent $\lambda_L$ characterizing the underlying classical Hamiltonian system.

In the same spirit, by replacing the tangent space dynamics in Eq. (3.4) with the one of the commutators $[\hat{q}_i(t), \hat{p}_j(0)]$ one can also define a quantum generalization of the full Lyapunov spectrum [106] and of the KS entropy [105]. In particular, the quantum KS entropy is believed to be a stronger indicator of quantum chaotic dynamics than the single $\lambda_L$ [106] and to accurately predict the entanglement growth, at early times and in a semi-classical limit, for a wide range of systems [108–110].

### 3.1.2 Fidelity susceptibility

The OTOC, defined in the previous section, is an effective probe for quantum chaos in systems possessing a well defined semi-classical [117] or large-$N$ [92, 98] limit. In general, this is not the case for spin-1/2 systems, where it has been proven that the OTOCs grow at most polynomially in time [118]. However, in the absence of any local conserved quantity beyond the Hamiltonian, spin-1/2 chains can still be *ergodic*, if they adhere to the eigenstate thermalization hypothesis (ETH), defined Eq. (1.11). The ETH ansatz has profound implications for the scaling of matrix elements of local operators. For instance, consider a quantum many-body system with a finite Hilbert space dimension $\mathcal{D}$ and a bounded spectrum. In this scenario, for two eigenstates $|E_n\rangle$ and $|E_m\rangle$ whose eigenvalues lie in the middle of the energy spectrum, the matrix elements of any local observable $\hat{O}$ are expected to scale to as

$$\langle E_n|\hat{O}|E_m\rangle \propto \mathcal{D}^{-1/2} \ , \tag{3.13}$$

for large $\mathcal{D}$[1] [19, 20]. Equation (3.13) has been confirmed by numerous numerical experiments [119–121]. This behaviour is opposed to the one displayed by integrable systems [122–126], where the matrix $\langle E_n|\hat{O}|E_m\rangle$ is sparse, featuring only few large off-diagonal matrix elements [120, 121].

It is therefore intriguing to explore whether, based on the scaling from Eq. (3.13), the notion of sensitivity to an external perturbation can be extended to quantum

[1] It is worth noting that, in the thermodynamic limit, we also expect the scaling $\mathcal{D} \propto \exp[S(E_\infty)]$. Here, $S(E)$ is the thermodynamic entropy and $E_\infty$ is the average energy at infinite temperature.

chaotic systems. This question has been recently addressed by M. Pandey [127], T. LeBlond [112] and their collaborators, who explored the potential sensitivity of a chaotic system's *eigenstates* to external perturbations. More precisely, they considered a generic Hamiltonian $\hat{H}_\lambda$, depending on an external parameter $\lambda$, whose spectrum is defined by the equation

$$\hat{H}_\lambda \left|E_n(\lambda)\right\rangle = E_n \left|E_n(\lambda)\right\rangle \ . \tag{3.14}$$

To investigate the response of an eigenstate with respect to a small shift $\lambda \to \lambda + \delta\lambda$, they analyzed the overlap

$$\langle E_n(\lambda+\delta\lambda)|E_n(\lambda)\rangle \sim 1 - \frac{1}{2}\chi_n \delta\lambda^2 + o(\delta\lambda^2) \tag{3.15}$$

between the perturbed and the original states. The average response $\chi = \mathcal{D}^{-1}\sum_n \chi_n$ of the eigenstates is referred to as the is also known as *fidelity susceptibility* [111] and was used in Refs. [112, 127] as a means to probe for chaos. More precisely, a standard calculation from non-degenerate perturbation theory [128] reveals that

$$\chi = \frac{1}{\mathcal{D}} \sum_n \sum_{m\neq n} \frac{|\,\langle E_n|\partial_\lambda \hat{H}_\lambda|E_m\rangle\,|^2}{(E_n - E_m)^2} \ . \tag{3.16}$$

Employing the scaling properties from RMT for the matrix elements $\langle E_n|\partial_\lambda \hat{H}_\lambda|E_m\rangle$ and substituting the denominator with the average inverse level spacing denoted as $\omega_L \propto \mathcal{D}^{-1}$, the authors established that the fidelity susceptibility scales as $\chi \sim \omega_L^{-1} \sim \mathcal{D}$, growing exponentially with the system size $L$. This exponential scaling, indicative of quantum chaos, was corroborated through extensive numerical simulations. In contrast, the studies on integrable models in the same works revealed a polynomial scaling behavior of $\chi$ with $L$. An even more surprising situation emerged when the Hamiltonian $\hat{H}_\lambda$ was close to an integrable one, with integrability spoiled by the perturbation in $\lambda$. In this scenario, the fidelity susceptibility diverged even faster with the system size, following a scaling law $\chi \sim \omega_L^{-\alpha}$, for $\alpha$ close to 2. Pandey and his collaborators also proved that the scaling of $\chi$ corresponding to $\alpha = 2$ was the fastest possible, highlighting the utmost fragility of eigenstates near the boundary between integrable and non-integrable regimes. Such scaling was observed in a region around the integrable point being exponentially small in the system size, when taking the thermodynamic limit. The same scalings for $\chi$ were retrieved by studying the approach to a disorder-localizated [126, 129–131] Hamiltonian, instead of the transition to an integrable one.

In summary, the fidelity susceptibility has been recently estabilished a sensitive probe for chaos and ergodicity breaking in quantum systems. In this chapter, in particular in Section 3.5 we will try to extend this results to the classical limit, where the dynamics is again asymptotically defined in terms of classical trajectories. Within the classical framework we can not directly study Eq. (3.15), as $\omega_L$ is expected to vanish and $\chi$ to diverge. Instead, we will study a regularized version of the fidelity, given by [127]:

$$\chi_\mu = \int \frac{d\omega}{2\pi} \frac{\omega^2}{(\omega^2+\mu^2)^2} \tilde{C}(\omega) \ , \tag{3.17}$$

where

$$\tilde{C}(\omega) = \sum_{m \neq n} |\langle E_n | \partial_\lambda \hat{H}_\lambda | E_m \rangle|^2 \delta(\omega - E_n + E_m) \tag{3.18}$$

is the spectral function. In a genuinely quantum system, the scaling $\chi \sim \omega_L^{-\alpha}$ would correspond to a divergence $\chi_\mu \sim \mu^{-\alpha}$ at small $\mu$ of the integral in Eq. (3.17) [127]. Thus, we will compute $\tilde{C}(\omega)$ classically and inspect the profile of $\chi_\mu$ for $\mu \to 0$.

## 3.2 Classical dynamics of the $p$-spin spherical model

Throughout the rest of this chapter, we will focus on the isolated dynamics of the $p$-spin glass Spherical Model (PSM), whose Hamiltonian

$$\hat{H}_J = \frac{1}{2M} \sum_{i=1}^{N} \hat{\Pi}_i^2 + V_J(\hat{\boldsymbol{\sigma}}), \tag{3.19}$$

with

$$V_J(\hat{\boldsymbol{\sigma}}) = - \sum_{1 \leq i_1 < \cdots < i_p \leq N} J_{i_1,\ldots,i_p} \hat{\sigma}_{i_1} \cdots \hat{\sigma}_{i_p} \ , \tag{3.20}$$

describes a system of $N$ spins interacting through random, all-to-all couplings $J_{i_1,\ldots,i_p}$, independently sampled from a Gaussian distribution with zero mean and variance $\overline{J^2} = 2p!J^2/N^{p-1}$. Here the spins $\hat{\sigma}_i$ are treated as continuous variables, obeying the spherical constraint $\sum_i \langle \hat{\sigma}_i^2 \rangle = N$ [132], and quantum fluctuations are implemented by the canonical quantization relations $[\hat{\sigma}_i, \hat{\Pi}_j] = i\hbar\delta_{ij}$. The term "spin glass" is attributed to the quantum PSM model, despite its use of position and momentum operators, due to historical reasons. The introduction of the quantum PSM can be traced back to Ref. [87], where it was revealed to manifest a thermodynamic phase transition from a paramagnetic to a spin glass state, driven by the temperature $T$ and by a dimensionless parameter $\Gamma = \sqrt{\hbar^2/MJ}$, which quantifies the strength of quantum fluctuations. The transition line $\Gamma_c(T)$ that separates these two phases shares qualitative features with the glass transition line experimentally observed in disordered spin 1/2 systems [85, 133], coupled to quantum fluctuations through an homogeneous transverse field. The nomenclature "spin glass" was then associated to the quantum PSM due to these observed similarities. The thermodynamic phase transition in the PSM is either of the first or second order depending on the strength of $\Gamma$ [87, 88] and its corresponding transition line can be parametrized also in terms of by a critical temperature $T_c(\hbar)$. At temperature $T_d(\hbar) \gtrsim T_c(\hbar)$, a dynamical, ergodicity-breaking transition is also observed [86], whose properties are sensitive to quenches in $\hbar$ in a non-trivial way [89]. In Refs. [93, 94], many-body chaos in the quantum PSM was studied using an OTOC in the large-$N$ limit and for a unitary evolution of the system from a thermal initial state. The OTOC grows exponentially at any temperature $T$, with a *quantum Lyapunov exponent* $\lambda_L(T)$, which displays qualitatively the same profile for a wide range of fixed values of $\hbar$ and in particular in the classical limit $\hbar \to 0$, having a single maximum at $T_m(\hbar) > T_d(\hbar)$ and vanishing in the low and high-temperature limits. In contrast to its fermionic counterpart, the Sachdev-Ye-Kitaev (SYK) model [98, 134, 135], in the PSM the bound on chaos $\lambda_L \leq 2\pi T/\hbar$, proven for a general quantum many-body system in

Ref. [101], is never saturated. A similarity between the Lyapunov exponent of the SYK model and that of the PSM only arises for $\hbar \to 0$, where the bound becomes trivial. In this case, the $\lambda_L(T)$ grows linearly with temperature $T$ at low $T$ for both cases [93, 136].

In this chapter we aim to gain physical insight on the behaviour of $\lambda_L$, by investigating the dynamics of the PSM in the classical limit $\hbar \to 0$ and at fixed energy-density $E$, a framework usually used for classical dynamical systems [14]. This goal can be achieved in the framework of Truncated Wigner Approximation (TWA) [137, 138], briefly reviewed in the following (see Refs. [139, 140] for further details). We begin by observing that, for a generic system with $N$-dimensional position and momentum-like degrees of freedom, like $\boldsymbol{\sigma}$ and $\boldsymbol{\Pi}$, the Heisenberg dynamics from an initial state $\hat{\rho}$ of any operator $\hat{O} = \mathcal{O}(\hat{\boldsymbol{\sigma}}, \hat{\boldsymbol{\Pi}})$ can be represented as

$$\langle \hat{O}(t) \rangle = \mathrm{Tr}[\hat{\rho}\ \hat{O}] = \int \frac{d\boldsymbol{\sigma} d\boldsymbol{\Pi}}{(2\pi\hbar)^N} W_\rho(\boldsymbol{\sigma}, \boldsymbol{\Pi}) O_W(\boldsymbol{\sigma}, \boldsymbol{\Pi}, t)\ , \tag{3.21}$$

where

$$O_W(\boldsymbol{\sigma}, \boldsymbol{\Pi}, t) = \int d\boldsymbol{\xi} \Big\langle \boldsymbol{\sigma} - \frac{\boldsymbol{\xi}}{2} \Big| \mathcal{O}(\hat{\boldsymbol{\sigma}}(t), \hat{\boldsymbol{\Pi}}(t)) \Big| \boldsymbol{\sigma} + \frac{\boldsymbol{\xi}}{2} \Big\rangle \exp\Big[ i \frac{\boldsymbol{\Pi} \cdot \boldsymbol{\xi}}{\hbar} \Big], \tag{3.22}$$

is called *Weyl symbol* of the operator $\hat{O}$, while the *Wigner function* $W_\rho(\boldsymbol{\sigma}, \boldsymbol{\Pi})$ is the Weyl symbol of the density matrix $\hat{\rho}$. The TWA is then a classical approximation for the dynamics of $O_W(\boldsymbol{\sigma}, \boldsymbol{\Pi}, t)$, summarized as

$$O_W(\boldsymbol{\sigma}, \boldsymbol{\Pi}, t) \simeq \mathcal{O}(\boldsymbol{\sigma}(t), \boldsymbol{\Pi}(t)) \tag{3.23}$$

where $(\boldsymbol{\sigma}(t), \boldsymbol{\Pi}(t))$ is the classical trajectory evolving from the initial condition $(\boldsymbol{\sigma}, \boldsymbol{\Pi})$ and determined by the following Hamilton equations:

$$\begin{cases} \partial_t \sigma_i = \Pi_i / M \\ \partial_t \Pi_i = -\sum_{j=1}^{N} \big( \delta_{ij} - \frac{\sigma_i \sigma_j}{N} \big) \frac{\partial V_J}{\partial \sigma_j} - \frac{\sum_i \Pi_i^2}{MN} \sigma_i\ . \end{cases} \tag{3.24}$$

The Eqs. (3.24) are essentially derived by adding to the Hamiltonian a Lagrange multiplier term $z(t)(\boldsymbol{\sigma}^2 - N)$, where $z(t)$ is determined in a self-consistent way so that the dynamics satisfies the spherical constraint at any time $t$ (see Appendix C.1 for more details). The TWA is believed to be valid at least up to an Ehrenfest time $t_{Ehr} \sim \log \hbar^{-1}$ [97] diverging for small-$\hbar$. In what follows, we will always fix $M = J = 1$.

To investigate the dynamics at fixed energy density $E$, the ideal setup would be to fix $\hat{\rho}$ as a micro-canonical state and compute the corresponding Wigner function, which is in general a formidable task. Instead, we fix an initial condition

$$\hat{\rho} = \frac{1}{\mathcal{N}_s} \sum_{l=1}^{\mathcal{N}_s} |\boldsymbol{\alpha}^{(l)}\rangle \langle \boldsymbol{\alpha}^{(l)}|\ , \tag{3.25}$$

as an ensemble of coherent states $|\boldsymbol{\alpha}^{(l)}\rangle = \otimes_{j=1}^{N} |\alpha_j^{(l)}\rangle$ [141]. These are eigenstates of the operators $\hat{a}_j = \hat{\sigma}_j/(\sqrt{2}l) + il\hat{\Pi}_j/(\sqrt{2}\hbar)$, for $j = 1, \ldots, N$ and a free parameter $l$.

Their respective eigenvalues are $\boldsymbol{\alpha}^{(l)} = \{\alpha_1^{(l)}, \dots, \alpha_N^{(l)}\}$. For each state $|\boldsymbol{\alpha}\rangle$, the Wigner function is the Gaussian wave-packet

$$W_{\boldsymbol{\alpha}}(\boldsymbol{\sigma}, \boldsymbol{\Pi}) = 2^N \prod_j \exp\Big\{ - \frac{(\sigma_j - \sigma_{\boldsymbol{\alpha}j})^2}{l^2} - \frac{l^2(\Pi_j - \Pi_{\boldsymbol{\alpha}j})^2}{\hbar^2} \Big\} \ . \tag{3.26}$$

In the following, we fix $l = \sqrt{\hbar}$, to have the same uncertainty in the variables $\boldsymbol{\sigma}$ and $\boldsymbol{\Pi}$. The centers $(\boldsymbol{\sigma}_{\boldsymbol{\alpha}}, \boldsymbol{\Pi}_{\boldsymbol{\alpha}})$ of the various wave-packets are chosen in a way that $\langle \boldsymbol{\alpha} | \hat{H}_J | \boldsymbol{\alpha} \rangle / N = E$. For the small values of $\hbar$ we are interested in, it can be easily shown that such choice is equivalent to fix the classical energy density

$$\frac{1}{N} \mathcal{H}_{cl}(\boldsymbol{\sigma}_{\boldsymbol{\alpha}}, \boldsymbol{\Pi}_{\boldsymbol{\alpha}}) = \frac{\boldsymbol{\Pi}_{\boldsymbol{\alpha}}^2}{2MN} + \frac{V_J(\boldsymbol{\sigma}_{\boldsymbol{\alpha}})}{N} \simeq E \ , \tag{3.27}$$

so that we can determine the centers of the wave-packets in Eq. (3.26) using the following "classical annealing" algorithm.

1. First extract a random configuration $(\boldsymbol{\sigma}_0, \boldsymbol{\Pi}_0)$ in phase space, with $\boldsymbol{\sigma}_0$ uniformly sampled on the $N$-sphere and $\boldsymbol{\Pi}_0$ sampled from the normal distribution with zero mean and unit variance.

2. To bring the system in a configuration at the desired energy density $E$, we integrate the dynamics starting from $(\boldsymbol{\sigma}_0, \boldsymbol{\Pi}_0)$ and defined by the equations

$$\begin{cases} \partial_t \sigma_i = \Pi_i / M \\ \partial_t \Pi_i = - \sum_{j=1}^{N} \big(\delta_{ij} - \frac{\sigma_i \sigma_j}{N}\big) \big( \frac{\partial V_J}{\partial \sigma_j} + \gamma \Pi_j \big) - \frac{\sum_i \Pi_i^2}{MN} \sigma_i \ , \end{cases} \tag{3.28}$$

   where a dissipative term of strength $\gamma > 0$ has been added. Notice that $\gamma > 0$ if $\mathcal{H}_{cl}(\boldsymbol{\sigma}_0, \boldsymbol{\Pi}_0) > NE$ and $\gamma < 0$ otherwise.

3. Finally stop the integration as soon as the system reaches a configuration $(\boldsymbol{\sigma}_1, \boldsymbol{\Pi}_1)$ such that $\mathcal{H}_{cl}(\boldsymbol{\sigma}_1, \boldsymbol{\Pi}_1) = NE$. Afterwards we may set $\gamma = 0$ and integrate the Hamilton dynamics (Eq. (3.24)) from $(\boldsymbol{\sigma}_1, \boldsymbol{\Pi}_1)$ for a time $t_{eq}$, to let the system reach a typical configuration on the corresponding classical microcanonical manifold, which we finally take as the center $(\boldsymbol{\sigma}_{\boldsymbol{\alpha}}, \boldsymbol{\Pi}_{\boldsymbol{\alpha}})$ of the wave-packet in Eq. (3.22). Throughout the rest of this chapter, we fix $\gamma = 0.5$ and $t_{eq} = 5$.

In practice, the Wigner function for the initial state in Eq. (3.25) is obtained taking the average over $\mathcal{N}_s$ different wave-packets, sampled from the classical annealing algorithm for the same fixed configuration of the disorder $\{J_{i_1,\dots,i_p}\}$, as

$$W_\rho(\boldsymbol{\sigma}, \boldsymbol{\Pi}) = \frac{1}{\mathcal{N}_s} \sum_{l=1}^{\mathcal{N}_s} W_{\boldsymbol{\alpha}^{(l)}}(\boldsymbol{\sigma}, \boldsymbol{\Pi}) \ . \tag{3.29}$$

We repeat the algorithm for each of the $\mathcal{N}_s$ states: the resulting set of points $\{(\boldsymbol{\sigma}_c^{(l)}, \boldsymbol{\Pi}_c^{(l)})\}_{l=1\dots\mathcal{N}_s}$ is then a non-uniform sampling of the classical microcanonical manifold at energy density $E$. As long as $\hbar$ is very small, TWA enables us to sample orbits

evolving from a neighborhood of each of each configuration $(\boldsymbol{\sigma}_{\boldsymbol{\alpha}}, \boldsymbol{\Pi}_{\boldsymbol{\alpha}})$, a feature which we will use in Section 3.3 to investigate classical chaos in the PSM from the average growth of the width of the wave-packets. We compute all the observables we are interested in by averaging over an ensemble of trajectories, evolving according to Eq. (3.24) from an initial condition $(\boldsymbol{\sigma}, \boldsymbol{\Pi})$ sampled from the distribution in Eq. (3.29). In the rest of this chapter, we will denote by $\langle \cdot \rangle$ the average over the sampled trajectories and by $\overline{(\cdot)}$ the one over the disorder configurations $\{J_{i_1 \dots i_p}\}$. We fix $\hbar = 10^{-8}$, $N = 100$ and we focus on the paradigmatic case of $p = 3$.

We conclude this section with two technical remarks. First, it is worth noting that the classical annealing algorithm described above allows us to sample energies that are arbitrarily high, but not arbitrarily low. Specifically, in the PSM, the local minima of the potential $V_J(\boldsymbol{\sigma})$ are situated below a characteristic energy scale of $E_{th} = -\sqrt{2(p-1)/p}$ [74] (also discussed in Section 3.4 and detailed in Appendix C.4). Due to this limitation, our classical annealing approach cannot explore phase space configurations with energies $E < E_{th}$, as the dissipative dynamics of Eq. (3.28) becomes trapped in the vicinity of the first encountered local minimum. As a result of this constraint on sampling low-energy configurations, we are unable to investigate the relationship between $\lambda_L$ and $E$ in the vicinity of the ground state. Consequently, we are also unable to make a comparison against the linear dependence of $\lambda_L$ on $T$, for small $T$, observed in Ref. [93]. The second remark is that our definition of the Wigner function is not rigorous for the degree of freedom $\boldsymbol{\sigma}$ lying on a compact configuration space (see also Ref. [142]). Specifically, the configurations $\boldsymbol{\sigma}$ sampled from the distribution in Eq. (3.29) are not confined to the $N$-sphere. Although our approximation fails in capturing precise quantum dynamics at finite $\hbar$, it is expected to be reliable in the limit of $\hbar \to 0$. For our investigative purposes, it serves merely as a tool to examine the classical trajectories evolving from nearby initial configurations sampled at low $\hbar$ (thus testing classical chaos). Furthermore, for $\hbar \to 0$, the configurations we extract are expected to asymptotically lie with the $N$-sphere. This is true as long as the center $\boldsymbol{\sigma}_c$ of each sampled wave-packet $W_{\boldsymbol{\alpha}^{(l)}}(\boldsymbol{\sigma}, \boldsymbol{\Pi})$ also resides on the $N$-sphere, a condition consistently met within the classical annealing algorithm.

## 3.3 Results: Chaos indicators

We present here our results for the chaos estimators of the PSM, starting from the Lyapunov exponent $\lambda_L$. In principle, $\lambda_L$ can be obtained as a function of $E$ by computing the Weyl symbol, defined in Eq. (3.22), of the OTOC [92]. However, in the $\hbar \to 0$ limit we are interested in, $\lambda_L$ becomes the exponential rate of divergence of pairs of nearby orbits of the emerging classical dynamics and can be computed from

$$d_J(t) = \frac{1}{2N\hbar} \frac{1}{\mathcal{N}_s} \sum_{l=1}^{\mathcal{N}_s} \sum_{i=1}^{2N} \langle \boldsymbol{\alpha}^{(l)} | \left[ \hat{y}_i(t) - \langle \alpha | \, \hat{y}_i(t) \, | \alpha \rangle \right]^2 | \boldsymbol{\alpha}^{(l)} \rangle \ , \tag{3.30}$$

where $\hat{\mathbf{y}} = (\hat{\sigma}_1, \dots, \hat{\sigma}_n, \hat{\Pi}_1, \dots, \hat{\Pi}_N)$ is the set operators corresponding to a classical phase space configuration. The quantity $d_J(t)$ is easier to compute than the OTOC in

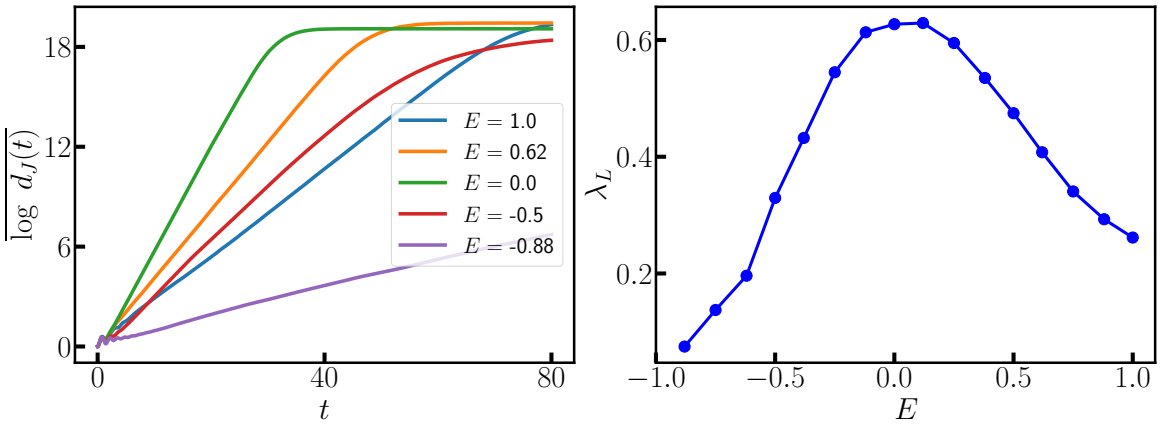


Figure 3.1: **(Left)** Time-evolution of the log-average over the disorder of the distance $d_J(t)$ in Eq. (3.30), reported for few paradigmatic energy densities . The average over the initial condition is performed extracting 25 random configurations from each of the $\mathcal{N}_s = 20$ wave-packets, defined in Eq. (3.26) and obtained through the classical annealing algorithm. The dynamics is integrated up to a time $t_{max} = 80$. The log-average over the disorder is taken over $\mathcal{N}_d = 30$ configurations. **(Right)** Lyapunov exponent $\lambda_L$, defined in Eq. (3.35), obtained through a linear fit of $\overline{\log d_J(t)}$ over a time window $[t_I, t_F]$, defined in such a way that, for each $E$, $t_I$ is beyond the oscillations at early times displayed by $\overline{\log d_J(t)}$ and $t_F$ is smaller than the saturation time-scale.

the TWA framework and its exponential growth rate is given by $\lambda_L$, in the classical limit, as we show in the following. First we rewrite each term in the right-hand side of Eq. (3.30) within the TWA framework, as

$$\langle\alpha|\left[\hat{y}_i(t) - \langle\alpha|\,\hat{y}_i(t)\,|\alpha\rangle\right]^2|\alpha\rangle = \int \frac{d^{2N}y}{(2\pi\hbar)^N} W_{\boldsymbol{\alpha}}(\mathbf{y})\left[\tilde{y}_i(\mathbf{y},t) - \langle\tilde{y}_i(\mathbf{y},t)\rangle_{\boldsymbol{\alpha}}\right]^2 . \tag{3.31}$$

The average $\langle\cdot\rangle_{\boldsymbol{\alpha}}$ on the right-hand side of Eq. (3.31) is itself performed over the coherent wave-packet

$$\frac{W_{\boldsymbol{\alpha}}(\mathbf{y})}{(2\pi\hbar)^N} = \frac{1}{(\pi\hbar)^N}\exp\Big\{-\frac{(\mathbf{y}-\mathbf{y}_{\boldsymbol{\alpha}})^2}{\hbar}\Big\} . \tag{3.32}$$

For $\hbar \to 0$, $W_{\boldsymbol{\alpha}}(\mathbf{y})$ becomes a $\delta$-function of 0 width. To investigate the behaviour of Eq. (3.31) in this limit, it is useful to perform the change of variable $\mathbf{y} = \mathbf{y}_{\boldsymbol{\alpha}} + \sqrt{\hbar}\mathbf{x}$. Then we have:

$$\begin{aligned} \tilde{\mathbf{y}}(\mathbf{y}_{\boldsymbol{\alpha}} + \sqrt{\hbar}\mathbf{x}, t) &\sim \tilde{\mathbf{y}}(\mathbf{y}_{\boldsymbol{\alpha}}, t) + \sqrt{\hbar}\frac{\partial\tilde{\mathbf{y}}(\mathbf{y}_{\boldsymbol{\alpha}}, t)}{\partial\mathbf{y}}\cdot\mathbf{x} + O(\hbar) , \\ \langle\tilde{\mathbf{y}}(\mathbf{y}_{\boldsymbol{\alpha}} + \sqrt{\hbar}\mathbf{x}, t)\rangle_{\boldsymbol{\alpha}} &\sim \tilde{\mathbf{y}}(\mathbf{y}_{\boldsymbol{\alpha}}, t) + O(\hbar) . \end{aligned} \tag{3.33}$$

Then, plugging Eqs. (3.33) into Eq. (3.31), averaging over the sites and performing a little algebra, we obtain

$$\frac{1}{N\hbar}\sum_{i=1}^{2N}\langle\alpha|\left[\hat{y}_i(t) - \langle\alpha|\,\hat{y}_i(t)\,|\alpha\rangle\right]^2|\alpha\rangle \sim \frac{1}{2N}\sum_{i,j=1}^{2N}\left|\frac{\partial\tilde{y}_i(\mathbf{y}_\alpha, t)}{\partial y_j}\right|^2 + O(\hbar) . \tag{3.34}$$

As argued in Section 3.1, the terms in the sum on the right-hand side of Eq. (3.34) grow exponentially in time, for a chaotic system. Equation (3.34) reproduces the dynamics of the derivative matrix only for a finite time-window: the noise produced by the fluctuations of order $\hbar$ eventually lead to a saturation of the typical distance between trajectories evolving from a neighbourhood of $\mathbf{y}_{\boldsymbol{\alpha}}$, on time scales longer than $t_{Ehr} \sim \log \hbar^{-1}$.

Small fluctuations on top of the exponential growth appear also at early times: to get rid of them, we compute the average over the disorder of the *logaritm* of $d_J(t)$, denoted as $\overline{\log d_J(t)}$, and retrieve a smooth linear growth

$$\overline{\log d_J(t)} \sim \lambda_L t \tag{3.35}$$

on intermediate time scales, as shown Fig. 3.1 (left). The corresponding Lyapunov exponent $\lambda_L$, shown in Fig. 3.1 (right) against the energy density $E$, has a clear peak close to $E = 0$, while it asymptotically vanishes at low and high energies. In Refs. [93, 94], it was shown that $\lambda_L$ has the same qualitative profile as a function of $T$, displaying for small $\hbar$ a single maximum around $T_m(\hbar) \simeq 1$: this maximum is consistent with the one we find at $E = 0$, since in the paramagnetic phase the classical energy density $E$ and the temperature $T$ are related by the equation $E = T/2 - 1/(2T)$ (as shown in Ref. [143]). Our computed results are also in close numerical agreement with those obtained in Refs. [93, 94], where the estimated maximum for the Lyapunov exponent was around $\lambda_L \simeq 0.6$, like in our findings. However, it is important to note that the order of operations in Eq. (3.35), involving a logarithm and an average over disorder, is reversed compared to previous studies (see Ref. [117] for a more general discussion). Consequently, we do not expect a perfect match between the $\lambda_L$ we compute here and results from Refs. [93, 94]. In summary, the exponent $\lambda_L$ we calculate is essentially classical, and the introduction of small fluctuations in the initial conditions is merely a tool we use to sample nearby trajectories starting from the same wave-packet. It is worth mentioning that, while we use quantum fluctuations to sample nearby configurations in phase space, classical chaos can also be probed using different kind of fluctuations (see Ref. [144] for an example).

In the classical limit, the strength of chaos at different energy densities can be also connected to entropy generation by looking at the Kolmogorov-Sinai (KS) entropy [8, 104]. As already discussed in Section 3.1, its density can be expressed as the average $\Lambda_{\text{KS}} = \sum_{i=1}^{N} \lambda_i / N$ over the positive elements of the ordered Lyapunov spectrum. As shown in Refs. [108, 110], the eigenvalues of the symmetric fluctuation matrix

$$\begin{aligned}\mathbf{G}_{jl}(t) = \frac{1}{2\hbar \mathcal{N}_s} \sum_{l=1}^{\mathcal{N}_s} \Big\langle \Big[ \big(\hat{y}_j(t) - \langle \hat{y}_j(t) \rangle\big) \big(\hat{y}_l(t) - \langle \hat{y}_l(t) \rangle\big) + \\ + \big(\hat{y}_l(t) - \langle \hat{y}_l(t) \rangle\big) \big(\hat{y}_j(t) - \langle \hat{y}_j(t) \rangle\big) \Big] \Big\rangle_{\boldsymbol{\alpha}^{(l)}} .\end{aligned} \tag{3.36}$$

diverge as $\exp(\lambda_i t)$ in the limit $\hbar \to 0$. Then, the KS entropy density is straightforwardly extracted from the growth rate of the quantity

$$S_{\text{KS}}(t) = \frac{1}{N} \overline{\log \det [\mathbf{G}_{ij}(t)]_{1 \le ij \le N}} \sim \Lambda_{\text{KS}} t \ , \tag{3.37}$$

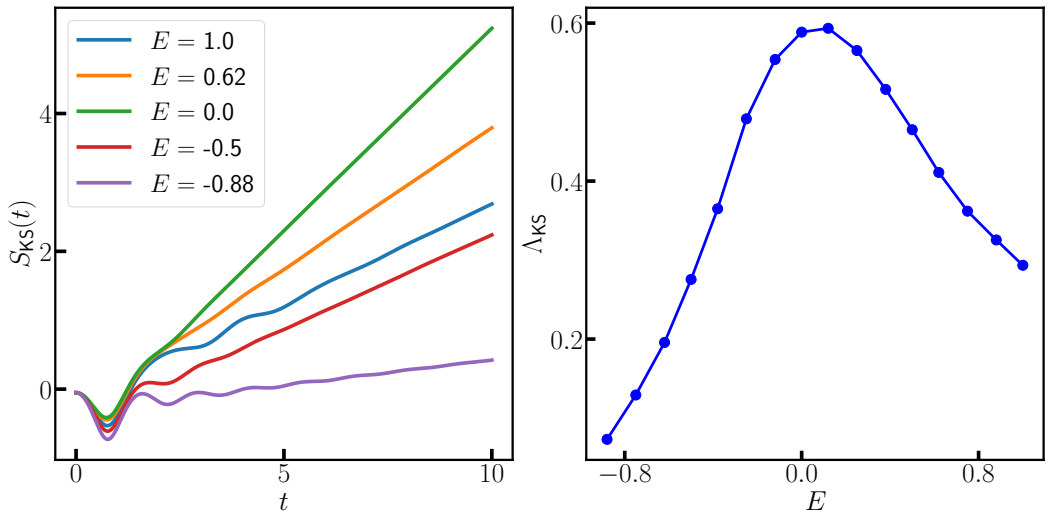


Figure 3.2: **(Left)** Time-evolution of the quantity $S_{\rm KS}$ defined in Eqs. (3.36) and (3.37), reported for few paradigmatic energy densities. The average over the initial condition is performed extracting 30 random configurations from each of the $\mathcal{N}_s = 30$ wave-packets, defined in Eq. (3.26) and obtained through the classical annealing algorithm. The dynamics is integrated up to a time $t_{max} = 80$. The log-average over the disorder is taken over $\mathcal{N}_d = 96$ configurations. **(Right)** Kolmogorov-Sinai entropy $\Lambda_{\rm KS}$, defined in Eq. (3.37), obtained through a linear fit of $S_{\rm KS}$ over a time window $[t_I, 10]$, where $t_I$ is beyond the scale of oscillations at early time displayed by $S_{\rm KS}$, for each $E$.

on intermediate time-scales. We observe that, within our framework, Eq. (3.37) can also be derived by a straightforward generalization of Eq. (3.34). We plot $S_{\rm KS}(t)$ in Fig. 3.2 (left) and, in Fig. 3.2 (right), its corresponding slope $\Lambda_{\rm KS}$, showing that the maximal chaos located at $E = 0$ can be detected also by the KS entropy. Notably, a similar result was recently derived also for a classical spin system without disorder [145].

## 3.4 Chaos, Ergodicity and Energy Landscape

In this section we elaborate further on the results of the previous section and try to provide a qualitative interpretation for the observed maximal chaos around energy $E = 0$ in the PSM. In particular, a natural question is whether this result can be understood from the relaxation dynamics of the PSM at fixed energy density, as probed for example from the spin correlation function, or related to properties of the energy landscape. As we are going to show, the maximal chaos around $E = 0$ in the PSM occurs when the spin relaxation is the fastest and when the complexity of the underlying energy landscape is maximal.

The relaxation dynamics for both classical [81, 82] and quantum [86] spin glasses is most often studied in presence of a finite temperature bath. Relaxation is usually

defined in terms of the (symmetric) correlation function

$$C(t,t') = \frac{1}{2N}\sum_{i=1}^{N} \overline{\langle \hat{\sigma}_i(t)\hat{\sigma}_i(t') + \hat{\sigma}_i(t')\hat{\sigma}_i(t)\rangle} \ . \tag{3.38}$$

At high temperatures, the function $C(t_w, t_w+\tau)$ becomes approximately time-translation invariant for moderately high values of $t_w$, and decays to zero for large $\tau$, indicating that the underlying dynamics of the system is ergodic. However, at sufficiently low temperatures, the system may exhibit the so-called '*weak ergodicity breaking* scenario' [81, 86, 146] (see Ref. [82] for a review), meaning that

$$\lim_{t_w\to\infty} C(t_w, t_w+\tau) = q_1 + C_{st}(\tau) \ , \tag{3.39}$$

with a finite dynamical overlap $q_1 > 0$ and where again $C_{st}(\tau)$ vanishes for $\tau \to \infty$, determining a non-ergodic dynamics. In spin glasses, ergodicity breaking is usually accompanied by a breaking of time-translation invariance in $C(t_w, t_w+\tau)$, a phenomenon usually referred to as *aging* [82, 147]: $C(t_w, t_w+\tau)$ has a plateau around $q_1$, whose finite length increases as $t_w$ grows (and diverging for $t_w \to \infty$), before eventually decaying to zero for longer time-scales. Here we are interested instead in the Hamiltonian relaxation dynamics, starting from fixed energy initial conditions. We note that the Hamiltonian dynamics of both classical and quantum PSMs starting from a finite temperature state has been studied recently [89, 143]. To this extent we compute $C(t_w, t_w+\tau)$ in the TWA formalism at finite energy density $E$, making use of Eq. (3.21) and of the identity

$$\frac{1}{2}\{\hat{\sigma}_i(t)\hat{\sigma}_i(t') + \hat{\sigma}_i(t')\hat{\sigma}_i(t)\}_W = \sigma_i(t)\sigma_i(t') \ . \tag{3.40}$$

The results in Fig. 3.3-(a) show that the correlation function undergoes a temporal crossover from high energies, where it displays wide oscillations, to low energies, where the dynamics slows down. Quite interestingly, at the maximally chaotic point $E = 0$ we observe the fastest relaxation of the correlation function, decaying to zero with few oscillations, again compatibly with Refs. [93, 94]. Upon decreasing further the energy below $E = 0$, the dynamics slows down and we expect a finite plateau around $q_1$ to to appear. Detecting this intermediate plateau within the given simulation time-window is challenging. Consequently, we compute $q_1$ as the value of the correlation function at $t_w = \tau = t_{max}/2$: our results are expected to converge to the ones predicted by Eq. (3.39) in the limit of $t_{max} \to \infty$. In Figure 3.3-(b) we show that $q_1$ becomes nonzero below a certain energy threshold, estimated to be around $E_d \simeq -0.38$, and that $q_1$ also increases as $E$ further decreases below the threshold. At the same time, the profiles of the correlation function shown in Fig. 3.3-(c) lose time-translation invariance again below $E \simeq -0.38$. Notably, these findings are also compatible with the ones obtained from the same simulations performed for a larger $t_{max}$, which are reported in Appendix C.2 and highlight that both a finite $q_1$ and a loss of time-traslational invariance are retrieved at the same energy scale. The results discussed above indicate signs of ergodicity breaking below the energy $E_d \lesssim -0.38$. However, we recognize that our findings, including our estimated value for $E_d$, might undergo quantitative changes with a more extensive analysis using a significantly larger $t_{max}$ than the values considered in this manuscript. Therefore, the ergodicity breaking we observe here should be

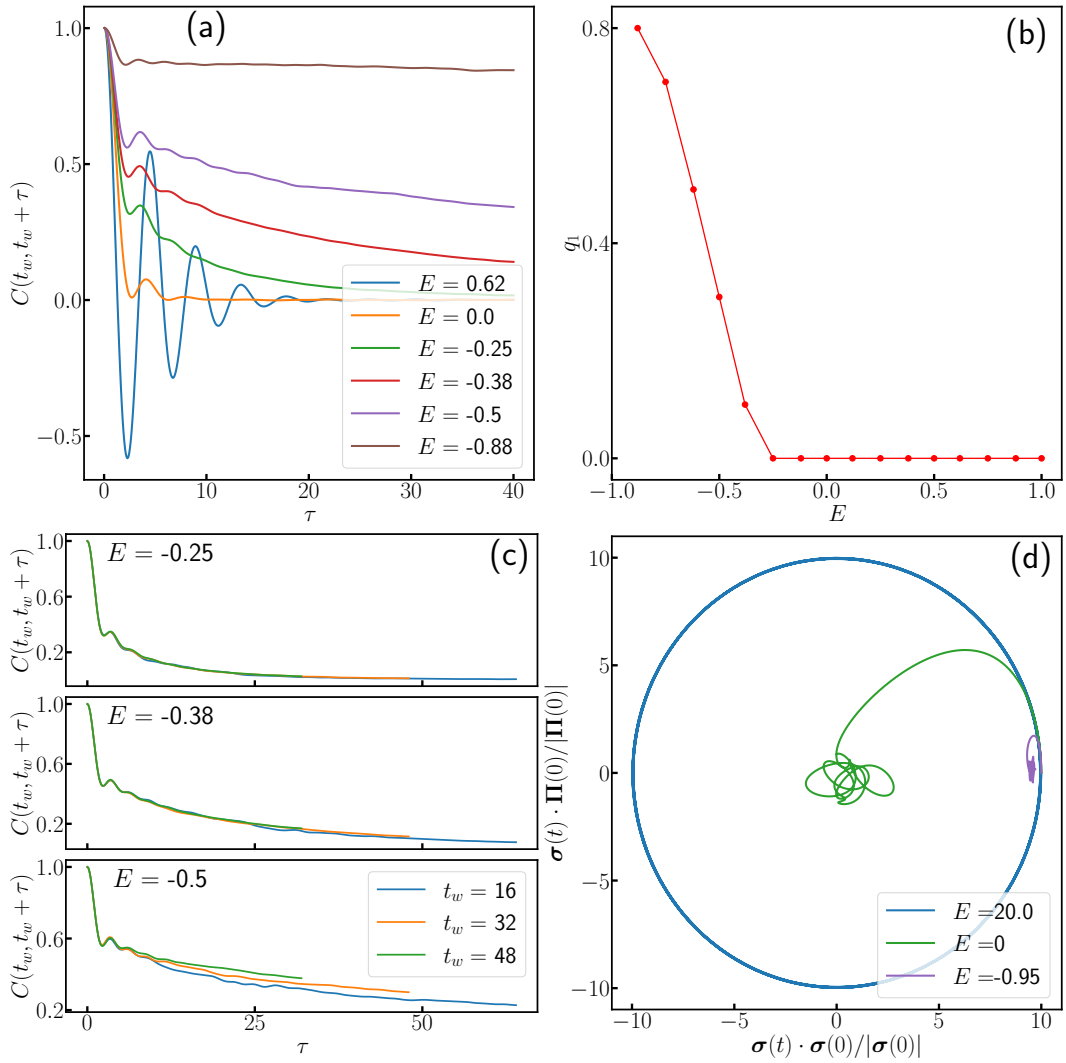


Figure 3.3: **(a)** Time-dependence of the correlation function, at fixed $t_w = 40$. **(b)** Asymptotic value $q_1$ of the correlation functions $C(t_w, t_w + \tau)$ reported in panel (a), obtained through the time-average of the latter over $\tau \in [39, 40]$. **(c)** Comparison between the profiles of $C(t_w, t_w = \tau)$ obtained fixing different values of $t_w$. Each panel corresponds to a different energy density $E$. **(d)** Time-evolution of three typical orbits, whose initial conditions are obtained extracting one configuration from the distribution in Eq. (3.29), at different energy densities $E$ and for the same configuration of the disorder. The orbits evolve in a 200-dimensional phase space and are projected over the two axes defined by the initial spin configuration $\boldsymbol{\sigma}(0)$ and the initial momentum $\boldsymbol{\Pi}(0)$.

interpreted as a regime where dynamics is sufficiently slow for the thermalization time to extend beyond $t_{max}$.

We now argue that both maximal chaoticity and fastest spin relaxation emerge alongside maximal complexity in the topology of the potential $V_J(\boldsymbol{\sigma})$, from Eq. (3.20), at the $E = 0$ level surface. To understand this connection, we first observe that the profile of the correlation function in Fig. 3.3-(a) can be associated to the typical

behaviour of the underlying trajectories, as sketched in Fig. 3.3-(d). While the regular oscillations at high energies are due to an underlying uniform circular motion on the $N$-sphere, in the limit of low energies the trajectories oscillate in a well around a local minimum of $V_J(\boldsymbol{\sigma})$, whose amplitude can be roughly estimated as the typical distance between two configurations of the same trajectory, observed at large times separation $\tau$:

$$\sum_{i=1}^{N}[\sigma_i(t_w+\tau)-\sigma_i(t_w)]^2 = 2N - 2\sum_{i=1}^{N}\sigma_i(t_w+\tau)\sigma_i(t_w) \simeq 2N(1-q_1)\ . \tag{3.41}$$

Chaos and relaxation emerge in between these two trivial limits, where the trajectories are scattered in neighbors of the unstable stationary configurations of the dynamics in Eq. (3.24) and explore the whole configuration space. The stationary configurations can be defined as solutions of the equations (see also Ref. [148])

$$\begin{cases} -\dfrac{\partial V_J}{\partial \sigma_i} + p\dfrac{V_J(\boldsymbol{\sigma})}{N}\sigma_i = 0 \\ \displaystyle\sum_i \sigma_i^2 = N \\ \quad \Pi_i = 0\ , \end{cases} \tag{3.42}$$

where in the first equation we used the identity $\sum_j \sigma_j \partial V_J/\partial\sigma_j = pV_J(\boldsymbol{\sigma})$, holding for the potential $V_J(\boldsymbol{\sigma})$ defined in Eq. (3.20). As discussed in Appendix C.4 the average number of solutions of Eq. (3.42), lying on the microcanonical manifold at energy density $E = \sum_i \Pi_i^2/2MN + V_J(\boldsymbol{\sigma})/N$, is in a one-to-one correspondence with the stationary points of the potential $V_J(\boldsymbol{\sigma})$ on the $N$-sphere. The average number of such stationary points can then be expressed as (see again Appendix C.4):

$$\overline{\mathcal{N}(E)} = \int D\sigma \overline{\prod_i \delta\Big(-\frac{p}{p!}\sum_{kl} J_{ikl}\sigma_k\sigma_l - pE\sigma_i\Big)\Big|\det\Big(-\frac{p(p-1)}{p!}\sum_k J_{ijk}\sigma_k - pE\delta_{ij}\Big)\Big|}\ . \tag{3.43}$$

For the classical potential $V(\boldsymbol{\sigma})$ in Eq. (3.20) and in the large-$N$ limit, the number of stationary points scales exponentially as $\overline{\mathcal{N}(E)} \simeq \exp\{N\Sigma(E)\}$ [74, 113], where $\Sigma(E)$ is usually referred to as *complexity*. At the same time, the stability of such stationary points is characterized by the index $k(E)$, where $Nk(E)$ is the average number of unstable directions around every stationary points. In Appendix C.4, we also derive the analytical expressions for both $\Sigma(E)$ and $k(E)$ as functions of $E$, finding that:

$$\Sigma(E) = \frac{\mathrm{Re}[z(E)]^2 - \mathrm{Im}[z(E)]^2}{p(p-1)} + \frac{1}{2}\log\left\{(\mathrm{Re}[z(E)]^2 - pE)^2 + \mathrm{Im}[z(E)]^2\right\} - E^2 - \frac{1}{2}\log\frac{p}{2} + \frac{1}{2}\ , \tag{3.44}$$

where

$$z(E) = \begin{cases} p\big(E + \sqrt{E^2 - 2(p-1)/p}\big)/2\ , & \text{if } |E| < |E_{th}| \equiv \sqrt{2(p-1)/p} \\ p\big(E - \sqrt{E^2 - 2(p-1)/p}\big)/2\ , & \text{if } |E| > |E_{th}| \end{cases}\ , \tag{3.45}$$

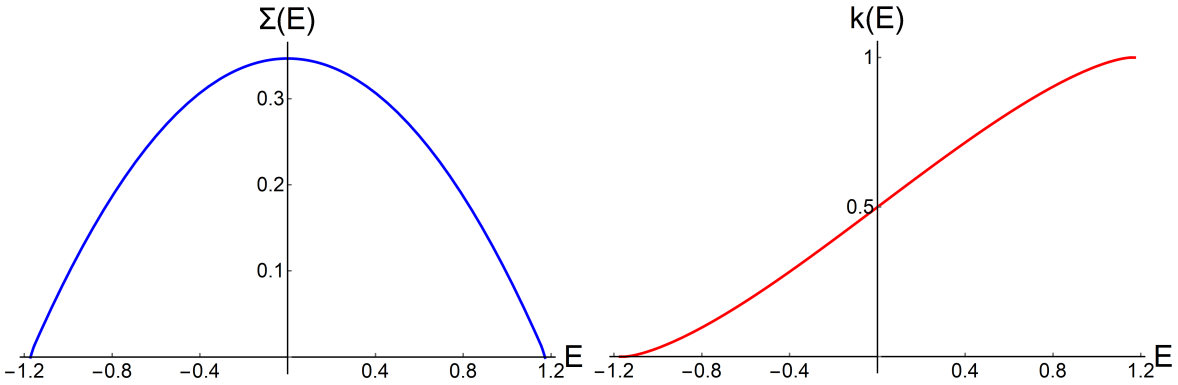


Figure 3.4: Plots of the complexity function $\Sigma(E)$ (left) and of the average stability index $k(E)$ (right), defined respectively in Eqs. (C.42) and (C.43), for $p = 3$.

and

$$k(E) = \begin{cases} 0 \ , \ \text{if } E < E_{th} \\ \frac{p}{2\pi(p-1)} E\sqrt{E_{th}^2 - E^2} + \frac{1}{\pi}\arctan\left(\frac{\sqrt{E_{th}^2 - E^2}}{E}\right) \ , \ \text{if } |E| < |E_{th}| \\ 1 \ , \ \text{if } E > |E_{th}| \end{cases} . \tag{3.46}$$

Intuitively, the value $E_{th} = -\sqrt{2(p-1)/p}$ appearing in the previous formulas represents the *threshold* energy density below which the stationary points are typically local minima of $V(\boldsymbol{\sigma})$, so that $k(E) = 0$ (similarly, $-E_{th}$ is the energy density above which all stationary points of $V(\boldsymbol{\sigma})$ are typically local maxima). Both $\Sigma(E)$ and $k(E)$ are plotted in Fig. 3.4. The first observation that we make is that the complexity $\Sigma(E)$ has a maximum on the $E = 0$ surface, where stationary points are predominantly saddles of $V_J(\boldsymbol{\sigma})$, surrounded on average by half stable and half unstable directions, as $k(E = 0) = 1/2$. Second, we notice that the complexity $\Sigma(E)$ vanishes at two points $E = \pm E_0$, with $E_0 > |E_{th}|$. Beyond $E_0$, we have $\Sigma(E) < 0$, which implies a vanishing number of stationary configurations, so we interrupt the plot at $E_0$. Intuitively, $-E_0$ ($E_0$) can be interpreted as the typical value of the absolute minimum (maximum) of $V_J(\boldsymbol{\sigma})/N$ [148], which is always finite for $\boldsymbol{\sigma}$ lying on the $N$-sphere. We observe that our results for the complexity at fixed energy are compatible with the ones in the literature obtained using different methods [113, 149]. The maximum of $\Sigma(E)$ at $E = 0$ unveils a correlation between the number of saddles in the energy landscape and the maximal chaos, detected by $\lambda_L$. This observation suggests that the scattering of trajectories against a maximal number of saddles could offer a potential explanation for the emergence of maximal chaos at $E = 0$.

## 3.5 The fidelity susceptibility against the dynamical slowing down

The results presented in Section 3.4 suggest a strong increase of the classical thermalization times below the threshold at $E_d \simeq -0.38$, possibly corresponding to ergodicity

breaking for a diverging simulation time and determined by the long-time behavior of the correlation function. Such slowdown in the dynamics is analogous to the ones observed in Refs. [112, 127] and discussed in Section 3.1.2, for a quantum Hamiltonian close to a non-integrable point (either integrable or disorder-localized), which corresponds to a fast divergence in the fidelity susceptiblity $\chi$.

In this section we test the possible emergence of such scaling for the classical dynamics we are interested in in this chapter. Specifically, we perturb the Hamiltonian in Eq. (3.19) with local magnetic fields $B_i$, summarized in the extra term

$$\hat{H}_1 = -\sum_i B_i \hat{\sigma}_i \ . \tag{3.47}$$

Then, by perturbation theory, the sensitivity $\chi_n^{(i)}$ of the $n$-th eigenstate to the magnetic field $B_i$ (posing $B_j = 0$ on every other site $j$), is defined by

$$\langle n(0)|n(B_i)\rangle = 1 - \frac{1}{2}\chi_n^{(i)} B_i^2 + O(B_i^3) \ . \tag{3.48}$$

We define the fidelity susceptibility as its average $\chi$ over the initial condition in Eq. (3.25) and the disorder configurations:

$$\chi = \frac{1}{N}\sum_{i=1}^{N}\sum_{n=0}^{\infty} \overline{\langle n|\hat{\rho}|n\rangle\, \chi_n^{(i)}} \ . \tag{3.49}$$

As outlined in Section 3.1.2, the vanishing of the average level spacing $\omega_L$ represent an obstruction to study Eq. (3.49) in the classical limit. Instead, we will study its regularized version,

$$\chi_\mu = \int \frac{d\omega}{2\pi} \frac{\omega^2}{(\omega^2+\mu^2)^2} \tilde{C}_{av}(\omega) \ , \tag{3.50}$$

where the spectral function $\tilde{C}_{av}(\omega)$ is obtained as the Fourier transform of the time-averaged correlation function

$$C_{av}(\tau) = \lim_{\mathcal{T}\to\infty} \frac{1}{\mathcal{T}} \int_0^{\mathcal{T}} dt_w C(t_w, t_w+\tau) \ . \tag{3.51}$$

Equation (3.50) is proven in Appendix C.3. The cutoff $\mu$ suppresses the contribution to the integral from frequencies $|\omega| \lesssim \mu$ and plays a role equivalent to the one played by $\omega_L$ in genuinely quantum systems. We determine the asymptotic profile of $\chi_\mu$ by analyzing its behaviour as $\mu \to 0$. We observe that an obstruction to this procedure is that in our simulations we do not have access to infinite-time average, so that the integral in Eq. (3.51) is performed over a finite time-window $[0, \mathcal{T}]$. While in the ergodic phase this is a good approximation of the long-time average, due to time-translation invariance, in the non-ergodic one $\chi$ always depends on choice of the time-window and converges to the definition in Eq. (3.49) only in the limit $\mathcal{T} \to \infty$. However, as shown in Appendix C.3, the qualitative profile we retrieve for $\chi_\mu$ is the same for a wide range of $\mathcal{T}$ between 0 and the maximum integration time $t_{max}$, so that here we can focus on

the specific case of $\mathcal{T} = t_{max}/2$.

We plot $\chi_\mu$, as a function of $E$ and for several values of $\mu$, in Fig. 3.5-(a): its profile has a peak close to the estimated "ergodicity breaking" energy scale $E \simeq -0.38$ and the maximum point has a little drifting to the left approaching small values of $\mu$. We also observe that a natural low-frequency cutoff $\Delta\omega \sim 2\pi/t_{max}$ emerges when discretizing the integral in Eq. (3.50) in our finite-time simulations, so that the asymptotic behaviour of $\chi_\mu$ can be studied only up to $\mu \gtrsim \Delta\omega$. Thus, to refine our analysis, we compute $\chi_\mu$ for a dynamics integrated for a larger $t_{max}$ so that $\Delta\omega < 3\mu$ for all the values of $\mu$ we investigate: the new results, shown in Fig. 3.5-(b), are qualitatively the same of the one shown in Fig. 3.5-(a), further validating our analysis. To complete the comparison between our classical analysis and the one performed in Ref. [112], we also analyze the scaling behavior of $\chi_\mu$ against $\mu$ and find that the fidelity susceptibility scales as $\chi_\mu \sim \mu^{-\alpha}$ in the range of values of $\mu$ explored, as shown in Fig. 3.5-(c). We compute the corresponding exponent $\alpha$ as a function of the energy density $E$ and plot it in Fig. 3.5-(d): in the ergodic phase, we find that $\alpha$ is slightly greater than 1 (see inset in Fig. 3.5-(d)), resulting in a scaling approximately consistent with random matrix theory[2], while $\alpha$ exhibits a maximum of $\alpha \simeq 1.8$ at $E \simeq -0.4$, close to the point where the thermalization time exceeds the simulation time window. Further insight is gained when investigating the profiles of the rescaled fidelities $\mu\chi_\mu$ against $E$, as done in the inset Fig. 3.5-(d): at high energy densities, the profiles collapse in a region which expands toward lower energies as we decrease $\mu$. This collapse will in general break down at low energies, in particular where the maximum of $\chi_\mu$ is expected to occur. It is also worth mentioning that, from a deeper inspection collapse of the various profiles, we could in principle extract the Thouless time [150], defined as the typical relaxation time-scale $\tau_{th}(E)$ of the correlation function at fixed energy density $E$, using the following prescription. First we define the cut-off $\mu_E$ as the largest number such that the profiles of $\chi_\mu$ collapse for all energy densities greater than $E$ and for all $\mu < \mu_E$; then the Thouless time can be easily obtained as $\tau_{th}(E) \sim \mu_E^{-1}$ [127]. We expect that $\tau_{th}(E)$ diverges as we the dynamics approaches the ergodicity breaking point from above.

As the cutoff $\mu$ plays the same role of the lowest level spacing for our analysis, these findings are consistent with those in Refs. [112, 127], which show that the fidelity exhibits the strongest divergence with $\mu$ when the corresponding spin relaxation dynamics slows down. We therefore conclude that the fidelity susceptibility could be a good indicator of ergodicity even in classical systems, which warrants further investigation.

## 3.6 Summary and perspectives

In this chapter we probed chaos in a $p$-spin glass spherical model. Within a classical framework, we found that classical chaos was maximised at energy density $E = 0$, as

[2] As our analysis is limited by the finite simulation times, we do not exclude that an even better agreement with random matrix predictions may be reached considering a larger $t_{max}$ and consequently a larger set of values for $t_w$

shown by two estimators: the maximal Lyapunov exponent $\lambda_L$ and the the Kolmogorov-Sinai entropy density $\Lambda_{KS}$. We observed that the fastest spin relaxation coincided with maximal chaos. We gave a physical interpretation of all our results in terms of the typical behaviour of the underlying trajectories, which either perform a uniform circular motion at asymptotically high energies or oscillate, at low energies, around a local minimum of the energy landscape. In between these two limits, we suggest that chaos emerges as the trajectories are scattered over the exponentially many saddles of the underlying landscape. Indeed a calculation of the number of stationary configurations shows that the complexity is also maximal at the same energy.

We also investigated the relaxation dynamics of the correlation function at low energies, uncovering a peculiar connection with the regularized fidelity susceptibility, $\chi$. Intriguingly, we observed that a slowdown in dynamics coincided precisely with the fastest divergence of $\chi$. This finding suggests a possible parallelism between the fragility of quantum eigenstates near a non-ergodic point, leading to a rapid scaling of $\chi$, and the fragility inherent in the topology of classical trajectories during the onset of slow dynamics in classical systems.

The results presented here hold true in the $\hbar \to 0$ limit, where the TWA faithfully reproduces the dynamics for the initial condition defined in Eq. (3.29). Our findings can be potentially extended beyond the realm of small $\hbar$, by utilizing a Wigner state that reproduces the same fluctuations of a realistic quantum micro-canonical or canonical state. In this context, the quantum Lyapunov exponent $\lambda_L$ can be computed even at finite $\hbar$, derived from the exponential growth of a classical analog of the OTOC [92, 97]. A similar rationale applies to the correlation function and subsequently to the fidelity susceptibility, where the latter can be computed using Eq. (3.50) for both classical and quantum dynamics. Our analysis can also be extended to the transverse-field counterpart of the $p$-spin glass model, where chaos has been recently observed experimentally [96] and where the energy minima exhibit a more complicate structure [151].

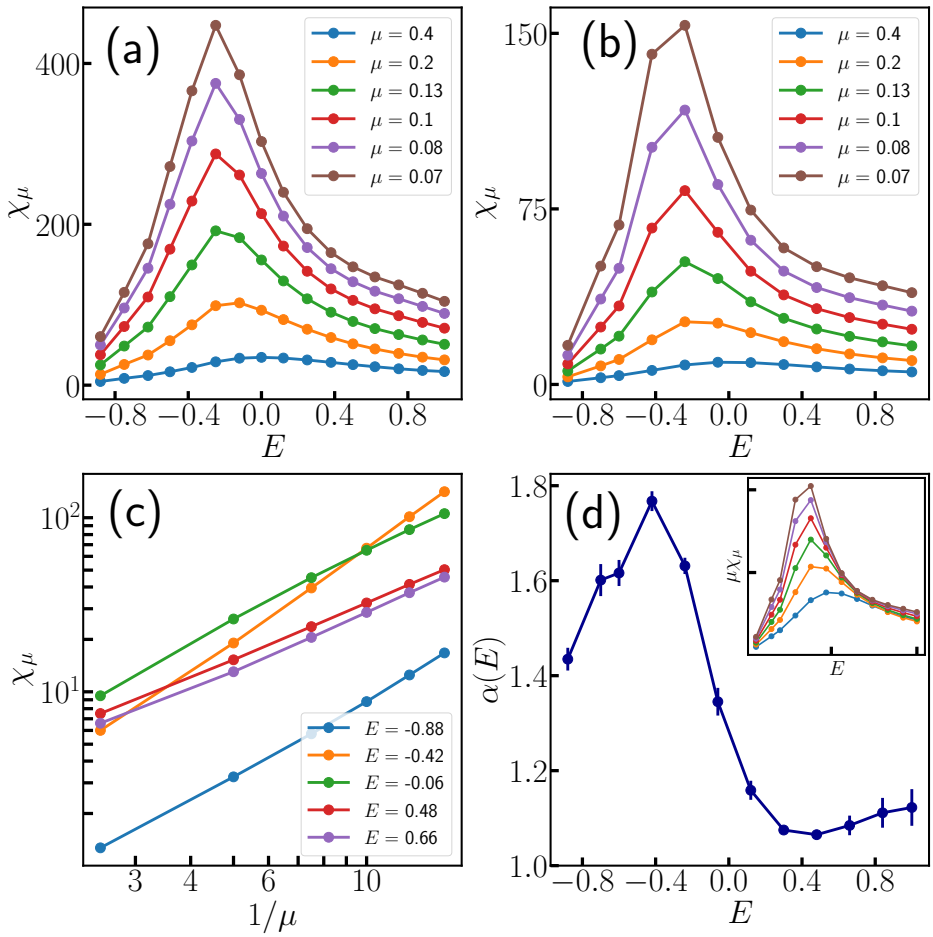


Figure 3.5: Fidelity susceptibility $\chi_\mu$ from Eq. (3.50). **(a)** $\chi_\mu$ is shown as a function of $E$ and fixing several values of the cut-off $\mu$. The data are obtained from a dynamics up to time $t_{max} = 80$, with the same parameters described in Fig. 3.3. The average time window for the correlation function in Eq. (3.51) is set to $[0, \mathcal{T}]$, with $\mathcal{T} = t_{max} = 40$. **(b)** Same plot of panel (a), for a dynamics integrated up to time $t_{max} = 320$. Here the average over the initial condition is performed over 5 random configurations extracted from each the $\mathcal{N}_s = 10$ wave-packets constructed by the classical annealing algorithm. We average over $\mathcal{N}_d = 42$ disorder configurations. **(c)** Same data of panel (b). $\chi_\mu$ is shown as a function of the cutoff $\mu$, on a log-log scale, for some fixed values of the energy density $E$. **(d)** Exponent $\alpha(E)$ obtained by a linear fit of $\log \chi_\mu$ against $-\log \mu$, at several fixed values of the energy density $E$. For each $E$, the data used for the fit are the ones from panel (b).

# Part II

# Periodically-driven dynamics of ergodic and long-range systems

# Chapter 4

# Heating to finite temperature in periodically driven ergodic systems

In Part I of this thesis, we explored the dynamics of *conservative* many-body systems, where energy remains constant over time. In contrast, this Part II focuses on situations where an external periodic drive induces energy oscillations or heats the system.

Periodically-driven systems, also known as *Floquet* systems, have revealed a plethora of non-trivial phenomena since their initial exploration. For instance, as discussed in Section 1.1, the simple Chirikov standard map from Eqs. (1.4) demonstrates how a periodic force can trigger a transition from integrable to chaotic dynamics. In the chaotic regime, the particle diffuses across the entire phase space. Interestingly, subsequent studies revealed that quantum fluctuations counter-intuitively suppress diffusion in the Chirikov map [152]. Another seminal contribution to this field came from P. Kapitza, who discovered that an inverted pendulum can be stabilized by an external force oscillating at a sufficiently high frequency [153].

While single-particle system have been the focus of research in the past decades, recently attention has shifted towards many-particle ones, which have proven to be valuable tools for reproducing a wide array of novel phases of matter experimentally [154–158]. This line of research usually is commonly referred to as *Floquet engineering* [159] and it encompasses various applications, including prominent ones like Floquet time Crystals [160], which we will explore in Chapter 5.

A major obstacle to the practical realization of Floquet systems has however been the fact that isolated many-body systems under a periodic drive tend to quickly heat up to a featureless infinite-temperature state due to the absence of conservation laws [25, 26, 161], as already discussed in Section 1.3. Heating to infinite-temperature can be either avoided by many-body localization [160, 162, 163] and integrability [164–167], or for generic short-range interacting systems subject to a high frequency drive in the prethermal stage of the dynamics. Prethermalization has been observed both in classical [31, 33, 34] and quantum Floquet systems [28, 168–172].

To date, heating due to driving has been predominantly explored in systems dis-

playing a bounded energy spectrum or phase space. For continuous degrees of freedom, relaxation to an infinite-temperature state has been conjectured to be a generic outcome as the driving frequency $\Omega$ tends to infinity, where the system is expected to first relax to a prethermal thermal state, whose temperature will afterwards slowly grow indefinitely [173]. Other studies of this phenomenon have been limited to systems either driven by kicks [29–31], where a non-linear impulsive force leads to a never-ending energy absorption even at finite $\Omega$, or systems coupled to an external noise [174].

In this chapter we address another aspect of this problem i.e. what happens when a system with an unbounded energy spectrum is subjected to a smooth periodic force. Our investigation covers a range of three models: a single-particle system, the Duffing oscillator, the $p$-spin spherical model (PSM), already introduced in Section 3.2 and a lattice $\phi^4$ model. The last two are many-body models, whose dynamics is ergodic at sufficiently high energies. For the Duffing oscillator, we observe that at moderate amplitudes of the driving field, the system exhibits behavior indicative of an emergent conservation law, in contrast to the unbounded diffusion observed in the kicked rotor system discussed in Section 1.1. Moving to the many-body systems, our numerical simulations reveal that both the PSM and the $\phi^4$ model reach a *finite-temperature* state within the simulated time scales. The finite temperature state is again determined by an emergent conservation law. We are able to compute the associated conserved quantity in specific, but not necessarily high frequencies, limit for both the Duffing oscillator and the $\phi^4$ model. The dynamics of the PSM exhibit a similar behavior, alongside the emergence of an approximate fluctuation-dissipation relation.

This chapter is organized as follows. In Section 4.1 we introduce the periodically driven Duffing oscillator and the multiple-scale analysis we will use to compute the conserved quantity in the classical limit. In Section 4.2 we extend our analysis to the lattice $\phi^4$ model. In Section 4.3 we discuss the periodically driven dynamics of the PSM in the thermodynamic limit and its possible thermalization from the two-point correlators. Finally, we summarize our results and perspectives in Section 4.4.

## 4.1 A multiple scale approach to the classical driven Duffing oscillator

In this section we discuss the dynamics of the simplest non-linear system, that is the single-particle quartic oscillator. When coupled to an external oscillating field, the dynamics is given by the Duffing equation [175]:

$$\ddot{x} + \omega_0^2 x + \lambda x^3 = B_0 \sin(\Omega t) \ . \tag{4.1}$$

In the following, we will denote by $E(t)$ the energy of the system,

$$E(t) = \frac{1}{2}\dot{x}(t)^2 + \frac{\omega_0^2}{2}x(t)^2 + \frac{\lambda}{4}x(t)^4 \ . \tag{4.2}$$

When the non-linearity is absent, $\lambda = 0$, Eq. (4.1) describes a simple harmonic oscillator and two scenarios are possible: if $\Omega \neq \omega_0$, the system oscillates at the driving

frequency $\Omega$; on the other hand, when $\Omega = \omega_0$, a *resonance* occurs and $E(t)$ grows unbounded [176]. However, as illustrated in Fig. 4.1-(a), even a small $\lambda > 0$ is sufficient to prevent indefinite absorption of energy in the case where $\Omega = \omega_0$: in this scenario, $E(t)$ exhibits bounded fluctuations, occurring on a timescale generally slower than the driving period, around a fixed time-averaged value $\overline{E}$, dependent on both the model parameters and the initial condition $x(0), \dot{x}(0)$. This phenomenon is qualitatively independent of the choice of the other parameters, as long as $\lambda > 0$, and of the initial condition (see Fig. 4.1-(b)). Additionally, we observe that trajectories corresponding to such finite energy oscillations are regular. This regularity is demonstrated in Fig. 4.1-(d), where we plot the Poincaré sections of the dynamics in phase space, at stroboscopic times $t_n = 2\pi n/\Omega$ for positive integer $n$, which exhibit the shape of a closed orbit.

From a physical perspective, the outcomes we obtain for a positive $\lambda$ contradict thermalization to infinite temperature, which necessitates the system to explore the entire phase space and undergo unbounded growth of $E(t)$. To gain analytical insight into our results, we study Eq. (4.1) in the limit of small non-linearity by rescaling $\lambda = \epsilon\tilde{\lambda}$, $B_0 = \epsilon\tilde{B}_0$, for some $\epsilon \ll 1$. We also assume that

$$\omega_0^2 = \Omega^2 - \epsilon\Delta\omega^2 \ , \tag{4.3}$$

so that the underlying harmonic motion is either in resonance or close to a resonance with the periodic driving. As the parameters we chose are close to the ones of a resonant harmonic oscillator, Eq. (4.1) can not be studied by standard perturbation methods, due to the proliferation of secular terms at each perturbative order [4]. These secularities do not manifest in the numerical simulations, which predict a bounded solution. We circumvent this issue by employing a multiple-scale analysis (MSA), which we briefly review in the following (see Ref. [177] for a pedagogical introduction).

The starting point of the multiple-scale analysis consists in introducing a redundant time variable $\tau = \epsilon t$. $\tau$ defines a long time scale, since it becomes significant only when $t$ is of order $\epsilon^{-1}$ or larger. Although we expect that the actual solution $x(t)$ to Eq. (4.1) is a function of $t$ alone, MSA seeks solutions which are functions of both variables $t$ and $\tau$, treated as independent from each other. Such expression of $x(t)$ as a function of two variables is an artifice to remove secular effects; the actual solution has $t$ and $\tau$ related by $\tau = \epsilon t$. The formal procedure consists of assuming a perturbative expansion in powers of $\epsilon$:

$$x(t) = x_0(t,\tau) + \epsilon\ x_1(t,\tau) + \dots \ , \tag{4.4}$$

for small $\epsilon$. We use the chain rule $d/dt = \partial_t + \epsilon\partial_\tau$ for partial differentiation to compute the derivatives of $x(t)$, obtaining

$$\frac{dx}{dt} = \frac{\partial x_0}{\partial t} + \epsilon\Big(\frac{\partial x_1}{\partial t} + \frac{\partial x_0}{\partial \tau}\Big) + O(\epsilon^2) \tag{4.5}$$

and

$$\frac{d^2x}{dt^2} = \frac{\partial^2 x_0}{\partial t^2} + \epsilon\Big(\frac{\partial^2 x_1}{\partial t^2} + 2\ \frac{\partial^2 x_0}{\partial t\ \partial \tau}\Big) + O(\epsilon^2) \ . \tag{4.6}$$

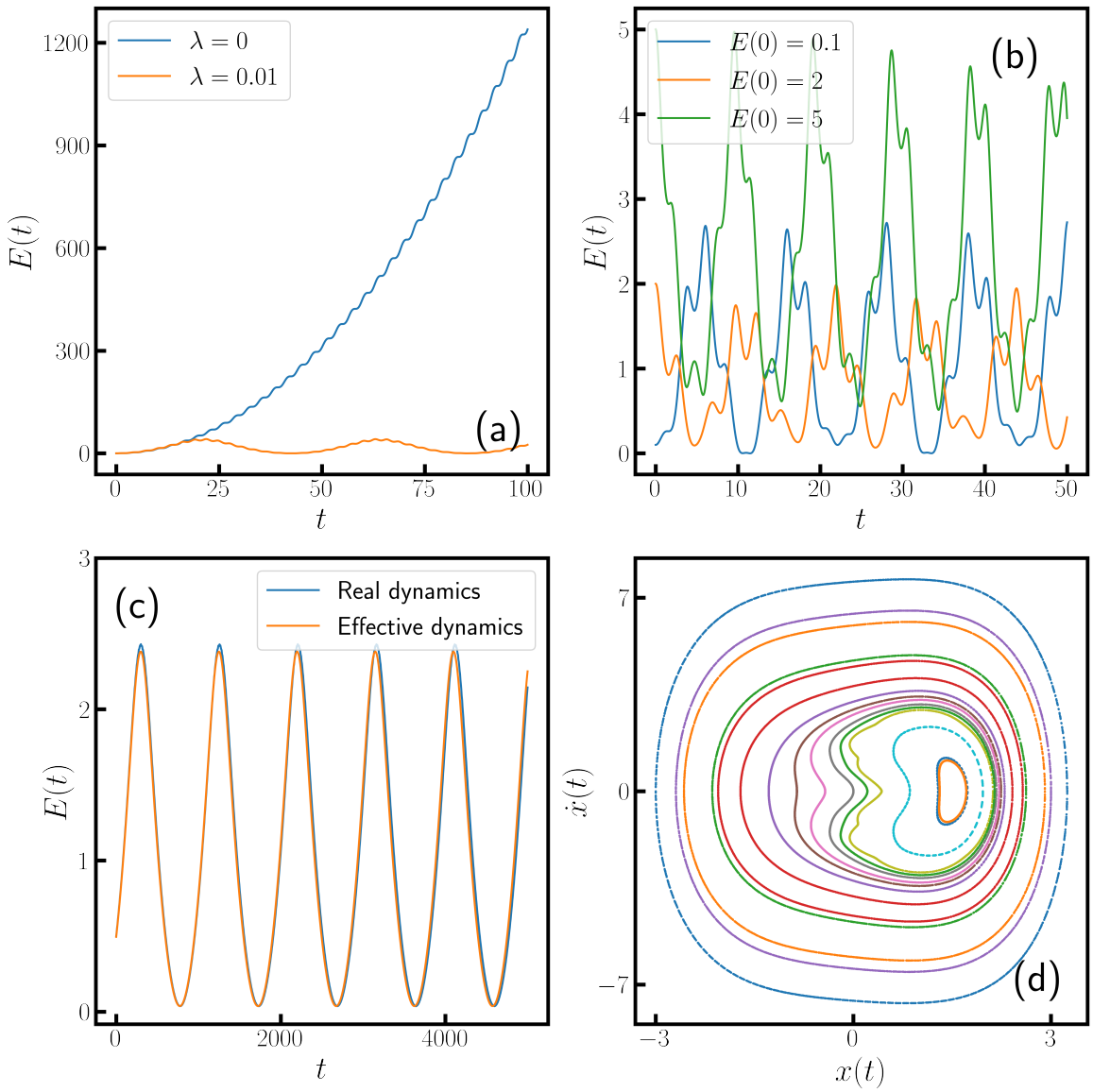


Figure 4.1: Dynamics of the Duffing oscillator, defined in Eq. (4.1). **(a-c)** Plots of the energy $E(t)$ from Eq. (4.2), for different initial conditions and integration parameters. **(a)** We chose a generic initial condition such that $E(0) = 1$, and fixed the parameters $\omega_0 = \Omega = B_0 = 1$. **(b)** The initial conditions are chosen in order to fix $E(0)$ to the values reported in the legend, other parameters are fixed to $\omega_0 = \omega = B_0 = \lambda = 1$. **(c)** Comparison of the plot between the real dynamics of $E(t)$, obtained from Eqs. (4.2) and (4.1), and the effective one obtained from Eqs. (4.13) and (4.15), for $\epsilon = 0.1$. Other parameters are fixed to $\Omega = \Delta\omega^2 = \tilde{B}_0 = \tilde{\lambda} = 1$. **(d)** Poincaré section of the dynamics in phase-space, for several initial conditions and at stroboscopic times $t_n = 2\pi\Omega^{-1}$, for $n = 1 \dots 5000$. We fix $\Omega = \sqrt{2}$ and $\omega_0 = B_0 = \lambda = 1$.

Substituting Eq. (4.6) in Eq. (4.1) and collecting powers of $\epsilon$, we obtain

$$\frac{\partial^2 x_0}{\partial t^2} + \Omega^2 x_0 = 0 \ , \tag{4.7}$$

$$\frac{\partial^2 x_1}{\partial t^2} + \Omega^2 x_1 = -2\frac{\partial^2 x_0}{\partial t\ \partial \tau} + \Delta\omega^2 x_0 - \tilde{\lambda} x_0^3 + \tilde{B}_0 \sin(\Omega t) \ . \tag{4.8}$$

The general solution of Eq. (4.7) is

$$x_0(t,\tau) = A(\tau)e^{i\Omega t} + A^*(\tau)e^{-i\Omega t} \ . \tag{4.9}$$

The slowly varying amplitude $A(\tau)$ and its complex conjugate $A^*(\tau)$ are determined by imposing that secular terms, proportional either to $e^{i\Omega t}$ or $e^{-i\Omega t}$, do not appear in the next order, that is on the right-hand-side of Eq. (4.8), as these would predict a divergence which we do not observe numerically. After some algebra, one can show that the contribution of such terms to the right-hand-side of Eq. (4.8) is given by the expression

$$2\ \mathrm{Re}\Big[e^{i\Omega t}\big(-2i\Omega\frac{dA}{d\tau} + \Delta\omega^2 A - 3\tilde{\lambda}A^2A^* - \frac{i}{2}\tilde{B}_0\big)\Big] \ .$$

The vanishing of secular terms thus leads to the following equation of motion for $A(\tau)$:

$$\frac{dA}{d\tau} = \frac{1}{2i\Omega}\left[\Delta\omega^2 A - 3\tilde{\lambda}A^2A^* - \frac{i}{2}\tilde{B}_0\right] \ . \tag{4.10}$$

We can rewrite Eq. (4.10) in terms of the coordinates $u(\tau) = A(\tau) + A^*(\tau)$ and $v(\tau) = [A(\tau) - A^*(\tau)]/i$, to obtain:

$$\begin{cases} \dfrac{du}{d\tau} = \dfrac{1}{2\Omega}\left[\Delta\omega^2\ v - \dfrac{3}{4}\tilde{\lambda}(u^2+v^2)v - \tilde{B}_0\right] \\ \dfrac{dv}{d\tau} = \dfrac{1}{2\Omega}\left[-\Delta\omega^2\ u + \dfrac{3}{4}\tilde{\lambda}(u^2+v^2)u\right] \ . \end{cases} \tag{4.11}$$

In terms of $u(\tau)$ and $v(\tau)$, the solution to Eq. (4.1) reads, at the leading perturbative order

$$x(t) \sim u(\tau)\cos(\Omega t) + v(\tau)\sin(\Omega t) + O(\epsilon) \ . \tag{4.12}$$

The system of Eqs. (4.11) is Hamiltonian, as it can be rewritten as

$$\begin{cases} \dfrac{du}{d\tau} = -\dfrac{\partial H_F}{\partial v} \\ \dfrac{dv}{d\tau} = \dfrac{\partial H_F}{\partial u} \ , \end{cases} \tag{4.13}$$

with an *effective Hamiltonian* given by

$$H_F(u,v) = \frac{1}{2\Omega}\Big[-\frac{\Delta\omega^2}{2}(u^2+v^2) + \frac{3}{16}\tilde{\lambda}(u^2+v^2)^2 + \tilde{B}_0 v\Big] \ . \tag{4.14}$$

We observe that Eqs. (4.14) were also derived in Ref. [178], by using a method equivalent to the one we employ here. However, unlike MSA used in our approach, the

method presented in Ref. [178] does not permit a systematic refinement of the asymptotic analysis through the inclusion of higher-order perturbative terms.

The multiple scale analysis allows also for a quantitative pertubative prediction of $E(t)$. Specifically, by plugging Eq. (4.9) into Eq. (4.2), we obtain

$$E(t) \sim \frac{\Omega}{2}\left(u(\tau)^2 + v(\tau)^2\right) + O(\epsilon) \ , \tag{4.15}$$

evaluated at $\tau = \epsilon t$. In Eq. (4.15) we omitted the order $\epsilon$ terms in $g$ and $\lambda$. In Fig. 4.1-(c), we compare the estimate of $E(t)$ from Eq. (4.15), calculated using Eq. (4.15), with the original computation obtained from Eq. (4.1) for small $\epsilon$. We observe excellent agreement between the two quantities for the small value of $\epsilon = 0.01$. We do not exclude that our prediction may be quantitatively accurate also for larger values of $\epsilon$, once we include also higher-order perturbative terms. Within the MSA, the existence of a finite time-averaged value of $E(t)$ can be deduced from the conservation of $H_F(u, v)$: the system can not explore the whole phase space, but only configurations within a microcanonical manifold of $H_F(u, v) = E_F$, $E_F$ being fixed by the choice of the initial condition. As a consequence of the conservation law, $E(t)$ can not grow indefinitely and oscillates around a microcanonical value predicted within the emergent microcanonical ensemble. The agreement between the original dynamics and the perturbative analysis hints the possible existence of an emergent conservation law even in the driven Duffing equation, which instead is absent in the kicked rotor discussed in Section 1.1.

We conclude by stressing that the multiple-scale analysis is a more general approach than the Floquet-Magnus expansion often employed for periodically driven systems in their high-frequency limit [168]. For Duffing oscillator, the high-frequency limit would correspond to $\Omega \sim O(1)$ and $\omega_0^2 \sim \epsilon$, rather than the scaling $\Omega^2 \sim \omega_0^2 + O(\epsilon)$ considered here. For single-particle Floquet systems, the validity of the MSA in the high-frequency limit was tested in Ref. [179].

## 4.2 The lattice $\phi^4$ model

The muliple-scale analysis discussed in the previous section can be generalized to a classical many-body system composed of interacting, non-linear oscillators. In particular, in this section we investigate the dynamics of a driven $\phi^4$ model on the lattice, generated by the Hamiltonian

$$H(\mathbf{x}, \mathbf{p}) = H_{\phi^4}(\mathbf{x}, \mathbf{p}) - B_0 \sin(\Omega t) \sum_i x_i \tag{4.16}$$

where $\mathbf{x} = (x_1, \ldots, x_n)$, $\mathbf{p} = (p_1, \ldots, p_n)$ and

$$H_{\phi^4}(\mathbf{x}, \mathbf{p}) = \sum_i \left[ \frac{p_i^2}{2} + \frac{\omega_0^2}{2} x_i^2 + \frac{\lambda}{4} x_i^4 + \frac{g}{2}(x_{i+1} - x_i)^2 \right] \ . \tag{4.17}$$

When $\lambda = 0$, the Hamiltonian (4.17) describes a set of independent Harmonic oscillators in momentum space, whose characteristic frequencies are given by

$$\omega_k = \sqrt{\omega_0^2 + 2g[1 - \cos(2\pi k/N)]} \tag{4.18}$$

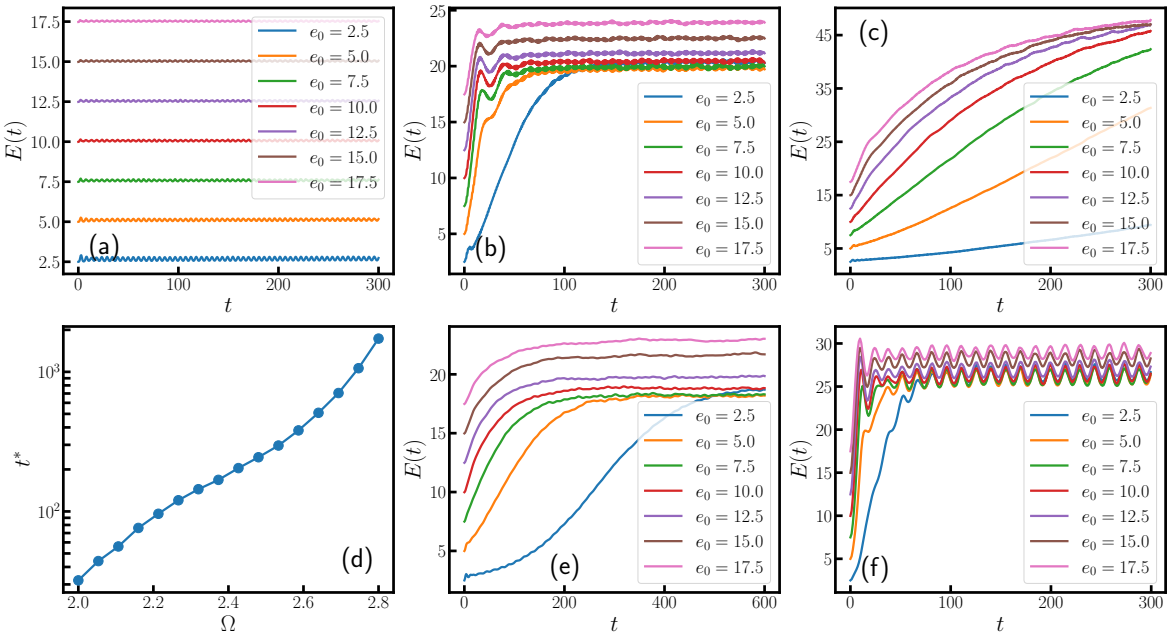


Figure 4.2: Results for the periodically driven dynamics of the lattice $\phi^4$ model, defined in Eq. (4.19). In all the panels, the dynamics is averaged over 300 initial conditions, randomly on a manifold $H_{\phi^4}(\mathbf{x}_0, \dot{\mathbf{x}}_0) = E_0$. We fix $N = 100$, $B_0 = g = \lambda = \omega_0^2 = 1$. **(a-c)** Plot of the average density $E(t) = \langle H_{\phi^4}(\mathbf{x}, \mathbf{p})\rangle$, for the dynamics generated by Eqs. (4.19), for $\Omega = 0.6, 2.4, 3.0$ (respectively from left to right). **(d)** Estimate of the prethermal time $t^*$ defined in the main text, for a threshold fixed to $E_1 = 8$ and initial energy $E_0 = 0.5$. **(e-f)** Time-evolution of $E(t)$ generated by the dynamics of the lattice $\phi^4$ model, driven by different non-linear pertubations, as expressed in Eqs. (4.20) and (4.21) (respectively from left to right). We fix $\Omega = 2.4$ and $\alpha = 1$ for both plots.

for $k = 1 \dots N$. The Hamilton dynamics evolving from a generic configuration at fixed energy displays ergodicity [180, 181] and chaos [182, 183]. A possible exception to the chaotic behaviour has been observed only for fine-tuned initial conditions at low-energies (see Ref. [182] for a discussion). Several experimental realization have been proposed for the quantum version of this model [184–186]. Given these characteristics, it is an intriguing subject to explore its behavior when subjected to periodic driving.

Specifically, we aim to investigate its driven dynamics given by the equations of motion

$$\ddot{x}_i + \omega_0^2 x_i + \lambda x_i^3 = B_0 \sin(\Omega t) + g\,(x_{i+1} - 2x_i + x_{i-1})\,, \tag{4.19}$$

for $i = 1 \dots N$. We use an ensemble of $\mathcal{N}$ initial configurations $(\mathbf{x}_0, \dot{\mathbf{x}}_0)$ randomly sampled on the manifold $H_{\phi^4}(\mathbf{x}_0, \dot{\mathbf{x}}_0) = NE_0$, for different values of $E_0$ and different choices of the driving frequency $\Omega$. In Fig. 4.2-(a-c), we plot the evolution of the average energy density $E(t) = \langle H_{\phi^4}(\mathbf{x}(t), \dot{\mathbf{x}}(t)\rangle_0 / N$. For all the values of $\Omega$ and $E_0$ and within the maximum time-scale reached in the integration, we find no signature of infinite-temperature heating, as $E(t)$ always tends to a finite value $E_\infty$. Specifically, we observe that no energy is absorbed at low driving frequencies $\Omega$, possibly due to the gap in the absorption spectrum. For intermediate values of $\Omega$, $E_\infty$ remains independent of the

initial energy state $E_0$ as long as the condition $E_0 \lesssim E_\infty$ holds. For large $\Omega$, the growth of $E(t)$ slows down. We quantitatively estimate the slowdown from the time-scale $t^*$ at which $E(t)$ crosses a threshold $E_1 \in [0, E_\infty]$, as a function of $\Omega$. In Fig. 4.2-(d) we show that $t^* \sim \exp(c\Omega)$ for sufficiently large $\Omega$. This dependence is reminiscent of the ones observed for the prethermalization time in classical and quantum spin chains [33, 172]. Our investigation also reveals that the relaxation of $E(t)$ to the finite value $E_\infty$ is not contingent on the specific form of the chosen driving mechanism. To prove it, we repeat the same analysis for different driven equations of motion, respectively given by:

$$\ddot{x}_i + \omega_0^2 x_i + \lambda x_i^3 + \alpha \sin(\Omega t) \cos(x_i/l_0) = g(x_{i+1} - 2x_i + x_{i-1}) \ , \tag{4.20}$$

$$\ddot{x}_i + \omega_0^2 x_i + \alpha \sin(\Omega t) x_i^2 + \lambda x_i^3 = g(x_{i+1} - 2x_i + x_{i-1}) \ . \tag{4.21}$$

and we set the dimensional scale $l_0$ to 1. The result, shown in Fig. 4.2-(e) and (f), is that the average energy density $E(t)$ again displays relaxation to a finite asymptotic value.

In a many-body system such as the one described by the $\phi^4$ model, the relaxation of the total energy density $E(t)$ to a finite value is consistent with the emergence of a conservation law, for an observable distinct from $H_{\phi^4}(\mathbf{x}, \dot{\mathbf{x}})$. As we did for the Duffing oscillator in Section 4.1, here we attempt to compute the corresponding conserved quantity in the limit of small driving and small interaction, rescaling $g = \epsilon \tilde{g}$, $\lambda = \epsilon \tilde{\lambda}$ and $B_0 = \epsilon \tilde{B}_0$ and develop a multiple scale analysis for $\epsilon \ll 1$. In particular, we fix $\omega_0^2 = \Omega^2 - \epsilon \Delta\omega^2$, to enable absorption through parametric resonances [187] even when Eqs. (4.19) are close to the ones of non-interacting harmonic oscillators at frequency $\omega_0$. We define once again the slow time-scale $\tau = \epsilon t$ and assume the validity of the expansion

$$x_i(t) = x_{0,i}(t, \tau) + \epsilon \ x_{0,i}(t, \tau) + \dots \ , \tag{4.22}$$

on every site $i = 1 \dots N$. Following the same recipe illustrated in Section 4.1, we obtain that, at the leading order, the solution to the equations of motion has the form

$$x_i(t) = u_i(\tau) \cos(\Omega t) + v_i(\tau) \sin(\Omega t) \ . \tag{4.23}$$

The slowly varying amplitudes $u_i(\tau)$ and $v_i(\tau)$ obey the Hamilton equations

$$\begin{cases} \dfrac{du_i}{d\tau} = -\dfrac{\partial H_F}{\partial v_i} \\ \dfrac{dv_i}{d\tau} = \dfrac{\partial H_F}{\partial u_i} \ , \end{cases} \tag{4.24}$$

generated by the many-body effective Hamiltonian

$$H_F(\mathbf{u}, \mathbf{v}) = \frac{1}{2\Omega} \sum_i \Big\{ -\frac{\Delta\omega^2}{2}(u_i^2 + v_i^2) + \frac{\tilde{g}}{2}\left[(u_{i+1} - u_i)^2 + (v_{i+1} - v_i)^2\right] + \tag{4.25}$$

$$+ \frac{3\tilde{\lambda}}{16}(u_i^2 + v_i^2)^2 + \tilde{B}_0 v_i \Big\} \ .$$

Within this perturbative analysis, we can also estimate $E(t)$. In particular, by plugging Eq. (4.23) into $H_{\phi^4}(\mathbf{x}(t), \dot{\mathbf{x}}(t))$, we obtain at the leading order

$$\begin{aligned} E(t) &\sim \frac{1}{N} \left\langle H_{\phi^4}[\mathbf{x}_0(t,\tau), \partial_t \mathbf{x}_0(t,\tau)] \right\rangle_0 \Big|_{\tau=\epsilon t} \\ &= \frac{1}{N} \left\langle \mathcal{H}_0[\mathbf{u}(\tau), \mathbf{v}(\tau)] \right\rangle_0 \Big|_{\tau=\epsilon t} + O(\epsilon) \ . \end{aligned} \tag{4.26}$$

where $\mathcal{H}_0(\mathbf{u}, \mathbf{v}) = \Omega^2 \sum_i (u_i^2 + v_i^2)/2$, in analogy with Eq. (4.15). Here the brackets $\langle \cdot \rangle_0$ indicates again that the average is performed over the micro-canonical manifold $H_0(\mathbf{x}_0, \dot{\mathbf{x}}_0) = NE_0$. We test the approximation for a fixed $\Omega$, as depicted in Fig. 4.3-(a): the MSA quantitatively reproduces the original dynamics and its saturation to a finite plateau at $E_\infty$. In particular, we compute the time-average

$$\Delta E = \lim_{\mathcal{T}\to\infty} \frac{1}{N\mathcal{T}} \int_0^{\mathcal{T}} dt |E^{(real)}(t) - E^{(eff)}(t)|^2 \ , \tag{4.27}$$

where $E^{(real)}(t)$ is the energy density computed from the original dynamics, from Eq. (4.19), while $E^{(eff)}(t)$ is estimated from Eq. (4.26). We plot $\Delta E$ in Fig. 4.3-(b), showing that it is a monotonically increasing function of $\epsilon$. Thus, the accuracy of the MSA improves for smaller values of $\epsilon$. The accuracy of the perturbative predictions may further improve by including contributions which are higher order in $\epsilon$.

The primary advantage of using the MSA in this many-body context is that we can explain the existence of a finite plateau at $E_\infty$ using a thermodynamic argument. In particular, we observe that a finite $E_\infty$ is naturally expected from the conserved-energy dynami cs in Eqs. (4.24) and $E(t)$ from Eq. (4.26) is expected to saturate to the average

$$E_\infty(E_F) = \langle \mathcal{H}_0(\mathbf{u}, \mathbf{v}) \rangle_{eff} / N \ , \tag{4.28}$$

over an *effective* microcanonical ensemble defined by $\mathcal{H}_F(\mathbf{u}, \mathbf{v}) = NE_F$. The corresponding conserved effective energy density $E_F$ is determined by the initial conditions,

$$E_F(E_0) = \langle \mathcal{H}_F(\mathbf{u}, \mathbf{v}) \rangle_0 / N \ . \tag{4.29}$$

Combining Eqs. (4.28) and (4.29), we obtain $E_\infty$ as a function of $E_0$ from the perturbative MSA. We test such relation against its dynamical counterpart, obtained by estimating $E_\infty$ from the long-time average

$$E_\infty(E_0) = \lim_{\mathcal{T}\to\infty} \frac{1}{N\mathcal{T}} \int_0^{\mathcal{T}} dt \left\langle H_{\phi^4}[\mathbf{x}(t), \dot{\mathbf{x}}(t)] \right\rangle_0 \tag{4.30}$$

of the *original* dynamics, in Eq. (4.19), evolving from an initial ensemble on the manifold $H_{\phi^4}(\mathbf{x}, \dot{\mathbf{x}}) = NE_0$. We plot the result in Fig. 4.3-(c), showing the two estimates of $E_\infty$ merge into each other as $\epsilon$ is sent to 0.

## 4.3 Periodically driven dynamics in a large-$N$ system: the $p$-spin spherical model

In this section, we attempt to extend our findings to the quantum regime, by investigating the periodically driven dynamics of the $p$-spin spherical model (PSM), already

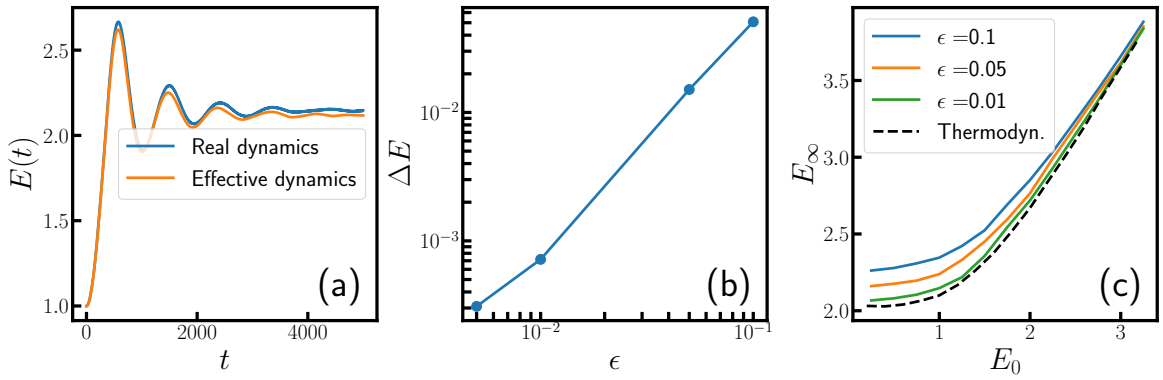


Figure 4.3: Multiple-scale analysis for the lattice $\phi^4$ model. We fix $N = 100$ and $\Omega = \tilde{\lambda} = \tilde{B}_0 = \tilde{g} = 1$. In all panels, the dynamics is always averaged over 1000 initial conditions. **(a)** Comparison between two profiles of $E(t)$, obtained either from the real dynamics in Eqs. (4.19) or from the effective one in Eqs. (4.24). We fix $\epsilon = 0.05$. The initial conditions are sampled from the microcanonical manifold $H_{\phi^4}(\mathbf{x}_0, \dot{\mathbf{x}}_0)/N = E_0 = 1$. **(b)** Behaviour of the time-averaged difference $\Delta E$, between the real and the effective dynamics, defined in Eq. (4.27). The time average is performed in an interval $[3/4t_{max}, t_{max}]$, where $t_{max}$ is the total simulation time we used. Within this interval, $E(t)$ has already reached its late time plateau. The initial conditions are sampled as in panel (a). **(c)** Estimates of the asymptotic energy density $E_\infty$ as a function of the initial one, $E_0$. For each solid line, $E_\infty$ is computed from the late-time average, in Eq. (4.30), of the original dynamics in Eqs. (4.19). To eliminate the contribution from the transient dynamics, we again perform the time-average over an interval $[3/4t_{max}, t_{max}]$. In the dashed line, $E_\infty$ is computed as an average over the effective microcanonical ensemble (solid line) defined through Eqs. (4.29) and (4.28).

introduced in Section 3.2. The driven version of its Hamiltonian is expressed as

$$\hat{H}_{PSM}(t) = \frac{1}{2M}\sum_{i=1}^{N}\hat{\Pi}_i^2 + \mathcal{J}(t)V_J(\hat{\boldsymbol{\sigma}}) - B(t)\sum_i \hat{\sigma}_i, \tag{4.31}$$

with $V_J(\hat{\boldsymbol{\sigma}})$ defined in Eq. (3.20). The driving is implemented by taking one taking either $B(t)$ and $\mathcal{J}(t)$ to be a periodic function, while we will set the other to 0 for simplicity. These will allow us to investigate the effect of different driving terms on the quantum dynamics of the PSM. As in this chapter we are interested in studying periodically driven ergodic models, we will restrict our analysis to temperatures above the ergodicity breaking threshold, $T > T_d(\hbar)$ [86].

We will focus in particular on the dynamical correlation and response function, defined respectively as

$$C(t,t') = \frac{1}{2N}\sum_{i=1}^{N}\langle\hat{\sigma}_i(t)\hat{\sigma}_i(t') + \hat{\sigma}_i(t')\hat{\sigma}_i(t)\rangle \tag{4.32}$$

$$R(t,t') = \theta(t-t')\frac{i}{\hbar N}\sum_i \langle[\hat{\sigma}_i(t), \hat{\sigma}_i(t')]\rangle \ . \tag{4.33}$$

The fully connected nature of the model defined in Eq. (4.31) allows us to derive closed dynamical equations that describe the evolution of correlation and response functions starting from an initial state uncorrelated with the disorder. Specifically, a straightforward generalization of the calculations presented in Refs. [86, 89, 188], leads to the following closed set of equations, in the large-$N$ limit and after disorder-averaging (see Appendix D.1 for more details):

$$[m\partial_t^2 + z(t)]R(t,t') = \delta(t-t') + \int_0^t dt''\Sigma(t,t'')R(t'',t'), \tag{4.34}$$

$$\begin{aligned}[m\partial_t^2 + z(t)]C(t,t') = &\int_0^t dt''\Sigma(t,t'')C(t'',t') + \int_0^{t'} dt''D(t,t'')R(t',t'') \\ &+ B(t)\int_0^{t'} dt''R(t',t'')B(t'') \ .\end{aligned} \tag{4.35}$$

Here $z(t)$ is a Lagrange multiplier enforcing the spherical constraint and the self-energies $\Sigma(t,t')$ and $D(t,t')$ are defined as follows:

$$\begin{aligned}\Sigma(t,t') = &-4\eta(t-t')\Theta(t_b-t)\Theta(t_b-t') + \\ &- \frac{p\mathcal{J}(t)\mathcal{J}(t')J^2}{\hbar}\mathrm{Im}\left[C(t,t') - \frac{i\hbar}{2}R(t,t')\right]^{p-1},\end{aligned} \tag{4.36}$$

$$\begin{aligned}D(t,t') = &2\hbar\ \nu(t-t')\Theta(t_b-t)\Theta(t_b-t') + \\ &+ \frac{p\mathcal{J}(t)\mathcal{J}(t')J^2}{2}\mathrm{Re}\left[C(t,t') - \frac{i}{2}(\hbar R(t,t') + \hbar R(t',t))\right]^{p-1}.\end{aligned} \tag{4.37}$$

The determination of the Lagrange multiplier $z(t)$ for our unitary driven dynamics is more intricate than in previously studied protocols [86]. For the sake of conciseness, we address this technical issue in Appendix D.2. Equations (4.34) and (4.35) are often referred to as Mode Coupling (MC) equations, due to the formal analogies with the mode-coupling theory for structural glasses [189–191]. In the classical limit of $\hbar \to 0$, the equations are equivalent to the ones studied in Ref. [192]. The terms $\eta(t-t')$ and $\nu(t-t')$ are the correlation and response functions of an external bath, in equilibrium at a temperature $T_0 < T_d(\hbar)$, that we couple to the system up to a time $t_b$. They are given by:

$$\eta(t-t') = -\Theta(t-t')\int_0^\infty d\omega I(\omega)\sin[\omega(t-t')], \tag{4.38}$$

$$\nu(t-t') = \int_0^\infty I(\omega)\coth\left(\frac{\hbar\omega}{2T_0}\right)\cos[\omega(t-t')] \ , \tag{4.39}$$

where $I(\omega)$ is the spectral function of the bath. We choose an Ohmic bath with $I(\omega) = \frac{1}{\pi}\exp(-|\omega|/\Lambda)$, for which explicit expressions for both $\nu(t-t')$ and $\eta(t-t')$ can be straightfowardly found, and we choose the integration cutoff to be $\Lambda = 5$. Making use of the spherical constraint and the causal structure of the response function, we can also obtain the equal-time relations:

$$C(t,t) = 1 \ , \qquad \partial_t C(t,t')|_{t'\to t^-} = \partial_t C(t,t')|_{t'\to t^+} = 0 \ , \tag{4.40}$$

$$R(t,t) = 0 \ , \qquad \partial_t R(t,t')|_{t'\to t^-} = \frac{1}{M} \ , \qquad \partial_t R(t,t')|_{t'\to t^+} = 0 \ . \tag{4.41}$$

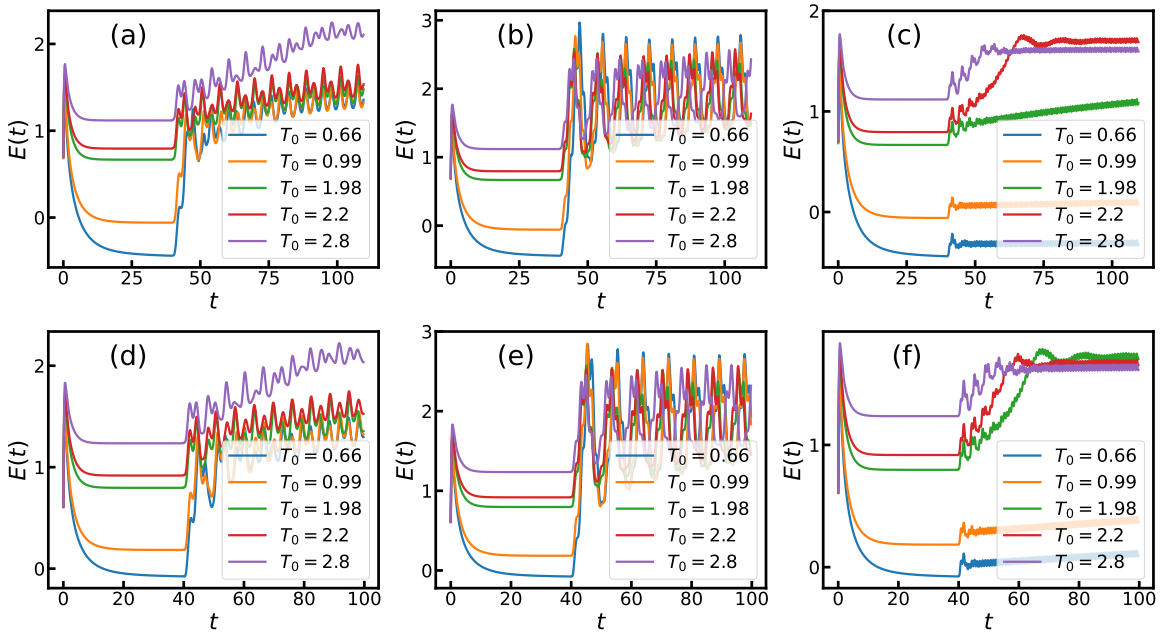


Figure 4.4: Time-evolution of the energy density $E(t)$, defined in Eq. (4.43), for the $p$-spin spherical model, for fixed $B_0 = 1$ and $\Delta = 0$. **(a)-(c)** We fix $\hbar = 0$. We set the driving frequency to $\Omega = 1.0, 1.5, 3.5$ respectively for the three panels, from left to right. **(d)-(f)** We fix $\hbar = 1$ and driving frequencies coinciding with the ones used respectively in panels from **(a)** to **(c)**.

In the following, we will fix the time-dependent fields as

$$\mathcal{J}(t) = \theta(t - t_b)[1 + \Delta \sin(\Omega t)] \ , \qquad B(t) = \theta(t - t_b) B_0 \sin(\Omega t) \ . \tag{4.42}$$

In this way, the system is first coupled to a bath for $0 < t < t_b$ in order to relax to a thermal state, then for $t > t_b$ it evolves unitarily under the effect of the driving fields.

To understand the fate of the periodically driven dynamics of the PSM, we compute the energy density $E(t) = \langle \hat{H}_J \rangle / N$, where $\hat{H}_J$ from is the Hamiltonian of the undriven PSM . In the thermodynamic limit $N \to \infty$, $E(t)$ can be expressed through the correlation and response function as [89, 143]

$$E(t) = -\frac{M}{2} \partial_t^2 C(t, t')\big|_{t' \to t^-} - \frac{1}{p} \int_0^t ds \, [\Sigma(t, s) C(t, s) + D(t, s) R(t, s)] \ . \tag{4.43}$$

In what follows, we will first fix $B_0$ and $\Delta = 0$ in Eq. (4.42), to isolate the effect of the magnetic field $B(t)$ from the one due to $\mathcal{J}(t)$. We solve the MC equations using a predictor-corrector scheme [193], reviewed in Appendix D.3, and compute $E(t)$ for a several values of the driving frequency $\Omega$ and initial temperature $T_0$. We plot the resulting profiles for $E(t)$ in Fig. 4.4, both for the case of $\hbar = 0$ and $\hbar = 1$. In both cases, $E(t)$ first saturates a first plateau for $t \lesssim t_b$, signalling that the system reached a thermal equilibrium with the bath, and oscillates around a second one at late times, centered around a finite value $E_\infty$. In particular, second saturation to $E_\infty$ is compatible with a finite temperature thermalization for the PSM, either in the classical and

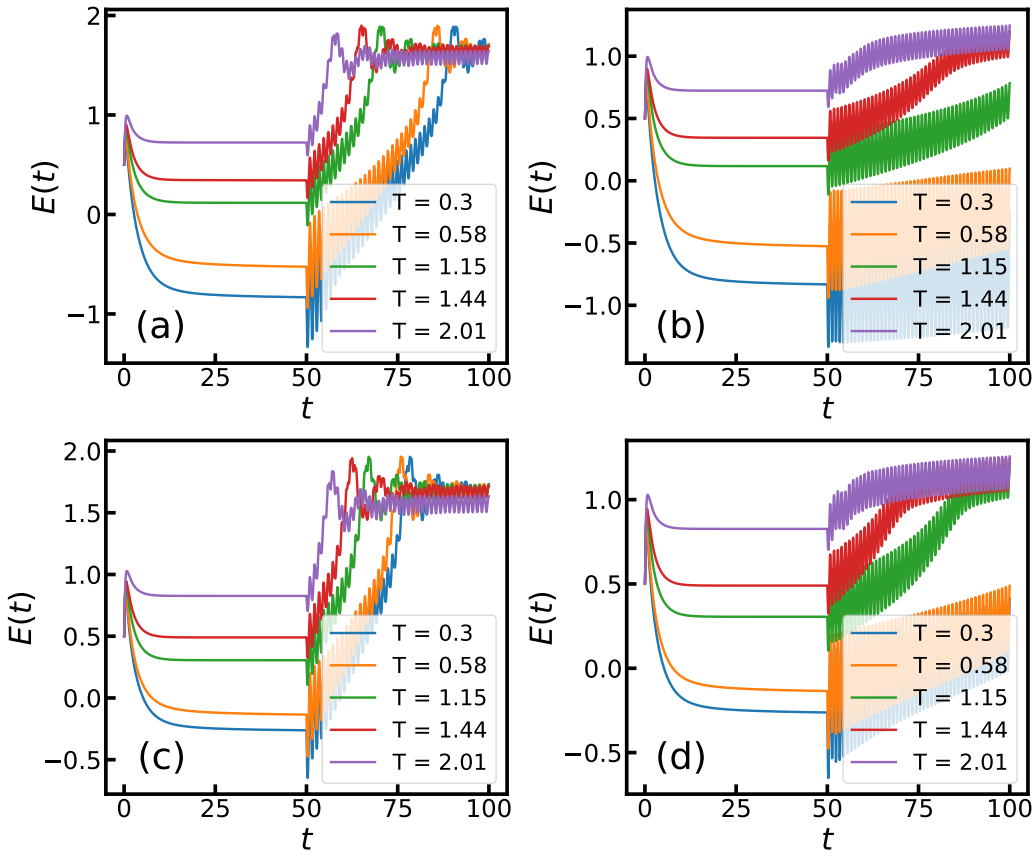


Figure 4.5: Time-evolution of the energy density $E(t)$, defined in Eq. (4.43), for the $p$-spin spherical model, for fixed $B_0 = 0$ and $\Delta = 1$. **(a)-(b)** We fix $\hbar = 0$ and set the driving frequency to $\Omega = 5.0, 6.0$, respectively from left to right in the panels. **(c)-(d)** Plots obtained for the same parameters used respectively in panels from **(a)** to **(c)**, the only difference being in $\hbar$ set to 1.

quantum regime. The qualitative analogy between the profiles obtained for $\hbar = 0$ and the ones at $\hbar = 1$ suggests a quantum-to-classical correspondence for the periodically driven dynamics of the PSM. We observe that $E_\infty$ does not depend on $T_0$, as long as $E(0) \lesssim E_\infty$, in analogy with the lattice $\phi^4$ model. Our results generalized to the case of $B_0 = 0$ and $\Delta = 1$, as shown in Fig. 4.5, where the periodic drive is due to a modulation in the interaction and we retrieve the same behaviour for $E(t)$, both in the classical and quantum case.

The numerical results we obtained for the PSM are also consistent with the emergence of a non-trivial conservation law. Unlike for the $\phi^4$ model, we can not perform a multi-scale analysis due to the difficulty in accounting for the spherical constraint. Instead, as we have direct access to the two-point functions, we search for further indications of of finite temperature thermalization from the Fluctuation-Dissipation Theorem (FDT) [194, 195], reviewed in the following. The classical version (at $\hbar = 0$) of the FDT states that, for a generic dynamics evolving from an equilibrium state, the

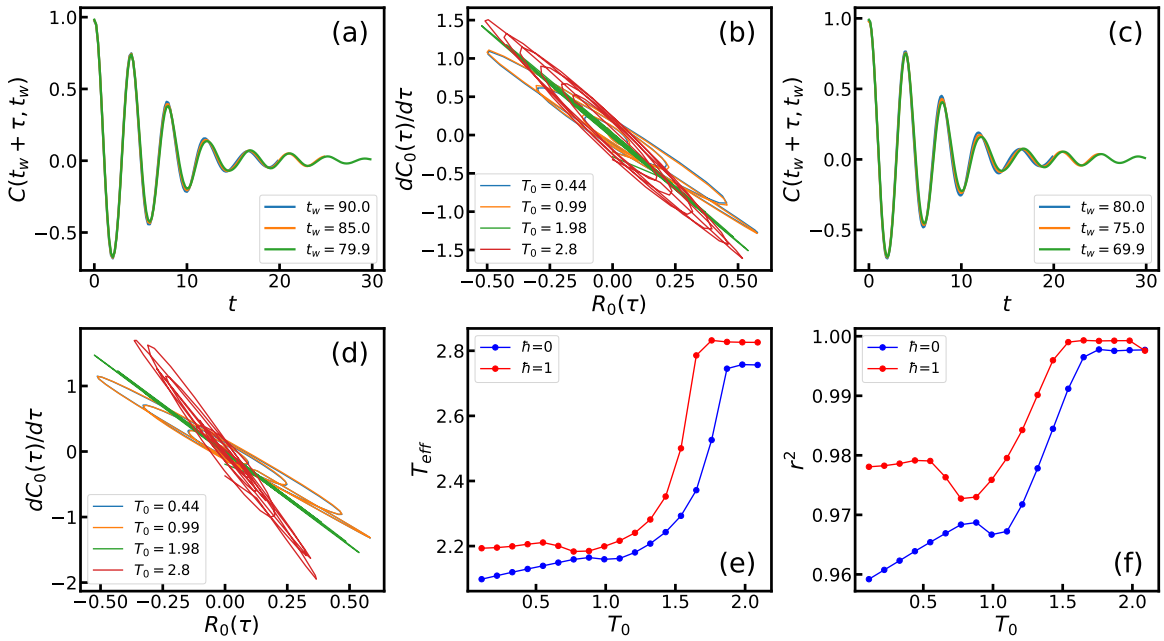


Figure 4.6: Plots for the correlation and response functions of the $p$-spin spherical model. **(a)-(d):** Plots for the correlation and response functions, either for $\hbar = 0$, in **(a-b)**, or $\hbar = 1$, in **(c-d)**. **(a,c):** Correlation function obtained from Eqs. (4.34) and (4.35), for , $T_0 = 0.99$ and $\Omega = 2.5$. **(b,d):** Time-averaged 2-point functions from Eq. (4.47), for $\Omega = 2.5$ and several values of $T_0$. **(e):** Effective temperature $T_{eff}$ obtained from a linear regression fit of Eq. (4.44), for the quantities $C_0(\tau)$ and $\chi_0(\tau)$ in panels **(b,d)**, $\Omega = 2.5$ and several values of $T_0$. **(f):** The corresponding $r^2$ value from the linear fit described in panel **(e)**.

correlation and response function are not independent and are related by the equation

$$\frac{d}{dt}C(t-t') = -T\ R(t-t')\ , \tag{4.44}$$

for $t > t'$, where $T$ is the temperature of the system. In Eq. (4.44), we used of the fact that, whenever the dynamics is stationary, the two-point functions depend only on the difference $t-t'$ of $t$ and $t'$. The generalization of the FDT to quantum systems is more easily expressed in Fourier space as

$$\tilde{C}(\omega) = \hbar \coth\left(\frac{\hbar\omega}{2T}\right)\tilde{R}(\omega)\ . \tag{4.45}$$

Here, $\tilde{f}(\omega) = \int dt f(t)\exp(i\omega t)/2\pi$. For an ergodic system in contact with a thermal bath and evolving from a generic state, $T$ coincides with the bath temperature, as thermal equilibrium is eventually reached. The relations established by FDT are proven to hold only when the system is in a stationary state. In principle, they are not expected to be valid when the dynamics is periodically driven. This becomes evident from the graphical representations in Fig. 4.4, where we observe that $E(t)$ consistently exhibits persistent oscillations around $E_\infty$ across the various timescales we explore numerically, signifying that the system does not reside in a stationary state during this interval. However, the results in Fig. 4.6-(a) and (c) reveal that, at large times and at intermediate values of $\Omega$, the correlation and response function become approximately invariant under the time translations of $2\pi/\Omega$, as expressed by the equations:

$$C(t,t') \simeq C(t+4\pi/\Omega, t'+4\pi/\Omega) \qquad R(t,t') \simeq R(t+4\pi/\Omega, t'+4\pi/\Omega) \tag{4.46}$$

This approximate time-translational invariance we observe in the two-point functions suggests the emergence of a quasi-stationary dynamics, at least at discrete times. Motivated by this observation, we explore a potential connection between the time-averaged quantities:

$$C_0(\tau) = \frac{\Omega}{4\pi}\int_{t_0}^{t_0+4\pi/\Omega} ds\,[C(s+\tau,s) - m(s+\tau)m(s)]\ , \tag{4.47}$$

$$R_0(\tau) = \frac{\Omega}{4\pi}\int_{t_0}^{t_0+4\pi/\Omega} dsR(s+\tau,s)\ . \tag{4.48}$$

Here, we subtracted the disconnected and oscillating component from $C(t,t')$ due to oscillations in the magnetization, which can be expressed as

$$m(t) = \frac{1}{N}\sum_{i=1}^{N}\langle\hat{\sigma}_i(t)\rangle = \int_0^t dsR(t,s)B(s)\ , \tag{4.49}$$

as shown in Appendix D.1. In Fig. 4.6-(b) and (d), we plot $R_0(\tau)$ against $dC_0(\tau)/d\tau$. For each initial bath temperature $T_0$, the data retrieved at late times oscillate around a well-defined linear slope $T_{eff}$. Thus, we calculate $T_{eff}$ through linear regression of Eq. (4.44), for $C_0(\tau)$ and $R_0(\tau)$, and display the results in Fig. 4.6-(e), as a function of $T_0$, for both the classical and quantum cases. We note that $T_{eff}$ remains relatively

constant across a broad spectrum of small to intermediate values of $T_0$. This pattern aligns with the trends observed in $E(t)$ for the PSM and is consistent with the outcomes depicted in Fig. 4.3-(d) for the lattice $\phi^4$ model. The corresponding $r^2$ value is illustrated in Fig. 4.6-(e), revealing its proximity to one across the entire range of $T_0$ values, regardless of whether $\hbar = 0$ or $\hbar = 1$. This observation confirms the accuracy of the linear relationship we hypothesized between $R_0(\tau)$ and $C_0(\tau)$ and suggest that, because the values of $T_{eff}$ are sufficiently high, the classical version of FDT from Eq. (4.44) approximately holds even if we set $\hbar = 1$.

## 4.4 Summary and perspectives

In this chapter, we studied the dynamics of three distinct systems: the classical Duffing oscillator, the classical $\phi^4$ model, and the PSM in both classical and quantum domains. In all the cases examined, the dynamics exhibited characteristics consistent with the presence of an emergent conservation law, evidenced by the bounded energy absorption even at extended times. To quantitatively analyze these emergent conservation laws, we developed a perturbative approach - the multiple-scale analysis- for the Duffing and $\phi^4$ models, enabling the explicit computation of the associated conserved quantity. Furthermore, in the case of the PSM, late-time thermalization was supported also by the observation of an approximate fluctuation-dissipation relation (FDT).

Our findings differ significantly from those obtained for quantum [25, 26] or classical [33, 34] spin chains. In these scenarios, the absence of local conserved quantities at stroboscopic times leads the system towards a featureless, infinite-temperature state. A promising avenue for future research involves attempting to apply the multiple-scale analysis also to many-body classical spin chains. Exploring this direction could provide a deeper understanding of the qualitative differences between classical spins and the systems with unbounded phase space. We also observe that our findings for the $\phi^4$ model have the potential to be extended to the quantum realm, by employing the same density-matrix renormalization group techniques as in Ref. [196].

It is important to note that we cannot definitively rule out the eventual relaxation to infinite temperature at times longer than the ones explored in our simulations; however, the time-scale of this process should be much larger than all the ones determined by the system's couplings that we are studying.

# Chapter 5

# From chaos to discrete Floquet time crystals in long-range systems

In Chapter 4, we investigated the dynamics of periodically driven systems, known as Floquet systems, which are usually expected to eventually reach a thermal equilibrium state. This general understanding, however, encounters a fascinating exception known as *discrete Floquet time crystals* (DFTCs) [160, 197–203]. DFTCs are defined as dynamical phases of matter where the system remains perpetually out of equilibrium, and local observables exhibit persistent oscillations with a period different from that of the driving force.

The name "time crystal" finds its roots in the pioneering works by F. Wilczek [197, 204]. Wilczek conjectured that certain autonomous systems can break continuous time translation symmetry, akin to space traslation symmetry breaking in crystals. For systems in thermal equilibrium, this possibility has been later ruled out by a no-go theorem [205]. In the realm of out-of-equilibrium scenarios, one of the initial concrete observations of a time crystal was made within the context of disorder-localized Floquet systems [160, 206, 207]. For such systems it was shown that local observables display periodic oscillations, which become persistent in the thermodynamic limit. Subsequently, the possibility of generating a DFTC in systems without disorder has been investigated in the context of long-range interacting models. These systems are defined on a $d$-dimensional lattice, where the interaction between lattice sites $\mathbf{i}$ and $\mathbf{j}$ follows a power-law decay pattern, $J_{\mathbf{i},\mathbf{j}} \sim |\mathbf{i}-\mathbf{j}|^{-\alpha}$. Notably, these models have garnered significant attention due to their experimental feasibility in various platforms, including atomic, molecular, and optical systems [208–215]. Instances of DFTC phases have been identified for $0 < \alpha < d$ [216, 217], while for $\alpha > d$ the oscillations fade away in the thermodynamic limit [202, 203, 218, 219].

In all instances mentioned above, the oscillations defining the the time crystalline behaviour were always observed to display a period $\mathcal{T}_B = n\mathcal{T}$, where $n$ is an integer and and $\mathcal{T} = 2\pi\Omega^{-1}$ is the period of the driving. The corresponding integer $n$, usually referred to as the *order* of the DFTC, was then connected to the explicit $\mathbb{Z}_n$ symmetry of the model [160, 216, 217]. Nevertheless, recent investigations [220–222] have revealed that DFTCs of order $n > 2$ can be observed in systems displaying only a $\mathbb{Z}_2$ symmetry.

The emergence of such higher-order DFTC phases was then explained in terms of an emergent, rather than fundamental, $\mathbb{Z}_n$ dynamical symmetry [223].

Despite the significant progress made in the last decade, DFTC phases remain elusive feature in the realm of out-of-equilibrium phenomena, because of the absence of a universal observable, such as an order parameter, capable of detecting them regardless of their order $n$. In this chapter we address this issue, focusing specifically on long-range models. We introduce a novel order parameter designed to identify time crystalline phases irrespective of their order, relying solely on the geometric properties of the dynamics. We concentrate our efforts on the Lipkin-Meshkov-Glick (LMG) model [224]. Additionally, we examine the robustness of the DFTC phases against weak perturbations, both short and long-range, utilizing the non-equilibrium spin-wave theory (NEQSWT) already discussed in Section 2.3 and Appendix B. At finite sizes, we interpret the DFTC phases of order $n$ through the lens of an emergent $\mathbb{Z}_n$ symmetry in the Floquet eigenstates. These eigenstates manifest as Bloch superpositions of $n$ localized, semi-classical states, a feature demonstrated for $n = 2$ in Ref. [216].

This chapter is organized as follows. In Section 5.1 we define the salient features of discrete Floquet time crystals. In Section 5.2 we define the order parameter we propose and discuss its ability to distinguish time crystals from other dynamical behaviours. We apply our definition to the LMG model in Section 5.3. We discuss the physical intrepretation of our results at finite sizes in Section 5.4. In Section 5.5 we discuss how our results are altered by the inclusion of perturbations beyond the fully-connected limit. We summarize our results in Section 5.6.

## 5.1 Review of discrete Floquet time crystals

In this section, we revisit the definition of a discrete Floquet time crystal, following Refs. [160, 216]. We start by examining a quantum Floquet system, characterized by a time-dependent Hamiltonian with periodicity $\hat{H}(t) = \hat{H}(t + \mathcal{T})$. The corresponding Floquet operator is defined as follows:

$$\hat{U}_F = \mathrm{T}\left\{\exp\left[-\frac{i}{\hbar}\int_0^{\mathcal{T}} ds\hat{H}(s)\right]\right\} , \tag{5.1}$$

where T represents the time ordering, and the integral spans a period $\mathcal{T}$. We will use the term *Floquet eigenstates* to refer to the eigenstates of $\hat{U}_F$. Additionally, we will also consider a state $|\Psi\rangle$ as *short-range correlated* if, for any local observable $\hat{A}_i$, the clustering condition

$$\lim_{|i-j|\to\infty}\left[\langle\Psi|\hat{A}_i\hat{A}_j|\Psi\rangle - \langle\Psi|\hat{A}_i|\Psi\rangle\langle\Psi|\hat{A}_j|\Psi\rangle\right] = 0 \tag{5.2}$$

holds.

In a driven system, a discrete Floquet time Crystal (DFTC) phase exists if, for a class of short-range correlated states $|\Psi\rangle$, there exists an observable $\hat{O}$ such that the

time-evolved expectation value in the thermodynamic limit ($N \to \infty$),

$$O(t) = \lim_{N\to\infty} \langle \Psi(t)|\hat{O}|\Psi(t)\rangle, \tag{5.3}$$

satisfies the following conditions [160]:

1. Time-translation symmetry breaking: $O(t+\mathcal{T}) \neq O(t)$, although $\hat{H}(t) = \hat{H}(t+\mathcal{T})$.
2. Rigidity: $O(t)$ must display periodic oscillations, in a finite and connected region of the Hamiltonian parameters space.
3. Persistence: in the large system size limit $N \to \infty$, the oscillations of $O(t)$ must persist for infinitely long time.

It has been proved that the first condition, the breaking of time-translation symmetry, is equivalent to the requirement of long-range correlations in the Floquet eigenstates [160]. The average observable $O(t)$ that fulfills the conditions 1-3 listed above is commonly used as an order parameter to detect the DFTC phase. From $O(t)$, the *order* of the time crystal can be computed. This order is defined as the smallest rational such that:

$$O(t) = O(t + n\mathcal{T}) \tag{5.4}$$

for every time $t$. In this context, $n = 1$ then corresponds to an "unbroken" time-translation symmetry, while $n = 2$ is usually called "period-doubling" phase [216]. DFTC phases are often detected as non-vanishing peaks in the Fourier spectrum of $O(t)$ with the corresponding frequency determining the order $n$.

## 5.2 The order parameter

When using the order parameter $O(t)$ from Eq. (5.3), we can not identify a DFTC from a single scalar quantity. As discussed in Section 5.1, DFTCs are in fact detected as a non-vanishing peak in the Fourier spectrum of $O(t)$, but the position of this peak depends on both the driving period $\mathcal{T}$ and the order of the DFTC. In this section, we demonstrate how this challenge can be overcome in the context of long-range systems. We achieve this by introducing an alternative order parameter, which solely relies on the geometric aspects of the system's dynamics.

To set the stage, let us consider a generic family driven Hamiltonian $\hat{H}(t)$, such that $\hat{H}(t) = \hat{H}(t+\mathcal{T})$. We assume that $\hat{H}(t)$ depends on a parameter (or a set of parameters) $\Lambda$. Let us denote the average at stroboscopic times of the operator $\hat{O}$ as

$$O_l(\Lambda) = \lim_{N\to\infty} \langle \Psi(l\mathcal{T})|O|\Psi(l\mathcal{T})\rangle \ . \tag{5.5}$$

We aim to use this operator to detect potential time-crystalline behavior for a fixed $\Lambda$. Then, we define the following quantity:

$$\zeta^2 = \lim_{\substack{n_{\max}\to\infty \\ \delta\Lambda\to 0}} \sum_{l=0}^{n_{\max}} \left[O_l(\Lambda+\delta\Lambda) - O_l(\Lambda)\right]^2 \ , \tag{5.6}$$

defined for a fixed $n_{\max}\,\delta\Lambda \sim O(1)$. Intuitively, $\zeta$ measures the robustness of persistent oscillations of $O_l$, with respect to changes in the driving parameter(s) $\Lambda$.

The key finding of this chapter is that when the stroboscopic dynamics of the observable $O_l$ can be uniquely associated with a classical trajectory, $\zeta$ serves as a period-blind order parameter, identifying DFTC phases regardless of their order $n$. This condition is satisfied, for example, in fully-connected models, as discussed in Section 2.1. To understand why, we first observe that the driven dynamics of semi-classical systems takes place in an effective two-dimensional phase space consisting of a blend of regular, *resonant* islands and chaotic regions, separated by "separatrix" orbits. This picture is a consequence of the Poincaré-Birkhoff theorem [15, 16], which we already discussed in Section 1.1, for a kicked rotor. In this classical context, a DFTC phase of order $n$, involves a regular, periodic hopping of the sequence $\{O_l(\Lambda)\}$ between $n$ resonant islands. This behavior was observed in Refs. [220, 222, 223] and is accompanied by a subtle 'micro-motion' within each island, as described in Ref. [220]. The presence of $n$ islands gives rise to an emergent dynamical $\mathbb{Z}_n$ symmetry. If we consider another sequence $\{O_l(\Lambda+\delta\Lambda)\}$ with $\delta\Lambda \ll 1$, the hopping behavior persists, leading to a linear divergence in the distance $|O_l(\Lambda+\delta\Lambda) - O_l(\Lambda)| \sim c|\delta\Lambda|l$, for some constant $c$ . From this linear divergence, we get the following scaling for the order parameter:

$$\zeta^2 \sim \frac{c^2}{n_{\max}} \sum_l \delta\Lambda^2 l^2 \sim c^2 (n_{\max}\delta\Lambda)^2 \tag{5.7}$$

Conversely, in the chaotic limit, $O_l(\Lambda)$ and $O_l(\Lambda+\delta\Lambda)$ uniformly spread outside the islands, becoming uncorrelated over a timescale $\log|\delta\Lambda|^{-1}$, shorter than $n_{\max} \sim |\delta\Lambda|^{-1}$. Consequently, we obtain a different saturation value for $\zeta$, given by:

$$\zeta^2 \simeq \langle O(\Lambda)\rangle_{cl}^2 \ . \tag{5.8}$$

Here $\zeta$ roughly scales as the square of the uniform (i.e. infinite-temperature) average over the classical phase space, here denoted as $\langle\cdot\rangle_{cl}$.

In addition, a third possible behavior emerges: a periodic dynamics $O_l(\Lambda)$ with an irrational and strongly $\psi$-dependent period. We refer to this phenomenon as a *quasi-periodic phase* and it is typically associated with KAM tori [8–10]. In this integrable dynamics, $|O_l(\Lambda+\delta\Lambda) - O_l(\Lambda)|$ still grows linearly with $l$ and $\zeta$ scales as in Eq. (5.7), although $\zeta$ is expected to saturate to values typically larger than in the DFTC phase, as the corresponding KAM tori encompass all the resonant islands. In Section 5.3, we will make the last statement quantitative for the specific case of the LMG model, where we will show that $\zeta$ exhibits a discontinuity when moving from a DFTC to a quasi-periodic phase, due to the different topologies of the corresponding trajectories.

Although the discussion above is expected to hold only in fully-connected models, we will demonstrate in Section 5.5 that our results remain valid for sufficiently long-range models or when a short-range weak perturbation is included. In these cases, the dynamics can still be rationalized as a single classical trajectory embedded in a self-generated bath of dynamical spin-waves, as previously discussed in Section 2.3.1.

## 5.3 The dynamical phase diagram of the Lipkin-Meshkov-Glick model

In this section, we compute the order parameter $\zeta$, defined in Section 5.2, for the specific case of a chain of $N$ spin 1/2 particles, interacting through the one-dimensional long-range driven Hamiltonian:

$$\hat{H}(t) = -\frac{\lambda}{2N_\alpha}\sum_{i>j}\frac{\hat{\sigma}_i^x\hat{\sigma}_j^x}{|i-j|^\alpha} + h(t)\sum_{i=1}^{N}\hat{\sigma}_i^z - J\sum_{i=1}^{N}\hat{\sigma}_i^x\hat{\sigma}_{i+1}^x \ , \tag{5.9}$$

for $\alpha < 1$. The operators $\hat{\sigma}_i^x$,$\hat{\sigma}_i^y$,$\hat{\sigma}_i^z$ are the Pauli matrices relative to the lattice site $i$ and $N_\alpha = \sum_{j\neq 0}|j|^{-\alpha}$ is the Kac scaling factor needed in order to have an extensive energy [225]. The magnetic field $h(t)$ is periodic with period $\mathcal{T}$ and is represented as a series of kicks:

$$h(t) = \psi\sum_{n=1}^{\infty}\delta(t-n\mathcal{T}) \ , \tag{5.10}$$

The strength of these kicks is determined by the parameter $\psi$. For convenience, assume periodic boundary conditions for the lattice and set $\lambda + J = 1$.

In the following we will focus on the case $\alpha = J = 0$, a condition that renders the dynamics effectively classical. In this particular instance, the Hamiltonian in Eq. (5.9) describes the driven version of the Lipkin-Meshkov-Glick (LMG) model [224], representing the $p = 2$ variant of the model introduced in Eq. (2.15). The effect of introducing fluctuations atop this classical dynamics will be discussed in Section 5.5. The kicked version of the LMG model has been previously investigated, for a fixed value of $\mathcal{T}$, in Refs. [216, 220]. These studies shown that the model exhibits a DFTC phases, whose $n$ can be an integer greater than 2, although the fundamental symmetry of the model is only $\mathbb{Z}_2$. The existence of these higher-order DFTC phases was explained in terms of the hopping mechanism, as we discussed in Section 5.2.

### 5.3.1 A stroboscopic map for the mean-field dynamics

In this section, we investigate the stroboscopic dynamics of the observables

$$\mathcal{S}_l^a = \frac{1}{N}\sum_{j=1}^{N}\langle\hat{\sigma}^a(l\mathcal{T})\rangle \ , \tag{5.11}$$

for $a = x, y, z$. To do so, we exploit the fact that the Floquet operator of the dynamics can be decomposed as a product two terms, due to the impulsive nature of the field $h(t)$:

$$\hat{U}_F = e^{-2i\psi\hat{S}^z}e^{i\lambda\mathcal{T}(\hat{S}^x)^2/N} \ , \tag{5.12}$$

Here, $\hat{S}^a = \frac{1}{2}\sum_j\hat{\sigma}_j^a$ are the global spin operators. The first term in the product on the right-hand side of Eq. (5.12) corresponds to an instantaneous rotation of the spin operator around the $z$-axis. Conversely, the second term describes the time evolution under the fully connected LMG Hamiltonian. Using the general theory from Section 2.1, in

the thermodynamic limit $N \to \infty$, the dynamics generated by this second term is given by:

$$\begin{cases} \dot{\mathcal{S}}^x &= 0 \\ \dot{\mathcal{S}}^y &= \lambda \mathcal{S}^x \mathcal{S}^z \\ \dot{\mathcal{S}}^z &= -\lambda \mathcal{S}^x \mathcal{S}^y \ . \end{cases} \tag{5.13}$$

Upon completing a cycle of period $\mathcal{T}$, this dynamics results in a rotation around the $x$-axis by an angle $\lambda \mathcal{T} \mathcal{S}^x(t)$, where $\mathcal{S}^x(t)$ denotes the configuration at the cycle's outset. To summarize, the dynamics of the set of operators $\mathbf{m}_l = \{\mathcal{S}^x(l\mathcal{T}), \mathcal{S}^y(l\mathcal{T}), \mathcal{S}^z(l\mathcal{T})\}$ is determined, in the thermodynamic limit, by the closed map:

$$\vec{\mathcal{S}}_{l+1} = \vec{f}(\vec{\mathcal{S}}_l) \equiv R_z(2\psi) R_x(-\mathcal{S}_l^x \mathcal{T}) \vec{\mathcal{S}}_l \ , \tag{5.14}$$

where $R_{x,y,z}(\xi)$ is the rotation matrix of an angle $\xi$ around the corresponding axis [223]. This dynamics is also constrained on the Bloch sphere, $|\vec{\mathcal{S}}|^2 = 1$. Examining Eq. (5.14), we also observe that the original $\mathbb{Z}_2$ symmetry of the model translates into an invariance of the dynamics under the transformations:

$$\begin{cases} \psi &\to \psi + \pi/2 \\ \vec{\mathcal{S}}_l &\to R_z(\pi l) \vec{\mathcal{S}}_l \end{cases} \tag{5.15}$$

We fix the initial condition at $t = 0$ as the ground state of the $h(t) = 0$ Hamiltonian, $|\Xi_0\rangle = |{\to}\cdots{\to}\rangle$, with $\hat{\sigma}_x |{\to}\rangle = |{\to}\rangle$. This initial state corresponds to the classical configuration $\vec{\mathcal{S}}_0 = (1, 0, 0)$.

Before going on to discuss the fate of the dynamics, it is worthy to notice that the map in Eq. (5.14) possesses an Hamiltonian structure. This is made transparent by mapping the collective spin into a pair of canonically conjugated action-angle variables as follows:

$$\vec{\mathcal{S}} = (\sqrt{1 - I^2} \cos\phi, \sqrt{1 - I^2} \sin\phi, I) \tag{5.16}$$

It is straightforward to show that the Poisson brackets $\{\mathcal{S}^\alpha, \mathcal{S}^\beta\} = \sum_\gamma \epsilon^{\alpha\beta\gamma} \mathcal{S}^\gamma$ are equivalent to $\{\phi, I\} = 1$. At $\mathcal{T} = 0$, the dynamics can thus be rewritten as

$$\begin{cases} I_{l+1} &= I_l \\ \phi_{l+1} &= \phi_l + 2\psi \ , \end{cases} \tag{5.17}$$

and corresponds to unperturbed tori with "period" $\pi/\psi$. As discussed in Section 1.1, the KAM theorem predicts that a deformation of these tori survives at small $\mathcal{T}$ whenever $\psi$ is not a rational multiple of $\pi$. On the other hand, for $\psi = \pi q/n$, with $q$ and $n$ coprime positive integers, the dynamics of the tori at $\mathcal{T} = 0$ is described by a discrete set of $n$ points. For small values of $\mathcal{T}$, we expect that these resonant tori will split into up into $n$ "islands" of the phase space, separated by the KAM tori through a series of separatrices. This outcome is predicted by the Poincaré-Birkhoff theorem. In this scenario, we expect a DFTC of order $n$ to emerge.

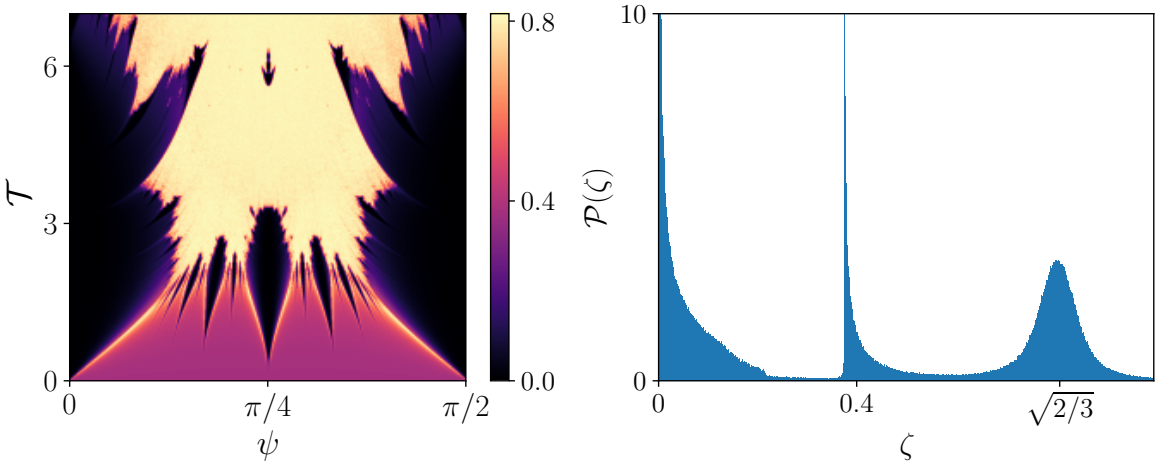


Figure 5.1: Plots of order parameter $\zeta$ from Eq. (5.18). We fix $n_{\max} = 300$ and $\delta\psi = 1.6 \cdot 10^{-3}$. **(Left):** Color plot of $\zeta$ as a function of the amplitude $\psi$ and the period $\mathcal{T}$ of the driving. **(Right):** Histogram of the occurrence $\mathcal{P}(\zeta)$ of $\zeta$ within the parameter region of the left panel, normalized at one.

### 5.3.2 Dynamical phase diagram

In this section compute the order parameter $\zeta$ from Eq. (5.1), tailored for our specific model:

$$\zeta^2 = \frac{1}{n_{\max}} \sum_{l=0}^{n_{\max}} \left[\mathcal{S}_l^x(\psi + \delta\psi) - \mathcal{S}_l^x(\psi)\right]^2 \ . \tag{5.18}$$

The dynamical symmetry in Eq. (5.15) permits us to confine our exploration to $\psi \in [0, \pi/2]$.

The corresponding phase diagram, illustrating $\zeta$ as a function of $\psi$ and $\mathcal{T}$ is presented in Fig. 5.1 (left-panel). For small, the quasi-periodic phase (violet) associated with KAM tori is prevalent. Simultaneously, by increasing $\mathcal{T}$ in correspondence of rational values of $\psi/\pi$, isolated regions of DFTC phases (dark blue) emerge. Initially, these regions expand with $\mathcal{T}$, but as they approach one another, chaos begins to encroach around their boundaries.

The size of these regions initially grows with $\mathcal{T}$ and, as they get closer to each other, chaos emerges around their boundaries. At larger $\mathcal{T}$, islands corresponding to a DFTC of order $p > 2$ are swallowed by a chaotic phase (yellow), the last of which corresponds to $p = 4$. We also observe a revival the $p = 4$ DFTC at larger values the driving period, around $\mathcal{T} \simeq 6$. The origin of this revival may depend on fine tuned characteristics of the model and eludes our current understanding.

In Fig. 5.1 (right), the histogram representing the occurrence frequency $\mathcal{P}(\zeta)$ reveals a discernible gap between $\zeta \lesssim 0.25$ and $\zeta \gtrsim 0.36$. Although not precisely zero, the occurrence frequency within this interval is very small. These values outline the boundaries of the DFTC and quasi-periodic phases, respectively. It is possible that these boundaries become even more distinct with an increase in the maximum number

of iterations $n_{\max}$ of the discrete-time dynamics.

## 5.4 Floquet eigenstates at finite size

In Section 5.3, we interpreted the dynamical phase using the language of classical dynamical systems, a possibility enabled by the effectively classical nature of the LMG model in the thermodynamic limit. However, it has been previously observed [160, 216] for a $n = 2$ DFTC that indications of DFTC phases manifest even at finite sizes. This is evidenced by the Floquet eigenstates appearing as long-range correlated cat states. In this section, we extend this observation to higher order DFTC phases.

We start by noting that the conservation of the total spin confines the dynamics to the totally symmetric subspace (TSS), as discussed in Section 2.1. The TSS corresponds to the maximal spin sector with $\hat{\mathbf{S}}^2 = Ns(Ns+1)$, for $s = 1/2$. As the dimensionality of the TSS is only polynomial in the system size $N$, we are able to perform exact diagonalization on the Floquet operator given in Eq. (5.1) for relatively large systems (up to $N = 800$) [216, 226]. To visualize the eigenstates in this subspace, we introduce the spin coherent states, defined as [71]

$$|\Omega(\theta,\phi)\rangle = e^{-i\mathbf{n}\cdot\hat{\mathbf{S}}}\,|\uparrow\ldots\uparrow\rangle \ . \tag{5.19}$$

Here $|\uparrow\ldots\uparrow\rangle$ is the eigenstate corresponding to the maximum projection of the spin along the $z$-axis and $\mathbf{n} = (\sin\theta\cos\phi, \sin\theta\sin\phi, \cos\theta)$. The overlap between two distinct coherent states is given by

$$\langle\Omega(\theta,\phi)|\Omega(\theta+\Delta\theta,\phi+\Delta\phi)\rangle = \left(\sin\frac{\Delta\theta}{2}e^{-i\Delta\phi}\right)^N \tag{5.20}$$

and diverges only for $N \to \infty$. Consequently, spin-coherent space form form an overcomplete basis for the Hilbert space at any finite $N$.

In Fig. 5.2, we illustrate the projection of selected Floquet eigenstates $|\eta_m\rangle$ onto the spin-coherent states. Distinct qualitative patterns emerge in the Floquet eigenstates across the three phases of the system: the chaotic phase displays no recognizable structure (Fig. 5.2, right panel), while in the quasi-periodic phase, eigenstates are localized in connected regions of the $(\theta,\phi)$ space (Fig. 5.2, left panel, curves (a) and (c)). In the $n = 4$ DFTC phase, eigenstates appear localized around four, $\mathbb{Z}_4$ symmetric, points (Fig. 5.2, left panel: curve (b)).

The localization in the DFTC phase can be explained on semi-classical ground. In fact, as we discussed in Section 5.3, the classical stroboscopic dynamics in the DFTC phase consists of an hopping into adiacent resonant islands of the phase space. Specifically, for $\psi = \pi q/n$, for $q$ and $n$ coprime positive integers, these islands are expected to appear around $\phi_k = \pi kq/n$, for $k = 1,\ldots,n$. At finite sizes, quantum fluctuations translate the classical hopping into long-range correlated Floquet states $|\eta_m\rangle$, each taking the form of a Bloch superposition:

$$\langle\Omega_{\theta,\phi}|\eta_m\rangle = \sum_{k=0}^{p-1} e^{2i\pi k/p} W_m^{(k)}(\theta, \phi - k\frac{q}{p}\pi) \ , \tag{5.21}$$

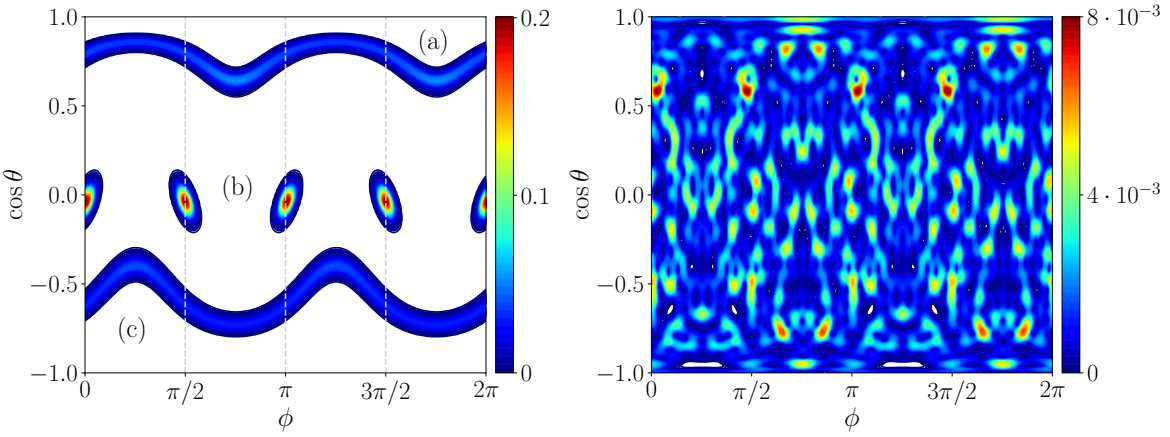


Figure 5.2: Color plot of the overlap $|\langle\Omega_{\theta,\phi}|\eta_m\rangle|^2$ between the spin coherent state $|\Omega_{\theta,\phi}\rangle$ and different Floquet eigenstates $|\eta_m\rangle$, corresponding to different phases, for $N = 800$, $\psi = \pi/2 + 0.01$, $\mathcal{T} = 1$ (left) and $\mathcal{T} = 10$ (right). While in the chaotic phase (right panel) the eigenstate has no structure, the eigenstate $(b)$ (left panel), which correspond to the DFTC phase with $n = 4$, clearly exhibits the structure of a Bloch wave-function localized around the $\mathbb{Z}_4$ symmetric wells. The eigenstate $(b)$ (left panel) has maximum overlap with the spin coherent state corresponding to the initial conditions $\cos\theta = 0$, $\phi = \pi/2$. Initial conditions localized around the eigenstates $(a)$ and $(c)$ (left panel) instead correspond to a quasi-periodic phase.

with each wave function $W_m^{(k)}(\theta, \phi - k\frac{q}{p}\pi)$ localized around $\phi = k\frac{q}{n}\pi$. We also wave-functions are mapped one into the other by the Floquet propagator:

$$\hat{U}_F W_m^{(k)}(I, \phi - k\frac{q}{n}\pi) = e^{i\beta_m} W_m^{(k+1)}(I, \phi - (k+1)\frac{q}{n}\pi) \ . \tag{5.22}$$

This conjecture, already verified for $n = 2$ DFTCs in the same model [216], implies that the overlap in Eq. (5.21) is localized in the union of the resonant islands and is confirmed by our numerical simulations.

## 5.5 Beyond mean-field: spin-wave fluctuations

In this section, we explore the robustness of DFTC phases beyond the fully-connected limit. Specifically, we examine the effects resulting from the inclusion of a short-ranged perturbation or from the substitution of the all-to-all coupling with a power-law decaying term. This is achieved by tuning either a small $\alpha$ or a small $J$ in Eq. (5.9).

We approach the problem using the non-equilibrium spin-wave theory (NEQSWT), already introduced in Section 2.3.1 and detailed in Appendix B. To facilitate the analysis, it is convenient to rewrite the perturbation in Fourier space. In Fourier space, the coupling of the nearest-neighbour interaction is straightforwardly given by $J\cos k$. However, calculating the Fourier modes corresponding to the power-law coupling $J_{ij} \sim |i-j|^{-\alpha}$ is a bit more intricate. These modes, denoted as $\tilde{\lambda}_k$, are defined

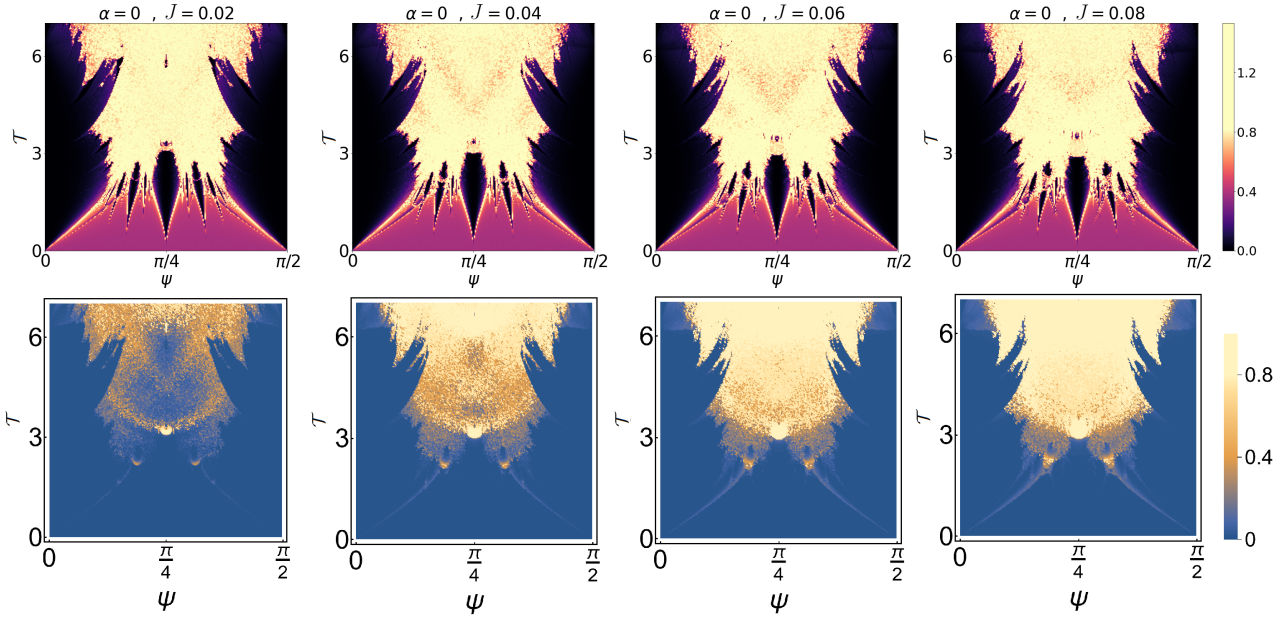


Figure 5.3: Phase diagrams resulting from the simultaneous integration of Eqs.(B.13) and (B.16), for $\tilde{J}_k = J\cos k$. We fix $\lambda = 1$. The momenta are discretized as $k = 2\pi m/N$, where $N = 50$. **(Top)** Color plot of the order parameter $\zeta$ as a function of the amplitude $\psi$ and the driving period $\mathcal{T}$, with $n_{max} = 300$, $\delta\psi = 1.6{\cdot}10^{-3}$. **(Bottom)** Color plot of the time-averaged spin-wave density $\bar{\epsilon}$, averaged up to a time $t = n_{max}\mathcal{T}$, where again $n_{max} = 300$, for the same orbits computed in the phase diagrams on top.

as follows:

$$\tilde{\lambda}_k = \frac{\lambda}{N_\alpha}\sum_{r=1}^{N/2-1}\frac{\cos(kr)}{r^\alpha}\ . \tag{5.23}$$

As shown in Ref. [227], the spectrum of $\tilde{\lambda}_k$ becomes discrete for $N\to\infty$ and can be expressed as:

$$\tilde{\lambda}_m^{(\alpha)} = \lim_{N\to\infty}\tilde{\lambda}_{k=2\pi m/N} = (1-\alpha)2^{1-\alpha}\int_0^{1/2}\frac{\cos(2\pi m s)}{s^\alpha}ds \tag{5.24}$$

Equation (5.24) is valid for $0<\alpha<1$. For large size, Hamiltonian in Eq. (5.9) can then be rewritten in Fourier space as:

$$\hat{H} = -\frac{\lambda}{4N}(\tilde{\sigma}_0^x)^2 + h(t)\tilde{\sigma}_0^z - \frac{1}{N}\sum_{k\neq 0}\tilde{J}_k\ \tilde{\sigma}_k^x\tilde{\sigma}_{-k}^x, \tag{5.25}$$

where $\tilde{J}_k = J\cos k + \tilde{\lambda}^{(\alpha)}_{m=Nk/2\pi}$. Here, the Fourier modes of the rescaled spin operators are defined as $\tilde{\sigma}_k^\alpha = \sum_{j=1}^N e^{-ikj}\hat{\sigma}_j^\alpha$ (with $\hat{\sigma}_j^\alpha = \hat{s}_j^\alpha/s$ being the rescaled spin operator on the lattice site $j$) and $k = 2\pi m/N$ for $m = 0,\dots,N-1$, with $N$ being the system size.

We apply the NEQSWT to the Hamiltonian in Eq. (5.25), by simultaneously integrating Eqs. B.13 and B.16. We still consider a fully polarized initial state, characterized by a magnetization $\vec{\mathcal{S}}_0 = (1,0,0)$. In spherical coordinates, this state can be

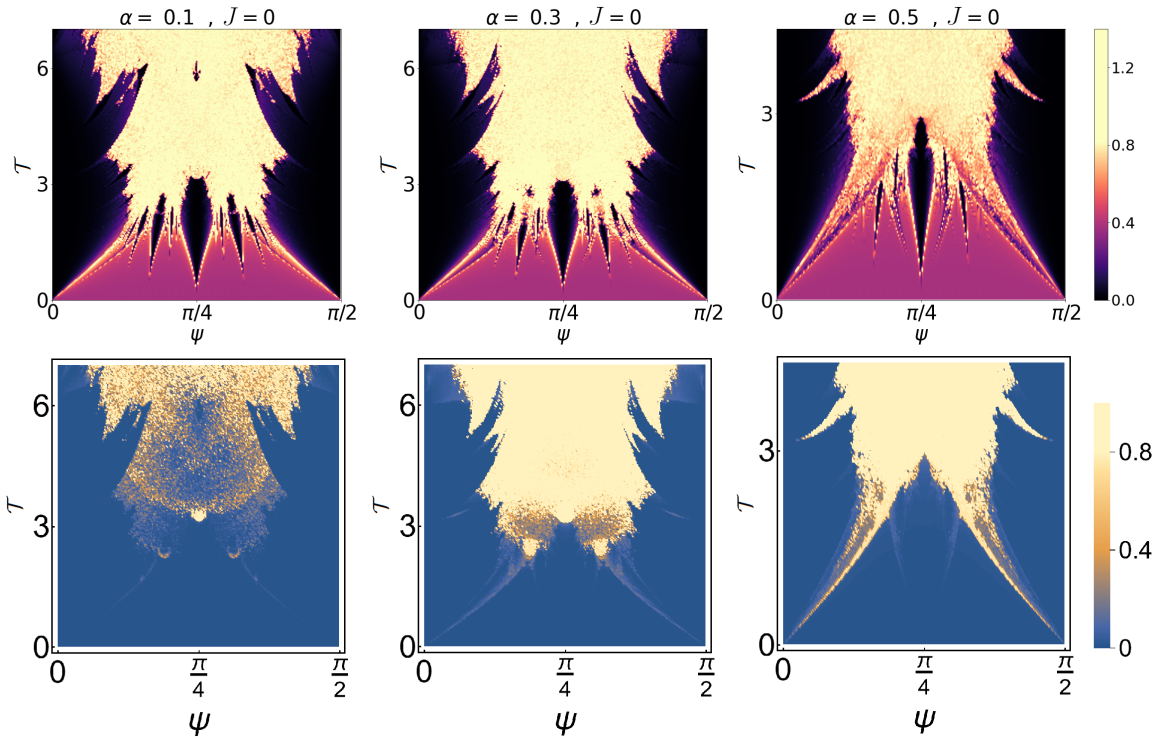


Figure 5.4: Phase diagrams resulting from the simultaneous integration of Eqs.(B.13) and (B.16), for a discrete long-range spectrum $\tilde{J}_{k=2\pi m/N} = \tilde{\lambda}_m^{(\alpha)}$, for $n = 1 \dots N$. We fix $\lambda = 1$ and $N = 50$. **(Top)** Color plot of the order parameter $\zeta$ as a function of the amplitude $\psi$ and the period $T$ of the driving, with $n_{max} = 300$, $\delta\psi = 1.6 \cdot 10^{-3}$. **(Bottom)** Color plot of the time-averaged spin-wave density $\bar{\epsilon}$, averaged up to a time $t = n_{max}\mathcal{T}$, where again $n_{max} = 300$, for the same orbits computed in the phase diagrams on top.

rewritten as

$$\theta(0) = \pi/2, \quad \phi(t=0) = 0 \ . \tag{5.26}$$

Additionally, in the fully polarized state, no spin-waves are initially excited, implying that:

$$\Delta_k^{qq}(t=0) = \Delta_k^{pp}(t=0) = 1/2, \qquad \Delta_k^{qp}(t=0) = 0 \ . \tag{5.27}$$

We integrate the dynamics evolving from this initial configuration, for various choices of the model parameters. For each integration, we compute the longitudinal magnetization $\mathcal{S}_l^x = \sin\theta(l\mathcal{T})\cos\phi(l\mathcal{T})$ [1]. Subsequently, we compute the order parameter $\zeta$ from Eq. (5.18). We plot the results in Figg. 5.3 and 5.4 (top), correspondingly separately to nearest-neighbour ($J \neq 0$ and $\alpha = 0$) and long-range ($J = 0$ and $\alpha \neq 0$) perturbations. Each panel corresponds to a fixed choice of $J$ and $\alpha$, and varying $\psi$ and $\mathcal{T}$.

[1] As discussed also in Section 2.3, the magnetization length can descrease when spin-waves are excited. Here we are working with a "normalized" magnetization, whose length is 1, in order to get a more clear comparison with the mean-field results.

The plotted results validate the robustness of the DFTC phases even beyond the fully-connected limit, for the range of parameters we considered. Specifically, the DFTC regions at low $\mathcal{T}$ are stable with respect to perturbations, while the isolated DFTC island around $\psi = \pi/4$ and $\mathcal{T} = 6$ shrinks and eventually vanishes with increasing the perturbation couplings. The stability of the phase-diagram with respect to spin-wave fluctuations can be understood also from Figg. 5.3 and 5.4 (bottom), where we show the time-average

$$\bar{\epsilon} = \lim_{t\to\infty} \frac{1}{t} \int_0^t \epsilon(\tau) d\tau \tag{5.28}$$

of the spin-wave density from Eq. (B.18). In the low-$\mathcal{T}$ sector of the phase diagram, where the quasi-periodic phase and the DFTC islands persist, $\bar{\epsilon}$ remains small. Conversely, we have $\bar{\epsilon} > 1$ in the chaotic region, where the system is expected to eventually thermalize [50] due the spin-wave excitation. This analysis extends the findings of Ref. [220], where the non-equilibrium spin-wave theory (NEQSWT) was employed to explore the stability of DFTC phases specifically at $\mathcal{T} = 1$.

## 5.6 Summary and perspectives

In this chapter we introduced a new order parameter $\zeta$, capable to detect DFTC phases in long-range systems, irrespective of their order. The pressing need for this study was generated by the recent depiction of high order DFTC phases [220, 223]. Our order parameter exploits the connection between DFTC and Poincaré-Birkhoff theorem [15, 16], whose quantum counterpart has also been explored in Ref. [228]. Choosing as a paradigmatic example the kicked LMG model, we are able to draw a new phase diagram. While our picture is exact in the mean-field limit ($\alpha = J = 0$), we verified that it is robust against the inclusion of fluctuations due either to power-law interaction or to perturbation represented as a nearest-neighbour interacting term.

Our newly introduced observable $\zeta$ is easily accessible in the experiments, so that our predictions on the phase diagram may be tested e.g. in NMR experiments on driven, ordered systems [203]. Our characterization of the higher-order, stable DFTC phases could thus pave the way for a series of advancement in the field of quantum technologies.

# Chapter 6

# Outlook

In this final section, we outline the key questions that remain unresolved in this thesis. The first one concerns the connection between the generation of chaos and the properties of the underlying energy landscape in Hamiltonian systems, a topic explored in Chapters 2 and 3. In Chapter 3, we investigated the chaotic behavior, quantified by the classical Lyapunov exponent, in a specific $p$-spin spherical model (PSM). We observed a correlation between maximal chaos and the presence of a maximal number of unstable stationary configurations on the corresponding energy shell. Our observation was empirical and we did not quantitatively connect the Lyapunov exponent to the number of stationary points. A more systematic investigation connecting chaos to the underlying energy landscape could involve investigating the curvature of the microcanonical manifold. Previous studies [183, 229] have shown that a reasonable estimation for the Lyapunov exponent can be derived from the average curvature, when the latter is negative, or from its fluctuations. From a technical point of view, adopting this approach in the spherical model is challenging due to the presence of the spherical constraint, yet extending it to other models with intricate energy manifold complexity remains a possibility. The second question, stemming from the first one, pertains to the possibility of extending the techniques from Refs. [183, 229] to quantum systems. Understanding how chaos connects to the manifold of the dynamics would be crucial, offering physical insight into the rigorous bound proposed in Ref. [101]. This bound is indeed saturated in models which are connected to the spreading of information in black holes [98, 135]. A third possible future direction for this thesis works arises from Chapter 4. Therein, we have demonstrated that an ergodic many-body system, with an unbounded energy spectrum and subject to a smooth periodic force, exhibits signatures of finite temperature thermalization at long times. This behavior contrasts sharply with the infinite temperature thermalization observed in spin systems and kicked rotors. However, the nature of the thermal ensemble we observed remains uncertain. Establishing whether it is a stationary state or merely a transient phenomenon presents intriguing puzzles for further investigation. In both cases, the physical origin of the different late dynamics, retrieved in the Floquet systems we studied and in the ones usually investigated in literature, remains elusive to us. Lastly, in Section 3.5, we computed the fidelity susceptibility $\chi$ for the classical PSM. Our findings indicate that $\chi$ can detect ergodicity breaking even in a classical dynamics. It would be worthy to test conjecture against a broader range of classical systems.

# Acknowledgements

In concluding this thesis work, I would like to express my gratitude to A. Silva, for supervising this thesis work in the last three years. I also acknowledge my collaborators, who contributed to develop some of the ideas at the core of this thesis work: L. F. Cugliandolo, N. Defenu, G. Giachetti, A. Polkovnikov, A. Solfanelli. A special acknowledgement goes to M. Schirò and Collège de France, who hosted me for a scientific collaboration for five months within the last year.

# Appendix

# Appendix A

# Details on the $p$-spin model without disorder

## A.1 The period of classical orbits and its relation with dynamical singularities

In this appendix we derive a closed formula for the period $T_{cl}(g)$ of the classical orbits discussed in Section 2.2.1 of the main text. In particular, we show that $T_{cl}(g)$ diverges logarithmically when approaching the transition point $g = g_{dyn}$ both from above and below and discuss how show that such a singularity is retrieved also in $\overline{\mathcal{S}^x}(g)$.

To compute $T_{cl}(g)$ do so, we first perform the change of variables:

$$\mathcal{S}^x = Q, \qquad \mathcal{S}^y = \sqrt{1-Q^2}\sin(P), \qquad \mathcal{S}^z = \sqrt{1-Q^2}\cos(P) \tag{A.1}$$

where $Q \in [-1,1]$ and $P \in [0,\pi]$. By doing so, it can be shown [47, 61] that the dynamics described by the equations (2.16) is an Hamilton dynamics induced by the effective Hamiltonian

$$\mathcal{H}_{cl}(Q,P) = -\lambda Q^P - g\sqrt{1-Q^2}\cos(P) \tag{A.2}$$

The first of the Hamilton equations is

$$\partial_t Q = g\sqrt{1-Q^2}\sin(P) \tag{A.3}$$

Plugging Eq. (A.3) into the expression (A.2), one straightforwardly obtains the following expression:

$$(\mathcal{H}_{cl}(Q,P) + \lambda Q^p)^2 = g^2(1-Q^2) - (\partial_t Q)^2 \tag{A.4}$$

Then, fixing the conserved energy as $\mathcal{H}_{cl}(Q(0),P(0)) = E_0$, we can solve the dynamics by separation of variables to obtain

$$t = \int_{\min(Q(0),Q(t))}^{\max(Q(0),Q(t))} \frac{dx}{\sqrt{g^2(1-x^2) - (E_0 + \lambda x^p)^2}} \tag{A.5}$$

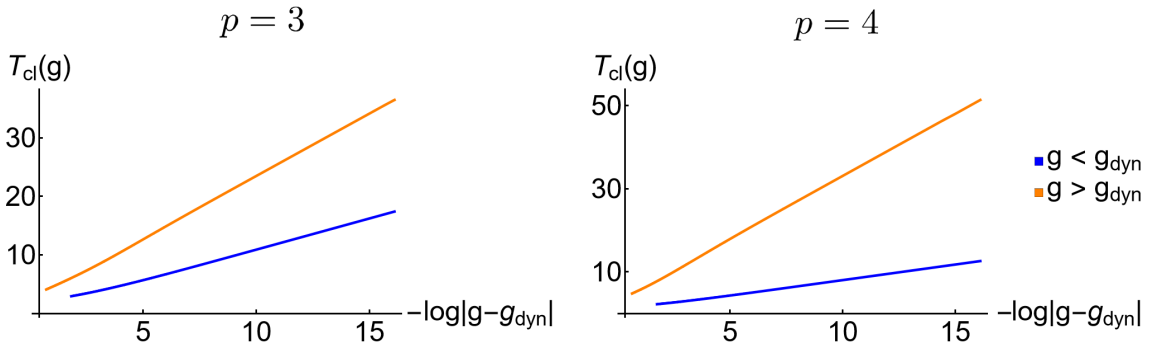


Figure A.1: Plot of the period $T_{cl}(g)$ of the classical trajectories originating from the dynamics discussed in Section 2.2.1 of the main text, respectively for $p = 3$ (left) and $p = 4$ (right). $T_{cl}(g)$ is compared against $\log|g - g_{dyn}|$, both for $g < g_{dyn}$ (blue) and $g > g_{dyn}$ (orange). We pose $\lambda = 1$, like in the main text.

This formula gives us the period of the classical orbits studied in the main text, if we fix the initial condition $\vec{S(0)} = \hat{\mathbf{x}}$ (i.e. $Q(0) = 1$, $P(0) = 0$ and $E_0 = -\lambda$), arriving at

$$T_{cl}(g) = 2\int_{q_1}^{1} \frac{dx}{\sqrt{g^2(1-x^2) - (\lambda x^p - \lambda)^2}} \tag{A.6}$$

where $q_1$ is the turning point of the orbit, obtained as the solution of the equation $\mathcal{H}_{cl}(Q, P = 0) = \mathcal{H}_{cl}(Q = 1, P = 0) = -\lambda$ (for $Q \neq 1$). We compute $T_{cl}(g)$ numerically from Eq. (A.6), for several values of $g$ and for the paradigmatic cases of $p = 3$ and $p = 4$. The result, shown in Fig. A.1, is that for $g \to g^{\pm}_{dyn}$ the period diverges as $T_{cl} \sim \log|g - g_{dyn}|^{-1}$, with a prefactor which is different above and below $g_{dyn}$.

The divergence of $T_{cl}(g)$ at $g_{dyn}$ is connected to change of topology of the underlying trajectories, being confined in a single ferromagnetic well for $g < g_{dyn}$ and exploring the whole landscape for $g > g_{dyn}$. In particular, at $g = g_{dyn}$ the trajectory is a *separatrix*, that is a singular, non-periodic orbit where any dynamics converges, for late times, to the nearest local maximum $\mathcal{S}^x_c$, separating the well where the motion takes place from the others. For any value of $p$, this implies that $\overline{\mathcal{S}^x}(g_{dyn}) = \mathcal{S}^x_c$. $T_{cl}(g)$ can be also connected to the type of singularity displayed by $\overline{\mathcal{S}^x}$, when approaching the transition point from below: as $g \to g^{-}_{dyn}$, the orbits evolving into the righmost ferromagnetic well develop a plateau of diverging length near $\mathcal{S}^x_c$ (see Fig. 2.2-(c) and (f) of the main text), so that $\overline{\mathcal{S}^x}$ can be qualitatively estimated as

$$\overline{\mathcal{S}^x}(g) = \frac{1}{T_{cl}(g)}\int_0^{T_{cl}(g)} dt\mathcal{S}^x(t) = \mathcal{S}^x_c + \frac{1}{T_{cl}(g)}\int_0^{T_{cl}(g)} dt\big(\mathcal{S}^x(t) - \mathcal{S}^x_c\big) \simeq \mathcal{S}^x_c + \frac{c}{T_{cl}(g)}, \tag{A.7}$$

if we assume that that the integral $\int_0^{T_{cl}(g)} dt\big(\mathcal{S}^x(t) - \mathcal{S}^x_c\big)$ is bounded and converges to a positive constant $c > 0$ at the transition point. The estimate in Eq. (A.7) implies that $\overline{\mathcal{S}^x} - \mathcal{S}^x_c \propto 1/\log(g_{dyn} - g)^{-1}$ approaching the transition from below: such a log-singularity is quantitatively confirmed by the results shown in Fig. A.2, obtained by

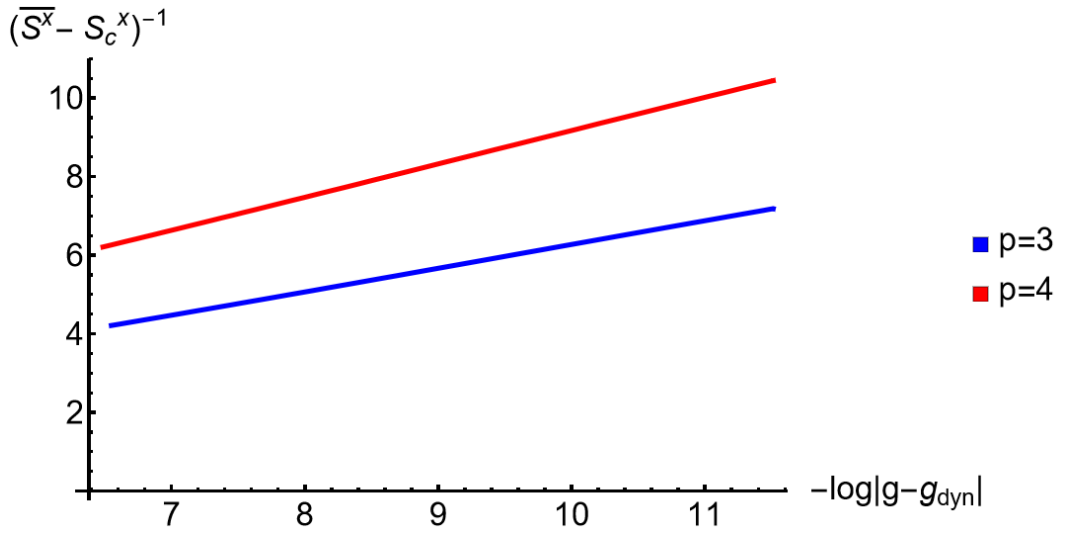


Figure A.2: Plot of the singularity of the time-average magnetization $\overline{\mathcal{S}^x}$, for the trajectories originating from the dynamics discussed in Section 2.2.1 of the main text, respectively for $p = 3$ (blue) and $p = 4$ (red). $\overline{\mathcal{S}^x}$ is plotted as a function of $g$ in the dynamical ferromagnetic phase, where $g < g_{dyn}$, and $\mathcal{S}_c^x$ is defined as an unstable stationary point of the potential in Eq. (2.17) of the main text at $g_{dyn}$.

computing $\overline{\mathcal{S}^x}$ numerically, as done also in Section 2.2.2, and $\mathcal{S}_c^x$ from the Eqs. (2.20) and (2.19).

While the singularities in the time-average magnetization $\overline{\mathcal{S}^x}$ are intimately connected to the one of the periods, its continuity is determined by the topology of the effective potential, as discussed in the main text, thus by the value of $p$. In particular:

- For $p \geq 3$ odd, the dynamics for $g \to g_{dyn}^+$ $\overline{\mathcal{S}^x}$ develops a plateau at the *only* local maximum of the landscape $\mathcal{S}_c^x$ (see Fig. 2.2-(c) of the main text), so that $\lim_{g \to g_{dyn}^+} \overline{\mathcal{S}^x} = \mathcal{S}_c^x$ and the transition is continuous in this case.

- For $p \geq 4$ even, $\overline{\mathcal{S}^x} = 0$ for any $g > g_{dyn}$, due to the symmetry of the orbits, so that $\overline{\mathcal{S}^x}$ is discontinuous at the transition. In particular, the plot in Fig. 2.2-(f) of the main text shows that the magnetization spends an equal, diverging amount of time near close to each of the two local maxima at $\mathcal{S}_c^x$ and $-\mathcal{S}_c^x$. At the origin of the discontinuity lies thus the non-symmetric role played by the opposite ferromagnetic maximum at $-\mathcal{S}_c^x$, respectively above and below the transition point.

## A.2 Details on the first-order transition line

In this appendix, examine in greater detail the discontinuity line $J = J_{dyn}(g)$, appearing in Fig. 2.4 (left) and Fig. 2.5 (right) of the main text, analyzing the cases of $p = 3$ and $p = 4$ separately.

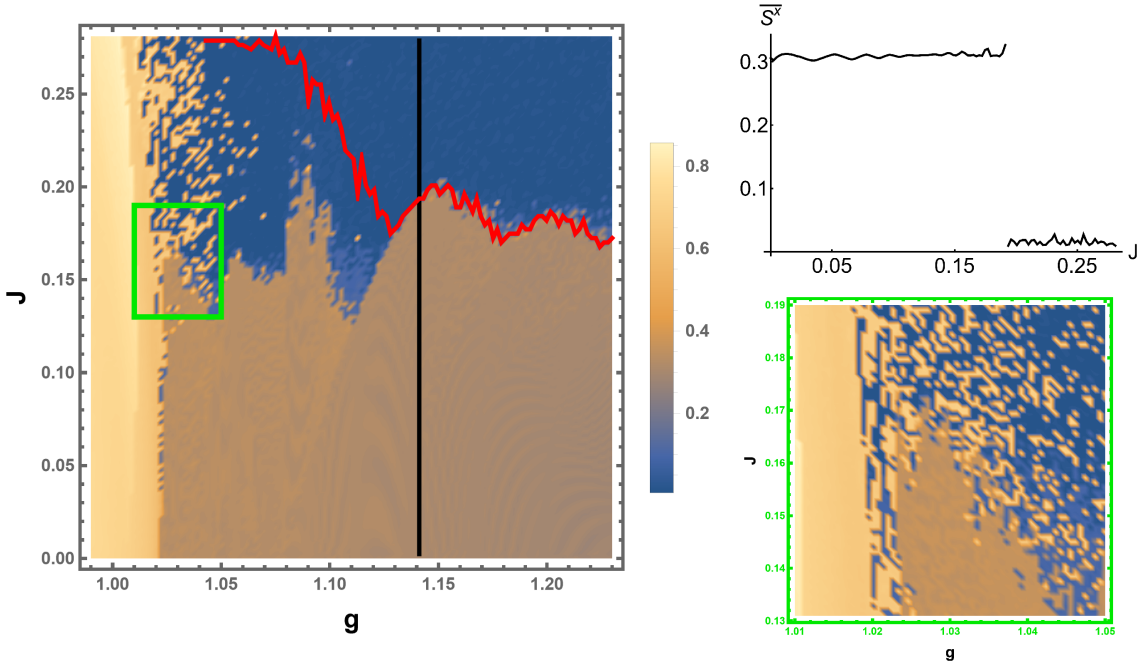


Figure A.3: Non-equilibrium phase diagram for the $p$-spin model in Eq. (2.15), for $p = 3$. **(Left)** Over the same phase diagram shown in Fig. 2.4 (left) of the main text, we plot the threshold line (red), above which $\bar{\epsilon} > \epsilon_{sp}$ (see details in Appendix A.2). The black vertical line and the green box indicate the values of $g$ and $J$ investigated in the plots on the right. **(Top-right)** Plot of the time-averaged magnetization $\overline{\mathcal{S}^x}$, as function of $J$ and at fixed $g \simeq 1.142$ (black line on the phase diagram on the left). $\overline{\mathcal{S}^x}$ is discontinuous around $J \simeq 0.194$. **(Bottom-right)** Inset from the phase diagram on the left (in the green box), around the chaotic region where the second-order and first-order transition line merge.

For $p = 3$, the transition line $J_{dyn}(g)$ emerges clearly fixing a sufficiently large value of $g$: the plot in Fig. A.3 (top-right) shows that the time-average magnetization $\overline{\mathcal{S}^x}$ has a discontinuity in $J$, though not being either completely smooth $J$ above and below the discontinuity point, because of the noise induced by the spin-wave emission. In this regime, it is possible to make a semi-analytical estimation of the point $J_{dyn}(g)$ where the transition happens, as discussed in the following. First we notice that, because of the squeezing of the potential, discussed in Section 2.3.3 and due to the spin-wave excitation, the dynamics is driven by an effective transverse field

$$g_\epsilon = \frac{g}{(1-\epsilon)^{p-1}} \tag{A.8}$$

which depends on time through $\epsilon$. Thus, for any fixed $g$ it exists a threshold value $\epsilon_{sp}$, set by the equation[1].

$$\frac{g}{(1-\epsilon)^{p-1}} = g_{sp} \tag{A.9}$$

[1]Here, $g_{sp}$ is $p$-dependent the value of the transverse field beyond which the effective potential displays a single paramagnetic well, as discussed also in Section 2.2.1

such that whenever $\epsilon > \epsilon_{sp}$, the squeezed potential in Eq. (2.35) displays a single paramagnetic well. An intuitive, *sufficient* condition for the localization of the magnetization in the paramagnetic well can be set by the statement that $\epsilon(t)$ is asymptotically greater $\epsilon_{sp}$ for large times, that is

$$\overline{\epsilon} = \lim_{T\to\infty} \frac{1}{T} \int_0^T \epsilon(t) > \epsilon_{sp} \tag{A.10}$$

This condition implies that, for large times, the squeezed potential from Eq. (2.35) displays a single, paramagnetic well, where the magnetization is by definition localized. The plots in Fig. A.3 (left) show that, fixing a sufficiently large $g$, the values of $J$ where $\overline{\epsilon}$ overcomes the threshold $\epsilon_{sp}$ matches the transition point $J_{dyn}(g)$: this provides a semi-analytical argument for the prediction of $J_{dyn}(g)$ at large $g$, as the threshold $\epsilon_{sp}$ can be predicted analytically, but there is no explicit formula relating $J_{dyn}(g)$ to $\overline{\epsilon}$. Our argument fails for smaller $g$, where the localization mechanism becomes more subtle (as discussed in Section 2.3.3 the main text) and the first-order transition line is smeared into a chaotic crossover close to the mean-field critical point $g_{dyn}$. A similar fate happens to the second-order critical line, extending from the point $(g, J) = (g_{dyn}, 0)$, to finite values of $J$, so that the chaotic crossover prevents the possibility of a precise estimation of the tricritical point where the two lines meet. However, we can roughly identify the transition point as the center of the finite-width area where the two transition lines merge completely with the chaotic region: in the inset in Fig. A.3 (bottom-right), we show that this happens approximately around $(g, J) \simeq (1.026, 0.17)$.
For $p = 4$, the results in Fig. A.4 (right) show a discontinuous transition driven by $J$, this time detected by the time-averaged fluctuations $\overline{(\delta\mathcal{S}^x)^2}$, even though the semi-analytical estimation of $J_{dyn}(g)$ fails in this case. Moreover, here both the mean-field dynamical transition, driven by $g$, as well as the one driven by $J$, are of the first-order, so that we do not retrieve the tricritical behaviour discussed for $p = 3$.

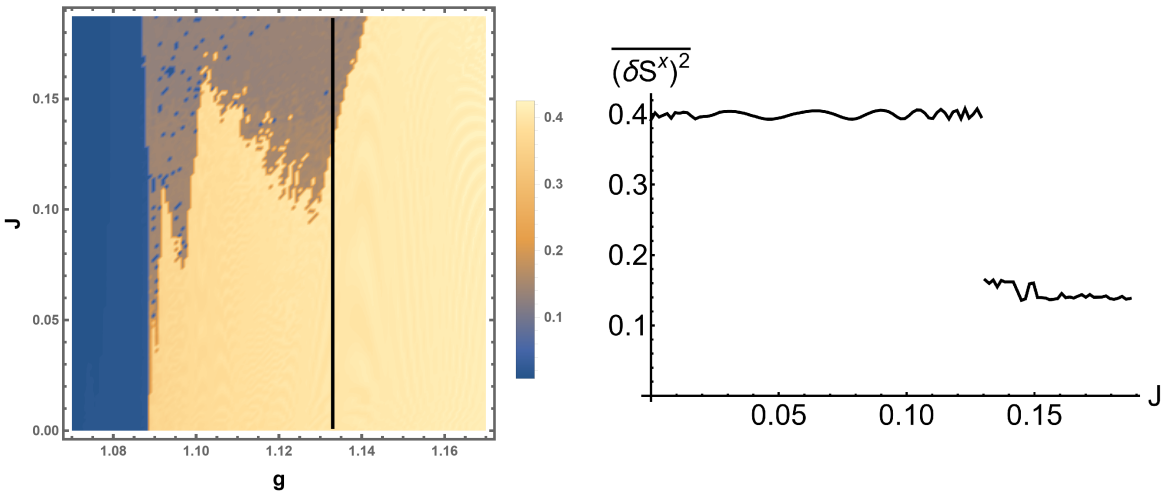


Figure A.4: Non-equilibrium phase diagram for the $p$-spin model in Eq. (2.15), for $p = 4$. **(Left)** Same phase diagram shown in Fig. 2.5 (left). The black vertical line and the green box indicate the values of $g$ and $J$ investigated in the plots on the right. **(Right)** Plot of the time-averaged fluctuations $\overline{(\delta\mathcal{S}^x)^2}$, as function of $J$ and at fixed $g \simeq 1.133$ (black line on the phase diagram on the left). $\overline{(\delta\mathcal{S}^x)^2}$ is discontinuous around $J \simeq 0.131$.

# Appendix B

# Review of the non-equilibrium spin-wave theory

In this appendix, we review the time-dependent spin-wave analysis, following Ref. [49]. This is implemented essentially in three steps:

1. first, we express the dynamical evolution in a rotating reference frame $\mathcal{R}$, defined in such a way that the magnetization is always aligned with the **Z**-axis;

2. performing an Holstein-Primakoff in $\mathcal{R}$, we introduce the *spin-waves*, defined as canonical coordinates representing the spatial fluctuation of the collective spin on various length scales;

3. we derive a set of coupled equations describing the evolution of the collective spin, which is obtained requiring that that the frame $\mathcal{R}$ is aligned with the collective spin at any time, and of the spin-wave correlators, which act as a quantum feedback on the former.

## B.1 Rotating frame of reference coordinates

We consider a generic fully-connected $p$-spin Hamiltonian, with an additional short-ranged interaction in the form of:

$$\hat{H} = -\frac{\lambda}{N^{p-1}}(\tilde{\sigma}_0^x)^p - g\tilde{\sigma}_0^z - \frac{1}{N}\sum_{k\neq 0} \tilde{J}_k \; \tilde{\sigma}_k^x \tilde{\sigma}_{-k}^x, \tag{B.1}$$

We assume that our systems lives on a one-dimensional lattice with periodic boundary conditions, although our calculations are straightforwardly generalized to any dimensionality. The Fourier modes are defined as $\tilde{\sigma}_k^\alpha = \sum_{j=1}^N e^{-ikj}\hat{\sigma}_j^\alpha$ (with $\hat{\sigma}_j^\alpha = \hat{s}_j^\alpha/s$ being the rescaled spin operator on the lattice site $j$) and $k = 2\pi n/N$ for $n = 0, \dots, N-1$, $N$ being the system size. The Hamiltonian can be also split into a mean-field term $\hat{H}_0 = \lambda(\tilde{\sigma}_0^x)^p/N^{p-1} - g\tilde{\sigma}_0^z$, depending on the collective spin only, and a short-range perturbation $\hat{U} = -\sum_{k\neq 0} \tilde{J}_k \; \tilde{\sigma}_k^x \tilde{\sigma}_{-k}^x/N$, as done in the main text. The reference frame $\mathcal{R}$ is identified by the time-dependent Cartesian vector basis $\{\mathbf{X}(t), \mathbf{Y}(t), \mathbf{Z}(t)\}$, whose components in the original frame $\{\mathbf{x}, \mathbf{y}, \mathbf{z}\}$ read as

$$\mathbf{X} = \begin{pmatrix} \cos\theta(t)\cos\phi(t) \\ \cos\theta(t)\sin\phi(t) \\ -\sin\theta(t) \end{pmatrix} ; \qquad \mathbf{Y} = \begin{pmatrix} -\sin\phi(t) \\ \cos\phi(t) \\ 0 \end{pmatrix} ; \qquad \mathbf{Z} = \begin{pmatrix} \sin\theta\cos\phi(t) \\ \sin\theta\sin\phi(t) \\ \cos\theta(t) \end{pmatrix}$$

and where the spherical angles $\theta(t)$ and $\phi(t)$ are defined so that the average magnetization $\vec{\mathcal{S}}(t) = \langle \sum_j \vec{\sigma}_j(t) \rangle / N$ is always aligned with $\mathbf{Z}(t)$. This change of frame is implemented on the spin Hilbert space by the time-dependent unitary rotation

$$V\big(\theta(t),\phi(t)\big) = \exp\left(-is\phi(t)\textstyle\sum_i \sigma_i^z\right)\exp\left(-is\theta(t)\textstyle\sum_i \sigma_i^y\right)$$

so that the spin operators transform accordingly :

$$V\hat{\sigma}_j^x V^\dagger = \mathbf{X}\cdot\vec{\sigma}_j \equiv \hat{\sigma}_j^X, \qquad V\hat{\sigma}_j^y V^\dagger = \mathbf{Y}\cdot\vec{\sigma}_j \equiv \hat{\sigma}_j^Y, \qquad V\hat{\sigma}_j^z V^\dagger = \mathbf{Z}\cdot\vec{\sigma}_j \equiv \hat{\sigma}_j^Z, \quad \text{(B.2)}$$

In this new frame, the Heisenberg equation of motion can be written as

$$\frac{d}{dt}\hat{\sigma}_j^\alpha = -i[\hat{\sigma}_j^\alpha, \tilde{H}] \quad \text{(B.3)}$$

where the modified Hamiltonian

$$\tilde{H} = H + iV\dot{V}^\dagger \quad \text{(B.4)}$$

includes an additional term $iV\dot{V}^\dagger = -s\vec{\omega}(t)\cdot\sum_j \vec{\sigma}_j$, where $\vec{\omega}(t) = (-\sin\theta\dot{\phi}, -\dot{\theta}, \cos\theta\dot{\phi})$, playing the same role of apparent forces in classical mechanics. In the rotating frame $\mathcal{R}$, $\tilde{H}$ has the following form:

$$\begin{aligned}\frac{\widetilde{H}}{N} = &-g\left[(\mathbf{X}\cdot\mathbf{z})\,\frac{\tilde{\sigma}_0^X}{N} + (\mathbf{Y}\cdot\mathbf{z})\,\frac{\tilde{\sigma}_0^Y}{N} + (\mathbf{Z}\cdot\mathbf{z})\,\frac{\tilde{\sigma}_0^Z}{N}\right] - \lambda\left[(\mathbf{X}\cdot\mathbf{x})\,\frac{\tilde{\sigma}_0^X}{N} + (\mathbf{Y}\cdot\mathbf{x})\,\frac{\tilde{\sigma}_0^Y}{N} + (\mathbf{Z}\cdot\mathbf{x})\,\frac{\tilde{\sigma}_0^Z}{N}\right]^p \\ &- \sum_{k\neq 0}\tilde{J}_k\left[(\mathbf{X}\cdot\mathbf{x})\,\frac{\tilde{\sigma}_k^X}{N} + (\mathbf{Y}\cdot\mathbf{x})\,\frac{\tilde{\sigma}_k^Y}{N} + (\mathbf{Z}\cdot\mathbf{x})\,\frac{\tilde{\sigma}_k^Z}{N}\right]\left[(\mathbf{X}\cdot\mathbf{x})\,\frac{\tilde{\sigma}_{-k}^X}{N} + (\mathbf{Y}\cdot\mathbf{x})\,\frac{\tilde{\sigma}_{-k}^Y}{N} + (\mathbf{Z}\cdot\mathbf{x})\,\frac{\tilde{\sigma}_{-k}^Z}{N}\right] \\ &+ \sin\theta\; s\dot{\phi}\,\frac{\tilde{\sigma}_0^X}{N} - s\dot{\theta}\,\frac{\tilde{\sigma}_0^Y}{N} - \cos\theta\; s\dot{\phi}\,\frac{\tilde{\sigma}_0^Z}{N},\end{aligned} \quad \text{(B.5)}$$

Once the equations of motion are formally written in the new frame, $\theta(t)$ and $\phi(t)$ are obtained self-consistently by imposing that

$$\begin{cases} \langle\tilde{\sigma}_0^X(t)\rangle = 0 \\ \langle\tilde{\sigma}_0^Y(t)\rangle = 0 \end{cases} \quad \text{(B.6)}$$

## B.2 Holstein-Primakoff transformation

The main idea at the basis of time-dependent spin-wave theory is that in the new frame, as long as the spatial fluctuations induced by the short-range coupling $J$ are weak enough, these act as a small perturbation on top of a “classical" average collective spin.

In this case, we can rewrite the spin operators via the well known Holstein-Primakoff transformation [71]

$$\begin{cases} \hat{\sigma}_j^X \sim q_j/\sqrt{s} + O(1/s^{3/2}) \\ \hat{\sigma}_j^Y \sim p_j/\sqrt{s} + O(1/s^{3/2}) \\ \hat{\sigma}_j^Z = 1 - \frac{q_j^2+p_j^2-1}{2s} \end{cases} \tag{B.7}$$

expanded in powers of $1/\sqrt{s}$ and truncated to the leading order. In terms of the Fourier space variables $\tilde{q}_k = \sum_r e^{-ikr} q_r/\sqrt{N}$ and $\tilde{p}_k = \sum_r e^{-ikr} p_r/\sqrt{N}$, can also be expressed as [71]:

$$\begin{cases} \frac{\tilde{\sigma}_k^X}{N} \sim \tilde{q}_k/\sqrt{Ns} + O(1/s^{3/2}) \\ \frac{\tilde{\sigma}_k^Y}{N} \sim \tilde{p}_k/\sqrt{Ns} + O(1/s^{3/2}) \\ \frac{\tilde{\sigma}_k^Z}{N} = 1 - \frac{1}{2Ns}\sum_{k'}(\tilde{q}_{k'}\tilde{q}_{k-k'} + \tilde{p}_{k'}\tilde{p}_{k-k'} - \delta_{k,0}) \end{cases} \tag{B.8}$$

This approximation is exact both in the limit of large spin $s \to \infty$, or, as stated before, when the spin-wave degree of excitation is kept small throughout the dynamics, in a sense which is made clear below.
The whole sense of our approximation is that we are expanding on-site fluctuations of the spin along the **Z**-axis in terms of harmonic excitations, defined in terms of ladder operators $\hat{a}_j = (q_j + ip_j)/\sqrt{2}$ and his conjugate $\hat{a}_i^\dagger$: their Fourier Transform $\tilde{a}_k = \sum_j e^{-ikj}\hat{a}_j/\sqrt{N}$ represent the spin-wave excitations which destroy coherence in the system, causing a depletion of the magnetization length, which can be rewritten as $|\langle\tilde{\sigma}_0^Z(t)\rangle/N| = 1 - \epsilon(t)$, where

$$\epsilon(t) \equiv \frac{1}{Ns}\sum_{k\neq 0}\langle\tilde{a}_k^\dagger\tilde{a}_k(t)\rangle = \frac{1}{Ns}\sum_{k\neq 0}\left\langle\frac{\tilde{q}_k(t)\tilde{q}_{-k}(t) + \tilde{p}_k(t)\tilde{p}_{-k}(t) - 1}{2}\right\rangle \tag{B.9}$$

is the spin-wave density. Thus, the the time-dependent spin-wave theory is valid as long as $\epsilon(t) \ll 1$.

## B.3 Equations of motion for weak spin-wave excitation

As long as the spin-wave excitation density $\epsilon(t)$ is small, it is reasonable to assume that the dynamics is dominated by terms of lowest nontrivial order in the operators $\{(\tilde{q}_k, \tilde{p}_k)\}$ (from Eq. (B.8)), that is by a Gaussian approximation, in our case. Exactly as in the case of Ref. [49], an expansion of the Hamiltonian in Eq. (B.5), this amounts

to keeping the terms

$$\begin{aligned}\hat{U}_1 =&\frac{\tilde{q}_0}{\sqrt{Ns}}\Big\{s\sin\theta\dot{\phi} - p\lambda(\mathbf{Z}\cdot\mathbf{x})^{p-1}(\mathbf{X}\cdot\mathbf{x})\Big(1-(p-1)\frac{\hat{n}_{SW}}{Ns}\Big) - g(\mathbf{X}\cdot\mathbf{z})+\\ &+\frac{2(\mathbf{Z}\cdot\mathbf{x})}{Ns}\sum_{k\neq 0}\tilde{J}_k\big[(\mathbf{X}\cdot\mathbf{x})\tilde{q}_k\tilde{q}_{-k}+(\mathbf{Y}\cdot\mathbf{x})\frac{\tilde{q}_k\tilde{p}_{-k}+\tilde{p}_k\tilde{q}_{-k}}{2}\big]\Big\}+\\ &+\frac{\tilde{p}_0}{\sqrt{Ns}}\Big\{-s\dot{\theta} - p\lambda(\mathbf{Z}\cdot\mathbf{x})^{p-1}(\mathbf{Y}\cdot\mathbf{x})\Big(1-(p-1)\frac{\hat{n}_{SW}}{Ns}\Big) - g(\mathbf{Y}\cdot\mathbf{z})+\\ &+\frac{2(\mathbf{Z}\cdot\mathbf{x})}{Ns}\sum_{k\neq 0}\tilde{J}_k\big[(\mathbf{Y}\cdot\mathbf{x})\tilde{p}_k\tilde{p}_{-k}+(\mathbf{X}\cdot\mathbf{x})\frac{\tilde{q}_k\tilde{p}_{-k}+\tilde{p}_k\tilde{q}_{-k}}{2}\big]\Big\}\end{aligned} \tag{B.10}$$

$$\hat{U}_2^{(0)} = (p\lambda(\mathbf{Z}\cdot\mathbf{x})^p + g(\mathbf{Z}\cdot\mathbf{z}) + s\cos\theta\dot{\phi})\frac{1}{Ns}\sum_{k\neq 0}\hat{n}_k \tag{B.11}$$

$$\hat{U}_2 = -\frac{1}{Ns}\sum_{k\neq 0}\tilde{J}_k\{(\mathbf{X}\cdot\mathbf{x})^2\tilde{q}_k\tilde{q}_{-k}+(\mathbf{Y}\cdot\mathbf{x})^2\tilde{p}_k\tilde{p}_{-k}+2(\mathbf{X}\cdot\mathbf{x})(\mathbf{Y}\cdot\mathbf{x})\frac{\tilde{q}_k\tilde{p}_{-k}+\tilde{p}_k\tilde{q}_{-k}}{2}\} \tag{B.12}$$

In particular, the terms $\hat{U}_2^{(0)}$ and $\hat{U}_2$ represent the quadratic part from the expansion of the mean-field term $\hat{H}_0$ and the short-range perturbation $\hat{U}$, respectively. Within such approximation, the dynamics of the time-dependent frame $\mathcal{R}$ is determined imposing the conditions (B.6), leading to

$$\begin{cases} s\dot{\phi} =p\lambda(\sin\theta)^{p-2}(\cos\phi)^p\cos\theta\big\{1-(p-1)\epsilon(t)\big\} - g+\\ \qquad -2J\delta^{qq}(t)\cos\theta\cos^2\phi + 2J\delta^{qp}(t)\sin\phi\cos\phi\\ s\dot{\theta} =p\lambda(\sin\theta\cos\phi)^{p-1}\sin\phi\{1-(p-1)\epsilon(t)\} - 2J\delta^{pp}(t)\sin\theta\sin\phi\cos\phi\\ \qquad +2J\delta^{qp}(t)\sin\theta\cos\theta\cos^2\phi\end{cases} \tag{B.13}$$

with the quantum feedback being $J\delta^{\alpha\beta}(t)\equiv\sum_{k\neq 0},\Delta_k^{\alpha\beta}\tilde{J}_k/(Ns)$ for $\alpha,\beta\in\{p,q\}$, as stated in the main text (the correlators $\Delta_k^{\alpha\beta}$ are defined also below). Here $J$ is a dimensionful energy scale that we factor out of the quantum feedback.
We see that, within time-dependent spin-wave theory, the motion of the collective spin is coupled to the one of the correlation functions

$$\begin{aligned}\Delta_k^{qq}(t) =&\langle\tilde{q}_{-k}(t)\tilde{q}_k(t)\rangle, \qquad \Delta_k^{qp}(t) = \langle\frac{\tilde{q}_{-k}(t)\tilde{p}_k(t)+\tilde{p}_{-k}(t)\tilde{q}_k(t)}{2}\rangle,\\ \Delta_k^{pp}(t) =&\langle\tilde{p}_{-k}(t)\tilde{p}_k(t)\rangle\end{aligned} \tag{B.14}$$

defined for $k\neq 0$, where all the averages are performed with respect to the initial state. The evolution of the variables $\{\Delta_k^{\alpha\beta}(t)\}$ is straightfowardly determined by the Heisenberg equations of motion for the canonical variables $\big(\tilde{q}_k,\tilde{p}_k\big)$:

$$\begin{cases} s\dfrac{d\tilde{q}_k}{dt} = \big(p\lambda(\sin\theta)^{p-2}(\cos\phi)^p - 2\tilde{J}_k\sin^2\phi\big)\ \tilde{p}_k + 2\tilde{J}_k\cos\theta\sin\phi\cos\phi\ \tilde{q}_k\\ s\dfrac{d\tilde{p}_k}{dt} = -\big(\lambda(\sin\theta)^{p-2}(\cos\phi)^p - 2\tilde{J}_k\cos^2\phi\cos^2\theta\big)\tilde{q}_k - \big(2\tilde{J}_k\cos\theta\sin\phi\cos\phi\big)\ \tilde{p}_k\end{cases} \tag{B.15}$$

and reads as

$$\begin{cases} s\dfrac{d}{dt}\Delta_k^{qq} = (4\tilde{J}_k \cos\theta \sin\phi \cos\phi)\Delta_k^{qq} + \\ \qquad\qquad + \{2p\lambda(\sin\theta)^{p-2}(\cos\phi)^p - 4\tilde{J}_k \sin^2\phi\}\Delta_k^{qp} \\ s\dfrac{d}{dt}\Delta_k^{qp} = -\{p\lambda(\sin\theta)^{p-2}(\cos\phi)^p - 2\tilde{J}_k \cos^2\phi\cos^2\theta\}\Delta_k^{qq} \\ \qquad\qquad + \{p\lambda(\sin\theta)^{p-2}(\cos\phi)^p - 2\tilde{J}_k \sin^2\phi\}\Delta_k^{pp} \\ s\dfrac{d}{dt}\Delta_k^{pp} = -\{2p\lambda(\sin\theta)^{p-2}(\cos\phi)^p - 4\tilde{J}_k \cos^2\phi\cos^2\theta\}\Delta_k^{qp} \\ \qquad\qquad - (4\tilde{J}_k \cos\theta \sin\phi \cos\phi)\Delta_k^{pp} \end{cases} \tag{B.16}$$

From equations Eq. (B.16), it is also possible to prove that, for any fixed momentum $k$, the time-evolution of the three spin-wave correlators is completely specified by two of them, as they have to satisfy the constraint

$$\left(\Delta_k^{qp}(t)\right)^2 = \Delta_k^{qq}(t)\Delta_k^{pp}(t) - \frac{1}{4}\,. \tag{B.17}$$

at any time $t$. The final result is that, within the framework of time-dependent spin-wave theory, the dynamics of the average magnetization $\vec{\mathcal{S}}(t)$ is coupled with that of the spin-wave correlation functions $\Delta^{\alpha\beta}(t)$, which also the determine the spin-wave density (see Eq. (B.9))

$$\epsilon(t) = \frac{1}{Ns}\sum_{k\neq 0}\frac{\Delta_k^{qq}(t) + \Delta_k^{pp}(t) - 1}{2}. \tag{B.18}$$

Integrating simultaneously the system of equations (B.13) and (B.16) and checking that $\epsilon(t) \ll 1$, one obtains the non-equilibrium dynamics of $\langle\vec{\mathcal{S}}(t)\rangle$, coupled to spin-wave fluctuations. The initial conditions are determined by the initial state $|\psi_0\rangle$. The case we studied is the one of a quench in the Hamiltonian (B.1), with pre-quenches values given by $g = g_0$ and $J = 0$, which correspond to

$$\begin{aligned} &\{\sin\theta(t=0)\}^{p-2}\cos\theta(t=0) = g_0/(\lambda p), \quad \phi(t=0) = 0, \\ &\Delta_k^{qq}(t=0) = \Delta_k^{pp}(t=0) = 1/2, \quad \text{and} \quad \Delta_k^{qp}(t=0) = 0, \end{aligned} \tag{B.19}$$

for every $k \neq 0$. This also imply that $\epsilon(t=0) = 0$, as the initial ground state $|\psi_0\rangle = |\rightarrow\cdots\rightarrow\rangle$ is perfectly coherent, with the spin on each lattice site point in the direction of the ferromagnetic minimum of $\hat{H}$. From the first and the second of Eq. (B.16), we can also get an evolution equation for $\epsilon(t)$, written as

$$\frac{d\epsilon(t)}{dt} = 4\frac{J}{s}\cos\theta\sin\phi\cos\phi\;\delta^{qq}(t) + 4\frac{J}{s}(\cos^2\theta\cos^2\phi - \sin^2\phi)\delta^{qp}(t). \tag{B.20}$$

The emission rate of spin waves, $d\epsilon/dt$, is determined by the coefficients $C_1(\theta,\phi) = \cos\theta\sin\phi$ and $C_2(\theta,\phi) = \cos^2\theta\cos^2\phi - \sin^2\phi$. These coefficients are derived from the quadratic approximation given in Eq. (B.12) of the short-term perturbation $\hat{U}$ in Eq. (2.25) and expressed in the rotating frame $\mathcal{R}$. Consequently, when altering the direction of the short-ranged interaction, we expect changes in $C_1(\theta,\phi)$ and $C_2(\theta,\phi)$.

It is crucial to note that these coefficients remain entirely independent of the fully-connected term $\hat{H}_0$ in the Hamiltonian.

In the fully-connected limit $\tilde{J}_k \to 0$ the evolution of the collective spin decouples from the fluctuations, and the equations (B.13) are identical to the ones predicted by the effective classical theory described in Ref. [47]. In this case, the spin-wave correlators still have nontrivial dynamics, but the spin-wave density is conserved and always vanishes.

# Appendix C

# Supplemental details about chaos in the $p$-spin spherical model

## C.1 The Truncated Wigner approximation for the p-spin spherical model

In this Appendix we show that, for the quantum spin glass defined in Eq. (3.19) of the main text in the Truncated Wigner Approximation (TWA) the dynamics is ruled by Eqs. (3.24) and that such approximation becomes exact in the classical limit. We begin by rewriting the Weyl symbol

$$O_W(\boldsymbol{\sigma},\boldsymbol{\Pi},t)=\int d\boldsymbol{\xi}\Big\langle \boldsymbol{\sigma}-\frac{\boldsymbol{\xi}}{2}\Big|\mathcal{O}(\hat{\boldsymbol{\sigma}}(t),\hat{\boldsymbol{\Pi}}(t))\Big|\boldsymbol{\sigma}+\frac{\boldsymbol{\xi}}{2}\Big\rangle\cdot\exp\left[i\frac{\boldsymbol{\Pi}\cdot\boldsymbol{\xi}}{\hbar}\right]\ , \tag{C.1}$$

for a generic operator

$$\mathcal{O}(\hat{\boldsymbol{\sigma}}(t),\hat{\boldsymbol{\Pi}}(t))=e^{i\hat{H}t}\mathcal{O}(\hat{\boldsymbol{\sigma}},\hat{\boldsymbol{\Pi}})e^{-i\hat{H}t}\ . \tag{C.2}$$

evolving in the Heisenberg picture. As shown in Ref. [140], the Eq. (C.1) can be represented in a path integral form, suitable to study both the $\hbar\to 0$ and the thermodynamic limit. Without reproducing the details of the calculation, here we just quote the final result:

$$\begin{aligned}O_W(\boldsymbol{\sigma},\boldsymbol{\Pi},t)=&\int D\boldsymbol{\sigma}\int D\boldsymbol{\Pi}\int D\boldsymbol{\xi}\int D\boldsymbol{\eta}\ O_W(\boldsymbol{\sigma}(t),\boldsymbol{\Pi}(t))\cdot\\ \cdot\exp\Big\{\frac{i}{\hbar}\int_0^t d\tau\Big[&\boldsymbol{\eta}(\tau)\cdot\frac{\partial\boldsymbol{\sigma}(\tau)}{\partial\tau}-\boldsymbol{\xi}(\tau)\cdot\frac{\partial\boldsymbol{\Pi}(\tau)}{\partial\tau}-\mathcal{H}_W\Big(\boldsymbol{\sigma}(\tau)+\frac{\boldsymbol{\xi}(\tau)}{2},\boldsymbol{\Pi}(\tau)+\frac{\boldsymbol{\eta}(\tau)}{2}\Big)\\ &+\mathcal{H}_W\Big(\boldsymbol{\sigma}(\tau)-\frac{\boldsymbol{\xi}(\tau)}{2},\boldsymbol{\Pi}(\tau)-\frac{\boldsymbol{\eta}(\tau)}{2}\Big)+z(\tau)\boldsymbol{\xi}\cdot\boldsymbol{\sigma}\Big]\Big\}\ ,\end{aligned} \tag{C.3}$$

with initial conditions $\boldsymbol{\sigma}(0)=\boldsymbol{\sigma}$, $\boldsymbol{\xi}(0)=\boldsymbol{\xi}$ and $\boldsymbol{\Pi}(0)=\boldsymbol{\Pi}$. The Weyl symbol of the Hamiltonian is defined as $\mathcal{H}_W\big(\boldsymbol{\sigma},\boldsymbol{\Pi}\big)=\boldsymbol{\Pi}^2/2M+V_J(\boldsymbol{\sigma})$, and we inserted a term proportional to the Lagrange multiplier $z(\tau)$ in the action, to enforce the spherical constraint (see also Ref. [86]).

It is straightforward to see that TWA is equivalent to a (classical) expansion of the action in the integrand of Eq. (C.3): indeed we obtain, at leading order, that

$$\begin{aligned} -\mathcal{H}_W\Big(\boldsymbol{\sigma}(\tau)+\frac{\boldsymbol{\xi}(\tau)}{2},\boldsymbol{\Pi}(\tau)+\frac{\boldsymbol{\eta}(\tau)}{2}\Big)+\mathcal{H}_W\Big(\boldsymbol{\sigma}(\tau)-\frac{\boldsymbol{\xi}(\tau)}{2},\boldsymbol{\Pi}(\tau)-\frac{\boldsymbol{\eta}(\tau)}{2}\Big)\sim \\ -\boldsymbol{\xi}(\tau)\cdot\frac{\partial\mathcal{H}_W(\boldsymbol{\sigma}(\tau),\boldsymbol{\Pi}(\tau))}{\partial\boldsymbol{\sigma}}+\boldsymbol{\eta}(\tau)\cdot\frac{\partial\mathcal{H}_W(\boldsymbol{\sigma}(\tau),\boldsymbol{\Pi}(\tau))}{\partial\boldsymbol{\Pi}}+O(\boldsymbol{\eta}^2,\boldsymbol{\xi}^2)\ . \end{aligned} \tag{C.4}$$

Integrating out the variables $\boldsymbol{\eta}(\tau)$ and $\boldsymbol{\xi}(\tau)$, we obtain a $\delta$-function constraint on the trajectories $\boldsymbol{\sigma}(\tau)$ and $\boldsymbol{\Pi}(\tau)$:

$$\begin{cases} \dfrac{\partial\boldsymbol{\sigma}}{\partial\tau}=\dfrac{\boldsymbol{\Pi}}{M} \\ \dfrac{\partial\boldsymbol{\Pi}}{\partial\tau}=-\dfrac{\partial V_J(\boldsymbol{\sigma},\boldsymbol{\Pi})}{\partial\boldsymbol{\sigma}}-z(t)\boldsymbol{\sigma}\ , \end{cases} \tag{C.5}$$

The Lagrange multiplier is obtained by imposing the constraint $\boldsymbol{\sigma}^2=N$, that by imposing that the total radial force appearing in the second of Eqs. (C.5) is the correct centripetal one:

$$-\frac{1}{N}\frac{\partial V_J(\boldsymbol{\sigma},\boldsymbol{\Pi})}{\partial\boldsymbol{\sigma}}\cdot\boldsymbol{\sigma}-z(t)=-\frac{\boldsymbol{\Pi}^2}{MN}\ . \tag{C.6}$$

Replacing the expression of $z(t)$ obtained in this way into Eqs. (C.5), we obtain exactly the Eqs. (3.24) of the main text. Such expansion at leading order is exact in the limit $\hbar\to 0$ where the dynamics is determined by the saddle point of the action appearing in the path-integral.

## C.2 Correlation function on a longer time-scale

In this Appendix, we discuss some results obtained from the dynamics of the $p$-spin model on larger time-scales. In particular, we integrate the dynamics according to the protocol described in Section 3.2 of the main text, and compute the corresponding correlation function $C(t,t')$ in Eq. (3.38). Here the averages are performed on fewer realizations, with respect to the results presented in the main text. The results in Fig. C.1 show that the correlation function seems to break time-translation invariance on energy scales between $-0.25$ and $-0.42$, even though the profiles of $C(t_w+\tau,t_w)$, for various $t_w$, are less smooth due to the noise induced by the fewer realization we took. The results shown here are anyway compatible with the ones presented in the main text. The results shown in Fig. C.1 are anyway compatible with the ones presented in the main text and are also qualitatively similar with the plots describing the correlation function of a classical spin-glass in the non-ergodic phase and in the large-$N$ limit, see for example Fig. (10) of Ref. [82].

## C.3 Details on the fidelity susceptibility

In this appendix, we prove the expression in Eq. (3.49) of the main text for the average fidelity susceptibility $\chi$. We also discuss how the qualitative profile of the fidelity $\chi_\mu$,

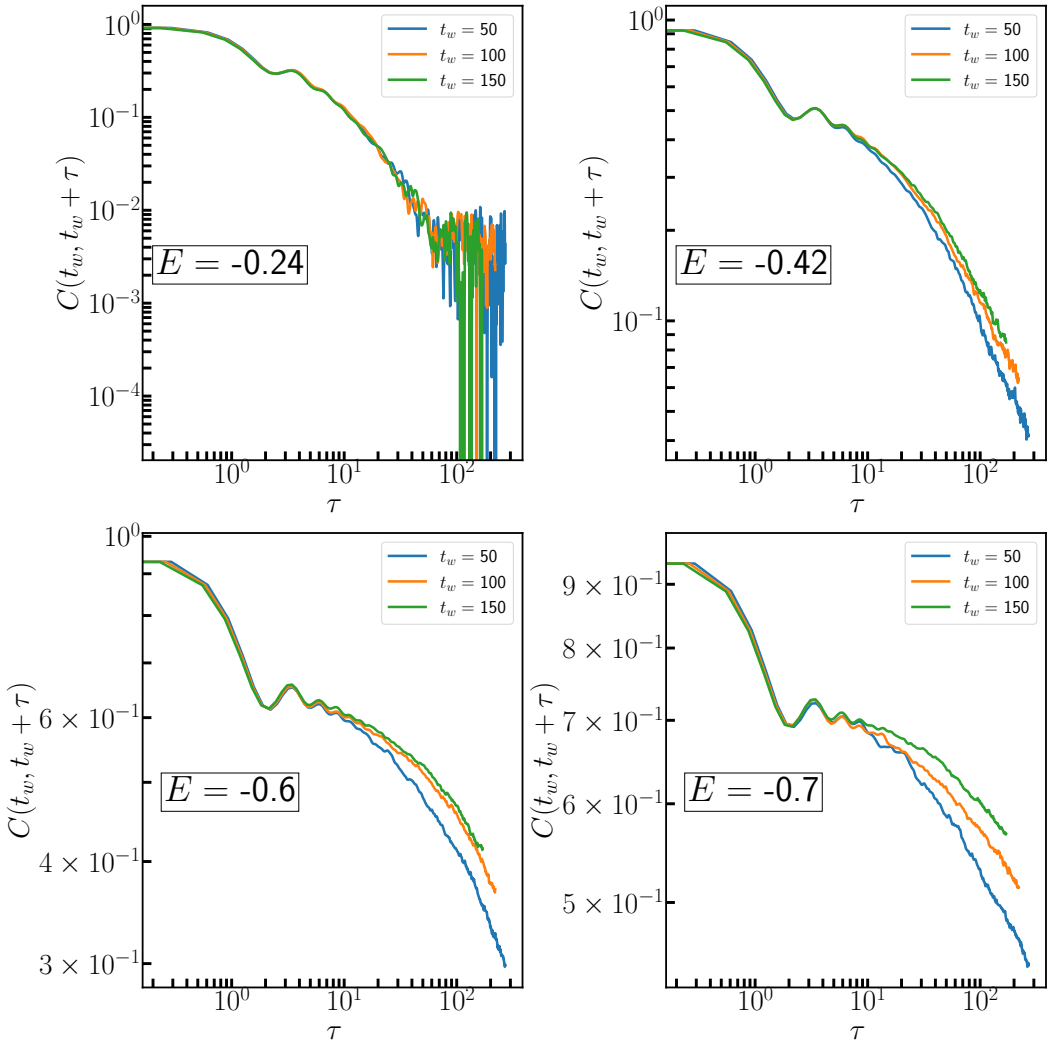


Figure C.1: Several plots of the correlation function $C(t_w + \tau, t_w)$, for different fixed values of the energy density $E$. For all the panels, the data are obtained from a dynamics up to time $t_{max} = 320$, with the same simulation parameters described in Fig. 3.5-(b) of the main text. The data are presented on a log-log scale.

defined in Eq. (3.50) and shown in Figg. 3.5-(a) and (b) of the main text, is independent both of the time window $[0, \mathcal{T}]$, over which we average the average correlation function in Eq. (3.51), and of the value of the cut-off $\mu$, provided that the latter is sufficiently small.

We begin by recalling our definition for the fidelity susceptibility. We perturb the Hamiltonian $\hat{H}_J = \frac{1}{2M}\sum_{i=1}^{N}\hat{\Pi}_i^2 + V_J(\hat{\boldsymbol{\sigma}})$ of the PSM with local magnetic fields, as

$$\hat{H}(\boldsymbol{B}) = \hat{H}_J - \sum_{i=1}^{N} B_i \hat{\sigma}_i \ , \tag{C.7}$$

and define the local susceptibilities of the as

$$\chi_n^{(i)} = \Big[ -\frac{\partial^2}{\partial B_i^2} \langle E_n | E_n(\boldsymbol{B}) \rangle \Big]_{\boldsymbol{B}=0} \ , \tag{C.8}$$

where $|E_n(\boldsymbol{B})\rangle$ is the $n$-th eigenstate of the perturbed Hamiltonian $\hat{H}(\boldsymbol{B})$ and $|E_n\rangle = |E_n(\boldsymbol{0})\rangle$. By standard calculations of non-degenerate perturbation theory [128], we have

$$\chi_n^{(i)} = \sum_{m\neq n} \frac{|\langle E_n|\hat{\sigma}_i|E_m\rangle|^2}{(E_n - E_m)^2} \tag{C.9}$$

where $E_n$ is the $n$-th unperturbed energy level of the Hamiltonian $\hat{H}_J$. For the initial state $\hat{\rho}$ defined in Eq. (3.25) of the main text, we define the fidelity susceptibility $\chi$ as the weighted average

$$\chi = \frac{1}{N}\sum_{i=1}^{N}\sum_n \overline{\langle E_n|\hat{\rho}|E_n\rangle \chi_n^{(i)}} = \frac{1}{N}\sum_{i=1}^{N}\sum_{n,m\neq n} \overline{|\langle E_n|\psi\rangle|^2 \frac{|\langle E_n|\hat{\sigma}_i|E_m\rangle|^2}{(E_n-E_m)^2}} \tag{C.10}$$

performed over the sites, the eigenstates and the disorder configurations. Then, we observe that $\chi$ is connected to the Fourier transform of the time-averaged correlation function

$$C_{av}(\tau) = \lim_{\mathcal{T}\to\infty}\frac{1}{\mathcal{T}}\int_0^{\mathcal{T}} dt_w C(t_w, t_w+\tau)\ . \tag{C.11}$$

In particular, $C(t_w, t_w+\tau)$ and $C_{av}(\tau)$ can be represented as follows:

$$\begin{aligned} C(t_w,t_w+\tau) &= \frac{1}{N}\sum_{i=1}^{N}\sum_{lmn} \overline{e^{i(E_l-E_n)t_w}e^{i(E_l-E_m)\tau}\langle E_l|\hat{\sigma}_i|E_m\rangle\langle E_m|\hat{\sigma}_i|E_n\rangle\langle\psi|E_l\rangle\langle E_n|\psi\rangle}\ , \\ C_{av}(\tau) &= \frac{1}{N}\sum_{i=1}^{N}\sum_n\sum_m \overline{|\langle E_n|\psi\rangle|^2 e^{i(E_n-E_m)\tau}|\langle E_n|\hat{\sigma}_i|E_m\rangle|^2}\ . \end{aligned} \tag{C.12}$$

The second line leads immediately to the Lehmann representation of the average correlation function, which reads as[1]

$$\tilde{C}_{av}(\omega) = \int_{-\infty}^{\infty} d\tau e^{-i\omega\tau} C_{av}(\tau) = \frac{2\pi}{N}\sum_{i=1}^{N}\sum_{nm} \overline{\langle E_n|\hat{\rho}|E_n\rangle\,|\langle E_n|\hat{\sigma}_i|E_m\rangle|^2\delta(\omega - E_n + E_m)}\ . \tag{C.13}$$

The latter is immediately related to the typical susceptibility $\chi$ in Eq. (C.10) via the expression

$$\chi = \int_{|\omega|>\omega_L}\frac{d\omega}{2\pi}\frac{\tilde{C}_{av}(\omega)}{\omega^2}\ , \tag{C.14}$$

where $\omega_L$ is the average spacing of the unperturbed energy levels [112].

As stated in the main text, within the TWA framework we can not compute the fidelity directly from Eq. (C.14) for two reasons: first, our simulations are performed up to a finite maximum time $t_{max}$, so that we can perform the average in Eq. (3.51) only on a finite time window $[0, \mathcal{T}]$, with $\mathcal{T} < t_{max}$; second, in the limit $\hbar \to 0$ we do not

[1] In our framework, $C(t_w\tau, t_w)$ is actually defined only for $\tau > t_w$. To compute the Fourier transform, we first symmetrized $C_{av}(\tau)$ with respect to $\tau$.

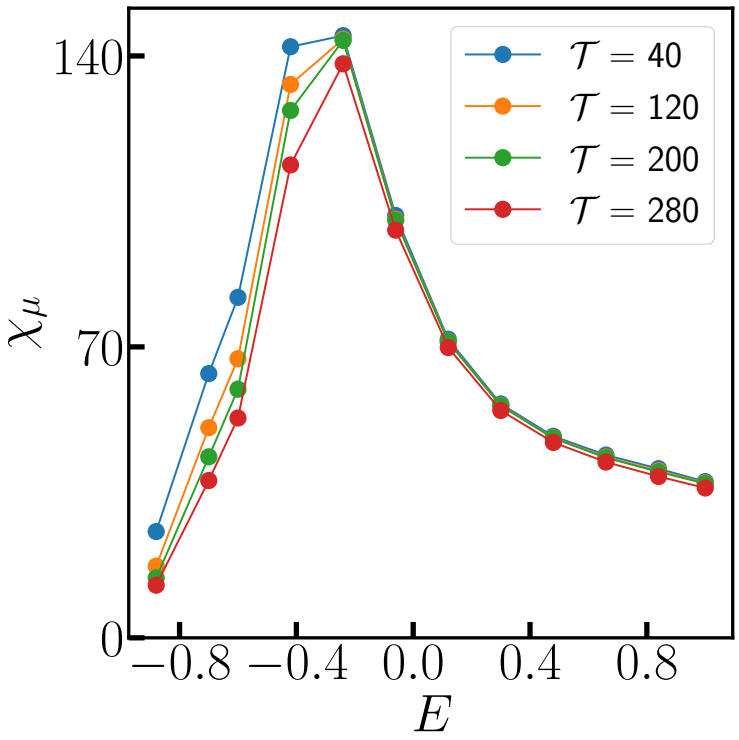


Figure C.2: Fidelity susceptibility $\chi_\mu$ from Eq. (3.50) of the main text, shown as a function of $E$ for a fixed cutoff $\mu = 0.07$. The average time window for the correlation function in Eq. (3.51) is set to $[0, \mathcal{T}]$, for several values of $\mathcal{T}$. The data are obtained from a dynamics up to time $t_{max} = 320$, with the same parameters described in Fig. 3.5-(b) of the main text.

have access to the spacing $\omega_L$ and have a frequency cut-off set by $\Delta\omega = 2\pi/t_{max}$. The second issue was already solved by using the regularized fidelity $\chi_\mu$, from Eq. (3.50) of the main text, in place of $\chi$. In Fig. C.2 we also show that the profile of $\chi_\mu$ is qualitatively the same for a wide range of $\mathcal{T}$ between 0 and $t_{max}$, so that the first issue is actually irrelevant for our results.

## C.4 Calculation of the complexity

In this appendix, we compute in detail the average number of stationary configurations of the dynamics induced by Eq. (3.24) of the main text. We start by rewriting the Eqs. (3.42), defining such stationary points:

$$\begin{cases} -\dfrac{\partial V_J}{\partial \sigma_i} + p\dfrac{V_J(\boldsymbol{\sigma})}{N}\sigma_i = 0 \\ \displaystyle\sum_i \sigma_i^2 = N \\ \quad \Pi_i = 0 \ . \end{cases} \tag{C.15}$$

More precisely, we look for a solution of Eq. (C.15) lying on a microcanonical manifold

defined by the equation

$$E = \frac{\sum_i \Pi_i^2}{2MN} + \frac{V_J(\boldsymbol{\sigma})}{N} \tag{C.16}$$

Thus, as the kinetic energy vanishes (as $\Pi_i = 0$ for every $i$), we can rewrite the equations for the stationary configurations in the following equivalent form:

$$\begin{cases} -\dfrac{\partial V_J}{\partial \sigma_i} + p\dfrac{V_J(\boldsymbol{\sigma})}{N}\sigma_i = 0 \\ \dfrac{V_J(\boldsymbol{\sigma})}{N} = E \\ \displaystyle\sum_i \sigma_i^2 = N \\ \Pi_i = 0 \ . \end{cases} \tag{C.17}$$

The system of Eqs. (C.17) can be further simplified by the following two observations. The first one is that, as we are interested in counting the number of the solutions of Eqs. (C.17), we can just focus on the number of solutions of the equations involving $\boldsymbol{\sigma}$, as the trivial equations $\Pi_i = 0$ do not bring any degeneracy. The second one is that the equations involving $\boldsymbol{\sigma}$, written in the first three lines of Eqs. (C.17), are equivalent to the following reduced system of equations

$$\begin{cases} -\dfrac{\partial V_J}{\partial \sigma_i} + p\dfrac{E}{N}\sigma_i = 0 \\ \displaystyle\sum_i \sigma_i^2 = N \ . \end{cases} \tag{C.18}$$

The equivalence can be seen by multiplying the first line of the system of Eqs. (C.18) by $\sigma_i$ and summing over $i$: by making use of the spherical constraint, one recovers the equation $E = V_J(\boldsymbol{\sigma})/N$; then, by substituting back $E = V_J(\boldsymbol{\sigma})/N$ in the first line of Eqs. (C.18), we obtain the first line of Eqs. (C.17).

To summarize, the number of stationary points of Eqs. (3.42) lying on a manifold at energy density $E$ coincides with the number of solution of the equations

$$-\frac{\partial V_J}{\partial \sigma_i} + p\frac{E}{N}\sigma_i = 0 \ , \tag{C.19}$$

for $i = 1, \dots, N$, lying on the $N$-sphere. In the spirit of Ref. [148], in what follows we will often write the indices for the $p = 3$ case, such that $J_{i1\dots ip}$ becomes $J_{ijk}$. However, to give formulas that are valid even in the general case, we will write all the factors containing a term $p$ for the generic $p$. Then, the average number of solutions of Eq. (C.19) on the $N$-sphere then reads:

$$\overline{\mathcal{N}(E)} = \int D\sigma \overline{\prod_i \delta\Big(-\frac{p}{p!}\sum_{kl} J_{ikl}\sigma_k\sigma_l - pE\sigma_i\Big)\Big|\det\Big(-\frac{p(p-1)}{p!}\sum_k J_{ijk}\sigma_k - pE\delta_{ij}\Big)\Big|} \ , \tag{C.20}$$

the overbar denoting the average over the disorder and the spherical constraint will be from now on hidden in the integration measure $D\sigma = \delta(\sum_i \sigma_i^2 - N)\prod_{i=1}^N d\sigma_i$. The

absolute value of the determinant appearing on the right-hand side is just a Jacobian factor appearing because the Eqs. (C.19) are written in an implicit form.

To compute $\overline{\mathcal{N}(E)}$ in the large-$N$ limit, we need two approximations. The first one consists in assuming that there is no correlation between the last two terms in the right-hand side of Eq. (C.20) [75, 148], that is

$$\overline{\delta\Big(-\frac{p}{p!}\sum_{kl}J_{ikl}\sigma_k\sigma_l-pE\sigma_i\Big)\Big|\det\Big(-\frac{p(p-1)}{p!}\sum_{k}J_{ijk}\sigma_k-pE\delta_{ij}\Big)\Big|}\simeq \overline{\delta\Big(-\frac{p}{p!}\sum_{kl}J_{ikl}\sigma_k\sigma_l-pE\sigma_i\Big)}\;\overline{\Big|\det\Big(-\frac{p(p-1)}{p!}\sum_{k}J_{ijk}\sigma_k-pE\delta_{ij}\Big)\Big|} \tag{C.21}$$

so that each the average of the $\delta$-function and the one of the determinant can be computed independently from each other. We compute the average $\delta$-function by using the exponential representation

$$\overline{\delta\Big(-\frac{p}{p!}\sum_{kl}J_{ikl}\sigma_k\sigma_l-pE\sigma_i\Big)}=\int\prod_i\frac{d\mu_i}{2\pi}\overline{e^{-ip/p!\sum_{ikl}J_{ikl}\mu_i\sigma_k\sigma_l}}e^{ipE\sum_j\mu_j\sigma_j} \tag{C.22}$$

and averaging out the disorder after a proper symmetrization of the exponent. Taking into account the spherical constraint $\sum_i\sigma_i^2=N$ and posing $J=1$ for simplicity, we get

$$\overline{\delta\Big(-\frac{p}{p!}\sum_{kl}J_{ikl}\sigma_k\sigma_l-pE\sigma_i\Big)}=\int\prod_i\frac{d\mu_i}{2\pi}\exp\Big\{-\frac{p}{4}\sum_j\mu_j^2-\frac{p(p-1)}{4N}(\sum_j\mu_j\sigma_j)^2+ipE\sum_j\mu_j\sigma_j\Big\} \tag{C.23}$$

To get rid of the term $(\sum_j\mu_j\sigma_j)^2$, we perform and extra Hubbard-Stratonovich transformation and perform straightforwardly all the remaining Gaussian integrals, posing again $\sum_i\sigma_i^2=N$ in all our expressions. The final result is:

$$\overline{\delta\Big(-\frac{p}{p!}\sum_{kl}J_{ikl}\sigma_k\sigma_l-pE\sigma_i\Big)}\simeq\frac{1}{(2\pi)^{N/2}}\exp\Big\{-N\Big(E^2+\frac{1}{2}\log\frac{p}{2}\Big)\Big\} \tag{C.24}$$

up to a multiplicative constant which becomes irrelevant in the thermodynamic limit. The integration of the Jacobian factor is a bit more tricky. To perform it, we make our second approximation by assuming that the sign of the determinant, for any fixed configuration of the disorder, is given by the average number of negative eigenvalues of the corresponding Hessian matrix at energy density $E$, that we write as $Nk(E)$. In formulas, this is equivalent to:

$$\overline{\Big|\det\Big(-\frac{p(p-1)}{p!}\sum_{k}J_{ijk}\sigma_k-pE\delta_{ij}\Big)\Big|}\simeq\overline{\det\Big(-\frac{p(p-1)}{p!}\sum_{k}J_{ijk}\sigma_k-pE\delta_{ij}\Big)}\cdot(-1)^{-Nk(E)} \tag{C.25}$$

$k(E)$ being the average *fraction* of negative eigenvalues. Once we got rid of the modulus, we rewrite the average of the determinant using a fermionic representation [230]:

$$\overline{\det\Big(-\frac{p(p-1)}{p!}\sum_{k}J_{ijk}\sigma_k-pE\delta_{ij}\Big)}=\int\prod_j d\psi_j d\overline{\psi}_j\overline{e^{-p(p-1)/p!\sum_{ikl}J_{ikl}\sigma_i\overline{\psi}_k\psi_l}}e^{-pE\sum_i\overline{\psi}_i\psi_i} \tag{C.26}$$

Integrating out the disorder and using again an Hubbard-Stratonovich transformation to get rid of quartic fermionic terms (see Ref. [148] for more details about this step), we arrive at

$$\overline{\det\Big(-\frac{p(p-1)}{p!}\sum_k J_{ijk}\sigma_k - pE\delta_{ij}\Big)} \propto \int_{-i\infty}^{i\infty} dz e^{NG(z)} \tag{C.27}$$

where $G(z) = \frac{z^2}{p(p-1)} + \log(z - pE)$. Plugging everything together, we have that (up to an irrelevant prefactor)

$$\overline{\mathcal{N}(E)} = (-1)^{Nk(E)} \exp\Big\{-N\Big(E^2 + \frac{1}{2}\log\frac{p}{2}\Big)\Big\} \int_{-i\infty}^{i\infty} dz e^{NG(z)} \tag{C.28}$$

Thus, we are left with the computation of the integral

$$I_\Gamma = \int_\Gamma dz e^{NG(z)} \tag{C.29}$$

along the imaginary axis $\Gamma$ in the complex plane. In the thermodynamic limit $N \to \infty$, this goal can be achieved by using the saddle-point method [177], which we briefly review in the following. First, we observe that, for generic $z = x + iy$ (for $x$, $y$ real numbers), the function $G(z) = u(x,y) + iv(x,y)$ can be decomposed in its real and imaginary parts as

$$\begin{cases} u(x,y) = \dfrac{1}{2}\log[(x-pE)^2 + y^2] + \dfrac{x^2 - y^2}{p(p-1)} \\ v(x,y) = \dfrac{2}{p(p-1)}xy + \arctan\dfrac{y}{x - pE} + \pi\Theta(pE - x)\mathrm{sign}(y) \end{cases} \tag{C.30}$$

In summary, the saddle point method states that if we find a deformation $\gamma$ of $\Gamma$ in the context plane such that:

1. $v(x,y)$ is constant over $\gamma$,
2. $u(x,y)$ has a global maximum along $\gamma$ at some point $z = z_0$,
3. $G(z)$ is analytic in the closed domain encompassed by the curves $\Gamma$ and $\gamma$,

we have that

$$I_\Gamma = I_\gamma \equiv \int_\gamma dz e^{NG(z)} \simeq \exp\big(NG(z_0) + o(N)\big)\ , \tag{C.31}$$

where the last asymptotic relation holds in the $N \to \infty$ limit and is known as Laplace method [177]. It is easy to see that the first condition is equivalent to state that $\gamma$ is parallel to $\nabla u(x,y)$, as the relation $\nabla u \cdot \nabla v = 0$ holds for the holomorphic function $G(z)$. Then if $\nabla u(x,y)$ vanishes along $\gamma$, it vanishes in the whole $\mathbb{R}^2$ plane, so that any maximum of $u(x,y)$ along $\gamma$ is a stationary point of $u(x,y)$ in $\mathbb{R}^2$.

However, the choice of a suitable $\gamma$ depends on the value of the energy density $E$, because $G(z)$ has a branch-cut on the half-line $\{z = x | x < pE\}$ (see the expression of $v(x,y)$ in eq (C.30)) and the position in the complex plane of the stationary points of $u(x,y)$, given by

$$z_\pm(E) = \frac{p}{2}\left(E \pm \sqrt{E^2 - \frac{2(p-1)}{p}}\right)\ , \tag{C.32}$$

also depends on $E$. In particular, we can identify four relevant energy windows, which we treat separately:

$$\begin{aligned} E < E_{th} \equiv -\sqrt{2(p-1)/p}\ , \qquad & E_{th} < E < 0, \\ 0 < E < |E_{th}|\ , \qquad & E > |E_{th}| \end{aligned} \tag{C.33}$$

For $E < E_{th}$, we can take the curve $\gamma$ as the level curve $v(x,y) = v(z^+(E)) = 0$[2] (shown in Fig. C.3-(a)). It is straightforward to show that $\gamma$ is the only deformation of $\Gamma$ along which $u(x,y)$ displays a maximum, located at $z = z_+(E)$. Thus for $N \to \infty$ we have $I_\Gamma \simeq \exp\{NG(z_+(E))\}$ and $\overline{\mathcal{N}(E)} \simeq \exp\{N\Sigma(E)\}$, where

$$\Sigma(E) = \frac{z_+(E)^2}{p(p-1)} + \log(z_+(E) - pE) - E^2 - \frac{1}{2}\log\frac{p}{2} + \frac{1}{2} \tag{C.34}$$

where we posed the phase $k(E) = 0$ in Eq. (C.28),as $\overline{\mathcal{N}(E)}$ has to be a positive real number. The physical meaning of having $k(E) = 0$ is that, in this energy range, the integral in Eq. (C.20) is dominated by local minima of the potential $V_J(\boldsymbol{\sigma})$, where the Hessian is positive definite.

For $E_{th} < E < 0$, the only suitable deformation of $\Gamma$ is $\gamma = \gamma_+ \cup \gamma_-$, where $\gamma_+$ and $\gamma_-$ are respectively the two level curves $v(z) = v(z_+(E))$ and $v(z) = v(z_-(E))$ of $v(z)$. The two curves intersect respectively the points $z_+(E)$ and $z_-(E)$ in the complex plane (see Fig. C.3-(b)), which in turn are maxima of $u(x,y)$ along each of the two curves. Then, as $u(z_+) = u(z_-)$ and $v(z_+) = -v(z_-)$, the $N \to \infty$ asymptotic value of $I_\Gamma$ is the sum of two contributions:

$$I_\Gamma \simeq \frac{e^{iNv(z_+)} + e^{-iNv(z_+)}}{2} e^{Nu(z_+)} \tag{C.35}$$

To give a physical interpretation to our result, let us first note that the function $Nk(E)$, defined in Eq. (C.25), is a non-negative integer. This is because $Nk(E)$ is the average number of negative eigenvalues of the Hessian matrix associated with $V_J(\boldsymbol{\sigma})$. Thus, even though the values of $k(E)$ become dense in the interval $[0,1]$ as $N$ approaches infinity, at any finite $N$ we must always have

$$(-1)^{Nk(E)} = (-1)^{-Nk(E)}\ . \tag{C.36}$$

Since $\overline{\mathcal{N}(E)}$ is a positive real number, any phase obtained from the integral $I_\Gamma$ must compensate for the one coming from $k(E)$. Therefore, with a bit of lack of rigor, we can conclude that for all physically meaningful values of $k(E)$, the following equalities hold:

$$e^{iNv(z_+)} = (-1)^{Nk(E)} = (-1)^{-Nk(E)} = e^{-iNv(z_+)} \tag{C.37}$$

and we write

$$I_\Gamma \simeq (-1)^{Nk(E)} \exp\{N\Sigma(E)\} \tag{C.38}$$

[2]To simplify notation, we will abuse notation by writing $v(z)$ to represent $v(\mathrm{Re}(z), \mathrm{Im}(z))$, and similarly for $u(x,y)$. This allows us to write equations more compactly and avoid cluttering them with repetitive expressions.

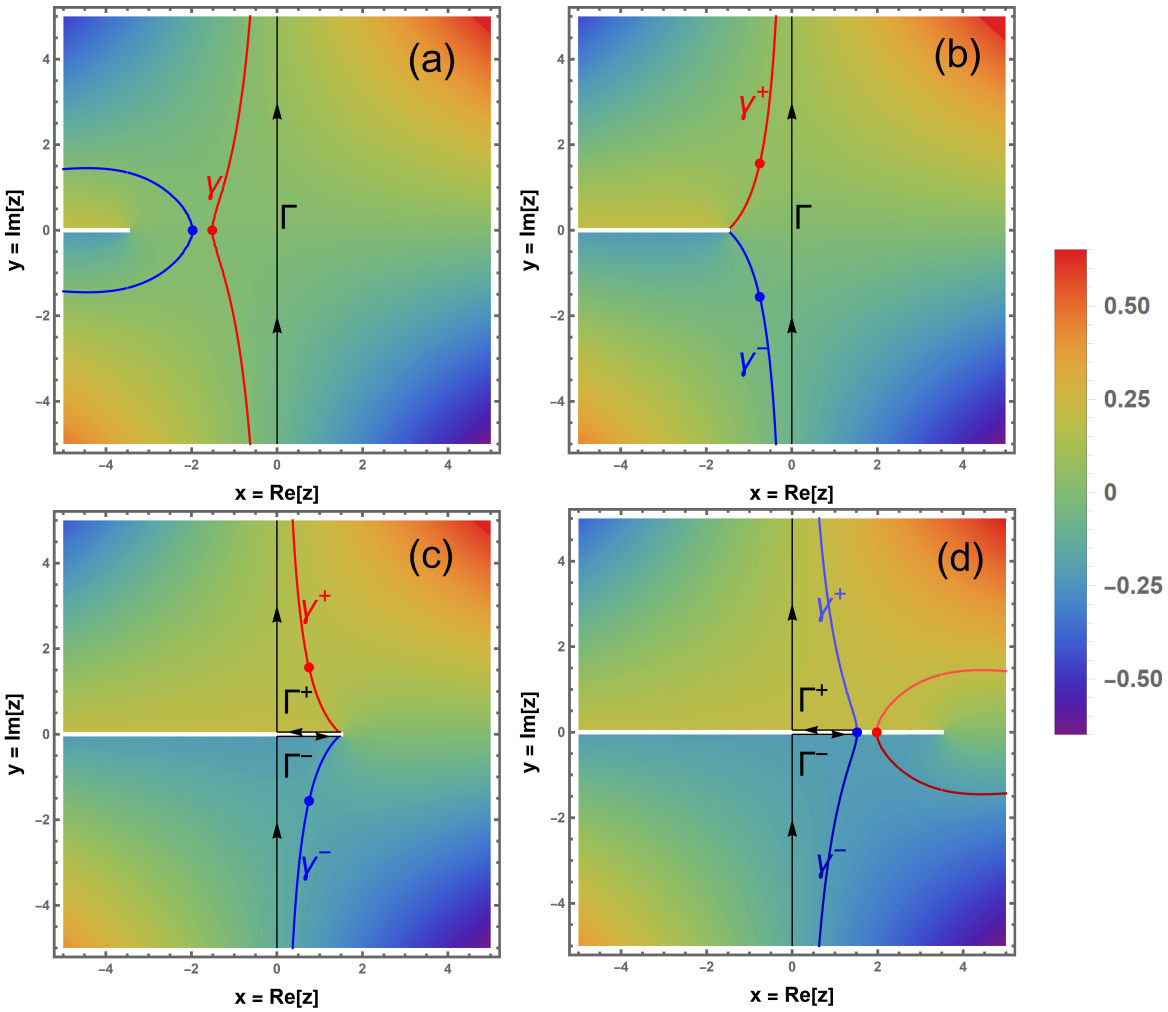


Figure C.3: Color map in the complex plane representing the values assumed by the function $v(x, y)$ defined in the appendix. Each panel corresponds to a different, fixed value of the energy density $E$, each representative of one of the four, qualitatively different cases studied in the appendix. Here we plot the results for $p = 3$. The white thick line correponds to the branch-cut of $v(z) = v(x, y)$ in the complex plane, where $z = x + iy$, while the black lines represent the integration contour $\Gamma$ or its deformation $\Gamma^+ \cup \Gamma^-$. The blue and the red lines correspond to the level curve of $v(z)$, passing respectively through $z^-(E)$ and $z^+(E)$. **(a)** $E < E_{th}$.**(b)** $E_{th} < E < 0$.**(c)** $0 < E < |E_{th}|$.**(d)** $E > |E_{th}|$.

with

$$k(E) = \frac{p}{2\pi(p-1)} E\sqrt{E_{th}^2 - E^2} + \frac{1}{\pi}\arctan\left(\frac{\sqrt{E_{th}^2 - E^2}}{E}\right). \tag{C.39}$$

and $\Sigma(E) = \mathrm{Re}[G(z_+(E))]$. Physically, having $k(E) > 0$ means that for $E > E_{th}$ the contribution to the integral in Eq. (C.20) is dominated by saddles having an extensive number of unstable direction: this is why in literature $E_{th}$ is referred to as the *energy threshold* where the local minima cease to dominate [74, 148].

For $0 < E < |E_{th}|$, the branch-cut crosses the integration path $\Gamma$ and we can not use the saddle-point method straightforwardly. Instead, we first notice that it exist two curve in the complex plane, $\gamma_+$ and $\gamma_-$, passing respectively through the saddle points $z_+(E)$ and $z_-(E)$ (both being maxima of $u(z)$ along such curves) and ending up in a point $z = x_1(E)$ on the branch-cut.
However, we observe that if we split $\Gamma$ in two curves, $\Gamma^+$ and $\Gamma^-$, defined in such a way that

$$\begin{aligned} I_{\Gamma^+} &= \int_{\Gamma^+} dz e^{NG(z)} \equiv \int_0^{i\infty} dz e^{NG(z)} - \int_0^{x_1(E)} dx e^{NG(x)} \\ I_{\Gamma^-} &= \int_{\Gamma^-} dz e^{NG(z)} \equiv \int_{-i\infty}^{0} dz e^{NG(z)} + \int_0^{x_1(E)} dx e^{NG(x)} \end{aligned} \tag{C.40}$$

then we have that $I_\Gamma = I_{\Gamma^+} + I_{\Gamma^-}$ and that $\Gamma^+$ and $\Gamma^-$ can be respectively deformed on $\gamma^+$ and $\gamma^-$, as shown in Fig. C.3-(c). In this way, we can use the saddle-point method to evaluate $I_{\Gamma^+}$ and $I_{\Gamma^-}$ separately. As the equalities $u(z_+) = u(z_-)$ and $v(z_+) = -v(z_-)$ hold like in the previous case, we find once again that $I_\Gamma \simeq (-1)^{Nk(E)} \exp\{N\Sigma(E)]\}$, with $k(E)$ given by Eq. (C.39), $\Sigma(E) = \mathrm{Re}[G(z_+(E))]$ and for $E$ in the range $[0, |E_{th}|]$.

Finally, for $E > |E_{th}|$ both the $z_+(E)$ and $z_-(E)$ lie on the branch-cut, like in Fig. C.3-(d). By some algebraic manipulations, one can show that $u(x, y)$ has an absolute maximum at the point $z_-(E)$ along the level curves $\gamma^+$ and $\gamma^-$ of $v(x, y)$ that intersect $z_-(E)$, while $u(x, y)$ has a minimum at the point $z_+(E)$ along the level curves of $v(x, y)$ that intersect $z_+(E)$. As done for the case $0 < E < |E_{th}|$ we divide once again $\Gamma$ in the curves $\Gamma^+$ and $\Gamma_-$, both ending in $z_-(E)$ and deform each of them respectively along $\gamma^+$ and $\gamma^-$ (see Fig. C.3-(d)). By observing that $v(z) = \pm\pi$ respectively along $\gamma^+$ and $\gamma^-$, we conclude that $k(E) = 1$ in the energy range taken into exam, meaning that for $E > |E_{th}|$ the majority of stationary points of $V_J(\boldsymbol{\sigma})$ are local maxima. At the same time, the application of the Laplace method gives us:

$$\Sigma(E) = \frac{z_+(E)^2}{p(p-1)} + \log(z_+(E) - pE) - E^2 - \frac{1}{2}\log\frac{p}{2} + \frac{1}{2}\,. \tag{C.41}$$

In summary, in the whole energy range studied we have

$$\Sigma(E) = \frac{z(E)^2}{p(p-1)} + \log(z(E) - pE) - E^2 - \frac{1}{2}\log\frac{p}{2} + \frac{1}{2} \tag{C.42}$$

where $z(E) = z_+(E)$ if $E < |E_{th}|$ and $z(E) = z_-(E)$ if $E > |E_{th}|$, while the average

stability index is given by

$$k(E) = \begin{cases} 0 \ , \text{ if } E < E_{th} \\ \frac{p}{2\pi(p-1)} E\sqrt{E_{th}^2 - E^2} + \frac{1}{\pi} \arctan(\frac{\sqrt{E_{th}^2 - E^2)}}{E}) \ , \text{ if } |E| < |E_{th}| \\ 1 \ , \text{ if } E > |E_{th}| \end{cases} \tag{C.43}$$

which is the result plotted in Figure 3.4 of the main text.

# Appendix D

# Derivation and details about the Mode-Coupling equations

## D.1 Derivation of the mode-coupling equations

The aim of this appendix is to derive the closed set of equations of motions (4.34) and (4.35), governing the dynamics of the correlation function $C(t,t')$ and response function $R(t,t')$ for a $p$-spin glass driven Hamiltonian:

$$\hat{H}_J = \frac{1}{2M}\sum_{i=1}^{N}\hat{\Pi}_i^2 - \mathcal{J}(t)\sum_{i_1<\cdots<i_p} J_{i_1,\ldots,i_p}\hat{\sigma}_{i_1}\cdots\hat{\sigma}_{i_p} - B(t)\sum_i \hat{\sigma}_i \tag{D.1}$$

with all-to-all couplings $J_{i_1,\ldots,i_p}$, independently sampled from a Gaussian distribution with zero mean and variance $\overline{J^2} = 2p!/N^{p-1}$. The spins $\hat{\sigma}_i$ obey the usual spherical constraint $\sum_i \langle\hat{\sigma}_i^2\rangle = N$. The canonical commutation relations $[\hat{\sigma}_j, \hat{\Pi}_k] = i\hbar\delta_{jk}$ hold. The unitary dynamics generated by the Hamiltonian in Eq. (D.1) can be expressed through a path integral on the Schwinger-Keldysh contour [230], whose generating functional reads as:

$$\mathcal{Z}[J] = \int \mathcal{D}\boldsymbol{\sigma}^+\mathcal{D}\boldsymbol{\sigma}^- \exp\left[i\left(S_s[\boldsymbol{\sigma}^+] - S_s[\boldsymbol{\sigma}^-]\right)/\hbar\right]\langle\boldsymbol{\sigma}^+|\hat{\rho}(0)|\boldsymbol{\sigma}^-\rangle \ . \tag{D.2}$$

Here, $\rho(0)$ represents the element of the initial density matrix at $t = 0$ and is chosen to be uncorrelated a random, infinite-temperature initial state, which is uncorrelated with the disorder. The action $S$ can be defined in terms of a quadratic term $S_0$ and a disordered interaction term $V_J[\boldsymbol{\sigma}]$ as follows:

$$S_s[\boldsymbol{\sigma}, J] = S_0[\boldsymbol{\sigma}] - \int_0^\infty dt\ \mathcal{J}(t)V_J[\boldsymbol{\sigma}], \tag{D.3}$$

$$S_0[\boldsymbol{\sigma}] = \int_0^\infty dt\left[\frac{M}{2}\dot{\boldsymbol{\sigma}}^2 - \frac{z(t)}{2}(\boldsymbol{\sigma}^2 - N)\right] - \sum_{i=1}^{N}\int_0^\infty dt B(t)\sigma_i(t), \tag{D.4}$$

$$V_J[\boldsymbol{\sigma}] = -\sum_{i_1<\ldots<i_p} J_{i_1\ldots i_p}\sigma_{i_1}\ldots\sigma_{i_p}. \tag{D.5}$$

The quadratic part $S_0$ contains a kinetic term, chosen such that the eventual dynamical equations are written in terms of second derivatives with respect to time. The time-dependent Lagrange multiplier $z(t)$ enforces the constraint $\sum_i^N \sigma_i^2 = N$. We also included in $S_0$ the coupling to the time-dependent field $B(t)$. This action can be split into components $\boldsymbol{\sigma}^+$ and $\boldsymbol{\sigma}^-$ residing on the forward and backwards Keldysh contours respectively, to give an action:

$$S[\boldsymbol{\sigma}^+, \boldsymbol{\sigma}^-, J] = S_0[\boldsymbol{\sigma}^+] - S_0[\boldsymbol{\sigma}^-] - \int_0^\infty dt \mathcal{J}(t) \left( V_J[\boldsymbol{\sigma}^+] - V_J[\boldsymbol{\sigma}^-] \right) \tag{D.6}$$

where the relative minus sign comes from reversing the integration limits on the reverse contour.

### D.1.1 System-Bath Coupling

The coupling between the system and bath can be treated exactly as in Ref. [86]. We couple the quantum $p$-spin Hamiltonian linearly to a bath of harmonic oscilllators, assumed to be in thermal equilibrium, for a time window $[0, t_b]$. This coupling can be described by the functional [230]:

$$\begin{aligned} S_{bath} = \frac{1}{\hbar} \int_0^{t_b} dt \int_0^{t_b} dt' \big( & - [\boldsymbol{\sigma}^+(t) - \boldsymbol{\sigma}^-(t)] \eta(t-t') [\boldsymbol{\sigma}^+(t') + \boldsymbol{\sigma}^-(t')] \\ & + i [\boldsymbol{\sigma}^+(t) - \boldsymbol{\sigma}^-(t)] \nu(t-t') [\boldsymbol{\sigma}^+(t') - \boldsymbol{\sigma}^-(t')] \big) \end{aligned} \tag{D.7}$$

where $\eta$ and $\nu$ are the correlation and response functions of the bath, and are time-translation invariant due to the bath being in equilibrium. They are given by:

$$\eta(t-t') = -\Theta(t-t') \int_0^\infty d\omega I(\omega) \sin[\omega(t-t')], \tag{D.8}$$

$$\nu(t-t') = \int_0^\infty I(\omega) \coth\left( \frac{1}{2} \beta \hbar_0 \omega \right) \cos[\omega(t-t')] \tag{D.9}$$

where $I(\omega)$ is the spectral function of the bath. We choose an Ohmic bath with $I(\omega) = \frac{1}{\pi} \exp(-|\omega|/\Lambda)$ and set the integration cutoff to be $\Lambda = 5$.

### D.1.2 Disorder Averaging

For an initial condition $\hat{\rho}(0)$ uncorrelated with the disorder, we can perform the disorder average explicitly. As in the Letter, we assume that the distribution of the disorder variable $J_{i_1 \ldots i_p}$ is given by the Gaussian distribution

$$P[J] = \sqrt{\frac{N^{p-1}}{\pi p! J^2}} \exp\left( -\frac{N^{p-1}}{p! J^2} \sum_{i_1 \neq \ldots \neq i_p} (J_{i_1 \ldots i_p})^2 \right) \tag{D.10}$$

with zero average and variance $\overline{(J_{i_1 \ldots i_p})^2} = (p! J^2)/(2N^{p-1})$. The disorder average reduces to just averaging over the terms proportional to $V_J[\boldsymbol{\sigma}]$, which are the only ones

depending on the disorder. By performing it explicitly, we obtain the disorder-averaged generating functional:

$$\overline{\mathcal{Z}[J]} = \int \mathcal{D}\sigma^- \mathcal{D}\sigma^+ \exp\left[i\left(S_{eff}[\boldsymbol{\sigma}^+, \boldsymbol{\sigma}^-]\right)\right] \ . \tag{D.11}$$

The effective action at the exponent is given by:

$$S_{eff}[\boldsymbol{\sigma}^+, \boldsymbol{\sigma}^-] = S_0[\boldsymbol{\sigma}^+] - S_0[\boldsymbol{\sigma}^-] - V_D[\boldsymbol{\sigma}^+, \boldsymbol{\sigma}^-] + S_{bath}[\boldsymbol{\sigma}^+, \boldsymbol{\sigma}^-], \tag{D.12}$$

$$V_D[\boldsymbol{\sigma}^+, \boldsymbol{\sigma}^-] = \frac{iN}{4} \int dt dt' \mathcal{J}(t)\mathcal{J}(t')J^2 \sum_{\alpha,\beta=\pm} \sum_{i=1}^{N} \alpha\beta \left(\frac{1}{N}\sigma_i^\alpha(t)\sigma_i^\beta(t')\right)^p \tag{D.13}$$

where $\alpha, \beta = \pm$ are the Schwinger-Keldysh contours.

### D.1.3 Transformed Order Parameters

The contribution to the action containing at most quadratic terms in the spins $\sigma_i^\alpha(t)$ can be written down as:

$$S_{eff}^{(2)}[\boldsymbol{\sigma}^+, \boldsymbol{\sigma}^-] = -\frac{1}{2} \int dt dt' \boldsymbol{\sigma}^\alpha(t) O_p^{\alpha\beta}(t,t') \boldsymbol{\sigma}^\beta(t') - \sum_{i\alpha} \int \frac{dt}{\hbar} \ \alpha B(t) \sigma_i^\alpha(t) \tag{D.14}$$

where the matrix elements are given by:

$$O_p^{++}(t,t') = \frac{1}{\hbar}[M\partial_t^2 + z^+(t)]\delta(t-t') - \frac{2}{\hbar_0}(i\nu(t-t') - \eta(t-t'))\Theta(t-t_q)\Theta(t'-t_q), \tag{D.15}$$

$$O_p^{+-}(t,t') = \frac{1}{\hbar_0}(2\eta(t-t') + 2i\nu(t-t'))\Theta(t-t_q)\Theta(t'-t_q), \tag{D.16}$$

$$O_p^{-+}(t,t') = \frac{1}{\hbar_0}(-2\eta(t-t') + 2i\nu(t-t'))\Theta(t-t_q)\Theta(t'-t_q), \tag{D.17}$$

$$O_p^{--}(t,t') = -\frac{1}{\hbar}[M\partial_t^2 + z^-(t)]\delta(t-t') - \frac{2}{\hbar_0}(i\nu(t-t') + \eta(t-t'))\Theta(t-t_q)\Theta(t'-t_q). \tag{D.18}$$

We now introduce new variables $Q^{\alpha\beta}(t,t')$ (where $\alpha, \beta = \pm$) which will allow us to decouple the $p$-interaction term:

$$1 = \int \prod_{\alpha\beta} \mathcal{D}Q^{\alpha\beta} \delta\left(\frac{1}{N}\boldsymbol{\sigma}^\alpha(t)\boldsymbol{\sigma}^\beta(t') - Q^{\alpha\beta}(t,t')\right), \tag{D.19}$$

$$\propto \int \prod_{\alpha\beta} \mathcal{D}Q^{\alpha\beta}\mathcal{D}\lambda^{\alpha\beta} \exp\left(-\frac{i}{2}\lambda^{\alpha\beta}\left(\boldsymbol{\sigma}^\alpha(t)\boldsymbol{\sigma}^\beta(t') - NQ^{\alpha\beta}(t,t')\right)\right). \tag{D.20}$$

### D.1.4 Saddle-Point Equations

Using a compact notation, the final form of the generating functional is

$$\overline{\mathcal{Z}[J]} = \int \mathcal{D}Q\mathcal{D}\lambda \exp\{NS[Q,\lambda]\} \tag{D.21}$$

where

$$S[Q,\lambda] = \sum_{\alpha\beta}\int dtdt'\Big\{\frac{i}{2}\lambda^{\alpha\beta}(t,t')Q^{\alpha\beta}(t,t') - \frac{1}{4}Q_{\alpha\beta}(t,t')\Big\} + \log Z[Q,\lambda] \tag{D.22}$$

and

$$Z[Q,\lambda] = \int \mathcal{D}\sigma^-\mathcal{D}\sigma^+ \exp\Big[-\frac{1}{2}\sum_{\alpha\beta}\int dtdt'\sigma^\alpha(t)[iO_p^{\alpha\beta}(t,t') + i\lambda^{\alpha\beta}(t,t')]\sigma^\beta(t') + \\ - i\sum_\alpha\int\frac{dt}{\hbar}\alpha B(t)\sigma_i^\alpha(t)\Big] \tag{D.23}$$

is the action of a single effective spin. Then, defining the matrix $M^{\alpha\beta}(t,t') = iO_p^{\alpha\beta}(t,t') + i\lambda^{\alpha\beta}(t,t')$, the saddle point equations for the $N\to\infty$ limit read

$$Q^{\alpha\beta}(t,t') = \langle\sigma^\alpha(t)\sigma^\beta(t')\rangle = (M^{-1})^{\alpha\beta}(t,t') + m(t)m(t') \tag{D.24}$$

$$i\lambda^{\alpha\beta}(t,t') = \frac{p}{2}F[Q]^{\alpha\beta}(t,t') \tag{D.25}$$

The average $\langle\cdot\rangle$ in Eq. (D.24) is performed over the partition function $Z[Q,\lambda]$ and the magnetization

$$m(t) = \langle\sigma(t)\rangle = \sum_\beta\int dt'\frac{i}{\hbar}(M^{-1})^{\alpha\beta}(t,t')\beta B(t') \tag{D.26}$$

does not actually depend on the Keldysh index $\alpha$, like every other one-time quantity. The matrices used in Eq. (D.24) are defined as

$$\mathcal{Q}(t,t') = \begin{bmatrix} Q^{++}(t,t') & Q^{+-}(t,t') \\ Q^{-+}(t,t') & Q^{--}(t,t')\end{bmatrix}, \quad \mathcal{M}(t,t') = \begin{bmatrix} M^{++}(t,t') & M^{+-}(t,t') \\ M^{-+}(t,t') & M^{--}(t,t')\end{bmatrix} \tag{D.27}$$

$$F[Q](t,t') = \begin{bmatrix} [Q^{++}(t,t')]^{p-1} & -[Q^{+-}(t,t')]^{p-1} \\ -[Q^{-+}(t,t')]^{p-1} & [Q^{--}(t,t')]^{p-1}\end{bmatrix}\frac{\mathcal{J}(t)\mathcal{J}(t')J^2}{\hbar^2} \tag{D.28}$$

using the same notation of Ref. [86]. Manipulating Eq. (D.24), we can rewrite the response function as

$$R(t,t') = \frac{i}{\hbar}[Q^{++}(t,t') - Q^{+-}(t,t')] = \frac{i}{\hbar}[(M^{-1})^{++}(t,t') - (M^{-1})^{+-}(t,t')] \tag{D.29}$$

so that, fixing $\alpha = +1$ in Eq. (D.26), the magnetization becomes

$$m(t) = \int dt' R(t,t')B(t') \tag{D.30}$$

Using Eq. (D.25) the variable $\lambda^{\alpha\beta}(t,t')$ and applying the matrix $\mathcal{M}$ on both sides of Eq. Eq. (D.24), we obtain the dynamical equations for all the two-point correlations on the Keldysh contour, represented in the following compact form:

$$iO_p\otimes\mathcal{Q}(t,t') = \mathcal{I} - \frac{p}{2}F[Q]\otimes\mathcal{Q}(t,t') + \mathcal{S}\ B(t)\langle\sigma(t')\rangle \tag{D.31}$$

where the matrix elements $\mathcal{S}^{\alpha\beta} = \alpha$ does not depend on the time indices.

### D.1.5 Dynamical Equations

Following the same prescription described in Ref. [86], it is straightforward to obtain a closed set of dynamical equations for the response function $R(t,t')$ and the (symmetric) correlation function

$$C(t,t') = \frac{1}{2}[Q^{+-}(t,t') + Q^{-+}(t,t')] \tag{D.32}$$

In particular, the equations of motion for the response function $R(t,t')$ are obtained by taking the difference of the $++$ and $+-$ components of Eq. (D.31), while the ones for $C(t,t')$ are obtained by taking the addition of the $+-$ and $-+$ components. After some algebra, the result is given by:

$$[m\partial_t^2 + z(t)]R(t,t') = \delta(t-t') + \int_0^t dt''\Sigma(t,t'')R(t'',t'), \tag{D.33}$$

$$\begin{aligned}[m\partial_t^2 + z(t)]C(t,t') = &\int_0^t dt''\Sigma(t,t'')C(t'',t') + \int_0^{t'} dt''D(t,t'')R(t',t'')+ \\ &+ B(t)\int_0^{t'} dt''R(t',t'')B(t'')\end{aligned} \tag{D.34}$$

where we have defined the self-energy $\Sigma(t,t')$ and the vertex $D(t,t')$ as the following:

$$\begin{aligned}\Sigma(t,t') = &-4\eta(t-t')\Theta(t_q-t)\Theta(t_q-t')+ \\ &- \frac{p\mathcal{J}(t)\mathcal{J}(t')J^2}{\hbar}\mathrm{Im}\left[C(t,t') - \frac{i\hbar}{2}R(t,t')\right]^{p-1},\end{aligned} \tag{D.35}$$

$$\begin{aligned}D(t,t') = &2\hbar_0\nu(t-t')\Theta(t_q-t)\Theta(t_q-t')+ \\ &+ \frac{p\mathcal{J}(t)\mathcal{J}(t')J^2}{2}\mathrm{Re}\left[C(t,t') - \frac{i}{2}(\hbar R(t,t') + \hbar R(t',t))\right]^{p-1}.\end{aligned} \tag{D.36}$$

## D.2 The evolution equation for the Lagrange multiplier

In this section we discuss how to self-consistently determine the Lagrange multiplier $z(t)$. The approach typically used in literature [86] consists in evaluating Eq. (4.35) at equal times $t' = t$:

$$z(t) = \int_0^t du\{\Sigma(t,u)C(u,t) + D(t,u)R(t,u)\} - m\partial_t^2 C(t,t')\big|_{t'\to t}. \tag{D.37}$$

However, we observe that Eq. (D.37) leads to ambiguities, as it tautologically depends on the second derivative of $C(t,t')$ at equal times. While this issue is irrelevant when the system is either coupled to an external bath [86] or evolves under energy-conserved dynamics [89, 143], Eq. (D.37) does not determine $z(t)$ for the driven dynamics and in absence of an external bath that we study for $t > t_b$. We solve this issue by

determining $z(t)$ straightforwardly from the spherical constraint. Specifically, we take the total derivative of the constraint equation $C(t,t) = 1$ multiple times and obtain:

$$\begin{aligned} 0 = \frac{d}{dt}C(t,t) &= \lim_{t'\to t} \partial_t C(t,t') \\ 0 = \frac{d^2}{dt^2}C(t,t) &= \lim_{t'\to t} [\partial_t^2 C(t,t') + \partial_t \partial_{t'} C(t,t')] \\ 0 = \frac{d^2}{dt^3}C(t,t) &= \lim_{t'\to t} [\partial_t^3 C(t,t') + 3\partial_t^2 \partial_{t'} C(t,t')] \end{aligned} \tag{D.38}$$

where we also made use of the symmetry relation $C(t,t') = C(t',t)$. It is easy to realize that the first of Eqs. (D.38) corresponds to some of the equal-time conditions described in Eqs. (4.41), that the second one is useless, as $\partial_t \partial_{t'} C(t,t')$ can not be computed using Eqs.(4.34) and (4.35), and that the third one can be rewritten in terms of the derivatives, with respect to $t$ and $t'$ respectively, of both sides of Eq. (4.35). After some algebra, we obtain:

$$\begin{aligned} \frac{dz}{dt} = &\int_0^t du \{\partial_t \Sigma(t,u) C(t,u) + \partial_t D(t,u) R(t,u) + 3\Sigma(t,u)\partial_t C(t,u) + 3D(t,u)\partial_t R(t,u)\} + \\ &+ \partial_t B(t) \int_0^t du R(t,u) B(u) + 3B(t) \int_0^t du \partial_t R(t,u) B(u) \end{aligned} \tag{D.39}$$

From Eq. (D.39) it is easy to determine the Lagrange multiplier in a causal form, as

$$\begin{aligned} z(t) = &\int_{t_0}^t ds \int_0^s du \{\partial_s \Sigma(s,u) C(t,u) + \partial_s D(s,u) R(s,u) + 3\Sigma(s,u)\partial_s C(s,u) + 3D(s,u)\partial_s R(s,u)\} \\ &+ \int_{t_0}^t ds \int_0^s du \Big\{\partial_s B(s) R(t,u) B(u) + 3B(s)\partial_s R(s,u) B(u)\Big\} + z(t_0) \end{aligned} \tag{D.40}$$

provided that we can access the value $z(t_0)$, for some $t_0$. Thus we first solve numerically the dissipative dynamics generated from Eqs. (4.34) and (4.35), for $0 < t < t_b$, using the standard expression from Eq. (D.37), then solve the "closed dynamics" for $t > t_b$ using the expression from Eq. (D.40), imposing continuity with the value $z(t_b)$, obtained from the previous algorithm. In the following, we will always set $m = J = 1$ and $p = 3$.

## D.3 Predictor-corrector scheme for the Mode-Coupling equations

To solve the Eqs. (4.34) and (4.35) of the main text, we first introduce a discrete time step $\Delta t$ and rewrite the two continuous times indices as $t = n\Delta t$ and $t' = m\Delta t$. We use a "forward" discretization scheme for the time derivatives, that is

$$\partial_t f(t,t') \approx (f_{n+1,m} - f_{n,m})/\Delta t \ , \tag{D.41}$$

for every two-point function $f(t,t')$. With this notation, the discretized version of Eqs. (4.34) and (4.35) equations is

$$\begin{cases} R_{n+1,m} = R_{n,m} + \Pi^{(R)}_{n,m}\Delta t/M \\ C_{n+1,m} = C_{n,m} + \Pi^{(C)}_{n,m}\Delta t/M \\ \Pi^{(R)}_{n+1,m} = \Pi^{(R)}_{n,m} - z_n \Delta t R_{n,m} + \delta_{n,m} + \Delta t F^{(1)}_{n,m} \\ \Pi^{(C)}_{n+1,m} = \Pi^{(C)}_{n,m} - z_n \Delta t C_{n,m} + \Delta t F^{(2)}_{n,m} \end{cases}$$

where

$$\begin{cases} F^{(1)}_{n,m} = \Delta t \sum_{j=m}^{n} \Sigma_{nj} R_{jm} \\ F^{(2)}_{n,m} = \Delta t \Big\{ \sum_{j=0}^{m} D_{nj} R_{jm} + \sum_{j=0}^{n} \Sigma_{nj} C_{jm} \Big\} \\ \Sigma_{n,m} = -\dfrac{p\mathcal{J}_n \mathcal{J}_m J^2}{\hbar} \mathrm{Im}\Big[ C_{n,m} - \dfrac{i\hbar}{2} R_{n,m} \Big]^{p-1} - 4\eta_{n,m}\Theta(t_b - n\Delta t)\Theta(t_b - m\Delta t) \\ D_{n,m} = \dfrac{p\mathcal{J}_n \mathcal{J}_m J^2}{\hbar} \mathrm{Re}\Big[ C_{n,m} - \dfrac{i\hbar}{2}\big(R_{n,m} + R_{m,n}\big) \Big]^{p-1} + 2\hbar\nu_{n,m}\Theta(t_b - n\Delta t)\Theta(t_b - m\Delta t) \end{cases} \tag{D.42}$$

where $\mathcal{J}_n = \mathcal{J}(n\Delta t)$. The equal time conditions (4.41) here assume the simple form

$$C_{n,n} = 0 \ , \qquad R_{n,n} = \Pi^{(R)}_{n,n} = \Pi^{(C)}_{n,n} = 0 \ . \tag{D.43}$$

It is easy to note that Eqs. (D.42) are causal, implying that we can iteratively compute each minor matrix $C_{0\le i\le n, 0\le j\le n}$ from the knowledge of $C_{0\le i\le n-1, 0\le j\le n-1}$. To understand in detail why, we notice that the row $C_{n,0\le j\le n-1}$ can be straightforwardly computed from the minor $C_{0\le i\le n-1,0\le j\le n-1}$ using Eqs. (D.42), then the column $C_{0\le i\le n-1,n}$ is immediately obtained from the symmetry relation $C_{n,m} = C_{m,n}$ and the diagonal element $C_{n,n} = 1$ is given by the spherical constraint. The same reasoning holds for the response function, with the only difference that $R_{n,m}$ is not symmetric and instead $R_{0\le i\le n-1,n} = 0$ due to causality.

We aim to integrate Eqs. (4.34) and (4.35) to some finite time $t_{max} = n_{steps}\Delta t$. With the discretization we chose, the error we make is of order $n_{steps}\Delta t^2$. In order to increase the precision of our results, we improve our method by employing a predictor-corrector algorithm, already used in a similar context in Ref. [193]. In a nutshell, we first predict the $(n+1)$-th row of the correlation and response function using Eq. (D.42), then we correct our result by inserting the result of the prediction in the right-hand sides of the

following equations of motion:

$$\begin{cases} \Pi^{(R)}_{n+1,m} = \Pi^{(R)}_{n,m} - \Delta t \dfrac{z_n R_{n,m} + z_{n+1} R_{n+1,m}}{2} + \delta_{n,m} + \Delta t \dfrac{F^{(1)}_{n,m} + F^{(1)}_{n+1,m}}{2} \\ \Pi^{(C)}_{n+1,m} = \Pi^{(C)}_{n,m} - \Delta t \dfrac{z_n C_{n,m} + z_{n+1} C_{n+1,m}}{2} + \delta_{n,m} + \Delta t \dfrac{F^{(2)}_{n,m} + F^{(2)}_{n+1,m}}{2} \\ R_{n+1,m} = R_{n,m} + \Delta t \dfrac{\Pi^{(R)}_{n,m} + \Pi^{(R)}_{n+1,m}}{2m} \\ C_{n+1,m} = C_{n,m} + \Delta t \dfrac{\Pi^{(C)}_{n,m} + \Pi^{(C)}_{n+1,m}}{2m} \end{cases} \tag{D.44}$$

For each $n$-th step, we take a loop over the predictor-corrector scheme $\mathcal{N}_L$ times. In this way, the error we make is of order $n_{steps}\Delta t^{(1+\mathcal{N}_L)}$. For the results presented in the main text, we have always fixed $\mathcal{N}_L = 2$.

At this point, we observe that Eqs. (D.44) alone still do not determine the Lagrange multiplier $z_n$, which is in principle determined by the non-causal equation (equivalent to Eq. (D.37) of the main text):

$$z_n = -\frac{\Pi^{(C)}_{n+1,n} - \Pi^{(C)}_{n,n}}{\Delta t} + \Delta t F^{(2)}_{n,m} \tag{D.45}$$

As long as the system is coupled to a thermal bath, we solve this issue by making the physical assumption that, due to dissipation, $z_n$ converges at large times to a stationary value, as also observed in Ref. [86]. Due to this asymptotic convergence, we can safely replace the difference $\Pi^{(C)}_{n+1,n} - \Pi^{(C)}_{n,n}$ with the one evaluated at the previous time step, $\Pi^{(C)}_{n,n} - \Pi^{(C)}_{n,n-1}$, in Eq. (D.45). However, this substitution is not valid for $t > t_b$, where the dynamics is isolated and periodically driven. In latter scenario, we proceed as discussed in Section D.2 and include the discretized version of Eq. (D.39) in the system of Eqs. (D.42), so that also $z_n$ can be computed using the predictor-corrector algorithm.

# Bibliography


[1] Lorenzo Correale and Alessandro Silva. Changing the order of a dynamical phase transition through fluctuations in a quantum p-spin model, 2021. URL https://arxiv.org/abs/2110.13524.

[2] Lorenzo Correale, Anatoli Polkovnikov, Marco Schirò, and Alessandro Silva. Probing semi-classical chaos in the spherical $p$-spin glass model. 2023. doi: 10.48550/ARXIV.2303.15393. URL https://arxiv.org/abs/2303.15393.

[3] Guido Giachetti, Andrea Solfanelli, Lorenzo Correale, and Nicolò Defenu. Fractal nature of high-order time crystal phases. *Phys. Rev. B*, 108:L140102, Oct 2023. doi: 10.1103/PhysRevB.108.L140102. URL https://link.aps.org/doi/10.1103/PhysRevB.108.L140102.

[4] H. Poincaré. *Les méthodes nouvelles de la mécanique céleste*. Les grands classiques Gauthier-Villars. Librairie Albert Blanchad, 1987. ISBN 9782853670937. URL https://books.google.it/books?id=8eJUAAAAYAAJ.

[5] Edward N. Lorenz. Deterministic nonperiodic flow. *Journal of the Atmospheric Sciences*, 20(2):130–141, March 1963. doi: 10.1175/1520-0469(1963)020<0130:dnf>2.0.co;2. URL https://doi.org/10.1175/1520-0469(1963)020<0130:dnf>2.0.co;2.

[6] Edward Lorenz. *Predictability: does the flap of a butterfly's wing in Brazil set off a tornado in Texas?* na, 1972. URL https://mathsciencehistory.com/wp-content/uploads/2020/03/132_kap6_lorenz_artikel_the_butterfly_effect.pdf.

[7] Eberhard Hopf. Abzweigung einer periodischen lösung von einer stationären lösung eines differentialsystems. *Ber. Math.-Phys. Kl Sächs. Akad. Wiss. Leipzig*, 94:1–22, 1942.

[8] A. N. Kolmogorov. A new metric invariant of transitive dynamical systems and automorphisms of Lebesgue spaces. *Trudy Mat. Inst. Steklov.*, 169:94–98, 254, 1985. ISSN 0371-9685. Topology, ordinary differential equations, dynamical systems.

[9] Vladimir I Arnold. Proof of a theorem of an kolmogorov on the invariance of quasi-periodic motions under small perturbations of the hamiltonian. *Collected Works: Representations of Functions, Celestial Mechanics and KAM Theory, 1957–1965*, pages 267–294, 2009.

[10] J Möser. On invariant curves of area-preserving mappings of an annulus. *Nachr. Akad. Wiss. Göttingen, II*, pages 1–20, 1962.

[11] V. I. Arnold. *Mathematical Methods of Classical Mechanics*. Springer New York, 1978. doi: 10.1007/978-1-4757-1693-1. URL https://doi.org/10.1007/978-1-4757-1693-1.

[12] H.S. Dumas. *The KAM Story: A Friendly Introduction to the Content, History, and Significance of Classical Kolmogorov-Arnold-Moser Theory*. G - Reference,Information and Interdisciplinary Subjects Series. World Scientific, 2014. ISBN 9789814556583. URL https://books.google.it/books?id=8QkOnwEACAAJ.

[13] B V Chirikov. *Research concerning the theory of non-linear resonance and stochasticity*. CERN, Geneva, 1971. URL https://cds.cern.ch/record/325497. Translated at CERN from the Russian (IYAF-267-TRANS-E).

[14] A. Vulpiani. *Chaos: From Simple Models to Complex Systems*. Series on advances in statistical mechanics. World Scientific, 2010. ISBN 9789814277662. URL https://books.google.it/books?id=_TuaDQAAQBAJ.

[15] H. Poincaré. Sur un théorème de géométrie. *Rendiconti del Circolo Matematico di Palermo*, 33(1):375–407, December 1912. doi: 10.1007/bf03015314. URL https://doi.org/10.1007/bf03015314.

[16] George D. Birkhoff. Proof of poincare's geometric theorem. *Transactions of the American Mathematical Society*, 14(1):14, January 1913. doi: 10.2307/1988766. URL https://doi.org/10.2307/1988766.

[17] K. Huang. *Statistical Mechanics*. Wiley, 1987. ISBN 9780471815181. URL https://books.google.it/books?id=M8PvAAAAMAAJ.

[18] Marcos Rigol, Vanja Dunjko, and Maxim Olshanii. Thermalization and its mechanism for generic isolated quantum systems. *Nature*, 452(7189):854–858, April 2008. doi: 10.1038/nature06838. URL https://doi.org/10.1038/nature06838.

[19] Mark Srednicki. Chaos and quantum thermalization. *Phys. Rev. E*, 50:888–901, Aug 1994. doi: 10.1103/PhysRevE.50.888. URL https://link.aps.org/doi/10.1103/PhysRevE.50.888.

[20] J. M. Deutsch. Quantum statistical mechanics in a closed system. *Phys. Rev. A*, 43:2046–2049, Feb 1991. doi: 10.1103/PhysRevA.43.2046. URL https://link.aps.org/doi/10.1103/PhysRevA.43.2046.

[21] Laura Foini and Jorge Kurchan. Eigenstate thermalization hypothesis and out of time order correlators. *Phys. Rev. E*, 99:042139, Apr 2019. doi: 10.1103/PhysRevE.99.042139. URL https://link.aps.org/doi/10.1103/PhysRevE.99.042139.

[22] Silvia Pappalardi, Laura Foini, and Jorge Kurchan. Eigenstate thermalization hypothesis and free probability. *Phys. Rev. Lett.*, 129:170603, Oct 2022. doi: 10.1103/PhysRevLett.129.170603. URL https://link.aps.org/doi/10.1103/PhysRevLett.129.170603.

[23] Silvia Pappalardi, Felix Fritzsch, and Toma Prosen. General eigenstate thermalization via free cumulants in quantum lattice systems, 2023. URL https://arxiv.org/abs/2303.00713.

[24] Luca D'Alessio, Yariv Kafri, Anatoli Polkovnikov, and Marcos Rigol. From quantum chaos and eigenstate thermalization to statistical mechanics and thermodynamics. *Advances in Physics*, 65(3):239–362, May 2016. doi: 10.1080/00018732.2016.1198134. URL https://doi.org/10.1080/00018732.2016.1198134.

[25] Luca D'Alessio and Marcos Rigol. Long-time behavior of isolated periodically driven interacting lattice systems. *Phys. Rev. X*, 4(4), December 2014. URL https://doi.org/10.1103/physrevx.4.041048.

[26] Achilleas Lazarides, Arnab Das, and Roderich Moessner. Equilibrium states of generic quantum systems subject to periodic driving. *Phys. Rev. E*, 90(1), July 2014. URL https://doi.org/10.1103/physreve.90.012110.

[27] Pedro Ponte, Anushya Chandran, Z. Papić, and Dmitry A. Abanin. Periodically driven ergodic and many-body localized quantum systems. *Ann. Phys.*, 353:196–204, February 2015. doi: 10.1016/j.aop.2014.11.008. URL https://doi.org/10.1016/j.aop.2014.11.008.

[28] Antonio Rubio-Abadal, Matteo Ippoliti, Simon Hollerith, David Wei, Jun Rui, S. L. Sondhi, Vedika Khemani, Christian Gross, and Immanuel Bloch. Floquet prethermalization in a bose-hubbard system. *Phys. Rev. X*, 10:021044, May 2020. doi: 10.1103/PhysRevX.10.021044. URL https://link.aps.org/doi/10.1103/PhysRevX.10.021044.

[29] Atanu Rajak, Roberta Citro, and Emanuele G Dalla Torre. Stability and prethermalization in chains of classical kicked rotors. *J. Phys. A: Math. Theor.l*, 51(46):465001, October 2018. doi: 10.1088/1751-8121/aae294. URL https://doi.org/10.1088/1751-8121/aae294.

[30] Atanu Rajak, Itzhack Dana, and Emanuele G. Dalla Torre. Characterizations of prethermal states in periodically driven many-body systems with unbounded chaotic diffusion. *Phys. Rev. B*, 100(10), September 2019. doi: 10.1103/physrevb.100.100302. URL https://doi.org/10.1103/physrevb.100.100302.

[31] Yonathan Sadia, Emanuele G. Dalla Torre, and Atanu Rajak. From prethermalization to chaos in periodically driven coupled rotors. *Phys. Rev. B*, 105(18), May 2022. doi: 10.1103/physrevb.105.184302. URL https://doi.org/10.1103/physrevb.105.184302.

[32] Francesco Peronaci, Marco Schiró, and Olivier Parcollet. Resonant Thermalization of Periodically Driven Strongly Correlated Electrons. *Physical Review Letters*, 120(19):197601, May 2018. ISSN 10797114. doi: 10.1103/PhysRevLett.120.197601.

[33] Owen Howell, Phillip Weinberg, Dries Sels, Anatoli Polkovnikov, and Marin Bukov. Asymptotic prethermalization in periodically driven classical spin chains. *Phys. Rev. Lett.*, 122(1), January 2019. URL https://doi.org/10.1103/physrevlett.122.010602.

[34] Andrea Pizzi, Andreas Nunnenkamp, and Johannes Knolle. Classical prethermal phases of matter. *Phys. Rev. Lett.*, 127(14), September 2021. URL https://doi.org/10.1103/physrevlett.127.140602.

[35] Giorgio Parisi and Jonathan Machta. Statistical field theory. *Am. J. Phys.*, 57 (3):286–287, March 1989. doi: 10.1119/1.16061. URL https://doi.org/10.1119/1.16061.

[36] Davide Rossini, Alessandro Silva, Giuseppe Mussardo, and Giuseppe E. Santoro. Effective thermal dynamics following a quantum quench in a spin chain. *Phys. Rev. Lett.*, 102:127204, Mar 2009. doi: 10.1103/PhysRevLett.102.127204. URL https://link.aps.org/doi/10.1103/PhysRevLett.102.127204.

[37] Pasquale Calabrese, Fabian H. L. Essler, and Maurizio Fagotti. Quantum quench in the transverse-field ising chain. *Phys. Rev. Lett.*, 106:227203, Jun 2011. doi: 10.1103/PhysRevLett.106.227203. URL https://link.aps.org/doi/10.1103/PhysRevLett.106.227203.

[38] Anna Maraga, Pietro Smacchia, Michele Fabrizio, and Alessandro Silva. Nonadiabatic stationary behavior in a driven low-dimensional gapped system. *Phys. Rev. B*, 90:041111, Jul 2014. doi: 10.1103/PhysRevB.90.041111. URL https://link.aps.org/doi/10.1103/PhysRevB.90.041111.

[39] Anatoli Polkovnikov. Universal adiabatic dynamics in the vicinity of a quantum critical point. *Phys. Rev. B*, 72:161201, Oct 2005. doi: 10.1103/PhysRevB.72.161201. URL https://link.aps.org/doi/10.1103/PhysRevB.72.161201.

[40] Wojciech H. Zurek, Uwe Dorner, and Peter Zoller. Dynamics of a quantum phase transition. *Phys. Rev. Lett.*, 95:105701, Sep 2005. doi: 10.1103/PhysRevLett.95.105701. URL https://link.aps.org/doi/10.1103/PhysRevLett.95.105701.

[41] Jacek Dziarmaga. Dynamics of a quantum phase transition: Exact solution of the quantum ising model. *Phys. Rev. Lett.*, 95:245701, Dec 2005. doi: 10.1103/PhysRevLett.95.245701. URL https://link.aps.org/doi/10.1103/PhysRevLett.95.245701.

[42] R. W. Cherng and L. S. Levitov. Entropy and correlation functions of a driven quantum spin chain. *Phys. Rev. A*, 73:043614, Apr 2006. doi: 10.1103/PhysRevA.73.043614. URL https://link.aps.org/doi/10.1103/PhysRevA.73.043614.

[43] Markus Heyl, Anatoli Polkovnikov, and Stefan Kehrein. Dynamical quantum phase transitions in the transverse-field ising model. *Phys. Rev. Lett.*, 110(13): 135704, 2013.

[44] Markus Heyl. Dynamical quantum phase transitions: a review. *Reports on Progress in Physics*, 81(5):054001, apr 2018. doi: 10.1088/1361-6633/aaaf9a. URL https://doi.org/10.1088/1361-6633/aaaf9a.

[45] Simon A. Weidinger, Markus Heyl, Alessandro Silva, and Michael Knap. Dynamical quantum phase transitions in systems with continuous symmetry breaking. *Phys. Rev. B*, 96:134313, Oct 2017. doi: 10.1103/PhysRevB.96.134313. URL https://link.aps.org/doi/10.1103/PhysRevB.96.134313.

[46] Bojan Žunkovič, Markus Heyl, Michael Knap, and Alessandro Silva. Dynamical quantum phase transitions in spin chains with long-range interactions: Merging different concepts of nonequilibrium criticality. *Phys. Rev. Lett.*, 120:130601, Mar 2018. doi: 10.1103/PhysRevLett.120.130601. URL https://link.aps.org/doi/10.1103/PhysRevLett.120.130601.

[47] Bruno Sciolla and Giulio Biroli. Dynamical transitions and quantum quenches in mean-field models. *J. Stat. Mech.*, 2011(11):P11003, November 2011. doi: 10.1088/1742-5468/2011/11/p11003. URL https://doi.org/10.1088/1742-5468/2011/11/p11003.

[48] P. Jurcevic, H. Shen, P. Hauke, C. Maier, T. Brydges, C. Hempel, B. P. Lanyon, M. Heyl, R. Blatt, and C. F. Roos. Direct observation of dynamical quantum phase transitions in an interacting many-body system. *Phys. Rev. Lett.*, 119: 080501, Aug 2017. doi: 10.1103/PhysRevLett.119.080501. URL https://link.aps.org/doi/10.1103/PhysRevLett.119.080501.

[49] Alessio Lerose, Jamir Marino, Bojan Žunkovič, Andrea Gambassi, and Alessandro Silva. Chaotic dynamical ferromagnetic phase induced by nonequilibrium quantum fluctuations. *Phys. Rev. Lett.*, 120:130603, Mar 2018. doi: 10.1103/PhysRevLett.120.130603. URL https://link.aps.org/doi/10.1103/PhysRevLett.120.130603.

[50] Alessio Lerose, Bojan Žunkovič, Jamir Marino, Andrea Gambassi, and Alessandro Silva. Impact of nonequilibrium fluctuations on prethermal dynamical phase transitions in long-range interacting spin chains. *Phys. Rev. B*, 99(4), January 2019. doi: 10.1103/physrevb.99.045128. URL https://doi.org/10.1103/physrevb.99.045128.

[51] Giulia Piccitto, Bojan Žunkovič, and Alessandro Silva. Dynamical phase diagram of a quantum ising chain with long-range interactions. *Phys. Rev. B*, 100:180402, Nov 2019. doi: 10.1103/PhysRevB.100.180402. URL https://link.aps.org/doi/10.1103/PhysRevB.100.180402.

[52] Giulia Piccitto and Alessandro Silva. Crossover from fast to slow dynamics in a long range interacting ising chain. *J. Stat. Mech.*, 2019(9):094017, sep 2019.

doi: 10.1088/1742-5468/ab3a27. URL https://doi.org/10.1088/1742-5468/ab3a27.

[53] Elena Canovi, Philipp Werner, and Martin Eckstein. First-order dynamical phase transitions. *Phys. Rev. Lett.*, 113:265702, Dec 2014. doi: 10.1103/PhysRevLett.113.265702. URL https://link.aps.org/doi/10.1103/PhysRevLett.113.265702.

[54] Pei Wang and Rosario Fazio. Dissipative phase transitions in the fully connected ising model with p -spin interaction. *Phys. Rev. A*, 103(1), January 2021. doi: 10.1103/physreva.103.013306. URL https://doi.org/10.1103/physreva.103.013306.

[55] Andreas Rückriegel, Andreas Kreisel, and Peter Kopietz. Time-dependent spin-wave theory. *Phys. Rev. B*, 85(5), February 2012. doi: 10.1103/physrevb.85.054422. URL https://doi.org/10.1103/physrevb.85.054422.

[56] R.K. Pathria and Paul D. Beale. Fluctuations and nonequilibrium statistical mechanics. In *Statistical Mechanics*, pages 583–635. Elsevier, 2011. doi: 10.1016/b978-0-12-382188-1.00015-3. URL https://doi.org/10.1016/b978-0-12-382188-1.00015-3.

[57] Alessio Lerose and Silvia Pappalardi. Origin of the slow growth of entanglement entropy in long-range interacting spin systems. *Phys. Rev. Res.*, 2:012041, Feb 2020. doi: 10.1103/PhysRevResearch.2.012041. URL https://link.aps.org/doi/10.1103/PhysRevResearch.2.012041.

[58] B. Derrida. Random-energy model: Limit of a family of disordered models. *Phys. Rev. Lett.*, 45(2):79–82, July 1980. doi: 10.1103/physrevlett.45.79. URL https://doi.org/10.1103/physrevlett.45.79.

[59] Bernard Derrida. Random-energy model: An exactly solvable model of disordered systems. *Phys. Rev. B*, 24(5):2613–2626, September 1981. doi: 10.1103/physrevb.24.2613. URL https://doi.org/10.1103/physrevb.24.2613.

[60] T. Jörg, F. Krzakala, J. Kurchan, A. C. Maggs, and J. Pujos. Energy gaps in quantum first-order mean-field–like transitions: The problems that quantum annealing cannot solve. *EPL (Europhys. Lett.)*, 89(4):40004, February 2010. doi: 10.1209/0295-5075/89/40004. URL https://doi.org/10.1209/0295-5075/89/40004.

[61] Victor Bapst and Guilhem Semerjian. On quantum mean-field models and their quantum annealing. *J. Stat. Mech.*, 2012(06):P06007, June 2012. doi: 10.1088/1742-5468/2012/06/p06007. URL https://doi.org/10.1088/1742-5468/2012/06/p06007.

[62] Arnab Das, K. Sengupta, Diptiman Sen, and Bikas K. Chakrabarti. Infinite-range ising ferromagnet in a time-dependent transverse magnetic field: Quench and ac dynamics near the quantum critical point. *Phys. Rev. B*, 74(14), October 2006.

doi: 10.1103/physrevb.74.144423. URL https://doi.org/10.1103/physrevb.74.144423.

[63] Michele Filippone, Sébastien Dusuel, and Julien Vidal. Quantum phase transitions in fully connected spin models: An entanglement perspective. *Phys. Rev. A*, 83:022327, Feb 2011. doi: 10.1103/PhysRevA.83.022327. URL https://link.aps.org/doi/10.1103/PhysRevA.83.022327.

[64] Manuel H. Muñoz Arias, Ivan H. Deutsch, Poul S. Jessen, and Pablo M. Poggi. Simulation of the complex dynamics of mean-field $p$-spin models using measurement-based quantum feedback control. *Phys. Rev. A*, 102:022610, Aug 2020. doi: 10.1103/PhysRevA.102.022610. URL https://link.aps.org/doi/10.1103/PhysRevA.102.022610.

[65] J Keeling, MJ Bhaseen, and BD Simons. Collective dynamics of bose-einstein condensates in optical cavities. *Phys. Rev. Lett.*, 105(4):043001, 2010.

[66] A. Gambassi and P. Calabrese. Quantum quenches as classical critical films. *EPL (Europhys. Lett.)*, 95(6):66007, September 2011. doi: 10.1209/0295-5075/95/66007. URL https://doi.org/10.1209/0295-5075/95/66007.

[67] Amit Dutta and JK Bhattacharjee. Phase transitions in the quantum ising and rotor models with a long-range interaction. *Phys. Rev. B*, 64(18):184106, 2001.

[68] Takashi Mori, Tatsuhiko N Ikeda, Eriko Kaminishi, and Masahito Ueda. Thermalization and prethermalization in isolated quantum systems: a theoretical overview. *J. Phys. B: At. Mol. Opt. Phys.*, 51(11):112001, May 2018. doi: 10.1088/1361-6455/aabcdf. URL https://doi.org/10.1088/1361-6455/aabcdf.

[69] M. Gring, M. Kuhnert, T. Langen, T. Kitagawa, B. Rauer, M. Schreitl, I. Mazets, D. Adu Smith, E. Demler, and J. Schmiedmayer. Relaxation and prethermalization in an isolated quantum system. *Science*, 337(6100):1318–1322, September 2012. doi: 10.1126/science.1224953. URL https://doi.org/10.1126/science.1224953.

[70] Tim Langen, Thomas Gasenzer, and Jörg Schmiedmayer. Prethermalization and universal dynamics in near-integrable quantum systems. *J. Stat. Mech.*, 2016(6):064009, June 2016. doi: 10.1088/1742-5468/2016/06/064009. URL https://doi.org/10.1088/1742-5468/2016/06/064009.

[71] Assa Auerbach. *Interacting electrons and quantum magnetism*. Springer Science & Business Media, 2012.

[72] V. Cannella, J. A. Mydosh, and J. I. Budnick. Magnetic susceptibility of au–fe alloys. *J. Appl. Phys.*, 42(4):1689–1690, March 1971. doi: 10.1063/1.1660392. URL https://doi.org/10.1063/1.1660392.

[73] S F Edwards and P W Anderson. Theory of spin glasses. *J. Phys. F: Met. Phys.*, 5(5):965–974, May 1975. doi: 10.1088/0305-4608/5/5/017. URL https://doi.org/10.1088/0305-4608/5/5/017.

[74] A. Crisanti and H.-J. Sommers. Thouless-anderson-palmer approach to the spherical p-spin spin glass model. *Journal de Physique I*, 5(7):805–813, July 1995. doi: 10.1051/jp1:1995164. URL https://doi.org/10.1051/jp1:1995164.

[75] Andrea Cavagna, Irene Giardina, and Giorgio Parisi. Stationary points of the thouless-anderson-palmer free energy. *Phys. Rev. B*, 57(18):11251–11257, May 1998. doi: 10.1103/physrevb.57.11251. URL https://doi.org/10.1103/physrevb.57.11251.

[76] Andrea Cavagna, Juan P. Garrahan, and Irene Giardina. Index distribution of random matrices with an application to disordered systems. *Phys. Rev. B*, 61 (6):3960–3970, February 2000. doi: 10.1103/physrevb.61.3960. URL https://doi.org/10.1103/physrevb.61.3960.

[77] Valentina Ros. Distribution of rare saddles in the p-spin energy landscape. *J. Phys. A: Math. Theor.l*, 53(12):125002, March 2020. doi: 10.1088/1751-8121/ab73ac. URL https://doi.org/10.1088/1751-8121/ab73ac.

[78] V. Ros, G. Biroli, and C. Cammarota. Complexity of energy barriers in mean-field glassy systems. *EPL (Europhys. Lett.)*, 126(2):20003, May 2019. doi: 10.1209/0295-5075/126/20003. URL https://doi.org/10.1209/0295-5075/126/20003.

[79] Valentina Ros, Giulio Biroli, and Chiara Cammarota. Dynamical instantons and activated processes in mean-field glass models. *SciPost Physics*, 10(1), January 2021. doi: 10.21468/scipostphys.10.1.002. URL https://doi.org/10.21468/scipostphys.10.1.002.

[80] Tommaso Rizzo. Path integral approach unveils role of complex energy landscape for activated dynamics of glassy systems. *Phys. Rev. B*, 104(9), September 2021. doi: 10.1103/physrevb.104.094203. URL https://doi.org/10.1103/physrevb.104.094203.

[81] L. F. Cugliandolo and J. Kurchan. Analytical solution of the off-equilibrium dynamics of a long-range spin-glass model. *Phys. Rev. Lett.*, 71(1):173–176, July 1993. doi: 10.1103/physrevlett.71.173. URL https://doi.org/10.1103/physrevlett.71.173.

[82] Jean-Philippe Bouchaud, Leticia F. Cugliandolo, Jorge Kurchan, and Marc Mézard. Out of equilibrium dynamics in spin-glasses and other glassy systems. In *Series on Directions in Condensed Matter Physics*, pages 161–223. WORLD SCIENTIFIC, December 1997. doi: 10.1142/9789812819437_0006. URL https://doi.org/10.1142/9789812819437_0006.

[83] Karl Heinz Hoffmann and Paolo Sibani. Relaxation and aging in spin glasses and other complex systems. *Zeitschrift fur Physik B Condensed Matter*, 80(3): 429–438, October 1990. doi: 10.1007/bf01323526. URL https://doi.org/10.1007/bf01323526.

[84] P. Granberg, P. Svedlindh, P. Nordblad, and L. Lundgren. Experiments on relaxation in metallic spin glasses. In *Heidelberg Colloquium on Glassy Dynamics*, pages 40–50. Springer Berlin Heidelberg, 1987. doi: 10.1007/bfb0057508. URL https://doi.org/10.1007/bfb0057508.

[85] Wenhao Wu, B. Ellman, T. Rosenbaum, G. Aeppli, and D. Reich. From classical to quantum glass. *Phys. Rev. Lett.*, 67(15):2076–2079, October 1991. doi: 10.1103/physrevlett.67.2076. URL https://doi.org/10.1103/physrevlett.67.2076.

[86] Leticia F. Cugliandolo and Gustavo Lozano. Real-time nonequilibrium dynamics of quantum glassy systems. *Phys. Rev. B*, 59(2):915–942, January 1999. doi: 10.1103/physrevb.59.915. URL https://doi.org/10.1103/physrevb.59.915.

[87] Leticia F. Cugliandolo, Daniel R. Grempel, and Constantino A. da Silva Santos. From second to first order transitions in a disordered quantum magnet. *Phys. Rev. Lett.*, 85:2589–2592, Sep 2000. doi: 10.1103/PhysRevLett.85.2589. URL https://link.aps.org/doi/10.1103/PhysRevLett.85.2589.

[88] Leticia F. Cugliandolo, D. R. Grempel, and Constantino A. da Silva Santos. Imaginary-time replica formalism study of a quantum spherical p-spin-glass model. *Phys. Rev. B*, 64:014403, Jun 2001. doi: 10.1103/PhysRevB.64.014403. URL https://link.aps.org/doi/10.1103/PhysRevB.64.014403.

[89] S. J. Thomson, P. Urbani, and M. Schiró. Quantum quenches in isolated quantum glasses out of equilibrium. *Phys. Rev. Lett.*, 125(12), September 2020. doi: 10.1103/physrevlett.125.120602. URL https://doi.org/10.1103/physrevlett.125.120602.

[90] Pierfrancesco Urbani. Quantum exploration of high-dimensional canyon landscapes, 2023. URL https://arxiv.org/abs/2301.11236.

[91] Davide Facoetti, Giulio Biroli, Jorge Kurchan, and David R. Reichman. Classical glasses, black holes, and strange quantum liquids. *Phys. Rev. B*, 100:205108, Nov 2019. doi: 10.1103/PhysRevB.100.205108. URL https://link.aps.org/doi/10.1103/PhysRevB.100.205108.

[92] Silvia Pappalardi, Anatoli Polkovnikov, and Alessandro Silva. Quantum echo dynamics in the Sherrington-Kirkpatrick model. *SciPost Phys.*, 9:021, 2020. doi: 10.21468/SciPostPhys.9.2.021. URL https://scipost.org/10.21468/SciPostPhys.9.2.021.

[93] Surajit Bera, K. Y. Venkata Lokesh, and Sumilan Banerjee. Quantum-to-classical crossover in many-body chaos and scrambling from relaxation in a glass. *Phys. Rev. Lett.*, 128:115302, Mar 2022. doi: 10.1103/PhysRevLett.128.115302. URL https://link.aps.org/doi/10.1103/PhysRevLett.128.115302.

[94] Tarek Anous and Felix M Haehl. The quantum p-spin glass model: a user manual for holographers. *J. Stat. Mech.*, 2021(11):113101, nov 2021. doi: 10.1088/1742-5468/ac2cb9. URL https://dx.doi.org/10.1088/1742-5468/ac2cb9.

[95] Michael Winer, Richard Barney, Christopher L. Baldwin, Victor Galitski, and Brian Swingle. Spectral form factor of a quantum spin glass. *J. High Energ. Phys.*, 2022(9), September 2022. doi: 10.1007/jhep09(2022)032. URL https://doi.org/10.1007/jhep09(2022)032.

[96] Michael Saccone, Francesco Caravelli, Kevin Hofhuis, Sergii Parchenko, Yorick A. Birkhölzer, Scott Dhuey, Armin Kleibert, Sebastiaan van Dijken, Cristiano Nisoli, and Alan Farhan. Direct observation of a dynamical glass transition in a nanomagnetic artificial hopfield network. *Nature Physics*, 18(5):517–521, March 2022. doi: 10.1038/s41567-022-01538-7. URL https://doi.org/10.1038/s41567-022-01538-7.

[97] A. I. Larkin and Yu. N. Ovchinnikov. Quasiclassical Method in the Theory of Superconductivity. *Soviet Journal of Experimental and Theoretical Physics*, 28: 1200, June 1969. URL http://jetp.ras.ru/cgi-bin/e/index/e/28/6/p1200?a=list.

[98] Alexei Kitaev. A simple model of quantum holography. *http://online.kitp.ucsb.edu/online/entangled15/kitaev/*, 2015. URL http://online.kitp.ucsb.edu/online/entangled15/kitaev/.

[99] Igor L. Aleiner, Lara Faoro, and Lev B. Ioffe. Microscopic model of quantum butterfly effect: Out-of-time-order correlators and traveling combustion waves. *Ann. Phys.*, 375:378–406, December 2016. doi: 10.1016/j.aop.2016.09.006. URL https://doi.org/10.1016/j.aop.2016.09.006.

[100] Jordan S. Cotler, Dawei Ding, and Geoffrey R. Penington. Out-of-time-order operators and the butterfly effect. *Ann. Phys.*, 396:318–333, September 2018. doi: 10.1016/j.aop.2018.07.020. URL https://doi.org/10.1016/j.aop.2018.07.020.

[101] Juan Maldacena, Stephen H. Shenker, and Douglas Stanford. A bound on chaos. *J. High Energ. Phys.*, 2016(8), August 2016. doi: 10.1007/jhep08(2016)106. URL https://doi.org/10.1007/jhep08(2016)106.

[102] Tianrui Xu, Thomas Scaffidi, and Xiangyu Cao. Does scrambling equal chaos? *Phys. Rev. Lett.*, 124(14):140602, 2020.

[103] Shenglong Xu and Brian Swingle. Scrambling dynamics and out-of-time ordered correlators in quantum many-body systems: a tutorial, 2022. URL https://arxiv.org/abs/2202.07060.

[104] J. Sinai. Flows with finite entropy. *Dokl. Akad. Nauk SSSR*, 125:1200–1202, 1959. ISSN 0002-3264.

[105] A. Hallam, J. G. Morley, and A. G. Green. The lyapunov spectra of quantum thermalisation. *Nature Communications*, 10(1), June 2019. doi: 10.1038/s41467-019-10336-4. URL https://doi.org/10.1038/s41467-019-10336-4.

[106] Hrant Gharibyan, Masanori Hanada, Brian Swingle, and Masaki Tezuka. Quantum lyapunov spectrum. *J. High Energ. Phys.*, 2019(4), April 2019. doi: 10.1007/jhep04(2019)082. URL https://doi.org/10.1007/jhep04(2019)082.

[107] A. M. LYAPUNOV. The general problem of the stability of motion. *International Journal of Control*, 55(3):531–534, March 1992. doi: 10.1080/00207179208934253. URL https://doi.org/10.1080/00207179208934253.

[108] Eugenio Bianchi, Lucas Hackl, and Nelson Yokomizo. Linear growth of the entanglement entropy and the kolmogorov-sinai rate. *J. High Energ. Phys.*, 2018 (3), March 2018. doi: 10.1007/jhep03(2018)025. URL https://doi.org/10.1007/jhep03(2018)025.

[109] Lucas Hackl, Eugenio Bianchi, Ranjan Modak, and Marcos Rigol. Entanglement production in bosonic systems: Linear and logarithmic growth. *Phys. Rev. A*, 97 (3), March 2018. doi: 10.1103/physreva.97.032321. URL https://doi.org/10.1103/physreva.97.032321.

[110] Alessio Lerose and Silvia Pappalardi. Bridging entanglement dynamics and chaos in semiclassical systems. *Phys. Rev. A*, 102:032404, Sep 2020. doi: 10.1103/PhysRevA.102.032404. URL https://link.aps.org/doi/10.1103/PhysRevA.102.032404.

[111] Wen-Long You, Ying-Wai Li, and Shi-Jian Gu. Fidelity, dynamic structure factor, and susceptibility in critical phenomena. *Phys. Rev. E*, 76(2), August 2007. doi: 10.1103/physreve.76.022101. URL https://doi.org/10.1103/physreve.76.022101.

[112] Tyler LeBlond, Dries Sels, Anatoli Polkovnikov, and Marcos Rigol. Universality in the onset of quantum chaos in many-body systems. *Phys. Rev. B*, 104(20), November 2021. doi: 10.1103/physrevb.104.l201117. URL https://doi.org/10.1103/physrevb.104.l201117.

[113] Antonio Auffinger and Gerard Ben Arous. Complexity of random smooth functions on the high-dimensional sphere. *Ann. Probab.*, 41(6), November 2013. doi: 10.1214/13-aop862. URL https://doi.org/10.1214/13-aop862.

[114] Giancarlo Benettin, Luigi Galgani, Antonio Giorgilli, and Jean-Marie Strelcyn. Lyapunov characteristic exponents for smooth dynamical systems and for hamiltonian systems; a method for computing all of them. part 1: Theory. *Meccanica*, 15(1):9–20, March 1980. doi: 10.1007/bf02128236. URL https://doi.org/10.1007/bf02128236.

[115] Giancarlo Benettin, Luigi Galgani, Antonio Giorgilli, and Jean-Marie Strelcyn. Lyapunov characteristic exponents for smooth dynamical systems and for hamiltonian systems; a method for computing all of them. part 2: Numerical application. *Meccanica*, 15(1):21–30, March 1980. doi: 10.1007/bf02128237. URL https://doi.org/10.1007/bf02128237.

[116] V. I. Oseledets. A multiplicative ergodic theorem. characteristic ljapunov, exponents of dynamical systems. *Trans. Moscow Math. Soc.*, 19:179–210, 1968. URL http://mi.mathnet.ru/mmo214.

[117] Efim B. Rozenbaum, Sriram Ganeshan, and Victor Galitski. Lyapunov exponent and out-of-time-ordered correlator's growth rate in a chaotic system. *Phys. Rev. Lett.*, 118(8), February 2017. doi: 10.1103/physrevlett.118.086801. URL https://doi.org/10.1103/physrevlett.118.086801.

[118] Ivan Kukuljan, Sa šo Grozdanov, and Toma ž Prosen. Weak quantum chaos. *Phys. Rev. B*, 96:060301, Aug 2017. doi: 10.1103/PhysRevB.96.060301. URL https://link.aps.org/doi/10.1103/PhysRevB.96.060301.

[119] R. Steinigeweg, A. Khodja, H. Niemeyer, C. Gogolin, and J. Gemmer. Pushing the limits of the eigenstate thermalization hypothesis towards mesoscopic quantum systems. *Phys. Rev. Lett.*, 112:130403, Apr 2014. doi: 10.1103/PhysRevLett.112.130403. URL https://link.aps.org/doi/10.1103/PhysRevLett.112.130403.

[120] Wouter Beugeling, Roderich Moessner, and Masudul Haque. Off-diagonal matrix elements of local operators in many-body quantum systems. *Phys. Rev. E*, 91:012144, Jan 2015. doi: 10.1103/PhysRevE.91.012144. URL https://link.aps.org/doi/10.1103/PhysRevE.91.012144.

[121] Ehsan Khatami, Guido Pupillo, Mark Srednicki, and Marcos Rigol. Fluctuation-dissipation theorem in an isolated system of quantum dipolar bosons after a quench. *Phys. Rev. Lett.*, 111:050403, Jul 2013. doi: 10.1103/PhysRevLett.111.050403. URL https://link.aps.org/doi/10.1103/PhysRevLett.111.050403.

[122] Lev Vidmar and Marcos Rigol. Generalized gibbs ensemble in integrable lattice models. *J. Stat. Mech.*, 2016(6):064007, June 2016. doi: 10.1088/1742-5468/2016/06/064007. URL https://doi.org/10.1088/1742-5468/2016/06/064007.

[123] Fabian H L Essler and Maurizio Fagotti. Quench dynamics and relaxation in isolated integrable quantum spin chains. *J. Stat. Mech.*, 2016(6):064002, June 2016. doi: 10.1088/1742-5468/2016/06/064002. URL https://doi.org/10.1088/1742-5468/2016/06/064002.

[124] Jean-Sébastien Caux. The quench action. *J. Stat. Mech.*, 2016(6):064006, June 2016. doi: 10.1088/1742-5468/2016/06/064006. URL https://doi.org/10.1088/1742-5468/2016/06/064006.

[125] Pasquale Calabrese and John Cardy. Quantum quenches in 1+1 dimensional conformal field theories. *J. Stat. Mech.*, 2016(6):064003, June 2016. doi: 10.1088/1742-5468/2016/06/064003. URL https://doi.org/10.1088/1742-5468/2016/06/064003.

[126] Romain Vasseur and Joel E Moore. Nonequilibrium quantum dynamics and transport: from integrability to many-body localization. *J. Stat. Mech.*, 2016 (6):064010, June 2016. doi: 10.1088/1742-5468/2016/06/064010. URL https://doi.org/10.1088/1742-5468/2016/06/064010.

[127] Mohit Pandey, Pieter W. Claeys, David K. Campbell, Anatoli Polkovnikov, and Dries Sels. Adiabatic eigenstate deformations as a sensitive probe for quantum chaos. *Phys. Rev. X*, 10:041017, Oct 2020. doi: 10.1103/PhysRevX.10.041017. URL https://link.aps.org/doi/10.1103/PhysRevX.10.041017.

[128] C. Cohen-Tannoudji, B. Diu, and F. Laloë. *Quantum Mechanics, Volume 2: Angular Momentum, Spin, and Approximation Methods*. Wiley, 2019. ISBN 9783527345540. URL https://books.google.it/books?id=o_bYEAAAQBAJ.

[129] Rahul Nandkishore and David A. Huse. Many-body localization and thermalization in quantum statistical mechanics. *Annu. Rev. Condens. Matter Phys.*, 6 (1):15–38, March 2015. doi: 10.1146/annurev-conmatphys-031214-014726. URL https://doi.org/10.1146/annurev-conmatphys-031214-014726.

[130] Ehud Altman and Ronen Vosk. Universal dynamics and renormalization in many-body-localized systems. *Annu. Rev. Condens. Matter Phys.*, 6(1):383–409, March 2015. doi: 10.1146/annurev-conmatphys-031214-014701. URL https://doi.org/10.1146/annurev-conmatphys-031214-014701.

[131] Dmitry A. Abanin, Ehud Altman, Immanuel Bloch, and Maksym Serbyn. *Colloquium*: Many-body localization, thermalization, and entanglement. *Rev. Mod. Phys.*, 91(2), May 2019. doi: 10.1103/revmodphys.91.021001. URL https://doi.org/10.1103/revmodphys.91.021001.

[132] J. M. Kosterlitz, D. J. Thouless, and Raymund C. Jones. Spherical model of a spin-glass. *Phys. Rev. Lett.*, 36:1217–1220, May 1976. doi: 10.1103/PhysRevLett.36.1217. URL https://link.aps.org/doi/10.1103/PhysRevLett.36.1217.

[133] Wenhao Wu, D. Bitko, T. F. Rosenbaum, and G. Aeppli. Quenching of the nonlinear susceptibility at $t = 0$ spin glass transition. *Phys. Rev. Lett.*, 71(12): 1919–1922, September 1993. doi: 10.1103/physrevlett.71.1919. URL https://doi.org/10.1103/physrevlett.71.1919.

[134] Subir Sachdev and Jinwu Ye. Gapless spin-fluid ground state in a random quantum heisenberg magnet. *Phys. Rev. Lett.*, 70(21):3339–3342, May 1993. doi: 10.1103/physrevlett.70.3339. URL https://doi.org/10.1103/physrevlett.70.3339.

[135] Juan Maldacena and Douglas Stanford. Remarks on the sachdev-ye-kitaev model. *Phys. Rev. D*, 94(10), November 2016. doi: 10.1103/physrevd.94.106002. URL https://doi.org/10.1103/physrevd.94.106002.

[136] Thomas Scaffidi and Ehud Altman. Chaos in a classical limit of the sachdev-ye-kitaev model. *Phys. Rev. B*, 100(15), October 2019. doi: 10.1103/physrevb.100.155128. URL https://doi.org/10.1103/physrevb.100.155128.

[137] M.J. Werner and P.D. Drummond. Robust algorithms for solving stochastic partial differential equations. *J. Comput. Phys.*, 132(2):312–326, April 1997. doi: 10.1006/jcph.1996.5638. URL https://doi.org/10.1006/jcph.1996.5638.

[138] M. J. Steel, M. K. Olsen, L. I. Plimak, P. D. Drummond, S. M. Tan, M. J. Collett, D. F. Walls, and R. Graham. Dynamical quantum noise in trapped bose-einstein condensates. *Phys. Rev. A*, 58:4824–4835, Dec 1998. doi: 10.1103/PhysRevA.58.4824. URL https://link.aps.org/doi/10.1103/PhysRevA.58.4824.

[139] P.B. Blakie†, A.S. Bradley†, M.J. Davis, R.J. Ballagh, and C.W. Gardiner. Dynamics and statistical mechanics of ultra-cold bose gases using c-field techniques. *Advances in Physics*, 57(5):363–455, September 2008. doi: 10.1080/00018730802564254. URL https://doi.org/10.1080/00018730802564254.

[140] Anatoli Polkovnikov. Phase space representation of quantum dynamics. *Ann. Phys.*, 325(8):1790–1852, August 2010. doi: 10.1016/j.aop.2010.02.006. URL https://doi.org/10.1016/j.aop.2010.02.006.

[141] C. Cohen-Tannoudji, B. Diu, and F. Laloë. *Quantum Mechanics, Volume 1: Basic Concepts, Tools, and Applications*. Wiley, 2019. ISBN 9783527345533. URL https://books.google.it/books?id=tVI_EAAAQBAJ.

[142] Timo Fischer, Clemens Gneiting, and Klaus Hornberger. Wigner function for the orientation state. *New J. Phys.*, 15(6):063004, June 2013. doi: 10.1088/1367-2630/15/6/063004. URL https://doi.org/10.1088/1367-2630/15/6/063004.

[143] Leticia F Cugliandolo, Gustavo S Lozano, and Emilio N Nessi. Non equilibrium dynamics of isolated disordered systems: the classical hamiltonian p-spin model. *J. Stat. Mech.*, 2017(8):083301, aug 2017. doi: 10.1088/1742-5468/aa7dfb. URL https://doi.org/10.1088/1742-5468/aa7dfb.

[144] Thomas Bilitewski, Subhro Bhattacharjee, and Roderich Moessner. Classical many-body chaos with and without quasiparticles. *Phys. Rev. B*, 103(17), May 2021. doi: 10.1103/physrevb.103.174302. URL https://doi.org/10.1103/physrevb.103.174302.

[145] Luis Benet, Fausto Borgonovi, Felix M. Izrailev, and Lea F. Santos. Quantum-classical correspondence of strongly chaotic many-body spin models. *Phys. Rev. B*, 107:155143, Apr 2023. doi: 10.1103/PhysRevB.107.155143. URL https://link.aps.org/doi/10.1103/PhysRevB.107.155143.

[146] Leticia F. Cugliandolo, Jorge Kurchan, and Luca Peliti. Energy flow, partial equilibration, and effective temperatures in systems with slow dynamics. *Phys. Rev. E*, 55(4):3898–3914, April 1997. doi: 10.1103/physreve.55.3898. URL https://doi.org/10.1103/physreve.55.3898.

[147] L. F. Cugliandolo, J. Kurchan, and F. Ritort. Evidence of aging in spin-glass mean-field models. *Phys. Rev. B*, 49(9):6331–6334, March 1994. doi: 10.1103/physrevb.49.6331. URL https://doi.org/10.1103/physrevb.49.6331.

[148] Tommaso Castellani and Andrea Cavagna. Spin-glass theory for pedestrians. *Journal of Statistical Mechanics: Theory and Experiment*, 2005(05):P05012, may 2005. URL https://dx.doi.org/10.1088/1742-5468/2005/05/P05012.

[149] J. Kurchan, G.Parisi, and M.A. Virasoro. Barriers and metastable states as saddle points in the replica approach. *J. Phys. I France*, 3(8):1819–1838, 1993. doi: 10.1051/jp1:1993217. URL https://doi.org/10.1051/jp1:1993217.

[150] D.J. Thouless. Electrons in disordered systems and the theory of localization. *Physics Reports*, 13(3):93–142, October 1974. doi: 10.1016/0370-1573(74)90029-5. URL https://doi.org/10.1016/0370-1573(74)90029-5.

[151] L De Cesare, K Lukierska-Walasek, I Rabuffo, and K Walasek. Replica-symmetry breaking and quantum fluctuation effects in the p-spin interaction spin-glass model with a transverse field. *J. Phys. A: Math. Gen.*, 29(8):1605–1618, April 1996. doi: 10.1088/0305-4470/29/8/009. URL https://doi.org/10.1088/0305-4470/29/8/009.

[152] Shmuel Fishman, D. R. Grempel, and R. E. Prange. Chaos, quantum recurrences, and anderson localization. *Phys. Rev. Lett.*, 49(8):509–512, August 1982. doi: 10.1103/physrevlett.49.509. URL https://doi.org/10.1103/physrevlett.49.509.

[153] P.L. Kapitza. Dynamic stability of the pendulum with vibrating suspension. *Uspekhi Fizicheskih Nauk*, 44(5):7–20, May 1951. doi: 10.3367/ufnr.0044.195105b.0007. URL https://doi.org/10.3367/ufnr.0044.195105b.0007.

[154] S. Iwai, M. Ono, A. Maeda, H. Matsuzaki, H. Kishida, H. Okamoto, and Y. Tokura. Ultrafast optical switching to a metallic state by photoinduced mott transition in a halogen-bridged nickel-chain compound. *Phys. Rev. Lett.*, 91:057401, Jul 2003. doi: 10.1103/PhysRevLett.91.057401. URL https://link.aps.org/doi/10.1103/PhysRevLett.91.057401.

[155] Gregor Jotzu, Michael Messer, Frederik Görg, Daniel Greif, Rémi Desbuquois, and Tilman Esslinger. Creating state-dependent lattices for ultracold fermions by magnetic gradient modulation. *Phys. Rev. Lett.*, 115:073002, Aug 2015. doi: 10.1103/PhysRevLett.115.073002. URL https://link.aps.org/doi/10.1103/PhysRevLett.115.073002.

[156] Victor Galitski and Ian B. Spielman. Spin–orbit coupling in quantum gases. *Nature*, 494(7435):49–54, February 2013. doi: 10.1038/nature11841. URL https://doi.org/10.1038/nature11841.

[157] Mikael C. Rechtsman, Julia M. Zeuner, Yonatan Plotnik, Yaakov Lumer, Daniel Podolsky, Felix Dreisow, Stefan Nolte, Mordechai Segev, and Alexander Szameit. Photonic floquet topological insulators. *Nature*, 496(7444):196–200, April 2013. doi: 10.1038/nature12066. URL https://doi.org/10.1038/nature12066.

[158] André Eckardt. Colloquium: Atomic quantum gases in periodically driven optical lattices. *Rev. Mod. Phys.*, 89:011004, Mar 2017. doi: 10.1103/RevModPhys.89.011004. URL https://link.aps.org/doi/10.1103/RevModPhys.89.011004.

[159] Takashi Oka and Sota Kitamura. Floquet engineering of quantum materials. *Annual Review of Condensed Matter Physics*, 10(1):387–408, 2019. URL https://doi.org/10.1146/annurev-conmatphys-031218-013423.

[160] Dominic V. Else, Bela Bauer, and Chetan Nayak. Floquet time crystals. *Phys. Rev. Lett.*, 117:090402, Aug 2016. doi: 10.1103/PhysRevLett.117.090402. URL https://link.aps.org/doi/10.1103/PhysRevLett.117.090402.

[161] Maximilian Genske and Achim Rosch. Floquet-boltzmann equation for periodically driven fermi systems. *Phys. Rev. A*, 92(6), December 2015. URL https://doi.org/10.1103/physreva.92.062108.

[162] Vedika Khemani, Achilleas Lazarides, Roderich Moessner, and S. L. Sondhi. Phase structure of driven quantum systems. *Phys. Rev. Lett.*, 116:250401, Jun 2016. doi: 10.1103/PhysRevLett.116.250401. URL https://link.aps.org/doi/10.1103/PhysRevLett.116.250401.

[163] N. Y. Yao, A. C. Potter, I.-D. Potirniche, and A. Vishwanath. Discrete time crystals: Rigidity, criticality, and realizations. *Phys. Rev. Lett.*, 118:030401, Jan 2017. doi: 10.1103/PhysRevLett.118.030401. URL https://link.aps.org/doi/10.1103/PhysRevLett.118.030401.

[164] Angelo Russomanno, Alessandro Silva, and Giuseppe E. Santoro. Periodic steady regime and interference in a periodically driven quantum system. *Phys. Rev. Lett.*, 109:257201, Dec 2012. doi: 10.1103/PhysRevLett.109.257201. URL https://link.aps.org/doi/10.1103/PhysRevLett.109.257201.

[165] Roberta Citro, Emanuele G. Dalla Torre, Luca DAlessio, Anatoli Polkovnikov, Mehrtash Babadi, Takashi Oka, and Eugene Demler. Dynamical stability of a many-body kapitza pendulum. *Ann. Phys.*, 360:694–710, 2015. ISSN 0003-4916. doi: https://doi.org/10.1016/j.aop.2015.03.027. URL https://www.sciencedirect.com/science/article/pii/S000349161500130X.

[166] Vladimir Gritsev and Anatoli Polkovnikov. Integrable Floquet dynamics. *SciPost Phys.*, 2:021, 2017. doi: 10.21468/SciPostPhys.2.3.021. URL https://scipost.org/10.21468/SciPostPhys.2.3.021.

[167] Takashi Ishii, Tomotaka Kuwahara, Takashi Mori, and Naomichi Hatano. Heating in integrable time-periodic systems. *Phys. Rev. Lett.*, 120:220602, May 2018. doi: 10.1103/PhysRevLett.120.220602. URL https://link.aps.org/doi/10.1103/PhysRevLett.120.220602.

[168] Tomotaka Kuwahara, Takashi Mori, and Keiji Saito. Floquet–magnus theory and generic transient dynamics in periodically driven many-body quantum systems. *Ann. Phys.*, 367:96–124, April 2016. doi: 10.1016/j.aop.2016.01.012. URL https://doi.org/10.1016/j.aop.2016.01.012.

[169] Takashi Mori, Tomotaka Kuwahara, and Keiji Saito. Rigorous bound on energy absorption and generic relaxation in periodically driven quantum systems. *Phys. Rev. Lett.*, 116(12), March 2016. doi: 10.1103/physrevlett.116.120401. URL https://doi.org/10.1103/physrevlett.116.120401.

[170] Dmitry Abanin, Wojciech De Roeck, Wen Wei Ho, and François Huveneers. A rigorous theory of many-body prethermalization for periodically driven and closed quantum systems. *Communications in Mathematical Physics*, 354(3):809–827, June 2017. doi: 10.1007/s00220-017-2930-x. URL https://doi.org/10.1007/s00220-017-2930-x.

[171] Dmitry A. Abanin, Wojciech De Roeck, Wen Wei Ho, and François Huveneers. Effective hamiltonians, prethermalization, and slow energy absorption in periodically driven many-body systems. *Phys. Rev. B*, 95(1), January 2017. doi: 10.1103/physrevb.95.014112. URL https://doi.org/10.1103/physrevb.95.014112.

[172] Wen Wei Ho, Takashi Mori, Dmitry A. Abanin, and Emanuele G. Dalla Torre. Quantum and classical floquet prethermalization. *Ann. Phys.*, 454:169297, July 2023. doi: 10.1016/j.aop.2023.169297. URL https://doi.org/10.1016/j.aop.2023.169297.

[173] Wade Hodson and Christopher Jarzynski. Energy diffusion and absorption in chaotic systems with rapid periodic driving. *Phys. Rev. Research*, 3(1), March 2021. doi: 10.1103/physrevresearch.3.013219. URL https://doi.org/10.1103/physrevresearch.3.013219.

[174] Simon A. Weidinger and Michael Knap. Floquet prethermalization and regimes of heating in a periodically driven, interacting quantum system. *Scientific Reports*, 7(1), April 2017. doi: 10.1038/srep45382. URL https://doi.org/10.1038/srep45382.

[175] Hamel. Georg duffing, ingenieur: Erzwungene schwingungen bei veränderlicher eigenfrequenz und ihre technische bedeutung. sammlung vieweg. heft 41/42, braunschweig 1918. vi+134 s. *ZAMM - Journal of Applied Mathematics and Mechanics / Zeitschrift für Angewandte Mathematik und Mechanik*, 1(1):72–73, 1921. doi: 10.1002/zamm.19210010109. URL https://doi.org/10.1002/zamm.19210010109.

[176] David Morin. *Introduction to Classical Mechanics*. Cambridge University Press, June 2012. doi: 10.1017/cbo9780511808951. URL https://doi.org/10.1017/cbo9780511808951.

[177] Carl M. Bender and Steven A. Orszag. *Advanced Mathematical Methods for Scientists and Engineers I*. Springer New York, 1999. ISBN 9781475730692. doi: 10.1007/978-1-4757-3069-2. URL https://doi.org/10.1007/978-1-4757-3069-2.

[178] JohTakashi Kanamaru. Duffing oscillator. http://www.scholarpedia.org/article/Duffing_oscillator, 2008. Accessed: July 2, 2023.

[179] Saar Rahav, Ido Gilary, and Shmuel Fishman. Effective hamiltonians for periodically driven systems. *Phys. Rev. A*, 68:013820, Jul 2003. doi: 10.1103/PhysRevA.68.013820. URL https://link.aps.org/doi/10.1103/PhysRevA.68.013820.

[180] G Parisi. On the approach to equilibrium of a hamiltonian chain of anharmonic oscillators. *Europhys. Lett. (EPL)*, 40(4):357–362, November 1997. doi: 10.1209/epl/i1997-00471-9. URL https://doi.org/10.1209/epl/i1997-00471-9.

[181] Gert Aarts, Gian Franco Bonini, and Christof Wetterich. On thermalization in classical scalar field theory. *Nuclear Physics B*, 587(1-3):403–418, October 2000. doi: 10.1016/s0550-3213(00)00447-8. URL https://doi.org/10.1016/s0550-3213(00)00447-8.

[182] Marco Pettini and Monica Cerruti-Sola. Strong stochasticity threshold in nonlinear large hamiltonian systems: Effect on mixing times. *Phys. Rev. A*, 44:975–987, Jul 1991. doi: 10.1103/PhysRevA.44.975. URL https://link.aps.org/doi/10.1103/PhysRevA.44.975.

[183] Marco Pettini. Geometrical hints for a nonperturbative approach to hamiltonian dynamics. *Phys. Rev. E*, 47(2):828–850, February 1993. doi: 10.1103/physreve.47.828. URL https://doi.org/10.1103/physreve.47.828.

[184] Efrat Shimshoni, Giovanna Morigi, and Shmuel Fishman. Quantum zigzag transition in ion chains. *Phys. Rev. Lett.*, 106(1), January 2011. doi: 10.1103/physrevlett.106.010401. URL https://doi.org/10.1103/physrevlett.106.010401.

[185] Pietro Silvi, Gabriele De Chiara, Tommaso Calarco, Giovanna Morigi, and Simone Montangero. Full characterization of the quantum linear-zigzag transition in atomic chains. *Annalen der Physik*, 525(10-11):827–832, July 2013. doi: 10.1002/andp.201300090. URL https://doi.org/10.1002/andp.201300090.

[186] Pietro Silvi, Tommaso Calarco, Giovanna Morigi, and Simone Montangero. *Ab initio* characterization of the quantum linear-zigzag transition using density matrix renormalization group calculations. *Phys. Rev. B*, 89(9), March 2014. doi: 10.1103/physrevb.89.094103. URL https://doi.org/10.1103/physrevb.89.094103.

[187] L.D. Landau and E.M. Lifshitz. *Mechanics: Volume 1*. Course of theoretical physics. Elsevier Science, 1976. ISBN 9780750628969. URL https://books.google.it/books?id=e-xASAehg1sC.

[188] G. Busiello, R. V. Saburova, V. G. Sushkova, and G. P. Chugunova. Nonequilibrium dynamics of quantum spin glass in an AC magnetic field. *Physics of the Solid State*, 46(2):316–325, February 2004. doi: 10.1134/1.1649431. URL https://doi.org/10.1134/1.1649431.

[189] T. R. Kirkpatrick and D. Thirumalai. $p$-spin-interaction spin-glass models: Connections with the structural glass problem. *Phys. Rev. B*, 36(10):5388–5397, October 1987. doi: 10.1103/physrevb.36.5388. URL https://doi.org/10.1103/physrevb.36.5388.

[190] E. Leutheusser. Dynamical model of the liquid-glass transition. *Phys. Rev. A*, 29(5):2765–2773, May 1984. doi: 10.1103/physreva.29.2765. URL https://doi.org/10.1103/physreva.29.2765.

[191] Wolfgang Götze. *Complex Dynamics of Glass-Forming Liquids*. Oxford University Press, December 2008. doi: 10.1093/acprof:oso/9780199235346.001.0001. URL https://doi.org/10.1093/acprof:oso/9780199235346.001.0001.

[192] L. Berthier, L. F. Cugliandolo, and J. L. Iguain. Glassy systems under time-dependent driving forces: Application to slow granular rheology. *Phys. Rev. E*, 63(5), April 2001. doi: 10.1103/physreve.63.051302. URL https://doi.org/10.1103/physreve.63.051302.

[193] Arijit Haldar, Prosenjit Haldar, Surajit Bera, Ipsita Mandal, and Sumilan Banerjee. Quench, thermalization, and residual entropy across a non-fermi liquid to fermi liquid transition. *Phys. Rev. Research*, 2:013307, Mar 2020. doi: 10.1103/PhysRevResearch.2.013307. URL https://link.aps.org/doi/10.1103/PhysRevResearch.2.013307.

[194] Johannes K. Nielsen and Jeppe C. Dyre. Fluctuation-dissipation theorem for frequency-dependent specific heat. *Phys. Rev. B*, 54(22):15754–15761, December 1996. doi: 10.1103/physrevb.54.15754. URL https://doi.org/10.1103/physrevb.54.15754.

[195] R Kubo. The fluctuation-dissipation theorem. *Reports on Progress in Physics*, 29(1):255–284, January 1966. doi: 10.1088/0034-4885/29/1/306. URL https://doi.org/10.1088/0034-4885/29/1/306.

[196] Pietro Silvi, Giovanna Morigi, Tommaso Calarco, and Simone Montangero. Crossover from classical to quantum kibble-zurek scaling. *Phys. Rev. Lett.*, 116 (22), June 2016. doi: 10.1103/physrevlett.116.225701. URL https://doi.org/10.1103/physrevlett.116.225701.

[197] Frank Wilczek. Quantum time crystals. *Phys. Rev. Lett.*, 109:160401, Oct 2012. doi: 10.1103/PhysRevLett.109.160401. URL https://link.aps.org/doi/10.1103/PhysRevLett.109.160401.

[198] Krzysztof Sacha. Modeling spontaneous breaking of time-translation symmetry. *Physical Review A*, 91(3), March 2015. doi: 10.1103/physreva.91.033617. URL https://doi.org/10.1103/physreva.91.033617.

[199] Dominic V. Else, Christopher Monroe, Chetan Nayak, and Norman Y. Yao. Discrete time crystals. *Annual Review of Condensed Matter Physics*, 11(1):467–499, 2020. doi: 10.1146/annurev-conmatphys-031119-050658. URL https://doi.org/10.1146/annurev-conmatphys-031119-050658.

[200] Pranjal Bordia, Henrik Lüschen, Ulrich Schneider, Michael Knap, and Immanuel Bloch. Periodically driving a many-body localized quantum system. *Nature Physics*, 13(5):460–464, January 2017. doi: 10.1038/nphys4020. URL https://doi.org/10.1038/nphys4020.

[201] J. Zhang, P. W. Hess, A. Kyprianidis, P. Becker, A. Lee, J. Smith, G. Pagano, I.-D. Potirniche, A. C. Potter, A. Vishwanath, N. Y. Yao, and C. Monroe. Observation of a discrete time crystal. *Nature*, 543(7644):217–220, March 2017. doi: 10.1038/nature21413. URL https://doi.org/10.1038/nature21413.

[202] Soonwon Choi, Joonhee Choi, Renate Landig, Georg Kucsko, Hengyun Zhou, Junichi Isoya, Fedor Jelezko, Shinobu Onoda, Hitoshi Sumiya, Vedika Khemani, Curt von Keyserlingk, Norman Y. Yao, Eugene Demler, and Mikhail D. Lukin. Observation of discrete time-crystalline order in a disordered dipolar many-body system. *Nature*, 543(7644):221–225, March 2017. doi: 10.1038/nature21426. URL https://doi.org/10.1038/nature21426.

[203] Jared Rovny, Robert L. Blum, and Sean E. Barrett. Observation of discrete-time-crystal signatures in an ordered dipolar many-body system. *Physical Review Letters*, 120(18), May 2018. doi: 10.1103/physrevlett.120.180603. URL https://doi.org/10.1103/physrevlett.120.180603.

[204] Alfred Shapere and Frank Wilczek. Classical time crystals. *Phys. Rev. Lett.*, 109: 160402, Oct 2012. doi: 10.1103/PhysRevLett.109.160402. URL https://link.aps.org/doi/10.1103/PhysRevLett.109.160402.

[205] Haruki Watanabe and Masaki Oshikawa. Absence of quantum time crystals. *Phys. Rev. Lett.*, 114:251603, Jun 2015. doi: 10.1103/PhysRevLett.114.251603. URL https://link.aps.org/doi/10.1103/PhysRevLett.114.251603.

[206] Vedika Khemani, Achilleas Lazarides, Roderich Moessner, and S. L. Sondhi. Phase structure of driven quantum systems. *Phys. Rev. Lett.*, 116:250401, Jun 2016. doi: 10.1103/PhysRevLett.116.250401. URL https://link.aps.org/doi/10.1103/PhysRevLett.116.250401.

[207] C. W. von Keyserlingk and S. L. Sondhi. Phase structure of one-dimensional interacting floquet systems. ii. symmetry-broken phases. *Phys. Rev. B*, 93:245146, Jun 2016. doi: 10.1103/PhysRevB.93.245146. URL https://link.aps.org/doi/10.1103/PhysRevB.93.245146.

[208] H. Haffner, C. Ross, and R. Blatt. Quantum computing with trapped ions. *Phys. Rep.*, 469(4):155–203, Dec 2008. ISSN 0370-1573. doi: 10.1016/j.physrep.2008.09.003. URL http://dx.doi.org/10.1016/j.physrep.2008.09.003.

[209] T Lahaye, C Menotti, L Santos, M Lewenstein, and T Pfau. The physics of dipolar bosonic quantum gases. *Rep. Prog. Phys.*, 72(12):126401, nov 2009. doi: 10.1088/0034-4885/72/12/126401. URL https://doi.org/10.1088/0034-4885/72/12/126401.

[210] M. Saffman, T. G. Walker, and K. Mølmer. Quantum information with rydberg atoms. *Rev. Mod. Phys.*, 82:2313–2363, Aug 2010. doi: 10.1103/RevModPhys.82.2313. URL https://link.aps.org/doi/10.1103/RevModPhys.82.2313.

[211] Helmut Ritsch, Peter Domokos, Ferdinand Brennecke, and Tilman Esslinger. Cold atoms in cavity-generated dynamical optical potentials. *Rev. Mod. Phys.*, 85:553–601, Apr 2013. doi: 10.1103/RevModPhys.85.553. URL https://link.aps.org/doi/10.1103/RevModPhys.85.553.

[212] Hannes Bernien, Sylvain Schwartz, Alexander Keesling, Harry Levine, Ahmed Omran, Hannes Pichler, Soonwon Choi, Alexander S. Zibrov, Manuel Endres, Markus Greiner, Vladan Vuletić, and Mikhail D. Lukin. Probing many-body dynamics on a 51-atom quantum simulator. *Nature*, 551(7682):579–584, November 2017. doi: 10.1038/nature24622.

[213] C. Monroe, W. C. Campbell, L.-M. Duan, Z.-X. Gong, A. V. Gorshkov, P. W. Hess, R. Islam, K. Kim, N. M. Linke, G. Pagano, P. Richerme, C. Senko, and N. Y. Yao. Programmable quantum simulations of spin systems with trapped ions. *Reviews of Modern Physics*, 93(2), April 2021. doi: 10.1103/revmodphys.93.025001. URL https://doi.org/10.1103/revmodphys.93.025001.

[214] Farokh Mivehvar, Francesco Piazza, Tobias Donner, and Helmut Ritsch. Cavity qed with quantum gases: new paradigms in many-body physics. *Adv. Phys.*, 70 (1):1–153, Jan 2021. ISSN 1460-6976. doi: 10.1080/00018732.2021.1969727. URL http://dx.doi.org/10.1080/00018732.2021.1969727.

[215] G Pagano, P W Hess, H B Kaplan, W L Tan, P Richerme, P Becker, A Kyprianidis, J Zhang, E Birckelbaw, M R Hernandez, Y Wu, and C Monroe. Cryogenic trapped-ion system for large scale quantum simulation. *Quantum Science and Technology*, 4(1):014004, October 2018. doi: 10.1088/2058-9565/aae0fe. URL https://doi.org/10.1088/2058-9565/aae0fe.

[216] Angelo Russomanno, Fernando Iemini, Marcello Dalmonte, and Rosario Fazio. Floquet time crystal in the lipkin-meshkov-glick model. *Phys. Rev. B*, 95:214307, Jun 2017. doi: 10.1103/PhysRevB.95.214307. URL https://link.aps.org/doi/10.1103/PhysRevB.95.214307.

[217] Federica Maria Surace, Angelo Russomanno, Marcello Dalmonte, Alessandro Silva, Rosario Fazio, and Fernando Iemini. Floquet time crystals in clock models. *Phys. Rev. B*, 99:104303, Mar 2019. doi: 10.1103/PhysRevB.99.104303. URL https://link.aps.org/doi/10.1103/PhysRevB.99.104303.

[218] Francisco Machado, Dominic V. Else, Gregory D. Kahanamoku-Meyer, Chetan Nayak, and Norman Y. Yao. Long-range prethermal phases of nonequilibrium matter. *Phys. Rev. X*, 10:011043, Feb 2020. doi: 10.1103/PhysRevX.10.011043. URL https://link.aps.org/doi/10.1103/PhysRevX.10.011043.

[219] Mario Collura, Andrea De Luca, Davide Rossini, and Alessio Lerose. Discrete time-crystalline response stabilized by domain-wall confinement, 2021.

[220] Andrea Pizzi, Johannes Knolle, and Andreas Nunnenkamp. Higher-order and fractional discrete time crystals in clean long-range interacting systems. *Nature Communications*, 12(1):2341, Apr 2021. ISSN 2041-1723. doi: 10.1038/s41467-021-22583-5. URL https://doi.org/10.1038/s41467-021-22583-5.

[221] Krzysztof Giergiel, Arkadiusz Kosior, Peter Hannaford, and Krzysztof Sacha. Time crystals: Analysis of experimental conditions. *Physical Review A*, 98(1), July 2018. doi: 10.1103/physreva.98.013613. URL https://doi.org/10.1103/physreva.98.013613.

[222] Shane Kelly, Eddy Timmermans, Jamir Marino, and S.-W. Tsai. Stroboscopic aliasing in long-range interacting quantum systems. *SciPost Physics Core*, 4(3), September 2021. doi: 10.21468/scipostphyscore.4.3.021. URL https://doi.org/10.21468/scipostphyscore.4.3.021.

[223] Manuel H. Muñoz-Arias, Karthik Chinni, and Pablo M. Poggi. Floquet time crystals in driven spin systems with all-to-all p-body interactions, 2022.

[224] H.J. Lipkin, N. Meshkov, and A.J. Glick. Validity of many-body approximation methods for a solvable model. *Nuclear Physics*, 62(2):188–198, February 1965. doi: 10.1016/0029-5582(65)90862-x. URL https://doi.org/10.1016/0029-5582(65)90862-x.

[225] A. Campa, T. Dauxois, D. Fanelli, and S. Ruffo. *Physics of Long-Range Interacting Systems*. Oxford University Press, August 2014. doi: 10.1093/acprof:oso/9780199581931.001.0001. URL https://doi.org/10.1093/acprof:oso/9780199581931.001.0001.

[226] Pedro Ribeiro, Julien Vidal, and Rémy Mosseri. Exact spectrum of the lipkin-meshkov-glick model in the thermodynamic limit and finite-size corrections. *Physical Review E*, 78(2), August 2008. doi: 10.1103/physreve.78.021106. URL https://doi.org/10.1103/physreve.78.021106.

[227] Nicolò Defenu. Metastability and discrete spectrum of long-range systems. *Proceedings of the National Academy of Sciences*, 118(30):e2101785118, 2021. doi: 10.1073/pnas.2101785118. URL https://www.pnas.org/doi/abs/10.1073/pnas.2101785118.

[228] D. A. Wisniacki, M. Saraceno, F. J. Arranz, R. M. Benito, and F. Borondo. Poincaré-birkhoff theorem in quantum mechanics. *Phys. Rev. E*, 84:026206, Aug 2011. doi: 10.1103/PhysRevE.84.026206. URL https://link.aps.org/doi/10.1103/PhysRevE.84.026206.

[229] Monica Cerruti-Sola, Guido Ciraolo, Roberto Franzosi, and Marco Pettini. Riemannian geometry of hamiltonian chaos: Hints for a general theory. *Phys. Rev. E*, 78:046205, Oct 2008. doi: 10.1103/PhysRevE.78.046205. URL https://link.aps.org/doi/10.1103/PhysRevE.78.046205.

[230] Alex Kamenev. *Field theory of non-equilibrium systems*. Cambridge University Press, 2011.